Fouling in Reverse Electrodialysis

MONITORING, MODELING, AND CONTROL

Diego Pintossi

PhD Thesis

Fouling in reverse electrodialysis

Monitoring, modeling, and control

Diego Pintossi

Fouling in reverse electrodialysis

Monitoring, modeling, and control

PROEFSCHRIFT

ter verkrijging van de graad van doctor aan de Technische
Universiteit Eindhoven, op gezag van de rector magnificus
prof.dr.ir. F.P.T. Baaijens, voor een commissie aangewezen door
het College voor Promoties, in het openbaar te verdedigen op
vrijdag 11 juni 2021 om 13:30 uur

door

Diego Pintossi

geboren te Bergamo, Italië

Dit proefschrift is goedgekeurd door de promotoren en de samenstelling van de promotiecommissie is als volgt:

voorzitter:	prof.dr.eng. F. Gallucci
1e promotor:	prof.dr.ir. D.C. Nijmeijer
2e promotor:	dr.ing. Z. Borneman
leden:	prof.dr.ir. R. Tuinier
	prof.dr. A. Verliefde (Universiteit Ghent)
	prof.dr.eng. G.D.M. Micale (Università degli Studi di Palermo)
	dr.ir. J.P.A. Heuts

Het onderzoek of ontwerp dat in dit proefschrift wordt beschreven is uitgevoerd in overeenstemming met de TU/e Gedragscode Wetenschapsbeoefening.

If there is magic on this planet, it is contained in water

- Loren Eiseley -

Table of Contents

Summary

Fouling in Reverse Electrodialysis
Monitoring, Modeling, and Control

Salinity gradient energy (SGE) is an energy source derived from the controlled mixing of low and high concentration water streams, e.g., river and seawater. **Reverse electrodialysis** (RED) is an electro-membrane process to harvest SGE. In RED, cation exchange membranes (CEMs) and anion exchange membranes (AEMs) are stacked alternately to create compartments where the sea and river water flow. The salinity gradient across the ion exchange membranes results in a potential difference over the membranes. When the external circuit is closed by connecting a load to the electrodes, this potential difference is used to drive an ionic current through the stack. This ionic current is converted into an electronic current by a suitable redox couple recirculated in the electrode compartments. If RED is used to harvest SGE from natural salinity gradients, undesired compounds in the feedwaters (e.g., colloids, multivalent ions, organic molecules, microorganisms) interact with the membranes leading to a decreased power density output. These phenomena are commonly referred to as **fouling**. An overview on these topics is given in Chapter 1.

In Chapter 2, the use of electrochemical impedance spectroscopy (EIS) for **fouling monitoring** at the RED stack level is presented. EIS was enabled by a local reduction in the active area of the stack to 1 cm^2 to achieve fast and reliable impedance measurements. Fouling and cleaning experiments with a model compound (sodium dodecylbenzenesulfonate, SDBS) showed how fouling evolved on different time scales for the AEM and CEM. First, the ohmic resistance of the AEM increased rapidly. Then, the non-ohmic component of the AEM resistance increased when SDBS domains started to grow on the membrane. On a longer time, a similar effect was observed for the non-ohmic resistance of the CEM, driven by the electric field, despite the unfavorable electrostatic repulsion between negative sulfonate charges inside the cation exchange membrane and negative foulant. Upon cleaning, the ohmic resistance recovered only partially, indicating irreversible fouling of the AEM due to SDBS absorption in the membrane, while the non-ohmic components of the AEM and CEM resistances recovered

completely, although recovery was much faster for the CEM than for the AEM. It is concluded that fouling monitoring with EIS enhances fouling management strategies by indicating in an early stage the need for cleaning and by quantifying the effect of cleaning.

In Chapter 3, the benefit of a zwitterionic surface chemistry to obtain **anti-fouling AEMs** is demonstrated. Commercial AEMs were coated with either polydopamine followed by grafting of zwitterionic monomers on its surface or with a modified polydopamine coating as surface initiator for atom transfer radical polymerization (ATRP) with sulfobetaine to graft zwitterionic brushes on the membrane surface. Both the polydopamine and the zwitterionic layers hardly affected the permselectivity nor the electrical resistance thanks to the net neutral charge of the coating and the thin grafting layers which were made by using short deposition and reaction times. The membrane hydrophilicity clearly increased offering a method to better mitigate fouling. The fouling resistance for both zwitterionic monomers and zwitterionic brushes membranes was improved. Where the zwitterionic monomers delayed the fouling onset, the zwitterionic brushes did not only cause a delay in the fouling onset but also slowed down the fouling layer growth. It was concluded that anion exchange membranes modified with zwitterionic layers showed a better and faster recovery after cleaning than unmodified AEMs.

In Chapter 4, a validated RED model and experimental investigation is presented that shows that **electrode segmentation** potentially reduces operating cost or capital expenditure. Operating cost likely decreased by increasing net energy efficiency at a given net power density (43 % relative increase in efficiency), which is beneficial in case of high costs for water pre-treatment to control fouling. Capital expenditure likely lowers at high net energy efficiencies by increasing the net power density with electrode segmentation decreasing the membrane area needed. The highest power density and efficiency gain were attained when optimizing the external ohmic loads for overall maximum power, rather than sequentially maximizing the power output of individual segments. At 40 % net energy efficiency, the net power density output for a segmented electrode was 39 % higher (0.67 $W \cdot m^{-2}$) than for a single electrode (0.47 $W \cdot m^{-2}$). This increase in net power density at equal net energy efficiency resulted from combining the increase in available power due to shorter residence time and the increased ion exchange enabled by electrode segmentation.

Our experiments on the effect of **multivalent anions** on AEMs in RED with standard grade and monovalent ion selective membranes (Chapter 5) shows that sulfate deteriorates RED performance due to the decreased open circuit voltage resulting from uphill transport and loss in membrane permselectivity, and increased membrane resistance during long term exposure to the multivalent anions. While these effects of multivalent anions are similar to those of multivalent cations, the narrower range of hydrated radii and hydration energies for anions resulted not only in a smaller electrical resistance increase over time, but also in lower monovalent ion selectivity, which is detrimental for the open circuit voltage. When sulfate was present on both sides of the anion exchange membranes, for the standard grade membranes Fujifilm AEM Type 10 the gross power density losses were up to 25 %. The monovalent ion selective membrane ACS of Neosepta reduced the uphill transport of multivalent ions, but it did so at the expense of higher electrical resistance, which increased even further in the presence of sulfate. Therefore, the normalized power density of the monovalent ion selective ACS was not higher than obtained with standard grade membranes. Although they were subject to the negative effect of uphill transport and loss in permselectivity in the presence of sulfate, standard grade membranes AEM type 10 of Fujifilm showed a limited increase in resistance, in the presence of multivalent anions. Thanks to its intermediate resistance and permselectivity, the standard grade type 10 membrane matched the performance of the monovalent ion selective ACS membrane. The results of the present study highlight the need to consider the negative effect of multivalent anions when developing new anion membranes that find a balance between RED performance and fouling.

Chapter 6 presents a **model** to predict **RED** performance considering the negative effects of the presence of **magnesium and sulfate** ions in the feedwaters on power production with RED. The presence of multivalent ions resulted in loss of power due to several effects that were now included in the model. The uphill transport was accounted for by balancing two voltage sources. The increased membrane resistance was introduced based on experimental resistance and selectivity data while the membrane permselectivity loss was introduced by empirical fitting of experimental data. The change in conductivity of the feedwaters was included by a correlation between total salt content and conductivity. Validation with experimental and literature data was performed, and it was confirmed that the model effectively described RED performance in the presence of sulfate or magnesium ions. Simulations of RED in various flow configurations and with a variety of feedwater compositions showed the importance of designing RED processes with the complexity of

natural feedwaters in mind. Simulated RED behavior in the presence of $MgSO_4$ drastically differed from the simulated behavior for feedwaters containing only NaCl. In particular, the advantages of electrode segmentation and multi-staging were partially mitigated by multivalent ions as the inhomogeneity of the electromotive force was reduced by uphill transport and permselectivity loss. The developed RED model is not only able to correctly describe experimental data but can also predict RED performance at specific process conditions and as such provides a very valuable tool to design RED process systems.

Finally, Chapter 7 presents the conclusions and outlook of RED based on the scientific advances presented in this dissertation. For fouling monitoring, optimization of the current design, measurement of the local impedance, and development of a RED fouling index are presented as tools. For membrane development, the use of genetic algorithms paired with high-throughput platforms is proposed to optimize RED performance, anti-fouling resistance, and membrane cost simultaneously. Finally, for RED modeling, stack modeling including ionic short-circuit currents is proposed with improvements with respect to previous modeling attempts, and data-driven approaches based on machine learning are proposed to include the effect of fouling in RED models.

Chapter 1

Introduction
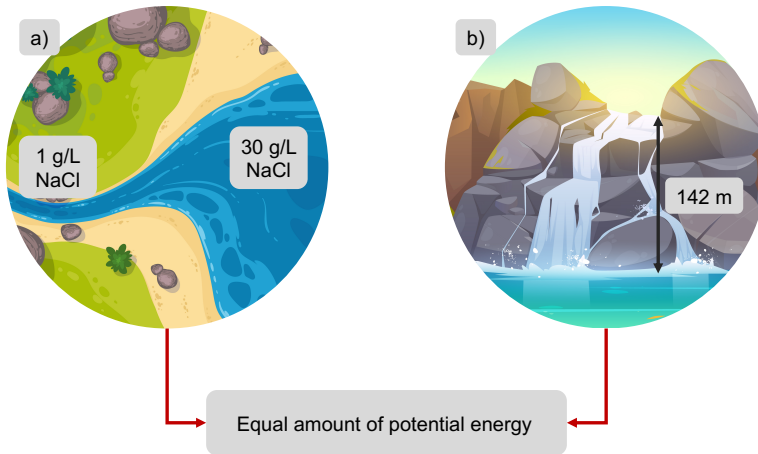
Figure 1.1 a) a river estuary where fresh water (salt content: 1 g L^{-1} NaCl) mixes with seawater (salt content: 30 g L^{-1}). b) a waterfall where water falls from a height of 142 m. Image sources: [1,2].

When considering a river (artificial salt content: 1 g L^{-1}) flowing into the sea (artificial salt content: 30 g L^{-1}), the potential energy stored in the salinity gradient is equal to that available with hydropower when there is a 142 m height difference between the reservoirs (Figure 1.1) [3]. To put this figure into perspective, the Three Gorges Dam on the Yangtze river (Hubei province, China) is 181 m high [4].

1.1 Context of the research

Climate change is a major challenge facing all humankind [5]. It is the consequence of increasing levels of CO_2 and other greenhouse gases (GHG) in the atmosphere, mainly deriving from the combustion of fossil fuels to meet the global energy demand [5,6]. To limit climate change, it is fundamental to pivot to renewable energy sources to satisfy the energy demand without harmful GHG emissions [7]. Solar and wind are examples of well-known renewable energy sources that experienced a meteoric rise in the past decades [8]. However, despite their enormous potential and sustained growth, solar and wind energy still represent just a fraction of the global electricity supply (approximately 10 % for solar and 20 % for wind) [9]. Additionally, their intermittent nature creates challenges for their integration in the energy mix [10]. Therefore, it is important to exploit all existing sources of renewable energy. Another promising source of sustainable energy, albeit little-known, is salinity gradient energy (SGE), also referred to as blue energy. SGE is the generation of electricity from the mixing of water streams with different salinity content, e.g., river and seawater [11]. The mixing of solutions containing different salt concentrations is a spontaneous process, thanks to the entropy gain associated with the mixing process [11]. At a global scale, SGE from natural salinity gradients has a theoretical potential to produce 2.6 TW of renewable power [12]. The hydrological cycle makes SGE a renewable energy source, and, unlike solar and wind, SGE is less susceptible to daily fluctuations in power output, although seasonal fluctuations are present.

The two main processes to harvest SGE are pressure retarded osmosis (PRO), where the osmotic pressure difference is the driving force, and reverse electrodialysis (RED), where the voltage difference is the driving force. Post et al. evaluated PRO and RED with a model comparison and found that PRO is best suited for power production using concentrated saline brines [12], whereas RED shows more potential when the salinity gradient stems from the difference in salt concentration between river and seawater [12]. RED is the process investigated in this thesis.

1.2 Reverse electrodialysis

RED is an electro-membrane process based on ion exchange membranes (IEMs) [13]. Figure 1.1 provides a schematic illustration of the RED principle.

Anion exchange membranes (AEMs), which selectively transport anions, and cation exchange membranes (CEMs), which selectively transport cations, are stacked alternately.
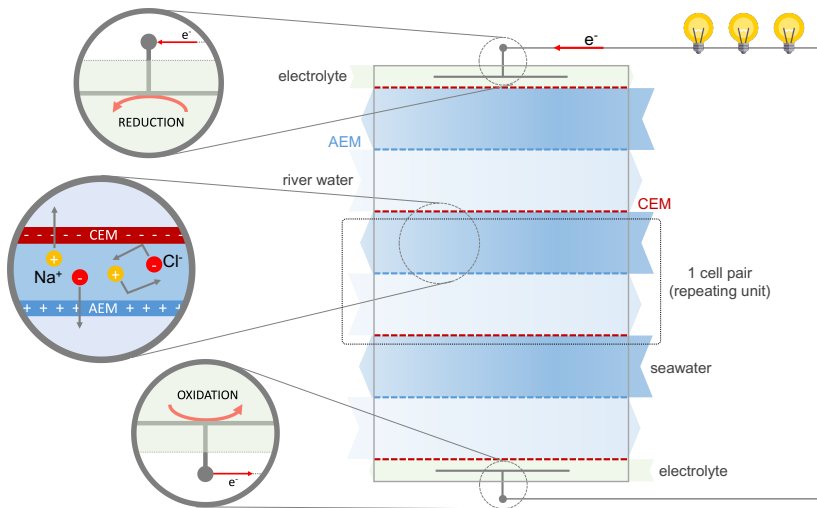
Figure 1.2 Schematic illustration of the RED principle. The inset shows the selective nature of the IEMs.

The space between the membranes is kept open by non-conductive spacers (for flat membranes) or by protruding structures on the membrane surface (for profiled membranes) to obtain the feedwater channels [14]. In these channels, river (with low salt concentration) and seawater (with high salt concentration) are flowing alternately. The concentration gradient across the IEMs results in a voltage difference over each membrane. When multiple membranes are stacked between two electrodes, the total voltage generated is the sum of the individual voltage differences [15]. When the external circuit connecting the two electrodes is closed, the voltage difference generated by the salinity gradients drives an ionic current through the stack and an electronic current through the external circuit, which can be used to power an external load. The conversion between the ionic and electronic current can be operated by a suitable redox couple which is recirculated in the electrode compartments at the two ends of the stack [16].

The RED concept was first published in Nature in 1954 by Pattle [17]. However, only few studies followed its publication. RED saw renewed interest in the '70s and '80s, but the cost of the membranes prevented this technology from being developed further [18]. In recent years, a RED renaissance took place, with the research carried out at Wetsus, European centre of excellence for sustainable water technology (The Netherlands) within the blue energy research theme, in parallel with efforts by the spin-off company REDstack BV (The Netherlands) to develop RED into a mainstream energy source. In 2014, REDstack inaugurated the world first RED demo pilot (50 kW) at the Afsluitdijk (The

Netherlands), where fresh water from the IJsselmeer and seawater from the Wadden sea are used as natural feedwaters for power generation [19].

1.3 Ion exchange membranes

Together with the salinity gradient, the IEMs are a fundamental element of RED. IEMs find application in many other processes, such as electrodialysis (ED), Donnan dialysis, chlor-alkali process, and fuel cells [20]. These non-porous membranes have fixed charge groups to allow selective transport of ions with opposite charge (counter-ions) due to Donnan exclusion of ions with the same charge (co-ions). In real membranes, exclusion of the co-ions is not perfect, and a small concentration of co-ions (much lower than in the external solution) is found inside the membrane. The membrane permselectivity is a macroscopic parameter describing the membrane ability to selectively exclude co-ions. The fixed charge groups have cationic nature in the AEMs (ternary ammonium groups for weakly basic membranes, quaternary ammonium groups for strongly basic membranes), and anionic nature for the cation exchange membranes (carboxylic acid groups for weakly acid membranes, sulfonic acid groups for strongly acidic membranes). There are two types of IEMs: homogeneous membranes, where fixed charges are evenly distributed throughout the polymeric matrix, and heterogeneous membranes, where charged resins are blended with uncharged polymers, leading to ionically conductive domains dispersed in a non-conductive matrix [21].
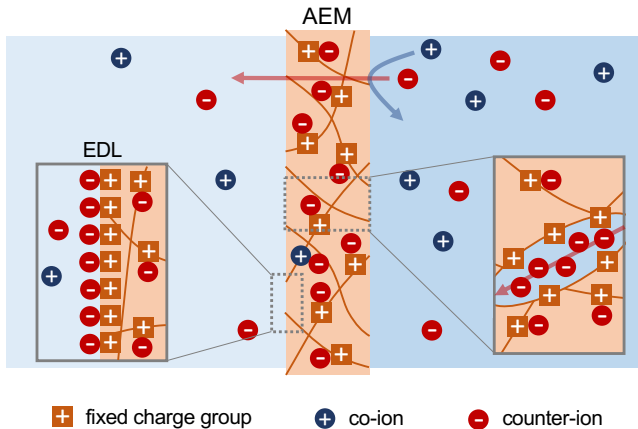
Figure 1.3 Homogeneous anion exchange membrane structure with detail of the electrical double layer (EDL, left) and ion transport channels (right).

When an ion exchange membrane is immersed in a salt solution, an electrical double layer (EDL) is formed at the membrane-solution interface (Figure 1.3), and the difference in

counter-ion concentration between the external solution and the membrane phase, where counter-ions are present to maintain electroneutrality with the fixed charge groups, leads to an electric potential difference across the membrane-solution interface (Donnan potential) [15]. If a salt concentration gradient is in place across the membrane, the Donnan potentials at the two membrane-solution interfaces are not equal. Thus, a net potential difference is established across the membrane, which is the electromotive force driving the RED process [15]. Ion transport through the membranes takes place via nano-sized channels and cavities containing salt solution, where the ions can move (Figure 1.3) [22]. The membrane electrical resistance is a macroscopic parameter describing the ease of ion transport through the membrane.

1.4 RED theory

The theoretical amount of energy that can be harvested from a salinity gradient is expressed by the Gibbs free energy of mixing:

$$\Delta G_{mix} = G_b - (G_{rw} + G_{sw}) \tag{Eq. 1.1}$$

Where G_b is the Gibbs free energy (J) of the brackish solution obtained after mixing, while G_{rw} and G_{sw} are the Gibbs free energy of river and seawater, respectively [11]. The Gibbs free energy of mixing can be calculated as:

$$\Delta G_{mix} = -T \cdot \Delta S = -T \cdot (S_b - S_{rw} - S_{sw}) \tag{Eq. 1.2}$$

$$S = -Rn_{TOT} \sum_i x_i ln(\gamma_i x_i) \tag{Eq. 1.3}$$

Where S is the entropy (J·K⁻¹), T is the absolute temperature (K), R is the universal gas constant (J·mol·K⁻¹), n_{TOT} is the total number of moles (mol), x_i is the fraction of component i (-), and γ_i is the molar activity coefficient of component i (-) to account for the non-ideality of the solutions [23].

The modified Nernst equation expresses the electromotive force (V) generated by the salinity gradient across a cell pair, accounting for the non-ideal permselectivity of the membranes:

$$E = (\alpha_{AEM} + \alpha_{CEM}) \frac{RT}{zF} ln \left(\frac{\gamma_{sw} c_{sw}}{\gamma_{rw} c_{rw}} \right) \tag{Eq. 1.4}$$

Where α is the permselectivity of AEM and CEM (-), z is the ion valence (-), F is the Faraday constant (C·mol⁻¹), and c is the salt concentration (mol·m⁻³).
The stack resistance (Ω) is given by:

$$R_{stack} = \frac{N_{cp}}{A} \left(R_{AEM} + R_{CEM} + \frac{1}{f} \frac{d_{rw}}{\kappa_{rw}} + \frac{1}{f} \frac{d_{sw}}{\kappa_{sw}} \right) + R_{blank} \tag{Eq. 1.5}$$

Where N_{cp} is the number of cell pairs in the stack (-), A is the active area (m²), R_{AEM} and R_{CEM} are the area electrical resistance of the AEM and CEM (Ω·m²), respectively, f is the spacer shadow factor (-), a parameter accounting for the presence of non-conductive spacers, d is the water compartment thickness (m), κ is the conductivity of the feedwaters (S·m⁻¹), and R_{blank} is the electrical resistance of the shielding CEMs and electrodes (Ω), which becomes negligible for large values of N_{cp}/A.

When the external circuit between the electrodes is closed, the current (A) is:

$$I = \frac{E}{R_{stack} + R_{load}} = \frac{E - U}{R_{stack}} \qquad \text{(Eq. 1.6)}$$

Where U is the ohmic voltage drop across the external load (V) and R_{load} is the external load (Ω).

The gross power produced by the stack is given by:

$$P_{gross} = U \cdot I \qquad \text{(Eq. 1.7)}$$

The power density is derived by dividing the power by the total membrane area ($A_{total} = 2 \cdot A \cdot N_{cp}$, accounting for the area of CEMs and AEMs in all cell pairs):

$$P_d = \frac{P}{2 \cdot A \cdot N_{cp}} \qquad \text{(Eq. 1.8)}$$

In Eq. 1.3, the flow rates of the feedwaters (m³·s⁻¹) can be used instead of the compartment volumes (m³). Then, n_{TOT} becomes the number of moles per second (mol·s⁻¹). Thus, the entropy is calculated per unit of time (W·K⁻¹), and Eq. 1.2 expresses the available power (W), which can be directly compared to the stack power output to calculate the energy efficiency of RED.

The (gross) energy efficiency (%) considers the gross power produced compared to the total available Gibbs free energy at the inlet (assuming complete mixing):

$$\eta_{energy} = 100 \cdot \frac{P_{gross}}{\Delta G_{in}} \qquad \text{(Eq. 1.9)}$$

Finally, to obtain net power density values, the pumping losses (W) are calculated as the energy consumed to pump the seawater and the river water:

$$P_{pump} = \phi_{rw}\Delta P_{rw} + \phi_{sw}\Delta P_{sw} \qquad \text{(Eq. 1.10)}$$

$$\Delta P_i = K \frac{W\phi_i}{Ld_i^{\,3}} \qquad \text{(Eq. 1.11)}$$

Where ΔP is the pressure drop between inlet and outlet (Pa), ϕ is the flow rate of the feedwater (m³·s⁻¹), and K is a fitting coefficient for experimental pressure losses (Pa·s).

By subtracting the pumping losses from the gross power, the net power (W) is obtained:

$$P_{net} = P_{gross} - P_{pump} \qquad \text{(Eq. 1.12)}$$

1.5 RED applications

The electrochemical cell illustrated in Figure 1.2 can operate in three different modes depending on the sign and magnitude of the external load voltage or applied voltage (Figure 1.4): ED, RED, and assisted-RED (ARED) [24].
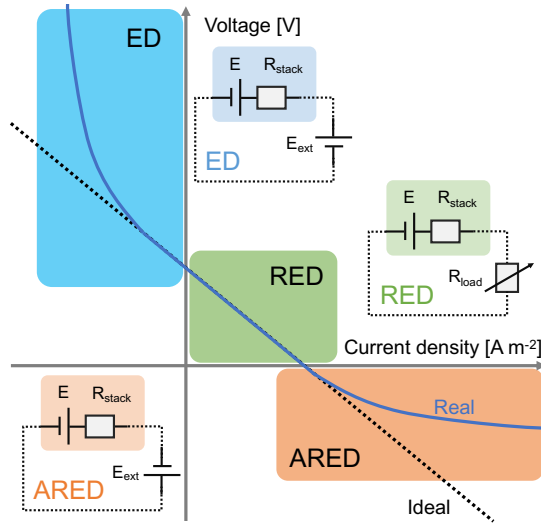
Figure 1.4 Working regimes for a (R)ED stack and their corresponding electrical circuits. IV curves adapted from [24]. Current and voltage sign conventions are chosen for positive power in RED mode.

In the RED regime, an external load across the stack closes the external circuit between the end electrodes, leading to an ionic current flowing through the membranes, with ions moving from the seawater to the river water. The ohmic voltage drop across the external voltage is lower than the electromotive force available from the salinity gradient. In RED mode, energy is harvested, and the salinity gradient is depleted. In RED, the IV curve is linear with the possibility of small deviations from the linear ohmic behavior (based on Ohm's law: $V = R \cdot I$) at high current densities, where the increased conductivity of river water can decrease the stack resistance (slope of the curve), as expressed by Eq. 1.5 [23]. In the assisted-RED (ARED) regime, ions still move from the sea to the river, but the mixing is not spontaneous as it is enhanced by an external energy input. For this purpose, an external voltage with the same polarity as the electromotive force generated by the salinity gradient is applied to the stack. In ARED, deviations from linearity are observed in the IV curve, especially at high current densities. As observed by Vanoppen et al., the

decreased resistance of the stack is the consequence of increased river water conductivity and decreased membrane resistance at higher concentrations of the solutions [22,24].

Finally, in the ED regime, the external voltage applied to the stack has the opposite polarity and ions move from the low concentration to the high concentration compartment. Therefore, in ED mode, energy is spent to desalinate the low concentration feedwater. In ED, the IV curve also deviates from the linear ohmic behavior at increasing (negative) current densities, when the limiting current density (LCD) is reached [24].

The use of RED to harvest SGE has been studied in a variety of scenarios and in combination with other technologies, such as reverse osmosis (RO), membrane capacitive deionization (MCDI), and water electrolysis. Figure 1.5 and Figure 1.6 show an assortment of RED applications.
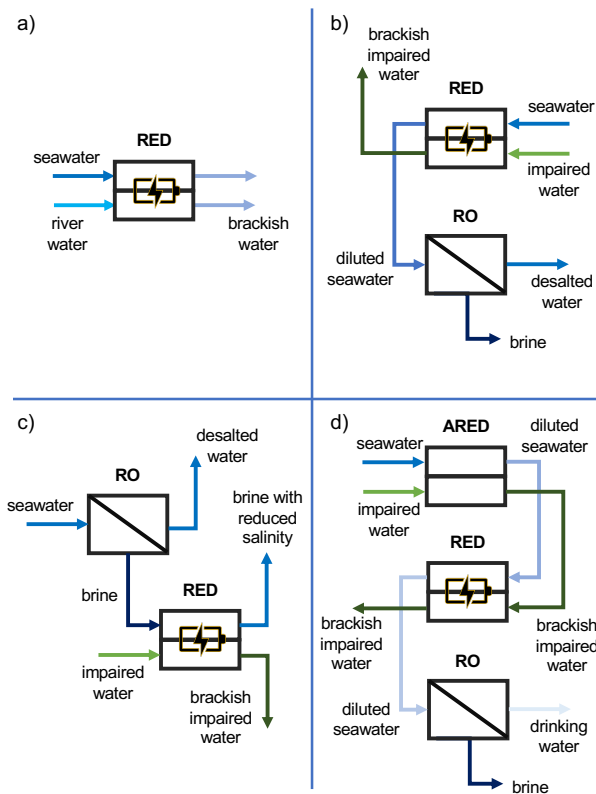
Figure 1.5 Illustration of RED applications: a) energy harvesting from natural salinity gradients; b) RED-RO hybrid system to recover energy and reduce seawater salinity before desalination; c) RO-RED hybrid system to recover energy and address the brine management issue; d) ARED-RED-RO hybrid system, where ARED increases the conductivity of the impaired water before energy recovery and seawater desalination.
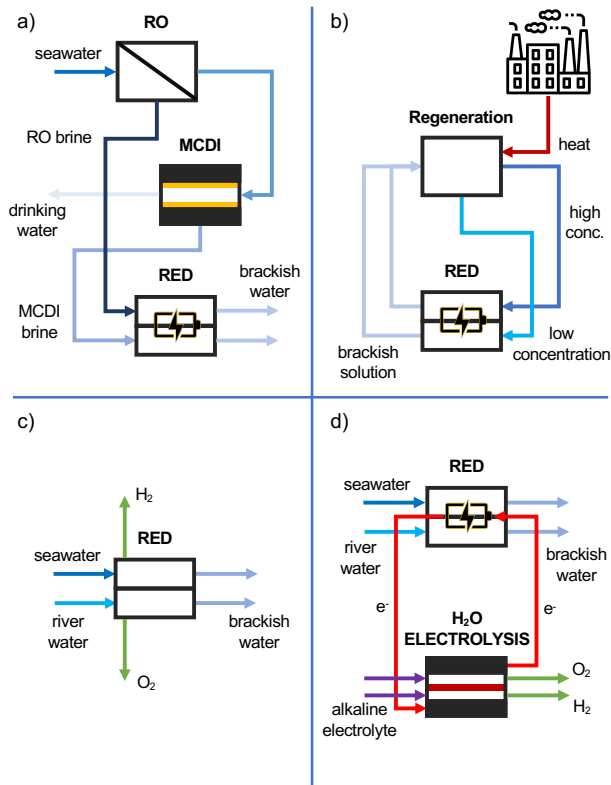
Figure 1.6 Illustration of RED applications: a) RO-MCDI-RED hybrid system to recover energy and address the issue of brine management; b) thermolytic salt RED engine to harvest energy from waste heat produced by industrial processes; c) green hydrogen production at the RED stack cathode; d) green hydrogen production from SGE harvested by RED and used to power an electrolyser.

In this dissertation, the main focus is the harvesting of energy from the concentration gradient between artificial river and seawater (Figure 1.5a). However, RED also found application in the harvesting of energy from the gradient between seawater and brines, with a lot of research carried out within the REAPower EU project [25]. A 1 kW pilot was installed in Trapani, Italy [26]. Additionally, Li et al. explored the possibility of pairing RED with RO in a variety of configurations, such as using RED to reduce the salinity of seawater and generate energy before seawater desalination with RO (Figure 1.5b) or using RED to produce energy while reducing the salinity of RO brines (Figure 1.5c) [27]. The results of their study show that the RED-RO and RO-RED combinations are promising, as the energy consumption is reduced thanks to the input from RED, in addition to having a brine management step embedded in the process [27]. Similarly, Vanoppen et al.

proposed the addition of an extra ARED step before the RED-RO combination (Figure 1.5d), when using impaired water as low concentration solution. The extra ARED step is shown to be beneficial when the conductivity of the impaired water is low, thus potentially increasing the energy recovery in the following RED step [24].

Choi et al. explored the combination of RED with RO and MCDI (Figure 1.6a) to produce drinking water with decreased energy consumption compared to a double-pass RO system [28]. Their results show decreased energy consumption for the RO-MCDI-RED system compared to the RO-RO configuration and the RO-RO-RED system [28]. Another application of RED is to harvest energy from waste heat in industrial installations. Low-grade heat is used to regenerate the salt gradient between thermolytic salt solutions (e.g., ammonium bicarbonate) which are then mixed in a RED stack to harvest energy (Figure 1.6b) [29,30]. Work on this topic has been carried out in the RED-heat-to-power EU project, which also resulted in a pilot installation in Tilburg, The Netherlands [31]. Among alternative applications of RED, the production of green hydrogen in the cathode compartment is getting increased attention. Instead of producing electricity, this approach stores renewable energy in the form of hydrogen. The number of papers published on this topic is on the rise, and a variety of approaches have been reported. Chen et al. used a RED stack to produce hydrogen directly in the electrode compartments (Figure 1.6c) [32], while Tufa et al. coupled a RED stack with an alkaline polymer electrolyte electrolysis cell (Figure 1.6d) [33]. Additionally, Skilbred et al. coupled RED with thermolytic salts to convert waste heat to hydrogen [34]. The concept of converting SGE to green hydrogen has been also explored at the pilot scale, with Higa et al. using a RED stack with 40 m^2 total membrane area fed with seawater and sewage treated water to produce hydrogen at the cathode with hydrogen evolution rates close to the theoretical maximum [35]. The wide variety of RED applications show that RED can play a flexible role in the field of water technology and in the energy transition.

1.6 Fouling in RED

When considering RED to harvest energy from natural salinity gradients, a major issue is fouling. Natural feedwaters contain many elements in addition to sodium chloride, including colloidal particles, multivalent ions, natural organic matter (NOM), and biological matter [36–39]. All of these elements can interact with the membranes and spacers and decrease the RED power output. Scanning electron microscope images of the membrane surface of fouled AEMs exposed to natural feedwaters are shown in Figure 1.7.
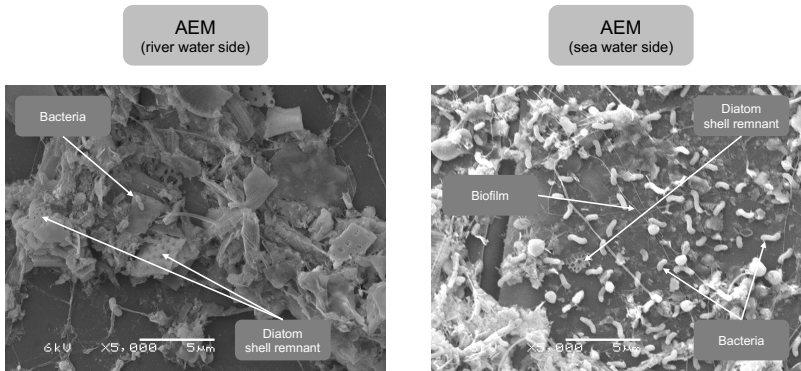
Figure 1.7 Scanning electron microscope images of the surface of membranes fouled during RED operation with natural feedwaters in the RED pilot plant at the Afsluitdijk (The Netherlands). Images courtesy of Bárbara Vital (Wetsus / Wageningen University of Research).

Fouling in natural and laboratory conditions has been extensively studied [36]. Vermaas et al. showed how colloidal particles accumulate in the feedwater channels, thus disrupting the water flow distribution in the compartments [40]. Additionally, the (partial) clogging of the feedwater channels leads to increased pressure drops, causing higher energy losses associated to pumping energy requirements [40]. Post et al., Rijnaarts et al., Moreno et al., and Vermaas et al. investigated the effect of multivalent ions in RED, with particular focus on the effect of multivalent cations (Mg^{2+} and Ca^{2+}) on CEMs [41]. The results of their studies show how multivalent ions negatively affect RED performance in multiple ways: increased membrane resistance, which is particularly pronounced for monovalent-ion selective membranes; decreased electromotive force due to the transport of multivalent ions against their concentration gradient (uphill transport); and decreased membrane permselectivity [36]. Rijnaarts et al. investigated the negative impact of NOM fouling on RED and found that humic acids affect both the membrane permselectivity and electrical resistance [40]. However, their impact is dependent on the nature of the membranes, with membranes based on an aliphatic backbone being less negatively affected than membranes based on an aromatic backbone [40]. Finally, biofouling has received less attention in previous studies, as the impact of colloidal fouling deteriorates RED performance on a time scale that is too fast for significant biofouling to be observed. Nevertheless, Post et al. showed that biofouling negatively affects RED performance mainly through clogging of the feedwater channels and increased pressure drops across the stacks, leading to higher pumping energy losses [41].

1.7 Fouling monitoring

Given the challenge posed by fouling to RED, fouling detection and monitoring are important aspects to understand the impact of fouling and plan effective fouling mitigation strategies in the form of water pre-treatment, membrane modification, and stack cleaning [42–44].

In fouling studies at the membrane level, the impact of fouling is evaluated both in real time and by measuring the difference between pristine and fouled membrane conditions. For real-time studies, the measurement of transition time is an established protocol to evaluate a membrane fouling tendency (Figure 1.8). In this direct current (DC) measurement, a membrane is exposed to solutions containing a model foulant (e.g., sodium dodecylsulfonate, SDS; humic acid, HA; sodium dodecylbenzenesulfonate, SDBS) while a constant current is applied to the cell. The voltage drop over the membrane is monitored using capillaries connected to reference electrodes, and the time when the voltage increase accelerates drastically is the so-called transition time, when fouling heavily affects ion transport through the membrane [45].
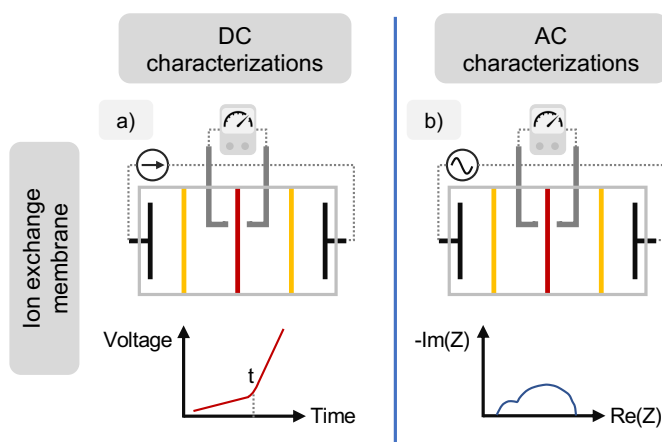
Figure 1.8 Fouling characterizations at the membrane level and their output. a) measurement of transition time, b) electrochemical impedance spectroscopy measurement of a membrane before or after fouling.

To evaluate membranes in the pristine and fouled state, several characterizations are possible: membrane permselectivity, membrane resistance (DC), and membrane impedance (alternating current, AC) [40,46]. The advantage of AC characterizations, in the form of electrochemical impedance spectroscopy (EIS), is that detailed information is provided on the ohmic and non-ohmic components of the membrane impedance [47]. However, the main drawback of fouling characterization at the membrane level is that the

conditions in which fouling occurs are often not representative of the conditions found inside a RED stack, where flow patterns and current distribution are very different [40,48]. Fouling monitoring at the RED stack level (Figure 1.9a) offers representative water flows and current distribution conditions, and it is typically performed by monitoring open circuit voltage (OCV), stack electrical resistance, power density, and pressure drop across the stack for the two feedwaters over time. These quantities provide information on the membranes permselectivity, resistance, and accumulation of particles in the channels [42,43,49]. However, this information is an average from all membranes and the whole active area.
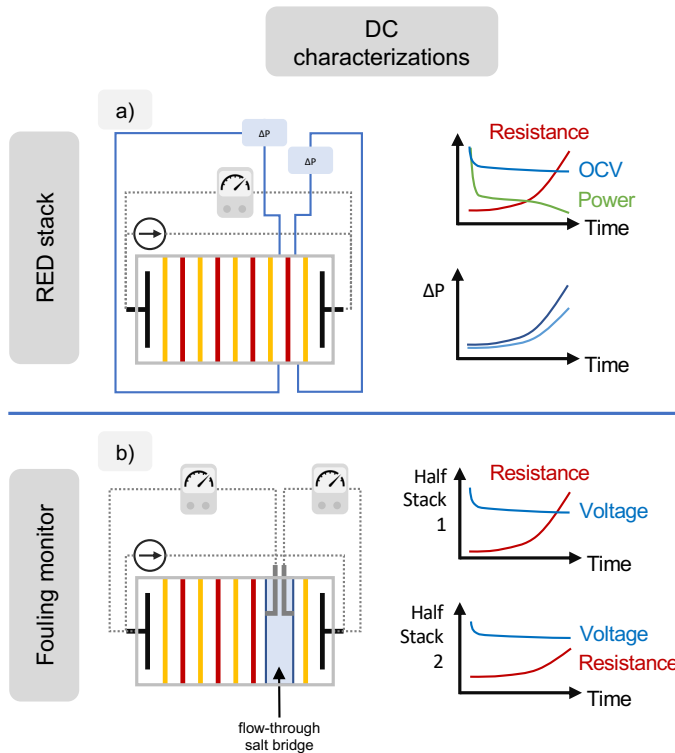
Figure 1.9 Fouling characterizations at the RED stack level and their output. A) evaluation of open circuit voltage, stack resistance, power density, and pressure drop over time, b) RED fouling monitor to measure specific fouling configurations [50].

To overcome this issue, Bodner et al. developed a novel design for a fouling monitor based on a normal RED stack (Figure 1.9b) [50]. A flow-through salt bridge is used to insert capillaries in the membrane stack, thus allowing the measurement of half-stack voltages, which provide extra information on the impact of fouling on the membrane in the right

half-stack (Figure 1.9b). Several combinations of feedwaters and membranes in the right half-stack allow the evaluation of fouling under different conditions [50].

1.8 Membrane modifications to control fouling

To mitigate fouling, a promising approach is the surface modification of IEMs. Depending on the field of application and its typical fouling type, a tailored surface chemistry of the membrane allows a reduction of the negative effects of fouling. In (R)ED literature, most efforts have been devoted to reducing the negative impact of multivalent ions either by electrostatic repulsion or by size exclusion, and to mitigate the negative influence of colloidal and organic fouling also by electrostatic repulsion of the mostly negatively charged foulants or by increasing the membrane hydrophilicity (Figure 1.10). A short overview of surface modification strategies for fouling control is given in this section.
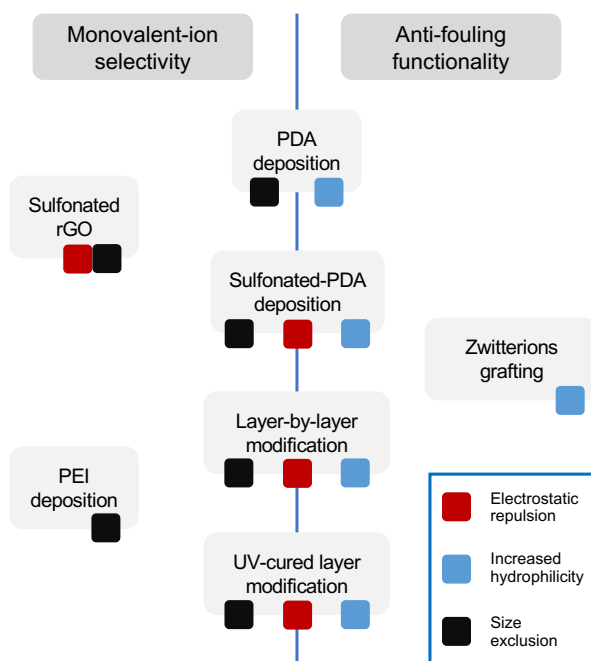
Figure 1.10 Strategies for surface modification of IEMs and their action mechanism to mitigate fouling. PDA=polydopamine; rGO= reduced Graphene Oxide; PEI= polyethyleneimine.

Vaselbehagh et al. used a polydopamine (PDA) layer to increase the hydrophilicity of an anion exchange membrane and increase its resistance to organic fouling. Their results showed that the fouling transition time is greatly increased for membranes modified with

16

a low concentration of PDA, as this increases hydrophilicity without enhancing the surface roughness, which is detrimental for fouling resistance [51]. Similarly, Ruan et al. showed that a dense PDA layer is not only beneficial for increased anti-fouling resistance, but also to increase the monovalent-ion selectivity of the underlying membrane, thanks to the size exclusion operated on larger multivalent ions [52]. Furthermore, when sulfonated dopamine is used to obtain the PDA surface layer, the benefits of anti-fouling resistance and monovalent-ion selectivity are increased even further, achieving selectivity that exceeds those of commercial monovalent-ion selective membranes [52]. However, the increased anti-fouling resistance and selectivity of the membranes are achieved at the expense of membrane resistance, which is greatly increased by the addition of a dense surface layer [52].

Alternatively, Pan et al. used electro-deposition of a dense but thin polyethyleneimine (PEI) layer on the surface of an AEM to increase its monovalent-ion selectivity by size exclusion, with a moderate increase in membrane resistance [53].

To obtain monovalent-ion selectivity in AEMs, sulfonated reduced graphene oxide (rGO) has been deposited on the membrane surface, in combination with a PDA layer to increase its stability. Sulfonated rGO provides monovalent-ion selectivity via electrostatic repulsion and size exclusion, while the PDA layer used to immobilize it contributes to increasing the hydrophilicity of the membrane surface, thus increasing anti-fouling resistance [54].

Polyelectrolyte layers or multilayers applied to the membrane by dip-coating, in the so-called Layer-by-Layer (LbL) approach, have also been used to increase monovalent-ion selectivity and anti-fouling resistance. Mulyati et al. applied a single layer of poly(sodium 4-styrene sulfonate) (PSS) to an AEM and measured increased anti-fouling resistance, thanks to the electrostatic repulsion of the negatively charged model foulant [55]. Similarly, when a polyelectrolyte multilayer is applied via LbL, alternating PSS and poly(allylamine hydrochloride) (PAH), not only the anti-fouling resistance of the underlying AEM is enhanced, but also the monovalent-ion selectivity increases thanks to electrostatic repulsion and size exclusion effects [56].

Another approach to obtain electrostatic repulsion between the membrane surface and foulants is the deposition of a thin UV-cured CEM layer on top of an AEM, as proposed by Güler et al. [45]. Their modified membranes exhibit higher monovalent-ion selectivity and anti-fouling resistance, thanks to the repulsion between the sulfonic groups in the CEM layer and the more negative sulfate or the negatively charged SDS [45].

Finally, to increase the anti-fouling resistance of membranes, the application of zwitterionic layers has received a lot of attention, especially in the field of porous membranes [57]. Zwitterionic molecules bear both a cationic and an anionic group, resulting in large hydration shells, which are very effective at increasing membrane hydrophilicity [58]. Ruan et al. reported the modification of an anion exchange membrane with PDA and a zwitterionic layer, resulting in increased anti-fouling resistance during ED operation with a model foulant [58].

Most of these surface modification strategies present trade-offs between the enhanced monovalent-ion selectivity or anti-fouling resistance and the electrochemical properties of the pristine membrane, which are slightly deteriorated by the membrane modification process. Additionally, most of these modifications have been developed to target fouling in ED, where a slight increase in membrane resistance or loss in membrane permselectivity is less relevant than in RED, where the power output is considerably affected by changes in the membrane properties. Another drawback of these studies is that the validation of the enhanced anti-fouling functionality is often performed with transition time measurement or short ED runs, where the outcomes are less representative than results obtained in a RED stack fouling experiment.

1.9 Aim of the thesis

Considering the current standing of fouling studies, monitoring, modeling, and control in RED, this dissertation aims to:

- increase the current understanding of fouling in RED
- provide tools for fouling monitoring at the stack level
- validate a promising strategy to mitigate organic fouling by surface modification of AEMs
- develop models that assist stack design and move beyond the current paradigm of modeled feedwaters containing only sodium chloride by introducing the effect of divalent cations and divalent anions on the stack performance

1.10   Outline of the thesis

Figure 1.11 provides a graphical outline of this dissertation.
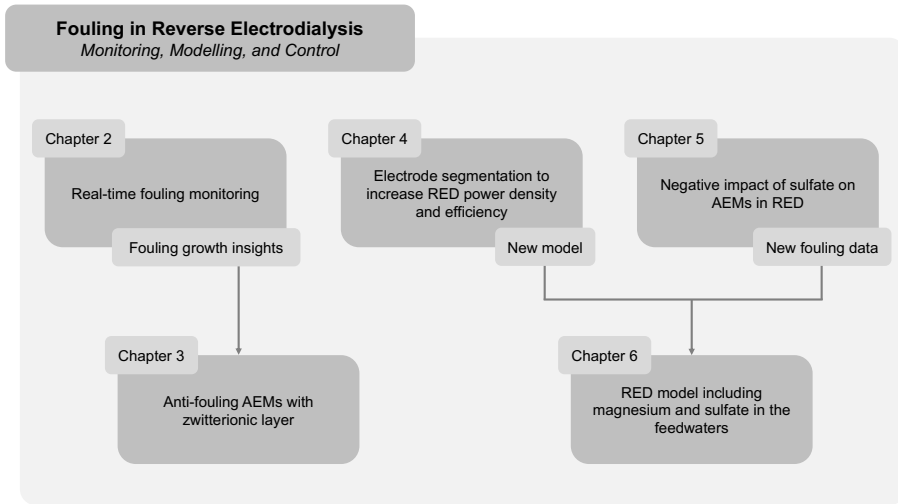
Figure 1.11 Graphical outline of the thesis, presenting the relationship between chapters.

After this introduction chapter, Chapter 2 presents the application of electrochemical impedance spectroscopy at the RED stack level for real-time fouling monitoring. Changes to the impedance spectra are related to the evolution of fouling with a model compound, highlighting its stages and the impact it has not only on AEMs, but also on CEMs.

Chapter 3 illustrates how the surface modification of AEMs with zwitterionic monomers and brushes increases the fouling resistance of the membranes and accelerates their recovery upon cleaning.

Chapter 4 shows the benefits of electrode segmentation for RED power density and efficiency with an experimental and model study using cross-flow stacks.

Chapter 5 presents a study into the effect of sulfate on different AEMs (standard grade and monovalent-ion selective) in RED. Membrane and stack characterizations are presented for a comprehensive overview of the negative impact of multivalent anions on RED.

Chapter 6 provides a new RED process model that includes the negative effect of multivalent ions together with its experimental validation and examples of its application to obtain more realistic predictions of power output.

Finally, Chapter 7 presents the general discussion and outlook with recommendations for future RED developments.

References

[1]   Water vector, (2020). https://www.freepik.com/free-vector/river-flow-into-sea-pond-top-view-cartoon-narrow-riverbed-going-wide-water-with-rocks_9396076.htm#page=1&query=river%20and%20sea&position=5 (accessed January 28, 2021).

[2]   Nature vector, (2020). https://www.freepik.com/free-vector/vector-cartoon-waterfall-rocks_6823190.htm#page=1&query=waterfall&position=16 (accessed January 28, 2021).

[3]   R.S. Norman, Water Salination: A Source of Energy, Science. 186 (1974) 350. https://doi.org/10.1126/science.186.4161.350.

[4]   Three Gorges Dam, Wikipedia. (2020). https://en.wikipedia.org/wiki/Three_Gorges_Dam (accessed January 2, 2021).

[5]   T.J. Crowley, Causes of climate change over the past 1000 years, Science. 289 (2000) 270–277. https://doi.org/10.1126/science.289.5477.270.

[6]   P.M. Cox, R.A. Betts, C.D. Jones, S.A. Spall, I.J. Totterdell, Acceleration of global warming due to carbon-cycle feedbacks in a coupled climate model, Nature. 408 (2000) 184–187. https://doi.org/10.1038/35041539.

[7]   J. Rogelj, M. den Elzen, N. Höhne, T. Fransen, H. Fekete, H. Winkler, R. Schaeffer, F. Sha, K. Riahi, M. Meinshausen, Paris Agreement climate proposals need a boost to keep warming well below 2 °c, Nature. 534 (2016) 631–639. https://doi.org/10.1038/nature18307.

[8]   Renewables 2020, Paris, 2020. https://www.iea.org/reports/renewables-2020 (accessed January 2, 2021).

[9]   Renewables 2020 Data Explorer, (2020). https://www.iea.org/articles/renewables-2020-data-explorer?mode=market&region=World&product=Total (accessed January 2, 2021).

[10]   E. Voumvoulakis, G. Asimakopoulou, S. Danchev, G. Maniatis, A. Tsakanikas, Large scale integration of intermittent renewable energy sources in the Greek power sector, Energy Policy. 50 (2012) 161–173. https://doi.org/https://doi.org/10.1016/j.enpol.2012.05.056.

[11]   J.W. Post, H.V.M. Hamelers, C.J.N. Buisman, Energy recovery from controlled mixing salt and fresh water with a reverse electrodialysis system, Environmental Science and Technology. 42 (2008) 5785–5790. https://doi.org/10.1021/es8004317.

[12]   J.W. Post, J. Veerman, H.V.M. Hamelers, G.J.W. Euverink, S.J. Metz, K. Nymeijer, C.J.N. Buisman, Salinity-gradient power: Evaluation of pressure-retarded osmosis and reverse electrodialysis, Journal of Membrane Science. 288 (2007) 218–230. https://doi.org/10.1016/j.memsci.2006.11.018.

[13]   J.W. Post, C.H. Goeting, J. Valk, S. Goinga, J. Veerman, H.V.M. Hamelers, P.J.F.M. Hack, Towards implementation of reverse electrodialysis for power generation from salinity gradients, Desalination and Water Treatment. 16 (2010) 182–193. https://doi.org/10.5004/dwt.2010.1093.

[14]   D.A. Vermaas, M. Saakes, K. Nijmeijer, Power generation using profiled membranes in reverse electrodialysis, Journal of Membrane Science. 385–386 (2011) 234–242. https://doi.org/10.1016/j.memsci.2011.09.043.

[15]   A.H. Galama, J.W. Post, H.V.M. Hamelers, V.V. Nikonenko, P.M. Biesheuvel, On the origin of the membrane potential arising across densely charged ion exchange membranes: How well does

the teorell-meyer-sievers theory work?, Journal of Membrane Science and Research. 2 (2016) 128–140.

[16]   J. Veerman, M. Saakes, S.J. Metz, G.J. Harmsen, Reverse electrodialysis: Evaluation of suitable electrode systems, Journal of Applied Electrochemistry. 40 (2010) 1461–1474. https://doi.org/10.1007/s10800-010-0124-8.

[17]   R.E. Pattle, Production of electric power by mixing fresh and salt water in the hydroelectric pile [19], Nature. 174 (1954) 660. https://doi.org/10.1038/174660a0.

[18]   G.L. Wick, Power from salinity gradients, Energy. 3 (1978) 95–100. https://doi.org/https://doi.org/10.1016/0360-5442(78)90059-2.

[19]   Afsluitdijk project, (2014). https://www.redstack.nl/en/projects/36/afsluitdijk-project (accessed January 2, 2021).

[20]   J. Veerman, The Effect of the NaCl Bulk Concentration on the Resistance of Ion Exchange Membranes—Measuring and Modeling, Energies . 13 (2020). https://doi.org/10.3390/en13081946.

[21]   P. Długołecki, K. Nymeijer, S. Metz, M. Wessling, Current status of ion exchange membranes for power generation from salinity gradients, Journal of Membrane Science. 319 (2008) 214–222. https://doi.org/10.1016/j.memsci.2008.03.037.

[22]   A.H. Galama, D.A. Vermaas, J. Veerman, M. Saakes, H.H.M. Rijnaarts, J.W. Post, K. Nijmeijer, Membrane resistance: The effect of salinity gradients over a cation exchange membrane, Journal of Membrane Science. 467 (2014) 279–291. https://doi.org/https://doi.org/10.1016/j.memsci.2014.05.046.

[23]   D.A. Vermaas, J. Veerman, N.Y. Yip, M. Elimelech, M. Saakes, K. Nijmeijer, High efficiency in energy generation from salinity gradients with reverse electrodialysis, ACS Sustainable Chemistry and Engineering. 1 (2013) 1295–1302. https://doi.org/10.1021/sc400150w.

[24]   M. Vanoppen, E. Criel, G. Walpot, D.A. Vermaas, A. Verliefde, Assisted reverse electrodialysis—principles, mechanisms, and potential, Npj Clean Water. 1 (2018) 9. https://doi.org/10.1038/s41545-018-0010-1.

[25]   REAPower, (2014). https://www.reapower.eu/ (accessed January 2, 2021).

[26]   M. Tedesco, A. Cipollina, A. Tamburini, G. Micale, Towards 1 kW power production in a reverse electrodialysis pilot plant with saline waters and concentrated brines, Journal of Membrane Science. 522 (2017) 226–236. https://doi.org/10.1016/j.memsci.2016.09.015.

[27]   W. Li, W.B. Krantz, E.R. Cornelissen, J.W. Post, A.R.D. Verliefde, C.Y. Tang, A novel hybrid process of reverse electrodialysis and reverse osmosis for low energy seawater desalination and brine management, Applied Energy. 104 (2013) 592–602. https://doi.org/10.1016/j.apenergy.2012.11.064.

[28]   J. Choi, Y. Oh, S. Chae, S. Hong, Membrane capacitive deionization-reverse electrodialysis hybrid system for improving energy efficiency of reverse osmosis seawater desalination, Desalination. 462 (2019) 19–28. https://doi.org/https://doi.org/10.1016/j.desal.2019.04.003.

[29]   F. Giacalone, F. Vassallo, F. Scargiali, A. Tamburini, A. Cipollina, G. Micale, The first operating thermolytic reverse electrodialysis heat engine, Journal of Membrane Science. 595 (2020). https://doi.org/10.1016/j.memsci.2019.117522.

[30]   F. Giacalone, F. Vassallo, L. Griffin, M.C. Ferrari, G. Micale, F. Scargiali, A. Tamburini, A. Cipollina, Thermolytic reverse electrodialysis heat engine: model development, integration and performance analysis, Energy Conversion and Management. 189 (2019) 1–13. https://doi.org/10.1016/j.enconman.2019.03.045.

[31]   RED-heat-to-power, (2017). http://www.red-heat-to-power.eu/ (accessed January 2, 2021).

[32]   X. Chen, C. Jiang, Y. Zhang, Y. Wang, T. Xu, Storable hydrogen production by Reverse Electro-Electrodialysis (REED), Journal of Membrane Science. 544 (2017) 397–405. https://doi.org/10.1016/j.memsci.2017.09.006.

[33]   R.A. Tufa, E. Rugiero, D. Chanda, J. Hnàt, W. van Baak, J. Veerman, E. Fontananova, G. di Profio, E. Drioli, K. Bouzek, K. Bouzek, E. Curcio, Salinity gradient power-reverse electrodialysis and alkaline polymer electrolyte water electrolysis for hydrogen production, Journal of Membrane Science. 514 (2016) 155–164. https://doi.org/10.1016/j.memsci.2016.04.067.

[34]   E.S. Skilbred, K.W. Krakhella, I.J. Haga, J.G. Pharoah, M. Hillestad, G.D.A. Serrano, O.S. Burheim, Using waste heat to set up concentration differences for reverse electrodialysis hydrogen production, in: ECS Transactions, 2018: pp. 147–161. https://doi.org/10.1149/08513.0147ecst.

[35]   M. Higa, T. Watanabe, M. Yasukawa, N. Endo, Y. Kakihana, H. Futamura, K. Inoue, H. Miyake, J. Usui, A. Hayashi, A. Hayashi, M. Matsuhashi, Sustainable hydrogen production from seawater and sewage treated water using reverse electrodialysis technology, Water Practice and Technology. 14 (2019) 645–651. https://doi.org/10.2166/wpt.2019.048.

[36]   D.A. Vermaas, J. Veerman, M. Saakes, K. Nijmeijer, Influence of multivalent ions on renewable energy generation in reverse electrodialysis, Energy Environ. Sci. 7 (2014) 1434–1445. https://doi.org/10.1039/C3EE43501F.

[37]   J. Moreno, V. Díez, M. Saakes, K. Nijmeijer, Mitigation of the effects of multivalent ion transport in reverse electrodialysis, Journal of Membrane Science. 550 (2018) 155–162. https://doi.org/10.1016/j.memsci.2017.12.069.

[38]   J.W.J.W. Post, H.V.M.H.V.M. Hamelers, C.J.N.C.J.N. Buisman, Influence of multivalent ions on power production from mixing salt and fresh water with a reverse electrodialysis system, Journal of Membrane Science. 330 (2009) 65–72. https://doi.org/10.1016/j.memsci.2008.12.042.

[39]   T. Rijnaarts, E. Huerta, W. van Baak, K. Nijmeijer, Effect of Divalent Cations on RED Performance and Cation Exchange Membrane Selection to Enhance Power Densities, Environmental Science and Technology. 51 (2017) 13028–13035. https://doi.org/10.1021/acs.est.7b03858.

[40]   T. Rijnaarts, J. Moreno, M. Saakes, W.M. de Vos, K. Nijmeijer, Role of anion exchange membrane fouling in reverse electrodialysis using natural feed waters, Colloids and Surfaces A: Physicochemical and Engineering Aspects. 560 (2019) 198–204. https://doi.org/10.1016/j.colsurfa.2018.10.020.

[41]   J.W. Post, Blue energy: electricity production from salinity gradients by reverse electrodialysis, 2009.

[42]   D.A. Vermaas, M. Saakes, K. Nijmeijer, Early detection of preferential channeling in reverse electrodialysis, Electrochimica Acta. 117 (2014) 9–17. https://doi.org/10.1016/j.electacta.2013.11.094.

[43]   D.A. Vermaas, D. Kunteng, J. Veerman, M. Saakes, K. Nijmeijer, Periodic feedwater reversal and air sparging as antifouling strategies in reverse electrodialysis, Environmental Science and Technology. 48 (2014) 3065–3073. https://doi.org/10.1021/es4045456.

[44]   J. Moreno, N. de Hart, M. Saakes, K. Nijmeijer, CO_2-saturated water as two-phase flow for fouling control in reverse electrodialysis, Water Research. 125 (2017) 23–31. https://doi.org/10.1016/j.watres.2017.08.015.

[45]   E. Güler, W. van Baak, M. Saakes, K. Nijmeijer, Monovalent-ion-selective membranes for reverse electrodialysis, Journal of Membrane Science. 455 (2014) 254–270. https://doi.org/10.1016/j.memsci.2013.12.054.

[46]   Z. Zhao, S. Shi, H. Cao, Y. Li, Electrochemical impedance spectroscopy and surface properties characterization of anion exchange membrane fouled by sodium dodecyl sulfate, Journal of Membrane Science. 530 (2017) 220–231. https://doi.org/10.1016/j.memsci.2017.02.037.

[47]   W. Zhang, P. Wang, J. Ma, Z. Wang, H. Liu, Investigations on electrochemical properties of membrane systems in ion-exchange membrane transport processes by electrochemical impedance spectroscopy and direct current measurements, Electrochimica Acta. 216 (2016) 110–119. https://doi.org/10.1016/j.electacta.2016.09.018.

[48]   D. Pintossi, M. Saakes, Z. Borneman, K. Nijmeijer, Electrochemical impedance spectroscopy of a reverse electrodialysis stack: A new approach to monitoring fouling and cleaning, Journal of Power Sources. 444 (2019). https://doi.org/10.1016/j.jpowsour.2019.227302.

[49]   D.A. Vermaas, D. Kunteng, M. Saakes, K. Nijmeijer, Fouling in reverse electrodialysis under natural conditions, Water Research. 47 (2013) 1289–1298. https://doi.org/10.1016/j.watres.2012.11.053.

[50]   E.J. Bodner, M. Saakes, T. Sleutels, C.J.N. Buisman, H.V.M. Hamelers, The RED Fouling Monitor: A novel tool for fouling analysis, Journal of Membrane Science. 570–571 (2019) 294–302. https://doi.org/10.1016/j.memsci.2018.10.059.

[51]   M. Vaselbehagh, H. Karkhanechi, S. Mulyati, R. Takagi, H. Matsuyama, Improved antifouling of anion-exchange membrane by polydopamine coating in electrodialysis process, Desalination. 332 (2014) 126–133. https://doi.org/10.1016/j.desal.2013.10.031.

[52]   H. Ruan, Z. Zheng, J. Pan, C. Gao, B. van der Bruggen, J. Shen, Mussel-inspired sulfonated polydopamine coating on anion exchange membrane for improving permselectivity and anti-fouling property, Journal of Membrane Science. 550 (2018) 427–435. https://doi.org/10.1016/j.memsci.2018.01.005.

[53]   J. Pan, J. Ding, R. Tan, G. Chen, Y. Zhao, C. Gao, Bart. van der Bruggen, J. Shen, Preparation of a monovalent selective anion exchange membrane through constructing a covalently crosslinked interface by electro-deposition of polyethyleneimine, Journal of Membrane Science. 539 (2017) 263–272. https://doi.org/https://doi.org/10.1016/j.memsci.2017.06.017.

[54]   Y. Li, S. Shi, H. Cao, Z. Zhao, C. Su, H. Wen, Improvement of the antifouling performance and stability of an anion exchange membrane by surface modification with graphene oxide (GO) and polydopamine (PDA), Journal of Membrane Science. 566 (2018) 44–53. https://doi.org/10.1016/j.memsci.2018.08.054.

[55]   S. Mulyati, R. Takagi, A. Fujii, Y. Ohmukai, T. Maruyama, H. Matsuyama, Improvement of the antifouling potential of an anion exchange membrane by surface modification with a

polyelectrolyte for an electrodialysis process, Journal of Membrane Science. 417–418 (2012) 137–143. https://doi.org/10.1016/j.memsci.2012.06.024.

[56]   S. Mulyati, R. Takagi, A. Fujii, Y. Ohmukai, H. Matsuyama, Simultaneous improvement of the monovalent anion selectivity and antifouling properties of an anion exchange membrane in an electrodialysis process, using polyelectrolyte multilayer deposition, Journal of Membrane Science. 431 (2013) 113–120. https://doi.org/10.1016/j.memsci.2012.12.022.

[57]   S.P. Nunes, Can fouling in membranes be ever defeated?, Current Opinion in Chemical Engineering. 28 (2020) 90–95. https://doi.org/10.1016/j.coche.2020.03.006.

[58]   H. Ruan, J. Liao, R. Tan, J. Pan, A. Sotto, C. Gao, J. Shen, Dual Functional Layers Modified Anion Exchange Membranes with Improved Fouling Resistant for Electrodialysis, Advanced Materials Interfaces. 5 (2018). https://doi.org/10.1002/admi.201800909.

1

1

Chapter 2

Electrochemical impedance spectroscopy of a reverse electrodialysis stack: a new approach to monitoring fouling and cleaning

Abstract

When harvesting salinity gradient energy via reverse electrodialysis (RED), stack performance is monitored using DC characterizations, which does not provide information about the nature and mechanisms underlying fouling inside the stack. In order to assess the potential of natural salinity gradients as a renewable energy source, progress in the fields of fouling monitoring and controlling is vital. To improve fouling and cleaning monitoring, experiments with sodium dodecylbenzenesulfonate (SDBS) were carried out while at the same time the electrochemical impedance spectroscopy (EIS) was measured at the RED stack level. EIS showed how SDBS affected the ohmic resistance of the stack, the non-ohmic resistance of the AEM and the non-ohmic resistance of the CEM on different time scales. Such detailed investigation into the effect of SDBS on different stack elements offered by EIS is not possible with traditional DC characterization. The results presented in this work illustrate the potential of EIS at the stack level for fouling monitoring. The knowledge presented shows the possibility of including EIS in up-scaled natural salinity gradient RED applications for fouling monitoring purposes.

2.1 Introduction

To harvest salinity gradient energy, reverse electrodialysis (RED) is a promising technology that generates electricity by controlled mixing of aqueous solutions with different salinities, such as river water and seawater [1]. RED uses non-porous ion exchange membranes (IEMs) that are permselective for cations (cation exchange membranes, CEMs) or anions (anion exchange membranes, AEMs). The IEMs are stacked alternately with high salt concentration and low salt concentration feedwaters flowing on either side along the membranes [2]. The difference in salt concentration between the feedwaters creates a potential difference across the membranes [3]. At the two ends of the stack, electronic redox reactions convert the ionic current into an electric current. The generated electrical current can then be used to power an external load [4].

In order to be able to use RED as a renewable energy source for a long time, fouling is one of the main challenges to be addressed [5]. There are many different forms of fouling affecting RED: colloidal fouling, inorganic fouling (scaling, uphill transport of multivalent cations like Ca^{2+} and Mg^{2+} and poisoning of the membranes due to multivalent ions), organic fouling and biofouling [6–8]. Although there are similarities with membrane fouling in water treatment, the nature, interactions and consequences are distinctively different in RED due to the use of charged anionic and cationic membranes, and the transport of ions instead of water molecules as in water treatment and purification [9].

In the natural environment and in laboratories, the study of fouling phenomena in RED happened at two levels: the stack level and the single membrane level. This approach on two different levels reflects the trade-off existing in RED fouling investigations: either a highly representative system where the available characterization tools are limited by the system intrinsic complexity (stack level) or a simplified system that allows more flexibility in terms of available characterizations techniques but at the same time does not truly reflect the hydrodynamic and physical conditions found in real, natural water, RED systems (membrane level). For the RED stack, electrolyte compartments, water compartments and membranes all contribute to the system performance. The traditional DC characterization applied at stack level implies a black box approach, where the overall behavior of the system is measured without the possibility to investigate in a non-destructive way the impact of fouling on the CEM or AEM in detail. Therefore, studies at the stack level monitor the effect of fouling on the complete stack, rather than monitoring fouling evolution and dynamics, relying on the evolution over time of electrochemical parameters, like open circuit voltage and stack electrical resistance, and other parameters, like pressure drop between feedwaters inlets and outlets [6,10]. Even a new stack design

based on the idea of dividing the RED stack in two halves allowing the monitoring of single membranes without affecting the hydrodynamics in the water compartment relies on the same DC characterization, thus limiting the amount of information that is extracted in real time from individual membranes in the stack [11]. Studies at the membrane level offer a wider set of available characterization techniques, including electrochemical impedance spectroscopy (EIS). The advantage of EIS over DC characterization is the possibility to investigate individual components that all contribute to the overall resistance. At membrane level, EIS was used to distinguish the contributions to the membrane resistance of membrane bulk, electrical double layer, diffusion boundary layer and fouling in clean or foulants containing water [12–21]. EIS enables the detailed observation of the effect of fouling not just on the overall resistance, but also how the fouling layers hinder ion transport in the diffusion boundary layer. However, studies at the membrane level are often carried out in systems with wide water compartments, where the absence of spacers and configuration of the inlets and outlets lead to very different flow and current fields over the membrane. Since flow and current fields have a huge influence on the fouling evolution of AEMs, results obtained in these studies at the membrane level cannot be directly translated into knowledge of membrane behavior inside the stack. Performing EIS at the stack level moves fouling monitoring and analysis in RED beyond the present trade-off. EIS at stack level unravels detailed information on how fouling builds up on the anion and cation exchange membranes in a highly representative RED stack environment, enabling real time and non-destructive fouling monitoring. RED stacks have a large capacitance due to large electrode-electrolyte and membrane-electrolyte interfaces. This leads to long EIS measurement times since the characteristic frequencies of systems with large capacitance are very low. Long measurement times in a fouling experiment make it difficult to assume steady-state of the system during the EIS scan. That is because the system performance deteriorates considerably over the scan time due to fouling, leading to the characterization of a system that changes significantly throughout the measurement, thus impairing the significance of the measured data. Additionally, when correctly measured, the meaning of impedance spectra of a stack needs to be unraveled to attribute spectral features to the single stack elements, namely electrodes and electrolyte, membranes and water compartments. Overcoming such issues is not trivial, as highlighted by the scarcity of studies reporting EIS at the stack level. Modulation of the active membrane area to limit interfacial capacitance is a promising strategy to reduce EIS measurement time and enable EIS at the stack level. In the RED literature, the only example of EIS at the stack level is provided by Choi et al., who studied the effect of

process parameters like flow rate and salt concentration on the RED performance in a small area stack with one cell pair [22]. Thanks to EIS, they could study the dependence of the resistance components on the process parameters under study.

This paper presents the use of EIS at the stack level for fouling monitoring and characterization. The modulation of active membrane area is the key to enable the measurement of impedance spectra at the stack level. To interpret spectra, a step-by-step procedure was adopted analyzing systems with increasing complexity, moving from a relatively simple system consisting of the electrodes and electrolyte to the full RED stack. A model compound, sodium dodecylbenzenesulfonate (SDBS) was used for fouling experiments. EIS successfully tracks fouling and cleaning in the stack, with more information on the interaction between the model compound and the membranes than the traditional DC characterization. Finally, based on the information provided by EIS, a mechanism for the evolution of fouling on the membranes is proposed. These results prove the feasibility of EIS as a tool for real-time and non-destructive fouling monitoring at the stack level, revealing how the foulants absorb in and adsorb on the ion exchange membranes, thus paving the way for tailored cleaning strategies, where the consumption of cleaning resources is minimized while maximizing their effect.

2.2 Theory

The underlying principle of electrochemical impedance spectroscopy is the application of a sinusoidal input to an electrochemical system, like a RED stack, and measurement of the corresponding sinusoidal output or response of the system under study. Such a process is repeated for a large set of frequencies, to identify phenomena that occur at different characteristic frequencies. As input, a current is employed with potential measured as the output, or vice versa. Input and output are sinusoidal functions with the same frequency, but their amplitudes differ. Additionally, whenever the system under investigation has a capacitive or inductive behavior, the output signal is characterized by a phase shift φ with respect to the input signal (Figure S2.1). Considering Ohm's law for a DC characterization:

$$U = R \cdot I \qquad (2.1)$$

Where U is the potential [V], R is the electrical resistance [Ω] and I is the current [A], a similar approach is adopted for EIS. Having a sinusoidal voltage as an input:

$$U(\omega, t) = U_0 \sin(\omega t) = U_0 e^{j\omega t} \qquad (2.2)$$

With U_0 the amplitude of the oscillation [V], j the imaginary base vector, ω the angular frequency ($\omega = 2\pi f$, where f is the frequency [Hz]) and t the time [s], the measured output will be:

$$I(\omega, t) = I_0 \sin(\omega t + \varphi) = I_0 e^{j(\omega t + \varphi)} \tag{2.3}$$

Where I_0 is the amplitude of the measured sinusoidal current. The relationship between the two quantities is given by a quantity called impedance:

$$Z(\omega) = \frac{U(\omega, t)}{I(\omega, t)} = \frac{U_0 e^{j\omega t}}{I_0 e^{j(\omega t + \varphi)}} = |Z| e^{-j\varphi} \tag{2.4}$$

It can be noted that the time dependency is lost when calculating the ratio between alternating voltage and alternating current. Thus, impedance is a time-independent quantity. However, impedance depends on frequency since the phase shift φ depends on frequency. For a time-independent impedance measurement, the electrochemical system under investigation should be linear and steady-state, at least for the duration of the EIS measurement. For IEMs, modeling and experimental work have been carried out to measure the impedance spectrum of single membranes [23,24]. The typical electrical equivalent circuit (EEC) for a single IEM is represented in Figure S2.2. The contribution from bulk of the membrane, electrical double layer and diffusion boundary layer to the membrane resistance can be identified based on their different characteristic frequencies. Since membrane resistance implies the conduction of ions, ionic movement at a longer scale results in a lower characteristic frequency for the spectral feature associated to that motion. The first element in the equivalent circuit, a resistor, represents the ohmic component of the membrane impedance (purely resistive behavior measured at high frequencies), the second element, a parallel of a resistor and capacitor, stands for the impedance of the electrical double layer (measured at intermediate frequencies, since it involves the migration of ions at the nanometer scale), while the last element, a parallel connection of a resistor and a CPE, represents the impedance of the diffusion boundary layer (measured at low frequencies, since it involves the diffusion of ions at the micrometer scale) [14,17].

For complex electrochemical systems, such as a RED stack, multiple phenomena contribute to a single spectral feature. Therefore, a single arc may result from the convolution of multiple arcs deriving from different phenomena.

2.3 Materials and methods

2.3.1 Materials

For the experiments, demineralized water (produced by an Osmostar S400, Lubron Waterbehandeling BV, the Netherlands) was used. Sodium chloride (NaCl, 99.5 % purity, ESCO, the Netherlands) and sodium dodecylbenzene sulfonate (SDBS, technical grade, Sigma-Aldrich, Germany) were used as solutes. Potassium hexacyanoferrate(II) trihydrate and potassium hexacyanoferrate(III) (both technical grade, at least 96 % purity, VWR Chemicals, Belgium) were used as electrolytes. For the stack assembly, the chosen AEMs and CEMs were homogeneous standard grade Fujifilm AEM type I (FUJIFILM Manufacturing Europe BV, the Netherlands) and homogeneous standard grade Neosepta CMX-fg (ASTOM Corp. Ltd., Japan), respectively. Neosepta AMX-fg was used as alternative AEM to investigate the effect of different AEMs on the impedance spectrum.

2.3.2 Stack configurations

The experiments were performed with cross-flow RED stacks (REDstack BV, the Netherlands) with an active area of 10 x 10 cm^2. The stack end plates embedded platinized titanium mesh electrodes (9.8 x 9.8 cm^2) (MAGNETO Special Anodes BV, the Netherlands). Spacers with a woven netting (Sefar 06-700/53, Sefar AG, Switzerland) and integrated silicone rubber gaskets with a custom design (AquaSEAL by AquaBattery, the Netherlands) were used to accommodate the feedwaters, seal the compartments, and reduce the active area of the cell from 100 cm^2 to 4 cm^2 and 1 cm^2. Two active areas and four different configurations were used to enable the interpretation of the impedance spectra of the RED stack. This approach made it possible to compare impedance spectra of similar systems of increasing complexity. These stack configurations are summarized in Table 2.1.

Table 2.1 Summary of the stack configurations used in the present work. Electrolyte solution is recirculated in the electrode compartments for all configurations. RW stands for river water compartment, SW stands for seawater compartment, N stands for no addition and Y stands for yes addition of SBDS.

Name	Area	CEM	AEM	RW	SW	SDBS	Aim
a	1 cm^2	0	0	0	0	N	Determine impedance of electrodes with reduced open area.
b	1 cm^2	1	0	0	0	N	Determine the impedance of electrodes separated by one CEM, with reduced active membrane area.
c	4 cm^2	1	0	0	0	N	Determine the effect of active membrane area on the impedance of system made of electrodes separated by one CEM.
d	1 cm^2	2	1	1	1	N	Study of complete RED stack impedance.
e	1 cm^2	2	1	1	1	Y	Monitoring of fouling and cleaning.

The configurations with one CEM are represented in Figure S2.3, while Figure S2.4 depicts the complete RED stack configuration with a complete cell pair consisting of a CEM, a river water compartment, an AEM, a seawater compartment, another sealing CEM, and the electrolyte compartments at both ends of the stack.

2.3.3 Feedwaters and electrolyte

NaCl solutions of 0.017 M and 0.508 M were used as artificial river water and seawater, respectively. 50 ppm and 100 ppm SDBS was added to the river water for the fouling experiments. SDBS was chosen as a model compound for organic fouling of the AEM, as it is known to interact with the membrane on a relatively short time scale, severely affecting the membrane properties [25,26]. Solutions of 0.05 M potassium hexacyanoferrate(II) / 0.05 M potassium hexacyanoferrate(III) were used as electrolyte. Sodium chloride (0.25 M) was added as a supporting electrolyte. Experiments were performed in the laboratory at 23.0 ± 0.5 °C. Temperature and conductivity of the artificial feedwaters were monitored before each experiment. The flow velocity was chosen to be 1 cm/s. Fresh feedwaters were continuously supplied to the RED stacks, in a single-pass configuration, while the electrolyte was recirculated in a closed loop. Peristaltic pumps (Masterflex L/S Digital drive, Cole-Palmer, USA) were used to pump the liquids through the hydraulic circuits. The electrolyte was kept at 0.3 bar overpressure using a diaphragm pressure control valve (KNF FDV 30, KNF-Verder BV, the Netherlands) to avoid bulging of the water compartments.

Configurations a-d in Table 2.1 were used to study the impedance spectra of the clean RED stack and understand their meaning by breaking down the systems in simpler configurations. In addition to those experiments, two more sets of experiments were carried out with configuration e in Table 2.1: 1) a fouling experiment, and 2) a fouling and cleaning experiment. For the fouling experiment, clean feedwaters containing only sodium chloride were supplied to the stack in the initial phase of the fouling experiment. Subsequently, clean river water was substituted with river water containing 50 ppm SDBS. Finally, the SDBS concentration in the river water was increased to 100 ppm. For the fouling and cleaning experiment, clean feedwaters containing only sodium chloride were supplied to the stack in the first step of the experiment. Then, clean river water was substituted with river water containing 100 ppm SDBS. Finally, clean river water containing only sodium chloride was supplied to the stack after fouling as a cleaning method.

2.3.4 Electrochemical measurements and data analysis

All electrochemical measurements were performed with an Autolab PGSTAT302N (Metrohm Autolab BV, the Netherlands). The software NOVA 2.1.3 was used to control the potentiostat. Electrochemical measurements were continuously repeated in a loop. A loop cycle consisted of one constant current step (10 A/m^2, galvanostatic mode), a chronopotentiometric series consisting of three current steps separated by open circuit steps (5, 10 and 15 A/m^2, galvanostatic mode), a second constant current step, a second chronopotentiometric series and, finally, an EIS scan (100 kHz – 10 mHz, 10 mV amplitude superimposed to a constant voltage equal to half of the open circuit voltage, potentiostatic mode). The choice of the frequency range was based on literature values and process conditions [16-19]. It is important to have a relatively fast impedance scan, otherwise the system will change considerably due to fouling or cleaning during the scan time. The galvanostatic mode, where the current is the input to the system and the voltage is the measured output, was chosen for the DC measurements since it is well established in RED literature [27–29]. The potentiostatic mode, where voltage is the input and current is the output from the system, was chosen for the AC measurement. A graphical representation of the current evolution during one measurement loop is provided in Figure S2.5. The duration of one loop cycle was approximately 1 hour. The open circuit voltage (OCV) was evaluated in the open circuit steps at the beginning of each chronopotentiometric series. Stack electrical resistance was evaluated from the slope of the I-V curve obtained from the chronopotentiometric series. The design of the experiment allowed the comparison of stack electrochemical indicators measured in DC mode (chronopotentiometric series) and AC mode (EIS). Matlab software (The MathWorks Inc., USA) was used for data analysis. Scripts were developed for the specific purpose of processing the data from the chronopotentiometric series and EIS scans. For the analysis of EIS data, the Zfit script [30], which performs fitting of experimental impedance data with a determined equivalent circuit, was integrated into our analysis procedure.

2.4 Results and discussion

In the next parts impedance spectra for a pristine, fouled and a cleaned RED stack are discussed to prove the feasibility of EIS at the stack level for fouling monitoring purposes. EIS spectrum of the pristine RED stack

To enable EIS at the stack level, the key is reducing the overall capacitance of the system as this otherwise highly dominates characteristic frequencies and measurement time. Since the capacitance of the system is mostly due to electrical double layers at the membrane-

solution interfaces, reducing the active membrane area decreases the overall system capacitance. This leads to higher characteristic frequencies, thus faster measurements. To evaluate this strategy, specially designed gaskets were employed in the electrolyte and water compartments (Figure S2.4). Two active membrane areas were used: 4 cm^2 and 1 cm^2. Figure 2.1 presents the spectra for a simplified system comprising of only electrodes separated by one CEM (Figure S2.3), measured for the two different active areas.
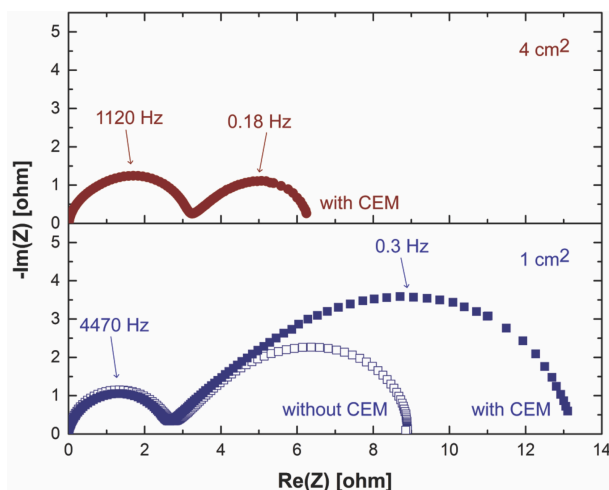
Figure 2.1 Nyquist plots for the electrode system with or without a CEM in between: red circles represent the system with 4 cm^2 active area comprising a CEM between the electrodes, empty blue squares represent the system with 1 cm^2 active area without a CEM between the electrodes, filled blue squares represent the system with 1 cm^2 active area comprising a CEM between the electrodes. The ohmic component of the spectra (intercept with x-axis at high frequencies) was subtracted for ease of comparison.

In accord with the theory we found that the characteristic frequencies for the two arcs are higher for the system with the smaller active area (blue squares) than those of the system with the larger active area (red circles). Therefore, the use of special gaskets to reduce the active area was effective in enabling fast EIS measurements at the stack level.

In Figure 2.1, for all system configurations, with and without a CEM separating the electrodes, the EIS spectra comprise two arcs. The smaller arc at high frequencies is almost constant for the two active areas, while the arc at lower frequencies changes considerably with the active area. The width on the real component axis (x-axis) of the lower frequency arc and its height on the imaginary component axis (y-axis) are larger for the smaller active membrane area. Such behavior suggests that the high frequency arc is related to the electrodes, while the lower frequency arc is related to the CEM. To investigate if the electrodes also affect the lower frequencies arc, an additional measurement was performed

with the 1 cm^2 system but without the CEM. The resulting spectrum shows two arcs representing the impedance of the charge transfer step at the electrode-electrolyte interface (high frequency response) and the mass transfer from the open area to the masked portion of the electrodes (lower frequency response). Comparing the spectra of the systems with and without the CEM, the effect of the membrane on the EIS spectrum is evident. Therefore, the high frequency arc is mainly dictated by the electrodes, while the low frequency arc combines both the electrodes and the CEM.

Figure 2.2 shows the measured spectrum for the one cell-pair RED stack (a CEM, a AEM/CEM pair and the electrodes) with 1 cm^2 active membrane area.
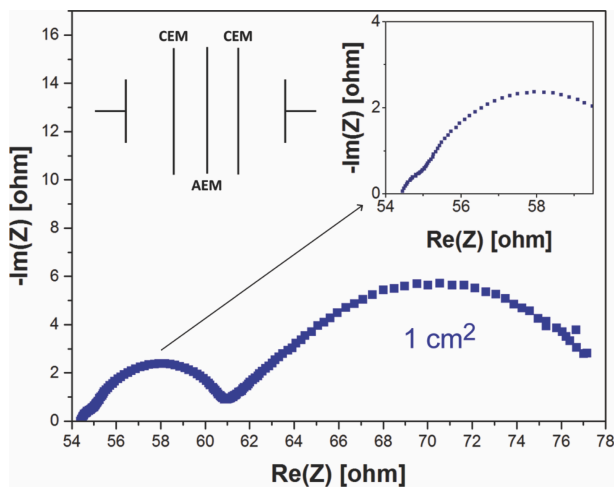
Figure 2.2 Nyquist plot for the one cell-pair RED stack (a CEM, an AEM/CEM pair and the electrodes) with 1 cm^2 active membrane area. The inset highlights the high frequency region displaying the small arc attributed to the AEM. For this plot for the complete stack, the ohmic component of the resistance (high frequency intercept with the x-axis) is not subtracted, since this spectrum represents the starting point for the fouling experiments, making the ohmic component a relevant parameter.

When comparing the spectrum of the complete RED stack (Figure 2.2) with that of the electrodes separated by one CEM only (Figure 2.1), a small third arc at high frequencies is visible (Figure 2.2, inset). This newly created high frequency arc is caused by the additional AEM. Also, the size of the corresponding arcs has changed and the electrode arc in Figure 2.1 has increased in Figure 2.2. This indicates that the addition of an AEM also influences that the low frequency arc. Therefore, in the complete RED stack this second arc is the convolution of the AEM and electrode response. To further verify this conclusion, another stack comprising a different AEM was assembled. Figure S2.6 shows the spectra for the two complete RED stacks one with a Fujifilm AEM type I and one with

a Neosepta AMX-fg membrane. Also in Figure S2.6 shows that changing the AEM affects the ohmic resistance and both arcs at high frequencies, thus confirming the influence of the AEM on both arcs. For the low frequency arc, the difference is that in Figure 2.1 only one CEM and in Figure 2.2 two CEMs are used. Since the two CEMs are assumed to have similar impedances, their spectra will coincide resulting in one larger arc derived from the convolution of the two single CEM arcs. This is the case for the low frequency arc in Figure 2.2.

With these results we now show the impedance spectrum of a full RED stack. Moreover, systematic build-up of the RED stack and measurement of the corresponding spectra allows the detailed identification of the contribution of each single stack element.

2.4.1 Fouling experiment

Subsequently, we used EIS to characterize fouling at the stack level using SDBS as model foulant.

Figure 2.3 shows the electrical resistance of the RED stack measured in DC.
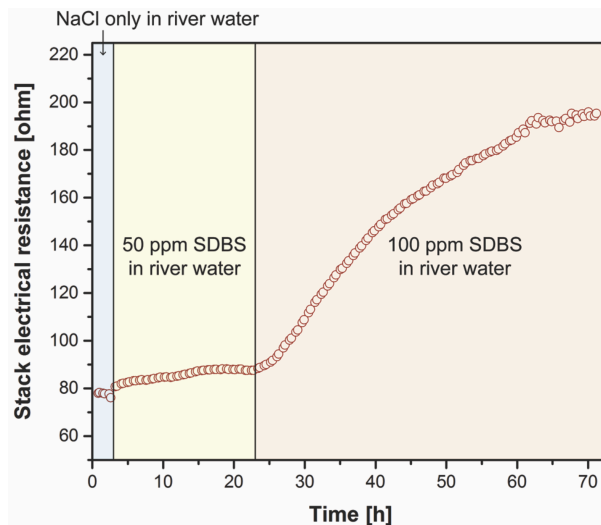
Figure 2.3 Evolution of the RED stack resistance over time during the fouling experiment.

The adsorption of SDBS on the membranes and in the stack resulted in an increase in electrical resistance. At 50 ppm SDBS in river water, fouling is limited and the stack electrical resistance plateaus at 84.7 Ω (+ 7.4 %). At 100 ppm SDBS, fouling is more severe, with the stack electrical resistance reaching 195.4 Ω (+ 147 %). Although interesting, DC characterization at the stack level does not provide information about the

specific location of the fouling in the stack. Since SDBS is a negatively charged model compound, the main contribution to the increased electrical resistance was due to fouling of the AEM. Where DC is unable to discriminate between the different components in the stack, EIS does have that possibility expanding the investigation of fouling in RED towards a previously impossible extension.

Figure 2.4 shows the corresponding EIS data in time (Figure S2.8 and Figure S2.9 present the corresponding Bode and Nyquist plots).
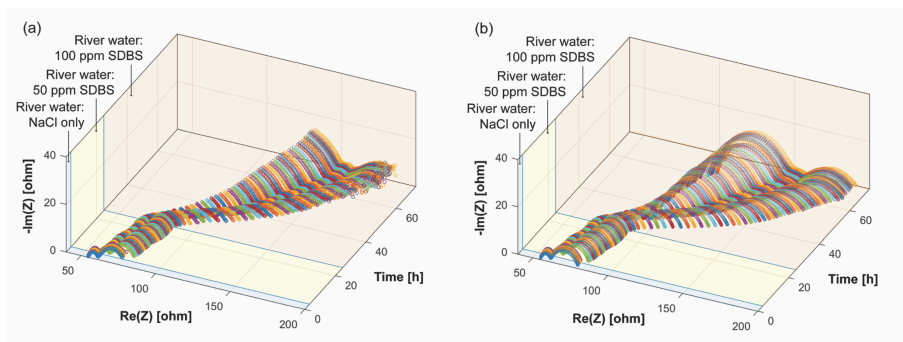
Figure 2.4 Evolution of the (a) experimental and (b) EEC$_2$ model impedance data (Nyquist plot) over time during the fouling experiment.

Upon fouling, the ohmic component of the stack (ohmic resistance of the AEM, the CEM, the water compartments and the electrodes) impedance increases (from initially 54.5 Ω to more than 100 Ω after 60 h of fouling). Figure 2.5 shows the evolution of this ohmic resistance over time. This increase is caused by the SDBS absorbing in the AEM, where it binds to the quaternary ammonium groups. The lower ion exchange capacity (IEC) and free volume available for ion transport determine such increase in electrical resistance.

For the pristine stack, the model (equation S2.11) predicts an ohmic resistance of 53.0 Ω, compared to the experimental value of 54.5 Ω measured experimentally. The contribution of the AEM is only 1.1 Ω. At the end of the fouling experiment, the ohmic resistance is 115.4 Ω (+ 112 %). This increase mostly stems from an increase in AEM ohmic resistance [25,26]. The 60-fold increase in membrane resistance is close to results from the literature, where 40-fold and 50-fold increases are reported, due to absorption and surface adsorption of SDBS forming micelles [19,31].

Figure 2.5 Evolution of the ohmic resistance (values from EEC fitting of experimental data) over time during the fouling experiment.

Figure 2.6 shows the fitting values for the RQ element describing the AEM non-ohmic resistance in EEC$_2$ (Figure S2.7) and its capacitance over time.

At low concentration of SDBS (50 ppm), the non-ohmic resistance does not significantly increase, while the capacitance associated to the AEM is reduced immediately when SDBS is added to the river water. The capacitance decreases until a plateau value was reached. Increasing the SDBS concentration in the river to 100 ppm water decreased the capacitance further. As soon as the capacitance reaches a plateau, the non-ohmic resistance started to increase until it reached a plateau value at the end of the experiment, reflecting the same trend observed for the overall resistance measured in DC mode. The evolution of non-ohmic resistance and capacitance suggests the formation of SDBS domains on the AEM surface, which negatively affects the double layer capacitance. Over time, these domains grow, thus leading to a further reduction of the AEM capacitance, until a homogenous fouling layer covering the full surface is formed that starts to affect the non-ohmic resistance, slowing down the transport of ions to the membrane. This finding is consistent with previous studies on the formation of SDBS micelle layers and its impact on membrane resistance [19,31]. The phase shift angle peak corresponding to the AEM (Figure S2.10) element shifts towards higher frequencies over time. This behavior is consistent with a reduction in the active area that is caused by the fouling domains on the AEM surface. This shift is only observed for the AEM, suggesting that SDBS is mostly affecting the AEM.

40
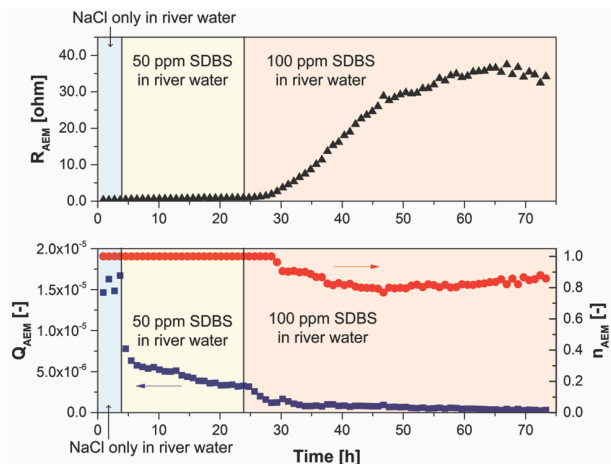
Figure 2.6 (top) Evolution of the non-ohmic AEM resistance (values from EEC fitting of experimental data) over time during the fouling experiment. (bottom) Evolution of the non-ideal capacitance and exponent over time during the fouling experiment for the CPE associated to the AEM.

Figure 2.7 shows the evolution of the fitting values for the non-ohmic resistance and capacitance of the mixed electrode-CEM element.
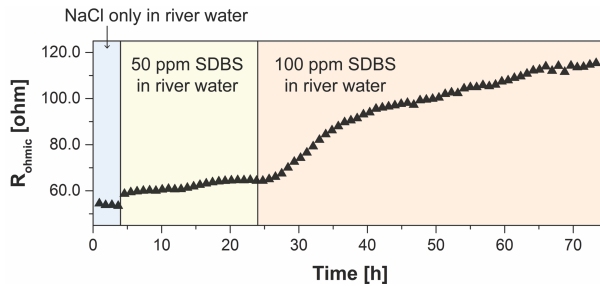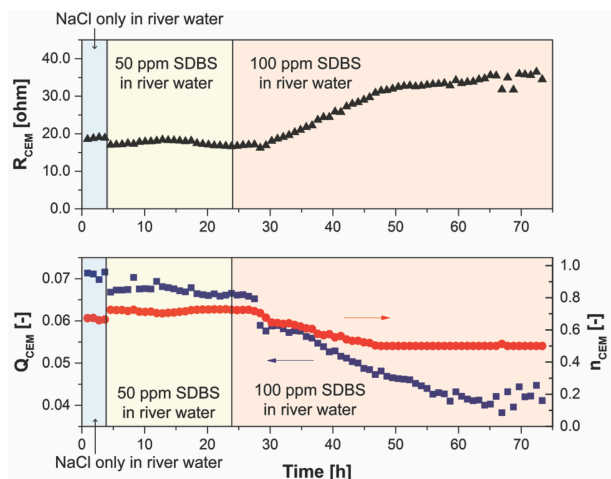

Figure 2.7 (top) Evolution of the non-ohmic CEMs resistance (values from EEC fitting of experimental data) over time during the fouling experiment. (bottom) Evolution of the non-ideal capacitance and exponent over time during the fouling experiment for the CPE associated to the CEMs.

The evolution of the non-ohmic resistance and capacitance of the CEM resembles that of the AEM, although the extent and rate of the non-ohmic resistance increase for the CEM is slower. The capacitance decreased only at high SDBS concentrations, suggesting that

SDBS partly also deposited on the CEM, but the domains remain mostly separated since the capacitance did not plateau until the end of the experiment. Fouling of the CEM by the negatively charged SDBS may seem counter-intuitive, but since SDBS was present in the river water compartment, the electric field pushed it towards the anode and thus the CEM. The concentration of SDBS at the CEM surface exceeded locally the critical micelle concentration (CMC) resulting in the local formation of a micellar configuration, shielding the negative charges of SDBS.

2.4.2 Fouling and cleaning experiment

Finally, the effect of a subsequent cleaning step after a 100 ppm SDBS fouling run is investigated using EIS.

Figure S2.11 shows the evolution of the stack electrical resistance as measured from the slope of the I-V curve in DC mode. The resistance increase upon fouling was even faster than in the previous experiment since the stack was exposed to the high (100 ppm) concentration of SDBS from the beginning of the fouling run. Upon cleaning by flushing the stack with clean river water the electrical resistance of the stack dropped quickly and then slowly decreased until it plateaus at a higher level than the original value. Therefore, the fouling is partly irreversible. Similar results were found by Zhao et al., who reported an irreversible resistance increase after membrane fouling by sodium dodecylsulfonate (SDS) [20]. Nevertheless, DC characterizations do not give any information about the cleaning effects of the different components present in the stack, e.g. whether both membranes were cleaned or only one of them and to what extent.

Figure 2.8 (Nyquist plot) and Figure S2.12 (Bode plots) show the evolution of the EIS spectra over time of the fouling and subsequent cleaning process.

Similar to the previous fouling experiment, upon fouling the ohmic component, and predominantly its AEM part, increased. The CEM arc was also influenced, although to a lesser extent, while fouling does not affect the arc in the center. When the cleaning run starts, all ohmic and non-ohmic resistances decrease, but on different time scales (Figure S2.13). The CEM non-ohmic resistance drops significantly in the first EIS scan after the change to clean river water (Figure S2.14). This indicates that fouling on the CEM surface was reversible and could be easily removed, due to the electrostatic repulsion of the negative charges of SDBS and the CEM. Moreover, during cleaning, the SDBS concentration at the membrane-solution interface decreases below the CMC. The cleaning of the AEM was much slower: only after 16 h of cleaning, the arc representing the AEM in the EIS spectrum was completely recovered. This slow recovery is caused by the

42

favorable electrostatic interaction between the negatively charged SDBS and the positively charged AEM.
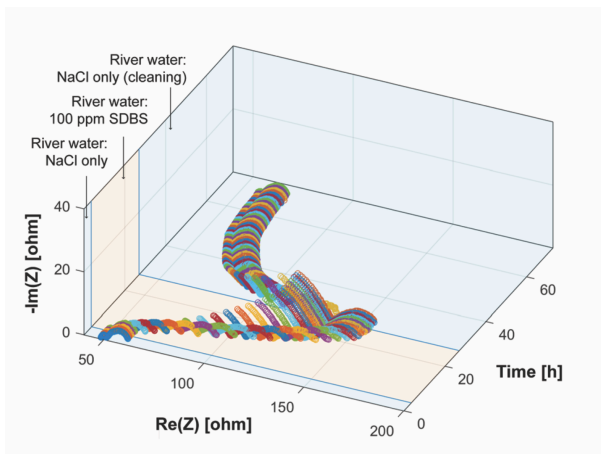
Figure 2.8 Evolution of the experimental impedance data over time (Nyquist plot) during the fouling and cleaning experiment.

Consistent with the DC results, also the EIS measurements show that there is an 11.5 Ω mismatch between the initial electrical resistance of the pristine RED stack and the stack resistance after the fouling-cleaning cycle. Opposite to the DC measurements however, the EIS spectra clearly shows that this mismatch is entirely due to an irreversible increase in the ohmic resistance so that the total stack ohmic resistance has not been fully recovered to its original value. Given that the resistance of the water compartments is the same before and after the fouling run and that the CEM was easily cleaned, t This irreversible increase in ohmic resistance of the stack must be attributed to the non-reversible increase in the ohmic resistance of the AEM. This indicates that SDBS is trapped in the AEM, where it bound to the positive groups. Thus, the membrane IEC andfree volume available for ion transport are not completely recovered. Further evidence of this behavior is the loss in open circuit voltage of the stack which decreased from 147 mV for the pristine stack to 143 mV after the fouling-cleaning cycle, indicating a permanent loss in permselectivity.

2.5 Conclusions

The reduction of the active membrane area in a RED-stack is the key to unravel fast and reliable EIS measurements at the real stack level. An EIS fouling experiment with SDBS added to river water revealed how the foulant impacted the elements of the stack on different time scales. Absorption of SDBS in the AEM leads to a fast increase in the ohmic

component. SDBS domains on the AEM nucleate at low concentration and grow, thus increasing the non-ohmic component of the AEM resistance. Longer exposure times to SDBS also affect the CEM despite the unfavorable electrostatic interaction with SDBS due to the direction of the electric field towards anode and CEM. Cleaning of the stack elements at different time scales and to different extents showed that the ohmic resistance decreased slowly and plateaued at a higher level than the original. This shows that SDBS is irreversibly absorbed in the AEM, where it ion exchanges with the quaternary ammonium groups, leading to lower ion exchange capacity and free volume available for ion transport. The non-ohmic component of the AEM recovered completely, as was the case for the CEM non-ohmic resistance. However, the CEM recovered faster, thanks to the electrostatic repulsion between sulfonic acid groups and the negatively charged SDBS. The new fouling monitoring strategy presented in this work is a big step towards effective RED exploitation using natural foulants containing salinity gradients. Fouling monitoring by EIS enables the use of efficient cleaning strategies, by making use of the knowledge of which individual stack elements are susceptible to fouling and provides guidance on how to control this fouling.

Glossary

(in alphabetical order)

AC	Alternating current
AEM	Anion exchange membrane
CEM	Cation exchange membrane
CPE	Constant phase element
DC	Direct current
EEC	Electrical equivalent circuit
EIS	Electrochemical impedance spectroscopy
I	Current
IEM	Ion exchange membrane
j	Imaginary unit
R	Resistance
RED	Reverse electrodialysis
RW	River water
SDBS	Sodium dodecylbenzenesulfonate
SDS	Sodium dodecylsulfonate
SW	Seawater
t	Time
U	Potential
Z	Impedance
φ	Phase shift
ω	Angular frequency

2

Supporting information
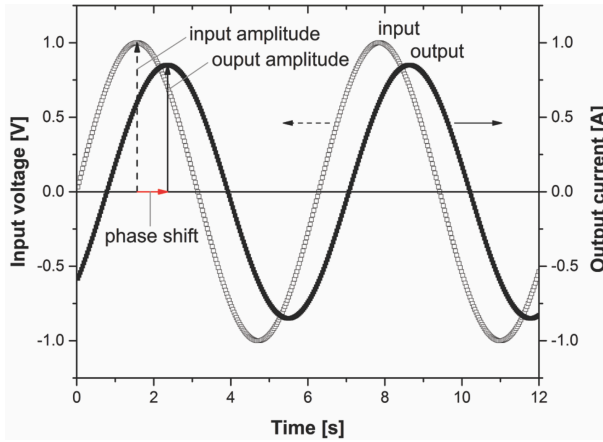
Figure S2.1 Sinusoidal input and output signals at a given frequency during an electrochemical impedance spectroscopy measurement.

Impedance equations for resistor, capacitor, and constant phase element

When applying Euler's formula (equation S2.1) to equation 2.4, the impedance can be re-written as follows:

$$e^{j\varphi} = \cos\varphi + j\sin\varphi \tag{S2.1}$$

$$Z(\omega) = |Z|e^{-j\varphi} = |Z|\cos\varphi - j\,|Z|\sin\varphi \tag{S2.2}$$

Therefore, the impedance Z is a complex quantity consisting of a real and imaginary part.

$$Z(\omega) = Re(Z) + j \cdot Im(Z) \tag{S2.3}$$

$$Re(Z) = |Z|\cos\varphi \tag{S2.4}$$

$$Im(Z) = -|Z|\sin\varphi \tag{S2.5}$$

For simple electrical elements, the impedance is derived in a simple form. In the case of a resistor, the system responds instantly to the input. Therefore, there is no phase shift and the impedance of a resistor is:

$$Z(\omega) = \frac{U(\omega, t)}{I(\omega, t)} = \frac{U_0 e^{j\omega t}}{I_0 e^{j\omega t}} = \frac{U_0}{I_0} = R \tag{S2.6}$$

It can be noted that for a resistor, impedance has only a real part and no dependency on frequency. For a pure capacitor, current and voltage are related through the capacitance C [F] ($I(t)dt = CdU(t)$). Its impedance will be given by:

$$Z(\omega) = \frac{U(\omega, t)}{I(\omega, t)} = \frac{U(\omega, t)}{C\dfrac{dU(t)}{dt}} = \frac{U_0 e^{j\omega t}}{CU_0 j\omega e^{j\omega t}} = \frac{1}{j\omega C} = \frac{-j}{\omega C} \qquad \text{(S2.7)}$$

Therefore, the impedance of a capacitor is purely imaginary, with phase shift angle equal to -90°, and is frequency dependent. For increasing frequencies, the capacitor impedance will decrease, while at low frequencies the capacitor impedance tends to infinite. Resistor and capacitors are ideal electrical elements. However, most electrochemical systems are not ideal due to defects and their finite size. Non-ideal elements, like the constant phase element (CPE), are introduced to represent real systems in the EEC analysis. The impedance of a CPE is given by:

$$Z(\omega) = \frac{1}{Q(j\omega)^n} \qquad \text{(S2.8)}$$

Q [S s^{-1}] and n [-] describe the CPE behavior. For n equal to 1, the CPE behaves like an ideal capacitor, while for n equal to 0 it describes a resistor. For n equal to 0.5, the impedance of an electrochemical system determined by mass transfer limitations is described [31].

Resistors, capacitors, CPE and many other elements can be combined into EECs to fit experimental spectra. Connection of elements can be in series or parallel. In the case of series connection, the overall impedance is given by the sum of the single element impedances:

$$Z_{series} = \sum Z_i \qquad \text{(S2.9)}$$

For parallel connection, the reciprocal of the overall impedance is given by the sum of reciprocals of the single element impedances:

$$\frac{1}{Z_{parallel}} = \sum \frac{1}{Z_i} \qquad \text{(S2.10)}$$
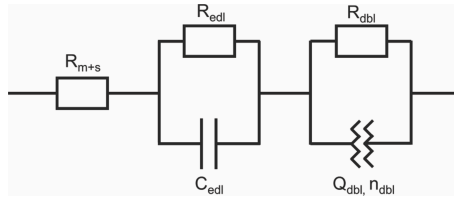
Figure S2.2 Equivalent circuit used for the fitting of single IEM impedance spectra. The first resistor represents the ohmic response of the membrane at high frequencies. The RC parallel element represents the response of the electrical double layer at intermediate frequencies. The RQ element represents the diffusion boundary layer behavior, which is measured at lower frequencies.
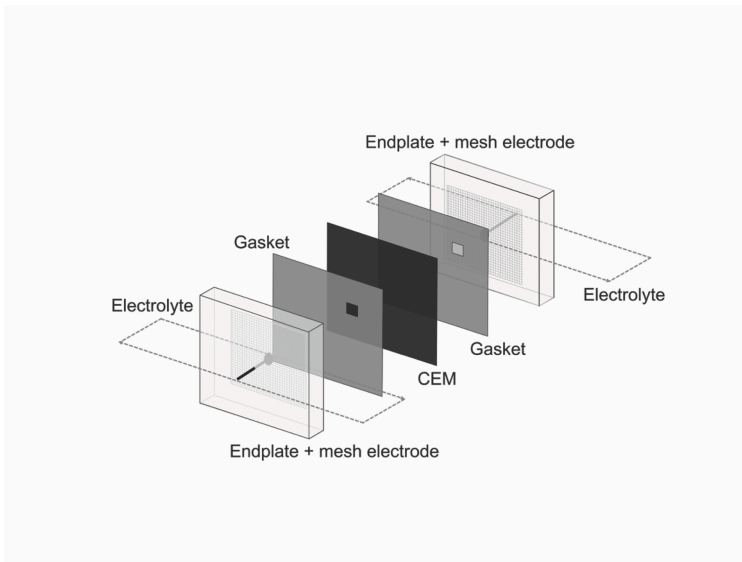
Figure S2.3 Stack configuration consisting of endplates separated by a CEM. The endplates house the electrolyte compartments where a platinized titanium electrode is located. Extended silicone rubber gaskets are employed to limit the active membrane area of the CEM separating the two compartments. Such configuration acts as a baseline measurement for a complete RED stack, since it consists of a stack where all active cell pairs have been removed, leaving the electrolyte compartments and the extra CEM as the only components still present. This configuration represents a system with reduced complexity with respect to the complete RED stack, thus representing an optimal starting point for the study of stack impedance spectra.
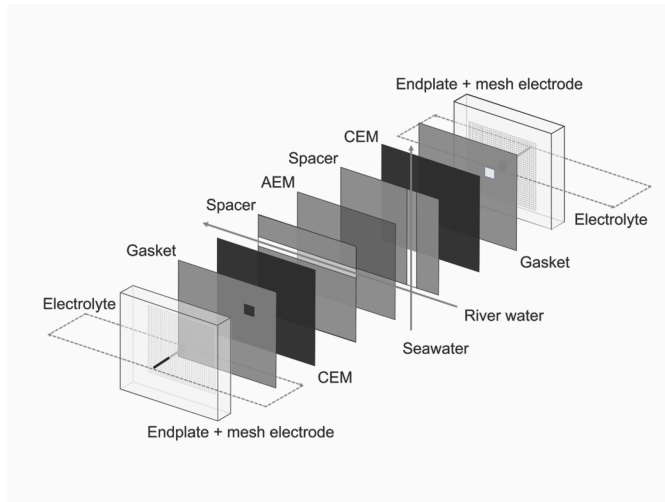
Figure S2.4 Complete RED stack. In this configuration one CEM and one AEM are separated by a spacer to accommodate the feedwaters, an extra CEM is present to seal the electrolyte compartment. The endplates house the electrolyte compartments where a platinized titanium electrode is located. Silicone rubber gaskets and spacers with integrated gaskets are used to limit the active area of the membranes.
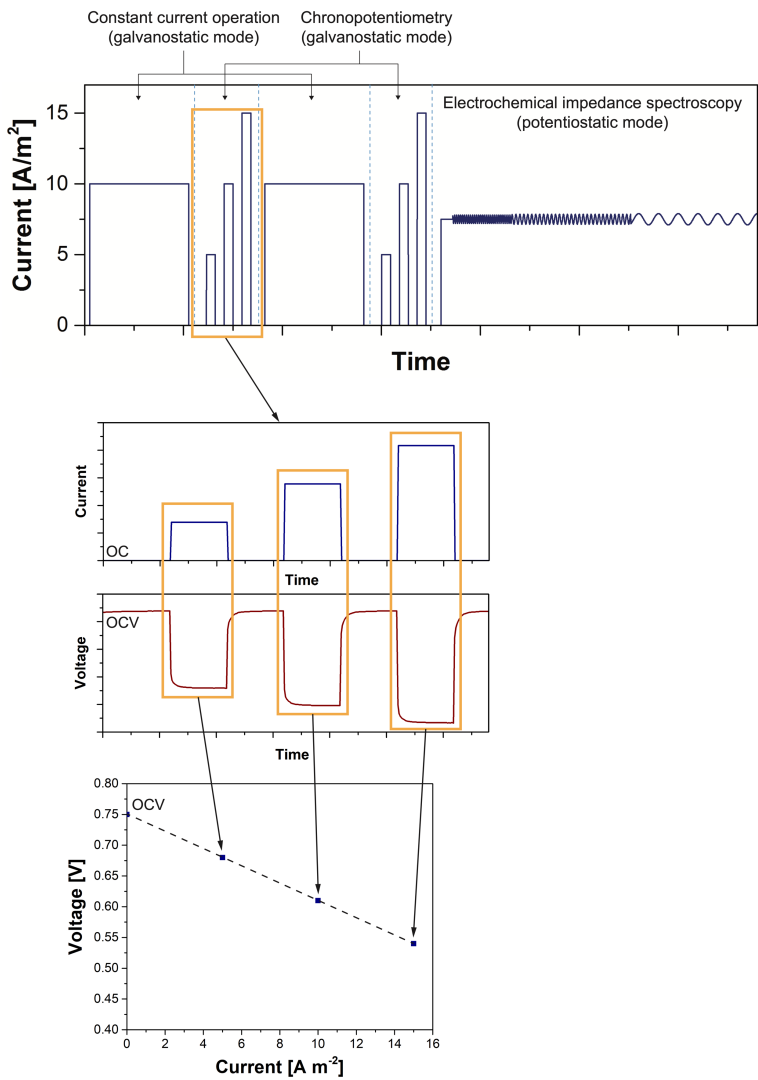
Figure S2.5 Evolution of the current over time during the sequence of electrochemical characterizations performed on the RED stack within one measurement cycle. Constant current step (10 A/m²), chronopotentiometric series consisting of three current steps (5, 10, 15 A/m²) separated by open circuit steps, a second constant current step, a second chronopotentiometric series, and electrochemical impedance spectroscopy (100 kHz – 0.01 Hz, 10 mV amplitude superimposed to constant voltage equal to half of the OCV). During the DC measurements, the current is the input to the system and the voltage is the output (galvanostatic mode). During the AC measurement, the current is the output from the system and the voltage is the input (potentiostatic mode).
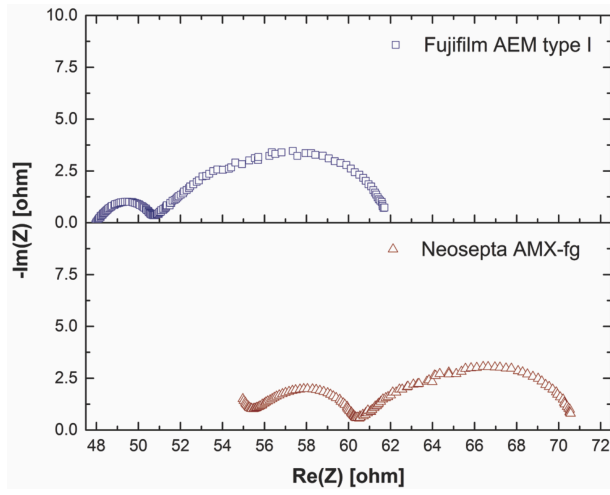
Figure S2.6 Comparison of impedance spectra for two stacks comprising the same CEMs, but different AEMs. (top) Fujifilm AEM type I and (bottom) Neosepta AMX-fg.

Equivalent circuit for fitting of experimental data

For a quantitative analysis of the spectra, two EEC were used: EEC_1 for the electrodes with and without CEM (Figure S2.6a), and EEC_2 for the complete RED stack (Figure S2.6b). These equivalent circuits differ from the EEC generally used for IEMs in the literature [14] because here the complete RED stack is considered, which is far more complex than a single IEM. As a consequence, the different elements of the IEM impedance are not visible due to overlapping and convolution of several contributions from electrodes, CEMs and AEM.
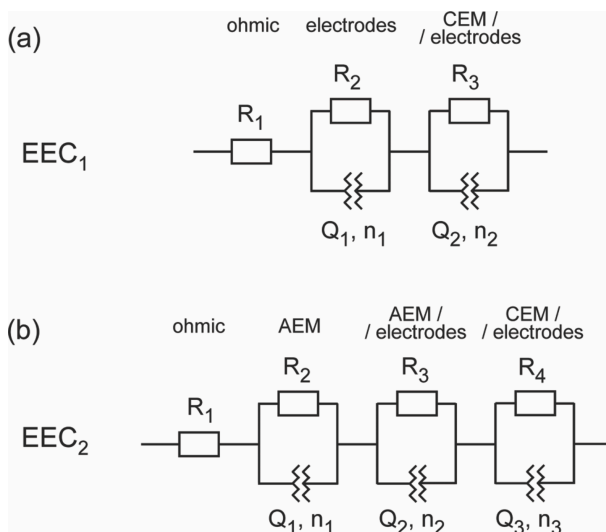
Figure S2.7 equivalent circuits used for the fitting of the measured spectra: EEC_1 for the endplates systems with one CEM and EEC_2 for the complete RED stack.
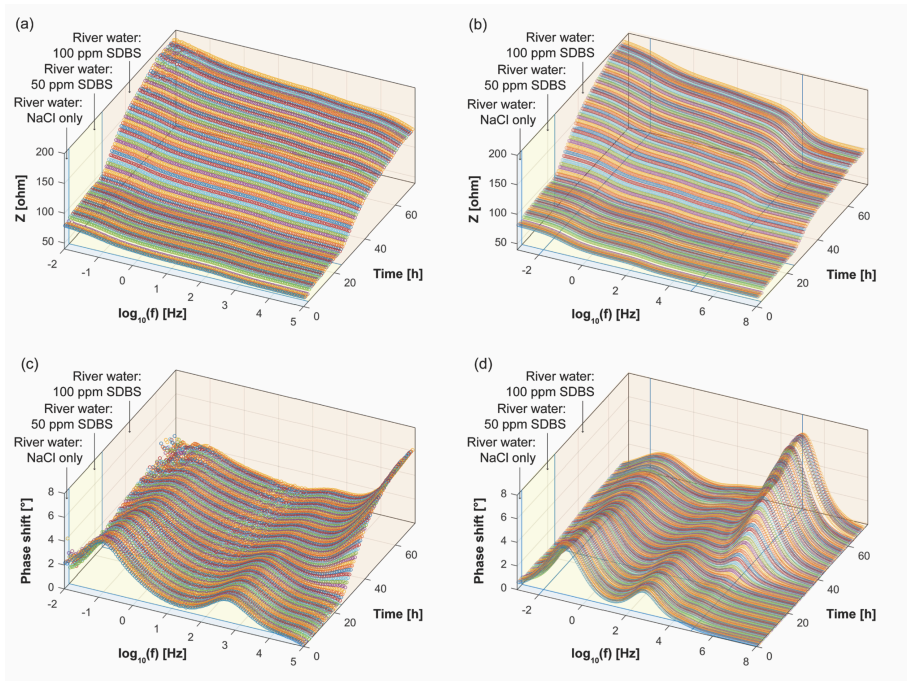
Figure S2.8 Evolution of the experimental (a, c) and EEC$_2$ model (b, d) impedance data over time during the fouling experiment. (a) Three-dimensional Bode plot (impedance modulus) with experimental data measured during the fouling experiment. (b) Three-dimensional Bode plot (impedance modulus) with EEC$_2$ model values calculated from fitting the experimental data from the fouling experiment. (c) Three-dimensional Bode plot (phase shift angle) with experimental data measured during the fouling experiment. (d) Three-dimensional Bode plot (phase shift angle) with EEC$_2$ model values calculated from fitting the experimental data from the fouling experiment. Values for frequencies below 10^{-2} Hz and above 10^{5} Hz (beyond the blue lines) have been extrapolated.
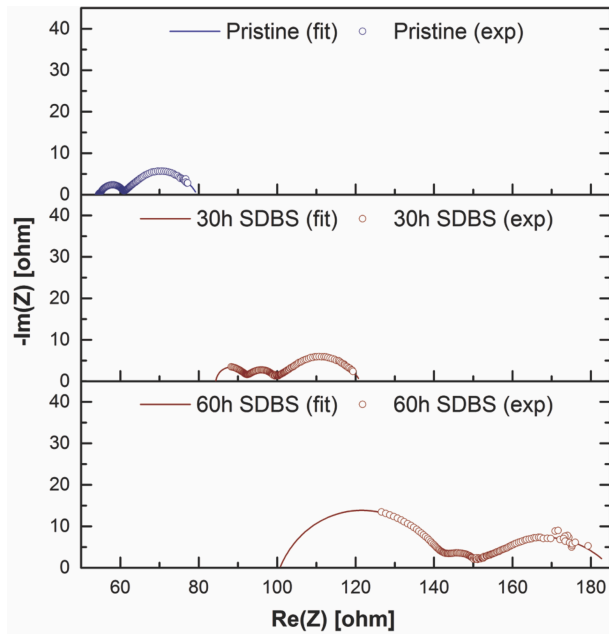
Figure S2.9 Representative Nyquist plots for the RED stack during the fouling experiment: Top picture: Clean stack; Middle picture: Stack after 30 hours fouling and Bottom picture: Stack after 60 hours fouling. Circles represent experimental data, while the solid line represents the fitted data based on EEC$_2$.
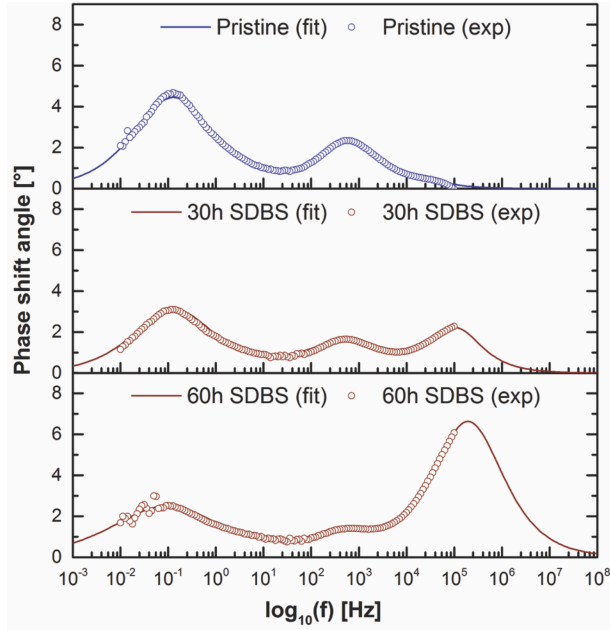
Figure S2.10 Representative Bode plots (phase shift angle) for the RED stack during the fouling experiment: Top picture: Clean stack; Middle picture: Stack after 30 hours fouling and Bottom picture: Stack after 60 hours fouling. Circles represent experimental data, while the solid line represents the fitted data based on EEC₂.

Stack electrical resistance model

To understand what determines this increase over time, it is worth considering the contributions to the ohmic resistance from different stack components. The following equation describes their influence on the ohmic resistance:

$$R_{ohmic} = R_{el} + R_{CEM} + R_{AEM} + \frac{1}{f}\frac{d_{rw}}{\kappa_{rw}} + \frac{1}{f}\frac{d_{sw}}{\kappa_{sw}} \tag{S2.11}$$

Where R_{el} is the resistance of the electrodes, f is the obstruction factor accounting for the spacers reducing the effective active membrane area for ion conduction, R_{CEM} and R_{AEM} are the resistances of the membranes, d_{rw} and d_{sw} are the thicknesses of the water compartments and κ_{rw} and κ_{sw} are the conductivities of the feedwaters, with the subscripts rw indicating river water and sw seawater.
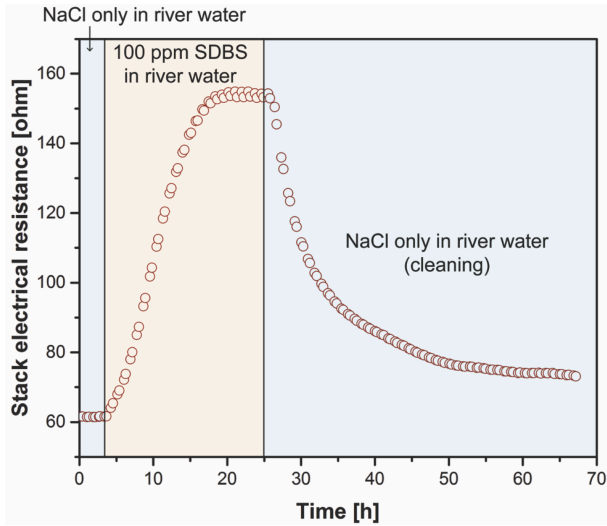
Figure S2.11 Evolution of the RED stack resistance over time during the fouling and cleaning experiment.
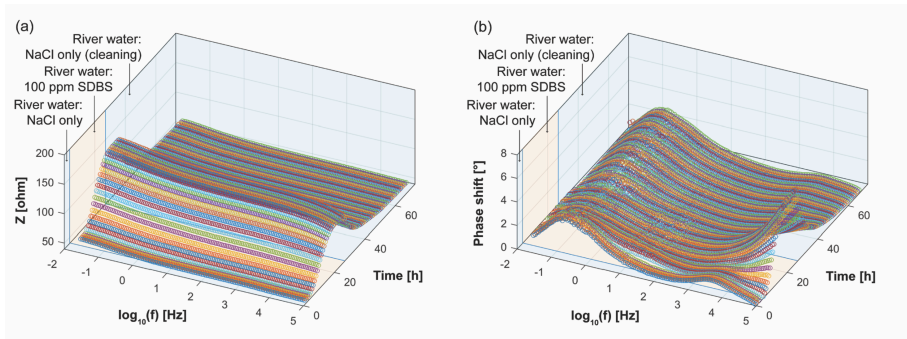
Figure S2.12 Evolution of the experimental impedance data over time during the fouling and cleaning experiment. (a) Three-dimensional Bode plot (impedance modulus) with experimental data measured during the fouling and cleaning experiment. (b) Three-dimensional Bode plot (phase shift angle) with experimental data measured during the fouling and cleaning experiment.
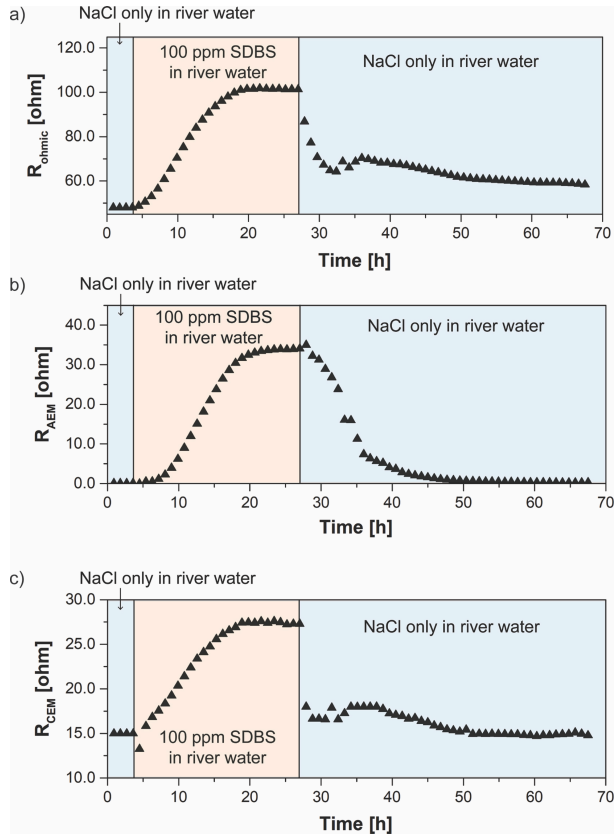
Figure S2.13 Evolution of the a) ohmic, b) non-ohmic AEM, and c) non-ohmic CEM resistances (values from EEC fitting of experimental data) during the fouling and cleaning experiment.
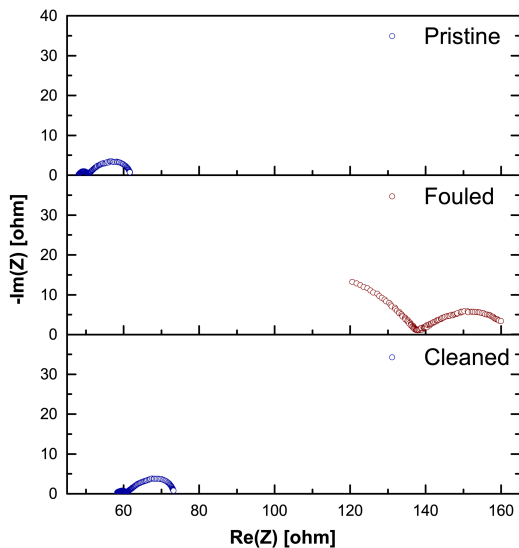
Figure S2.14 Representative Nyquist plots (experimental data) for the RED stack during the fouling and cleaning experiment. Top picture: pristine stack; Middle picture: Stack at the end of the fouling step; Bottom picture: stack at the end of the cleaning step.

References

[1]   J.W. Post, J. Veerman, H.V.M. Hamelers, G.J.W. Euverink, S.J. Metz, K. Nymeijer, C.J.N. Buisman, Salinity-gradient power: Evaluation of pressure-retarded osmosis and reverse electrodialysis, J. Memb. Sci. 288 (2007) 218–230. doi:10.1016/j.memsci.2006.11.018.

[2]   J.W. Post, H.V.M. Hamelers, C.J.N. Buisman, Energy recovery from controlled mixing salt and fresh water with a reverse electrodialysis system, Environ. Sci. Technol. 42 (2008) 5785–5790. doi:10.1021/es8004317.

[3]   A.H. Galama, J.W. Post, H.V.M. Hamelers, V.V. Nikonenko, P.M. Biesheuvel, On the origin of the membrane potential arising across densely charged ion exchange membranes: How well does the teorell-meyer-sievers theory work?, J. Membr. Sci. Res. 2 (2016) 128–140.

[4]   J. Veerman, M. Saakes, S.J. Metz, G.J. Harmsen, Reverse electrodialysis: Evaluation of suitable electrode systems, J. Appl. Electrochem. 40 (2010) 1461–1474. doi:10.1007/s10800-010-0124-8.

[5]   E. Güler, K. Nijmeijer, Reverse electrodialysis for salinity gradient power generation: Challenges and future perspectives, J. Membr. Sci. Res. 4 (2018) 108–110. doi:10.22079/JMSR.2018.86747.1193.

[6]   D.A. Vermaas, D. Kunteng, M. Saakes, K. Nijmeijer, Fouling in reverse electrodialysis under natural conditions, Water Res. 47 (2013) 1289–1298. doi:10.1016/j.watres.2012.11.053.

[7]   D.A. Vermaas, D. Kunteng, J. Veerman, M. Saakes, K. Nijmeijer, Periodic feedwater reversal and air sparging as antifouling strategies in reverse electrodialysis, Environ. Sci. Technol. 48 (2014) 3065–3073. doi:10.1021/es4045456.

[8]   M. Vaselbehagh, H. Karkhanechi, R. Takagi, H. Matsuyama, Biofouling phenomena on anion exchange membranes under the reverse electrodialysis process, J. Memb. Sci. 530 (2017) 232–239. doi:10.1016/j.memsci.2017.02.036.

[9]   D.M. Warsinger, S. Chakraborty, E.W. Tow, M.H. Plumlee, C. Bellona, S. Loutatidou, L. Karimi, A.M. Mikelonis, A. Achilli, A. Ghassemi, L.P. Padhye, S.A. Snyder, S. Curcio, C.D. Vecitis, H.A. Arafat, J.H. Lienhard, A review of polymeric membranes and processes for potable water reuse, Prog. Polym. Sci. 81 (2018) 209–237. doi:10.1016/j.progpolymsci.2018.01.004.

[10]   J. Moreno, N. de Hart, M. Saakes, K. Nijmeijer, CO2saturated water as two-phase flow for fouling control in reverse electrodialysis, Water Res. 125 (2017) 23–31. doi:10.1016/j.watres.2017.08.015.

[11]   E.J. Bodner, M. Saakes, T. Sleutels, C.J.N. Buisman, H.V.M. Hamelers, The RED Fouling Monitor: A novel tool for fouling analysis, J. Memb. Sci. 570–571 (2019) 294–302. doi:10.1016/j.memsci.2018.10.059.

[12]   G. Di Profio, 2.13 Membranes and Interfaces Characterization by Impedance Spectroscopy, Compr. Membr. Sci. Eng. (2017) 393–410. doi:10.1016/B978-0-12-409547-2.12238-3.

[13]   J.-S. Park, J.-H. Choi, J.-J. Woo, S.-H. Moon, An electrical impedance spectroscopic (EIS) study on transport characteristics of ion-exchange membrane systems, J. Colloid Interface Sci. 300 (2006) 655–662. doi:10.1016/j.jcis.2006.04.040.

2

[14] P. Długołecki, P. Ogonowski, S.J. Metz, M. Saakes, K. Nijmeijer, M. Wessling, On the resistances of membrane, diffusion boundary layer and double layer in ion exchange membrane transport, J. Memb. Sci. 349 (2010) 369–379. doi:10.1016/j.memsci.2009.11.069.

[15] W. Zhang, J. Ma, P. Wang, Z. Wang, F. Shi, H. Liu, Investigations on the interfacial capacitance and the diffusion boundary layer thickness of ion exchange membrane using electrochemical impedance spectroscopy, J. Memb. Sci. 502 (2016) 37–47. doi:10.1016/j.memsci.2015.12.007.

[16] A.H. Avci, P. Sarkar, R.A. Tufa, D. Messana, P. Argurio, E. Fontananova, G. Di Profio, E. Curcio, Effect of Mg^{2+}ions on energy generation by Reverse Electrodialysis, J. Memb. Sci. 520 (2016) 499–506. doi:10.1016/j.memsci.2016.08.007.

[17] E. Fontananova, D. Messana, R.A. Tufa, I. Nicotera, V. Kosma, E. Curcio, W. van Baak, E. Drioli, G. Di Profio, Effect of solution concentration and composition on the electrochemical properties of ion exchange membranes for energy conversion, J. Power Sources. 340 (2017) 282–293. doi:10.1016/j.jpowsour.2016.11.075.

[18] J.-S. Park, J.-H. Choi, K.-H. Yeon, S.-H. Moon, An approach to fouling characterization of an ion-exchange membrane using current-voltage relation and electrical impedance spectroscopy, J. Colloid Interface Sci. 294 (2006) 129–138. doi:10.1016/j.jcis.2005.07.016.

[19] H.J. Lee, M.K. Hong, S.D. Han, J. Shim, S.H. Moon, Analysis of fouling potential in the electrodialysis process in the presence of an anionic surfactant foulant, J. Memb. Sci. 325 (2008) 719–726. doi:10.1016/j.memsci.2008.08.045.

[20] Z. Zhao, S. Shi, H. Cao, Y. Li, Electrochemical impedance spectroscopy and surface properties characterization of anion exchange membrane fouled by sodium dodecyl sulfate, J. Memb. Sci. 530 (2017) 220–231. doi:10.1016/j.memsci.2017.02.037.

[21] Z. Zhao, S. Shi, H. Cao, B. Shan, Y. Sheng, Property characterization and mechanism analysis on organic fouling of structurally different anion exchange membranes in electrodialysis, Desalination. 428 (2018) 199–206. doi:10.1016/j.desal.2017.11.021.

[22] I. Choi, J.Y. Han, S.J. Yoo, D. Henkensmeier, J.Y. Kim, S.Y. Lee, J. Han, S.W. Nam, H.-J. Kim, J.H. Jang, Experimental investigation of operating parameters in power generation by lab-scale reverse electro-dialysis (RED), Bull. Korean Chem. Soc. 37 (2016) 1010–1019. doi:10.1002/bkcs.10810.

[23] V.V. Nikonenko, A.E. Kozmai, Electrical equivalent circuit of an ion-exchange membrane system, Electrochim. Acta. 56 (2011) 1262–1269. doi:10.1016/j.electacta.2010.10.094.

[24] P. Sistat, A. Kozmai, N. Pismenskaya, C. Larchet, G. Pourcelly, V. Nikonenko, Low-frequency impedance of an ion-exchange membrane system, Electrochim. Acta. 53 (2008) 6380–6390. doi:10.1016/j.electacta.2008.04.041.

[25] H.-J. Lee, M.-K. Hong, S.-D. Han, J. Shim, S.-H. Moon, Analysis of fouling potential in the electrodialysis process in the presence of an anionic surfactant foulant, J. Memb. Sci. 325 (2008) 719–726. doi:10.1016/j.memsci.2008.08.045.

[26] H.-J. Lee, M.-K. Hong, S.-D. Han, S.-H. Cho, S.-H. Moon, Fouling of an anion exchange membrane in the electrodialysis desalination process in the presence of organic foulants, Desalination. 238 (2009) 60–69. doi:10.1016/j.desal.2008.01.036.

2

[27]   J. Veerman, M. Saakes, S.J. Metz, G.J. Harmsen, Reverse electrodialysis: Performance of a stack with 50 cells on the mixing of sea and river water, J. Memb. Sci. 327 (2009) 136–144. doi:10.1016/j.memsci.2008.11.015.

[28]   D.A. Vermaas, J. Veerman, M. Saakes, K. Nijmeijer, Influence of multivalent ions on renewable energy generation in reverse electrodialysis, Energy Environ. Sci. 7 (2014) 1434–1445. doi:10.1039/c3ee43501f.

[29]   J. Moreno, V. Díez, M. Saakes, K. Nijmeijer, Mitigation of the effects of multivalent ion transport in reverse electrodialysis, J. Memb. Sci. 550 (2018) 155–162. doi:10.1016/j.memsci.2017.12.069.

[30]   J.-L. Dellis, Zfit, MATLAB Cent. File Exch. (2010). https://nl.mathworks.com/matlabcentral/fileexchange/19460-zfit (accessed September 11, 2018).

[31]   Z. Zhao, S. Shi, H. Cao, B. Shan, and Y. Sheng, Property characterization and mechanism analysis on organic fouling of structurally different anion exchange membranes in electrodialysis. Desalination 428 (2018), 199–206. doi:10.1016/j.desal.2017.11.021

2

Chapter 3

Tailoring the surface chemistry of anion exchange membranes with zwitterions: towards anti-fouling RED membranes

Abstract

Fouling is a pressing issue for harvesting salinity gradient energy with reverse electrodialysis (RED). In this work, anti-fouling membranes were fabricated by surface modification of a commercial anion exchange membrane with zwitterionic layers. Either zwitterionic monomers or zwitterionic brushes were applied on the surface. Zwitterionic monomers were grafted to the surface by deposition of a polydopamine layer followed by an aza-Michael reaction with sulfobetaine. Zwitterionic brushes were grafted on the surface by deposition of polydopamine modified with a surface initiator for subsequent atom transfer radical polymerization to obtain polysulfobetaine. As expected, the zwitterionic layers did increase the membrane hydrophilicity. The anti-fouling behavior of the membranes in RED was evaluated using artificial river and seawater and sodium dodecylbenzenesulfonate as model foulant. The zwitterionic monomers are effective in delaying the fouling onset, but the further built-up of the fouling layer is hardly affected, finally resulting in similar power density losses as for the unmodified membranes. Membranes modified with zwitterionic brushes show a high potential for application in RED as they not only delay the onset of fouling and are easier to clean, but they also slow down the growth of the fouling layer, thus retaining higher power density outputs.

3.1 Introduction

Salinity gradient energy (SGE) is an energy source derived from the controlled mixing of low and high concentration water streams, e.g., river and seawater, seawater and desalination brines, or thermolytic salt solutions in closed-loop applications [1–6]. SGE has the potential to meet the increasing renewable energy demand without the intermittency issues that plague solar and wind energy. SGE from natural salinity gradients alone has an estimated technical potential of 0.64 to 0.98 TW, accounting for feasibility and efficiencies [7].

Reverse electrodialysis (RED) is an electro-membrane technology to harvest SGE [8,9]. In RED, cation exchange membranes (CEMs) and anion exchange membranes (AEMs) are stacked alternately to create feedwater compartments where the high and low concentration solutions (e.g., 30 and 1 g L^{-1} NaCl) flow. The salinity gradient across the selective ion exchange membranes results in a potential difference that increases with the number of cell pairs in the RED stack [10]. When an external load is connected to the electrodes at the two ends of the stack to close the circuit, this potential difference can be used to drive an ionic current through the stack. The ionic current is converted into an electronic current by a suitable redox couple flowing in the electrode compartments [11]. The potential of RED as a large-scale energy source has been investigated at the laboratory and pilot plant scale [5,12,13] and the main obstacles for large-scale RED implementation with natural salinity gradients are fouling and more in general costs [14–16]. Fouling is caused by colloids, natural organic matter, multivalent ions, and micro-organisms deteriorating the membrane properties, yielding lower RED power output [14,17,18]. Anion exchange membranes are particularly prone to fouling due to electrostatic interaction between their positive charge and the net negative charge carried by most foulants. In addition also affinity interactions between the organic contaminants and the polymeric membranes do play a dominant role [19–26].

To mitigate fouling, stack cleaning protocols and membrane modifications have been thoroughly investigated [27–29]. Periodic feed water reversal, air sparging, and CO$_2$ sparging are effective strategies to recuperate fouled membranes and spacers [27,28]. For membrane modification, desired properties are monovalent-ion selectivity and anti-fouling functionality to increase the RED power output and the ability to retain it over time [16,30]. Improved resistance to organic fouling is typically obtained by increasing the hydrophilicity of the membrane surface or by deposition of a thin negatively charged layer [29,31–33].

A promising approach is the use of polydopamine (PDA) to mitigate fouling. Although the application of thick polydopamine layers on the membrane increases the hydrophilicity of the membrane reducing fouling and induces monovalent-ion selectivity by size exclusion, this is done at the expense of decreased membrane charge density and increased membrane resistance [29,34–38]. On the other hand, PDA in the form of a thin layer on a membrane surface is a versatile platform for membrane modification thanks to its functional groups that can undergo further reactions [39,40].

Zwitterionic coatings are well-known in the biomedical field, where they are used to reduce fouling of surfaces in contact with biological fluids [41,42]. Recently, zwitterionic layers are gaining prominence as effective anti-fouling layers in the field of water treatment [43–47]. In her review on tackling membrane fouling, Nunes indicated zwitterions grafting as one of the strategies for the fabrication of fouling-resistant membranes [48]. In this regard, Virga et al. recently showed that a zwitterionic top layer is effective in preventive fouling of nanofiltration hollow-fiber membranes during treatment of natural waters [49]. Zwitterionic layers (e.g., polysulfobetaine) are highly hydrophilic due to their ability to retain large hydration shells through hydrogen bonding [50]. Their hydrophilicity combined with a net neutral charge of the zwitterionic layer leads to low interaction with organic pollutants [44]. Liu et al. modified a thin-film-composite membrane first coated with polydopamine with an atom transfer radical polymerization (ATRP) initiator, followed by grafting of polysulfobetaine brushes on the surface [40] and used it in reverse osmosis (RO) for water purification. Their results show that the zwitterionic brushes impart fouling resistance to the membrane.

Although frequently studied in water purification applications, Ruan et al. provided the only example to date of zwitterionic surface modification of an ion exchange membrane with polysulfobetaine to induce fouling resistance, showing promising results during electrodialysis (ED) of a solution containing sodium dodecylbenzenesulfonate (SDBS) as model foulant, although their investigation spans a limited time scale (2h) only [39].

In the present work, we chemically modify the surface of a commercially available AEM with polydopamine bearing zwitterionic functionalities. Two different approaches are investigated to assess the anti-fouling performance of zwitterionic monomers and zwitterionic polymer brushes: 1) AEMs with polydopamine bearing zwitterionic monomer grafts obtained via aza-Michael reaction or 2) AEMs with polydopamine bearing zwitterionic brushes obtained via ATRP. This modification strategy is chosen for its versatility. As a natural adhesive, polydopamine ensures the possibility of modifying any base membrane, irrespective of its chemistry. Additionally, the aza-Michael reaction and

ATRP can be used to apply a variety of chemistries on the membrane surface, starting with unsaturated monomers containing the desired functional groups, such as sulfobetaine to obtain a zwitterionic layer. As such, this modification strategy is a platform meant to explore changes to the surface chemistry, and the current work does not intend to show up-scaled applications.

After extensive characterization of the applied layers and the obtained membranes, the membranes are applied in RED to investigate their fouling behavior in time. The membrane electrical resistance, permselectivity, surface composition and contact angle with water are evaluated at different stages in the modification processes. The fouling resistance of the membranes and their cleaning ability are measured in RED stack experiments where SDBS is added to the river water compartment as a model foulant.

3.2 Materials and methods

3.2.1 Materials

Fujifilm AEM type I membranes (Fujifilm Manufacturing Europe BV, The Netherlands) were used as base membranes for surface modification. The membranes were conditioned at room temperature and stored at 4°C in 0.1 M NaCl solutions before modification. *N,N*-dimethylformamide (DMF, 99.99 %), absolute ethanol, and 2-propanol (IPA, 99.5 %) were used as solvents and purchased from Sigma-Aldrich (The Netherlands). Dopamine hydrochloride (DA), triethylamine (TEA, ≥ 99.5 %), 2-bromoisobutyril bromide (BiBB), tris(hydroxymethyl) aminomethane (Tris), and [2-(methacryloyloxy)ethyl]dimethyl-(3-sulfopropyl)ammonium hydroxide (known as sulfobetaine methacrylate, SBMA), copper(II) chloride, L-ascorbic acid, and sodium dodecylbenzenesulfonate (SDBS) were also purchased from Sigma-Aldrich. Tris(2-pyridylmethyl)amine (TPMA) was purchased from TCI Chemicals (Belgium). Hydrogen peroxide in 30 % solution, copper sulfate pentahydrate, and potassium hexacyanoferrate (both ferri- and ferrocyanide, ≥ 96 %) were purchased from VWR Chemicals (Belgium). NaCl (99.5 %) was purchased from ESCO (The Netherlands).

3.2.2 Surface modification: Aza-Michael

3.2.2.1 Deposition of polydopamine

To improve the homogeneity of the polydopamine (PDA) layers at short deposition times, the procedure used by Zhang et al. was followed [51]. A solution of Tris (700 mg, 5.8 mmol, pH 8.5) and copper sulfate pentahydrate (250 mg, 1 mmol) in 200 mL milli-Q water was prepared. 407 µL of hydrogen peroxide solution (3.9 mmol) was added to the solution

right before deposition. To obtain unmodified polydopamine layers (Figure 3.1, step 1a), a solution of 2 g dopamine hydrochloride in 200 mL milli-Q water (Merck Millipore, Germany) was prepared. A pristine membrane (11x11 cm^2) was clamped at the bottom of the reactor (Figure S3.1 in the Supporting Information, open area: 8x8 cm^2). The Tris solution was added in the reactor, quickly followed by 50 mL of polydopamine solution. The reactor was placed on a shaking plate (60 rpm) for 1 hour after ensuring adequate mixing of the two solutions. Compressed air was flowing over the solution to ensure oxygen availability inside the reactor was not limited. After modification the membrane was rinsed in demineralized water and stored in 0.1 M NaCl at 4°C. The membrane obtained after polydopamine deposition is named AEM+PDA in the following.
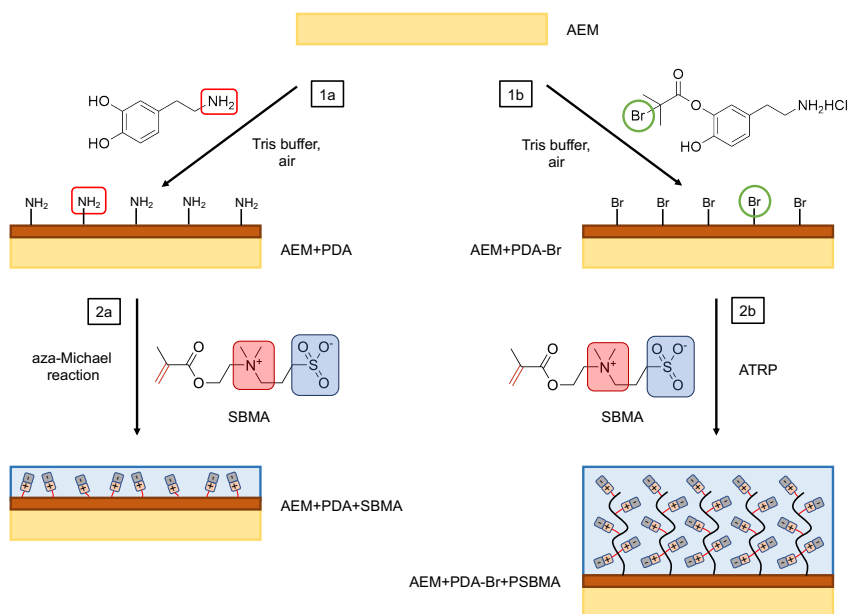
Figure 3.1 Schematic representation of the two surface modification strategies. 1a) Deposition of polydopamine. 2a) Aza-Michael reaction to graft zwitterionic monomers to the membrane surface. 1b) Deposition of polydopamine modified with BiBB. 2b) Atom transfer radical polymerization (ATRP) to graft zwitterionic brushes from the membrane surface.

3.2.2.2 Aza-Michael reaction

The procedure for membrane modification with aza-Michael reaction was used as presented by Ruan et al. [39] (Figure 3.1, step 2a, and Figure S3.2 in the Supporting Information). Briefly, the membrane modified with polydopamine was immersed in 660

mL water, 130 mL absolute ethanol, 5 mL TEA (acid neutralizer and catalyst for the aza-Michael reaction [52]), and 21 g SBMA in a round-bottom flask. The solution was heated to 55°C in an oil bath and gently stirred for 24 hours to avoid damage to the membrane. After modification the membrane was rinsed in demineralized water and stored in 0.1M NaCl at 4°C. The membrane obtained after aza-Michael reaction is named AEM+PDA+SBMA in the following.

3.2.3 Surface modification: ATRP
3.2.3.1 Synthesis of dopamine-BiBB

For the chemical modification of dopamine hydrochloride, the procedure reported in the literature by Liu et al. was followed (Figure S3.3 in the Supporting Information) [40]. Dopamine hydrochloride (2 g, 10.5 mmol) was dissolved in 200 mL DMF inside a three-neck round-bottom flask equipped with a condenser. Nitrogen was bubbled in the solution for 30 min. 748 µL TEA (5.3 mmol) and 652 µL BiBB (5.3 mmol) were added while stirring. The solution was stirred under nitrogen atmosphere at room temperature for 24h.

3.2.3.2 Atom transfer radical polymerization (ATRP)

The AEMs modified with the synthesized polydopamine-BiBB (following the same deposition process presented in section 3.2.2.1, Figure 3.1, step 1b, named in the following AEM+PDA-Br) were further modified by atom transfer radical polymerization (ATRP) to grow zwitterionic brushes on their surface with a grafting approach, similar to the process presented by Liu et al. [40] (Figure 3.1, step 2b). The same reactor design was used as for the surface modification with polydopamine (Figure S3.1 in the Supporting Information), with the polydopamine-BiBB layer facing the reaction solution. 5.15 g SBMA (18.4 mmol) was added to a 1:1 mixture of milli-Q water and IPA in a brown glass bottle. 8 mL of a stock solution of $CuCl_2$ and TPMA (50 mg $CuCl_2$ and 700 mg TPMA in 100 mL of water and IPA mixture 1:1, stored under nitrogen) were added to the SBMA solution. The solution was poured in the reactor, in contact with the membrane. Nitrogen bubbles were blown through the reactor liquid for 30 min. A solution of 25 mL solution of water and IPA mixed 1:1 and 1.2 g of L-ascorbic acid was prepared. The reactor was placed on a shaking plate (60 rpm) and the ascorbic acid solution was added to start the ATRP process. Nitrogen was bubbled through the solution during the entire reaction time. After 1 hour, the nitrogen flow was interrupted and the reactor was opened to stop the ATRP. After modification the membrane was rinsed in demineralized water and stored at 4°C. The membrane obtained after ATRP is named AEM+PDA-Br+PSBMA in the following.

3.2.4 Membrane characterizations

The surface composition of the membranes before and after surface modification was analyzed with Scan Electron Microscopy (SEM) and Energy Dispersed X-ray spectroscopy (EDS) scans. For this the membrane samples were dried in a vacuum oven at 35°C for 24 hours. The dried membranes were twice gold coated in a JEOL JFC-1200 fine coater (Jeol (Europe) BV, The Netherlands) at 25 mA for 15 s. The samples were analyzed with SEM-EDS (JEOL JSM-6480LV, Jeol (Europe) BV, The Netherlands). SEM images were obtained with 5000x magnification, with a 6 kV accelerating voltage. The SEM images for EDS measurements were conducted at 100x magnification, applying a 12 kV accelerating voltage.

The surface composition of the membranes was characterized with attenuated total reflectance Fourier transform infrared spectroscopy (ATR-FTIR), using a Varian 3100 FTIR Excalibur Series (Agilent Technologies, USA) equipped with a Specac Golden Gate ATR insert (Specac Ltd., United Kingdom). The hydrophilicity of the membranes was evaluated with captive bubble contact angle measurements. The measurements were performed with a Dataphysics OCA 35 (DataPhysics Instruments GmbH, Germany) with a custom 3D-printed membrane holder immersed in milli-Q water. The water contact angle was obtained as the difference between 180° and the contact angle with air.

Membrane electrical resistance and permselectivity were evaluated according to procedures available in the literature using a six-compartment cell and two-compartment cell setup, respectively [53,54].

3.2.5 Stack assembly

A cross-flow RED stack with an active area of 6.5x6.5 cm^2 was obtained from REDstack BV (The Netherlands). The end-plates housed Ti electrodes coated with 50 g/m^2 galvanized Pt (MAGNETO Special Anodes BV, The Netherlands). Gasket-integrated spacers with a woven netting (470 µm thickness, from Saati SpA, Italy) were obtained from Deukum GmbH (Germany). The AEMs used in this study were pristine and modified Fujifilm AEM type I (pristine, PDA, PDA-BiBB, zwitterionic monomers, and zwitterionic brushes), while the CEMs were Neosepta CMX-fg (ASTOM, Japan) sourced from Eurodia SA (France).

3.2.6 Feedwaters

Artificial feedwaters were used for this study. Artificial seawater contained 30 g NaCl L^{-1} and artificial river water 1 g NaCl L^{-1} both were prepared with demineralized water

(produced by an Osmostar S400, Lubron Waterbehandeling BV, The Netherlands). For fouling experiments, the model compound used was sodium dodecylbenzenesulfonate (SDBS), which was added to the river water with a concentration of 100 ppm. The sequence of feedwaters used in the stack experiments was: 1) artificial river and seawater without foulant (8 hours); 2) clean seawater, river water containing 100 ppm SDBS as a foulant (16 hours, based on the time needed for unmodified membranes to reach a stable fouling level); and 3) again artificial river and seawater without foulant to investigate the reversibility of the fouling (3 hours).

3.2.7 Electrochemical measurements

Stack electrochemical measurements were performed with an Iviumstat controlled by IviumSoft (IVIUM Technologies BV, The Netherlands), while measurements with the two- and six-compartment cells were performed with an Autolab PGSTAT30 controlled by the NOVA 2.1.3 software (Metrohm Autolab BV, The Netherlands). The stack measurements were performed in a loop where constant current (10.5 A m^{-2}) was alternated with a chronopotentiometric series ($0 – 3.5 – 7.0 – 10.5 – 14.0$ A m^{-2}) every 15 min. This loop was running continuously during the stack experiments, with the exception of an interruption during the run with unmodified membranes. Stack open circuit voltage (OCV) was determined from the average voltage calculated on the last 10 s at 0 A m^{-2}. The stack electrical resistance was calculated from the slope of the current-voltage curve based on the chronopotentiometric series data. Power density was calculated from the stack OCV and electrical resistance:

$$P_{dens}[W \cdot m^{-2}] = \frac{OCV^2[V^2]}{4 \cdot 2N_{cp}[-] \cdot Area[m^2] \cdot ER[\Omega]}$$

Where P_{dens} is the maximum gross power density, OCV is the stack open circuit voltage, N_{cp} is the number of cell pairs, $Area$ is the active area, and ER is the stack electrical resistance. This formula is derived from the assumption that maximum gross power density is attained when the external load is equal to the stack internal resistance [55]. The values of stack OCV, electrical resistance, and gross power density were normalized to highlight the impact of fouling on the membranes. Normalization was performed by dividing all the values by the last values measured in the first experimental stage with clean waters and multiplying them by 100.

3.3 Results and discussion

3.3.1 Membrane characterizations

The surface composition of the membranes before (AEM) and after modification with PDA (AEM+PDA), zwitterionic monomers (aza-Michael, AEM+PDA+SBMA), PDA-BiBB (AEM+PDA-Br), and zwitterionic brushes (ATRP, AEM+PDA-Br+PSBMA) was analyzed with SEM-EDS. Figure 3.2 compares the relative composition of the surface of these membranes for carbon, sulfur, and bromine.
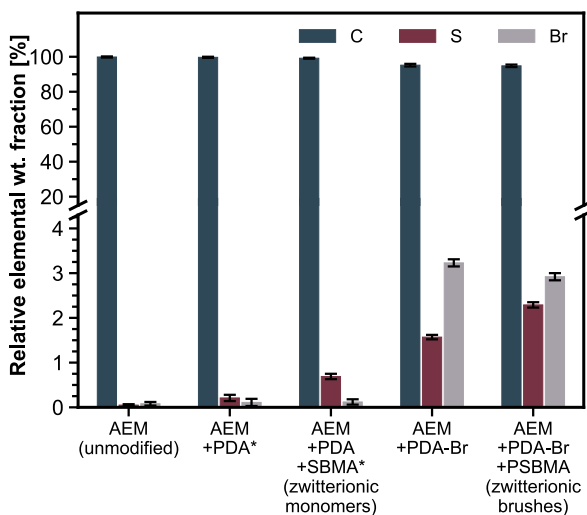
Figure 3.2 Relative weight fractions measured in the SEM-EDS spectra of the membrane surfaces for carbon (dark blue), sulfur (dark red), and bromine (grey). The error bars illustrate the measurement error as reported by the instrument. * = samples that were equilibrated in 0.5 M NaCl prior to the analysis to reduce the amount of non-chemically bound sulfate.

Figure 3.2 clearly shows carbon as the most abundant element, both in the PDA and the aza-Michael (zwitterionic monomers) modified membranes. Simultaneously, a minor contribution of sulfur is observed for the PDA-modified membrane (AEM+PDA). Given the chemistry of the applied layer and that the unmodified membrane (Fujifilm AEM type I) is obtained from cross-linking of an acrylamide monomer carrying a quaternary ammonium group with *N,N'*-methylene bis(acrylamide) on a polyolefine-based porous support [56], the presence of sulfur is not expected. The results of the SEM-EDS analysis on unmodified membranes (AEM) indeed confirm the absence of sulfur and bromine. The very small amount of S observed in the PDA-modified membrane originates from residual sulfate ions (introduced by the addition of copper sulfate pentahydrate) exchanged with

chloride ions during the surface modification process and still present in the membranes in small amounts despite the equilibration in 0.5 M NaCl prior to the surface characterization. As expected, the amount of sulfur significantly increases when the PDA modified membrane is grafted with sulfobetaine monomers (via aza-Michael reaction, AEM+PDA+SBMA), due the presence of sulfonic groups in the monomers. The amount of sulfate seems low, however, this is the amount relative to a large volume of unmodified material. The results thus confirm the successful grafting of the zwitterionic monomers on the membrane surface via the aza-Michael reaction. The presence of bromine in the PDA-BiBB sample (AEM+PDA-Br) indicates that the modification of dopamine with BiBB is also successful. Again, the presence of sulfate in the PDA-BiBB sample derives from the copper sulfate pentahydrate that was used in the deposition of PDA-BiBB. Figure 3.2 shows that after modification with zwitterionic brushes via ATRP (AEM+PDA-Br+PSBMA), the relative fraction of sulfate increases, confirming the grafting of polysulfobetaine to the membrane surface.

In the Supporting Information, Figure S3.4 shows the SEM images of the membrane surface during the various stages of the surface modification. After polydopamine deposition (Figure S3.4b and S3.4d), PDA aggregates become visible on the membrane surface, consistently with the observations of Ruan et al. [39]. Upon aza-Michael reaction (Figure S3.4c) and ATRP (Figure S3.4e), the aggregates are less visible and the membrane surface appears more corrugated, due to the presence of the zwitterionic layers and the exposure to solvents during the surface modification process. Additional evidence of the surface modification is provided in Figure S3.5 in the Supporting Information, with the ATR-FTIR spectra of the membranes at various stages of the surface modification. The emergence of new peaks in the spectra of AEM+PDA+SBMA (Figure S3.5a) and AEM+PDA-Br+PSBMA (Figure S3.5b) at 1726 cm^{-1} (carbonyl group from SBMA) and at 1039 cm^{-1} (sulfonate group from SBMA) indicates the successful grafting to the membrane surface of (poly)sulfobetaine. While these characterizations determine the successful modification of the membranes, the determination of grafting density and chain length is hampered by the difficulty of determining the amount of immobilized initiator available on the surface of the membrane prior to the grafting via aza-Michael reaction and ATRP [57].

Subsequently, the permselectivity and electrical resistance of the resulting membranes is determined to evaluate the effect of the membrane modifications on membrane properties and with that on RED performance. Figure 3.3 shows the membrane permselectivity at different stages of the two membrane surface modification processes, which quantifies co-

ion leakage and the ability of the membrane to generate a voltage when exposed to a salt concentration gradient across it

Figure 3.3 Membrane permselectivity for the membranes at different stages of surface modification. The error bars illustrate the minimum and maximum measured values (2 samples).

Independent of the modification step, the permselectivity is high and remains constant at 89.0 ± 0.1 % for all samples. The permselectivity is not compromised because the layers are very thin due to the short deposition times. Additionally, both the PDA layer and the zwitterionic layer have a net neutral charge. Therefore, they are not expected to negatively affect the charge density of the membrane and its electrical properties. Permselectivity data for AEMs modified with PDA are scarce in literature, nevertheless, Vaselbehagh et al. reported a decreased OCV [58], which is directly related to permselectivity, for AEMs modified with PDA, but in that case the modification time was much longer than in the present study (24h versus 1h) and the deposition temperature (30 ºC versus room temperature) was higher, with both time and temperature strongly enhancing layer formation and thus decreasing the overall membrane properties [59].

Figure 3.4 shows the membrane electrical resistance measured at the different stages in the surface modification process.

Figure 3.4 Membrane electrical resistance for the membranes at different stages of surface modification. The error bars illustrate the minimum and maximum measured values (2 samples).

The average electrical resistance values seem to increase slightly upon surface modification, but the increase is very limited and within the experimental measurement error. This is consistent with the results of Ruan et al., who also did not report an increase in electrical resistance or selectivity (chloride over sulfate) of polydopamine modified membranes for modification times below or equal to 4.5 hours. Only at 8 hours deposition time a very small increase in electrical resistance and selectivity were observed in their study [38,39]. Additionally, Liu et al. also measured comparable permeability and salt rejection for the pristine and modified thin-film composite membranes in their study, thus reinforcing the expectation that the surface modification based on polydopamine deposition and grafting of a zwitterionic layer does not negatively impact transport through the membrane [40]. So, although an additional layer is applied on top of the membrane with every modification step (Figure 3.1), this layer is so thin that it does not affect the membrane properties (Figure 3.3 and 3.4).

To evaluate the effect of both the zwitterionic monomers (aza-Michael) and the zwitterionic brushes (ATRP) on the hydrophilicity of the membranes, contact angle measurements of the modified membranes were determined (Figure 3.5). The measured air contact angles are reported in Figure S3.6 in the Supporting Information, together with images of the measured air bubbles.
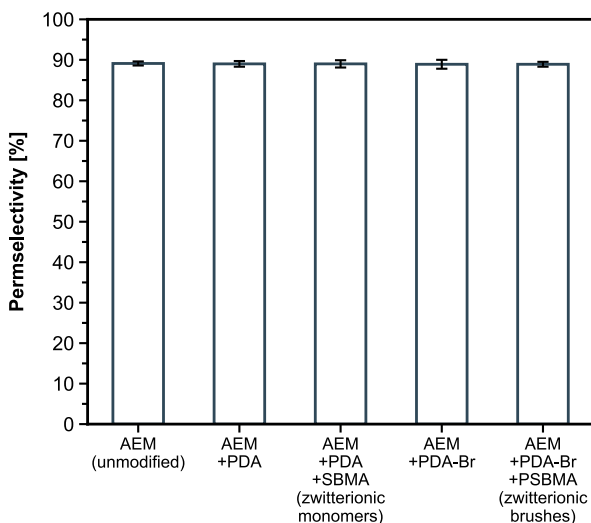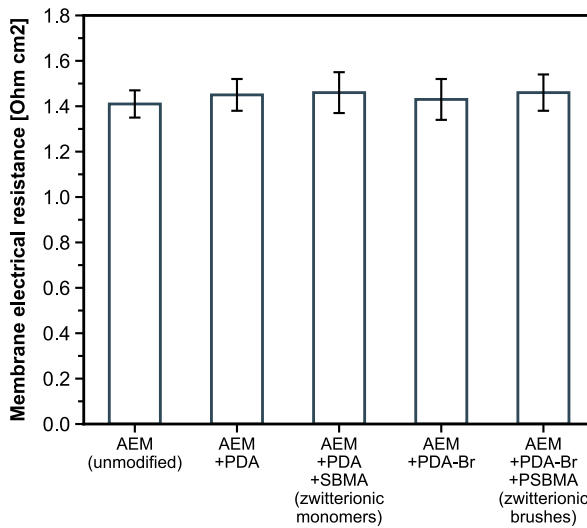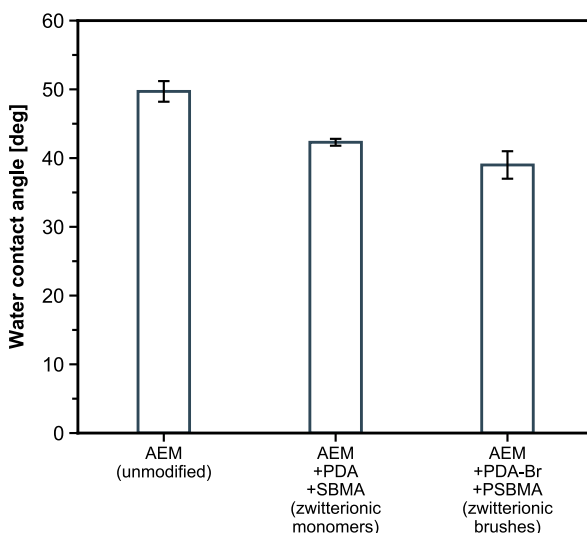
Figure 3.5 Water contact angle for the membranes at different stages of surface modification. The error bars illustrate the minimum and maximum measured values (3 samples).

The introduction of both the zwitterionic monomers (aza-Michael, AEM+PDA+SBMA) and brushes (ATRP, AEM+PDA-Br+PSBMA) decreases the contact angle of the membranes with water. The decrease in contact angle means an increased hydrophilicity of the modified membranes induced by the larger hydration shell of (poly)sulfobetaine [50]. Thanks to the larger number of zwitterionic units present in the polymeric brushes (ATRP) than in the monomers (aza-Michael), the amount of bound water is larger for AEM+PDA-Br+PSBMA than for AEM+PDA+SBMA. Therefore, the contact angle decreases further for the zwitterionic polymer brushes. Additionally, the decrease in contact angle confirms the successful grafting of zwitterionic monomers and brushes on the AEM surface.

Contact angle values reported in literature for other surfaces modified with (poly)sulfobetaine vary over a wide range. Liu et al. report a decrease from 75° to 20° with very short PDA deposition time and subsequent polysulfobetaine surface modification [40], while Ruan et al. report a decrease from around 78° to 65° for short PDA deposition times (up to 12 hours), and to 60° for longer PDA deposition times (18-24 hours), accompanied with sulfobetaine monomers surface modification [39]. The variety of values in the literature indicates that the priming layer below the zwitterionic layer, the thickness of the zwitterionic layer, as well as the coverage of the zwitterionic layer all play a role in determining the surface wettability. Based on the work of Vaselbehagh et al., PDA layers

alone can already decrease the water contact angle to values as low as 30° [35]. The differences in absolute value of the contact angles measured in this work and those determined by Liu et al. [40] and Ruan et al. [39] may stem from different membrane coverage, surface roughness and PDA deposition times. Nevertheless, clearly, the hydrophilicity of the zwitterionically (both with monomers and brushes) modified membranes increased compared to the non-modified counterpart.

3.3.2 Stack characterizations

Subsequently, the fouling behavior using a frequently used model compound (SDBS) and subsequent cleaning strategies of the modified membranes in RED operation is analyzed and compared to that of their unmodified counterparts. Figure 3.6 shows the evolution of the normalized stack electrical resistance during the RED fouling and cleaning experiments for the stack with unmodified membranes (AEM), the stack with membranes modified with zwitterionic monomers (aza-Michael, AEM+PDA+SBMA), and the stack with membranes modified with zwitterionic brushes (ATRP, AEM+PDA-Br+PSBMA).

Figure 3.6 Normalized electrical resistance of the RED stacks during the first 8 hours with river and seawater containing only NaCl (light blue), during the fouling stage with SDBS in river water (pink), and during the cleaning stage (light blue) of the RED experiment. For the stack with unmodified membranes, the fouling onset (purple) and fouling growth (yellow) stage are highlighted.

During the first four hours of operation with NaCl only in the feedwaters, the stack electrical resistance decreases as the membranes equilibrate in the new solutions and air bubbles that may be trapped in the spacers are slowly expelled from the stack. After 4

hours of RED operation, all stacks reached a stable stack resistance value. In our previous fouling study, electrochemical impedance spectroscopy showed that the fouling onset is associated with a decrease of the capacitive behavior of the AEM-water interface due to the nucleation of SDBS domains on the AEM surface [60]. These domains then grow to form a layer, which is then visible as a plateauing of the capacitive components and an increase non-ohmic resistance of the AEM [60]. This evolution is now also mirrored in the behavior of the stack resistance over time in this work (indicated by the yellow and orange highlighted areas in Figure 3.6). The behavior over time during the fouling stage for the stack with unmodified AEMs (Figure 3.6) can be divided into three phases: fouling onset (8 – 12 h), growth of the fouling layer (12 – 22 h), and plateauing (22 – 23.5 h) [60]. Both stacks with zwitterionic layers on the AEMs only show the first two phases of this process, with the fouling onset stage taking longer compared to the unmodified membranes. The fouling onset stage corresponds to the formation of SDBS domains, and the layer growth is reflected in the steady increase in stack electrical resistance in phase 2. The delayed onset of fouling for the stacks with zwitterionic monomers and brushes indicates that the growth of SDBS domains on these membranes takes more time. The lower interaction forces between the hydrophobic model foulant and the surface of the membranes modified with zwitterionic monomers (aza-Michael) and brushes (ATRP) explain the delay in the fouling onset. The water contact angle measurements are an indication of this decreased interaction. Additionally, Liu et al. performed membrane-foulant interaction force measurements, which showed a greatly reduced interaction force for membranes modified with zwitterionic brushes compared to pristine membranes [40]. In this respect, zwitterionic monomers are less effective than zwitterionic brushes as visible in a faster increase of the electrical resistance during the fouling growth stage. This highlights the benefit of longer zwitterionic grafts. Upon removal of SDBS from the river water, during the cleaning stage, the stack with the unmodified membranes recovers 52 % of its original resistance while the stack with the zwitterionic monomer modified membranes recovers 56 % and the stack with membranes modified with zwitterionic brushes recovers 67 % of its electrical resistance increase respectively. The faster recovery of the electrical resistance is also favored by the lower membrane-foulant interaction forces for the membranes with zwitterionic surface chemistry.

Figure 3.7 shows the evolution of the normalized OCV over time during the fouling and cleaning stages of the stack experiments for the stack with unmodified membranes, the stack with membranes modified with zwitterionic monomers (aza-Michael), and the stack with membranes modified with zwitterionic brushes (ATRP).

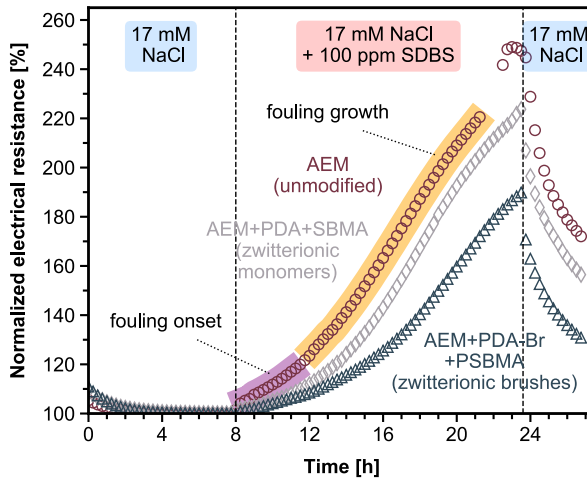**Figure 3.7** Normalized OCV of the RED stacks during the first 8 hours with river and seawater containing only NaCl (light blue), during the fouling stage with SDBS in river water (pink), and during the cleaning stage (light blue) of the RED experiment. For the stack with unmodified membranes, the fouling onset (purple) and fouling growth (yellow) stages are highlighted.

During the first two hours of operation with only NaCl in river and seawater, the stack OCVs reach an equilibrium value due to the membrane conditioning in the newly assembled stack. Surprisingly, for all membranes, the OCV increases in the first hours after the introduction of SDBS in the river water (8 – 10 h). Considering that 100ppm SDBS introduces around 10 % extra sodium in the river water as well, the opposite (a reduction of the OCV upon addition of SDBS in the river water) is expected due to the corresponding decrease in sodium gradient over the CEMs. However, this is not detected. This behavior was consistently observed for all experiments.

Despite this anomaly, the evolution of the OCV closely resembles the evolution of the stack electrical resistance, albeit with fouling leading to a loss of OCV. The three stages of fouling onset, fouling growth, and plateau (only for the unmodified membranes) are identified for the OCV as well. The OCV loss is caused by the accumulation of negatively charged SBDS on the surface of the AEM. This negatively charged layer promotes transport of positive co-ions that are normally repelled by the positively charged AEM. The increased transport of co-ions results in a reduced membrane permselectivity, and in turn a reduced OCV. Equally to the membrane resistance, also here, the reduced membrane-foulant interaction forces for the membranes modified with a zwitterionic layer lead to a slower accumulation of SDBS on the membrane surface, which is observed in

the longer onset stage for the modified membranes, particularly in the case of zwitterionic brushes (ATRP). Additionally, the reduced interaction forces with the foulants leads to faster OCV recovery for the modified membranes during the cleaning stage of the experiment.

Figure 3.8 shows the evolution of the stack gross power density over time during fouling and cleaning experiments for the stack with unmodified membranes, the stack with membranes modified with zwitterionic monomers (aza-Michael), and the stack with membranes modified with zwitterionic brushes (ATRP).
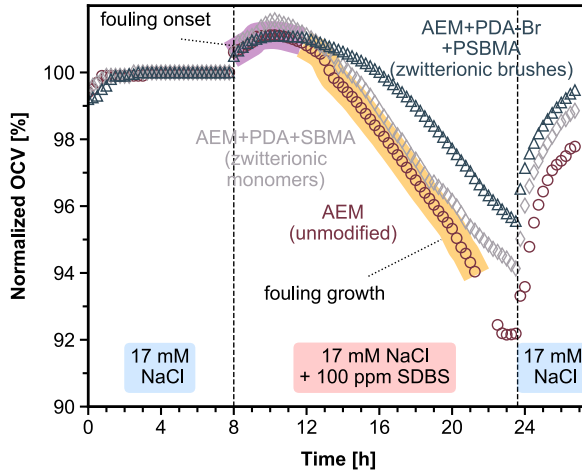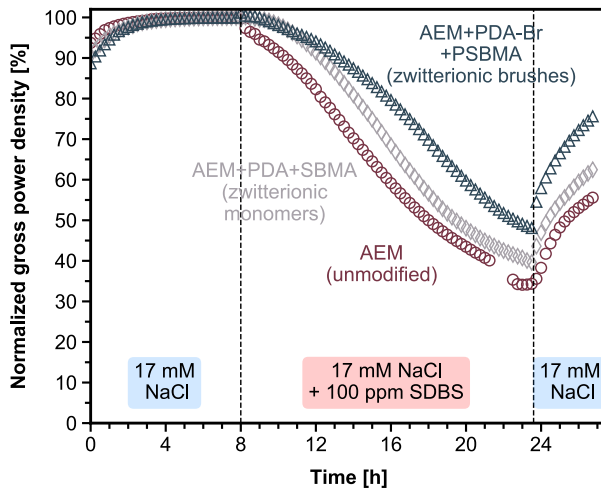

Figure 3.8 Normalized gross power density of the RED stacks during the first 8 hours with river and seawater containing only NaCl (light blue), during the fouling stage with SDBS in river water (pink), and during the cleaning stage (light blue) of the RED experiment.

The trends observed for OCV and electrical resistance are now combined, and it is evident that the surface modification with zwitterionic monomers and zwitterionic brushes is effective in reducing the power density loss upon membrane fouling with SDBS. In the fouling experiment, the stack with unmodified AEMs lost 65 % of its initial gross power density, while the stack with membranes modified by zwitterionic monomers and brushes lost 60 and 52 %, respectively. The reduced losses registered for modified membranes derive from their reduced interaction with the hydrophobic SDBS, resulting in a longer duration of the fouling onset stage and a slower fouling growth, especially in the case of the membranes modified with zwitterionic brushes. While zwitterionic monomers are effective in delaying the onset of fouling, as observed by Ruan et al. in their 2h experiments [39], on a longer term, the power loss very much approaches that of the

unmodified membranes. Zwitterionic brushes on the other hand are more effective in not only delaying the fouling onset but also in reducing the fouling growth rate due to their more hydrophilic nature, which stem from the longer chains and the corresponding larger number of zwitterionic moieties that cover the membrane surface. For instance, after 9 hours of exposure to a high concentration of model foulant, the power loss for the stack with membranes modified with zwitterionic brushes is about half of the power loss registered for the stack with unmodified membranes. Therefore, this research proves that in reverse electrodialysis modification of anion exchange membranes with zwitterionic brushes is a promising modification route to improve the anti-fouling properties of AEMs, especially in combination with periodic cleaning strategies.

3.4 Conclusion

Anti-fouling AEMs were prepared by coating of a commercial AEM with either polydopamine followed by grafting of zwitterionic monomers on its surface or with a modified polydopamine-BiBB coating as surface initiator for ATRP with sulfobetaine to graft zwitterionic brushes on the membrane surface. Both the polydopamine and the zwitterionic layers hardly affect the permselectivity nor the electrical resistance compared to the non-modified membranes thanks the thin grafting layers which is made by using short deposition and reaction times. Their membrane hydrophilicity clearly increased offering a method to better mitigate fouling. The fouling resistance for both zwitterionic monomers and zwitterionic brushes membranes was improved. Where the zwitterionic monomers delay the fouling onset, in addition the zwitterionic brushes do not cause only a delay in the fouling onset but also slow down the fouling layer growth. Furthermore, membranes modified with zwitterionic layers show a better and faster recovery after cleaning than unmodified AEMs.

Supporting Information
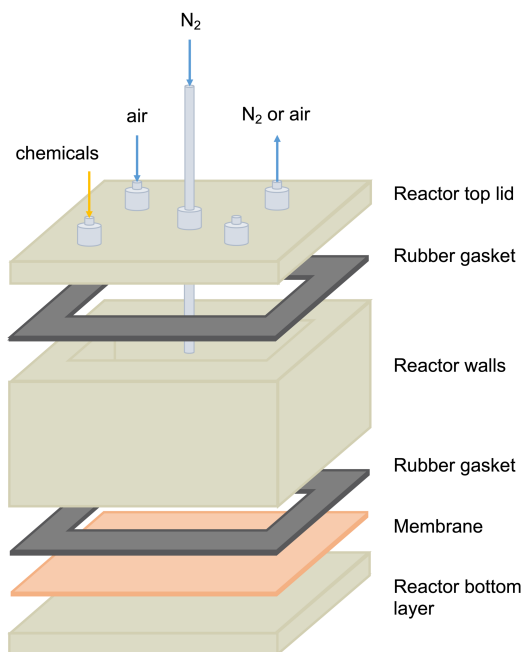
Figure S3.1 Exploded view (simplified design without screws and nuts) of the reactor used for the surface modification of the anion exchange membranes with polydopamine, aza-Michael reaction, and atom transfer radical polymerization.
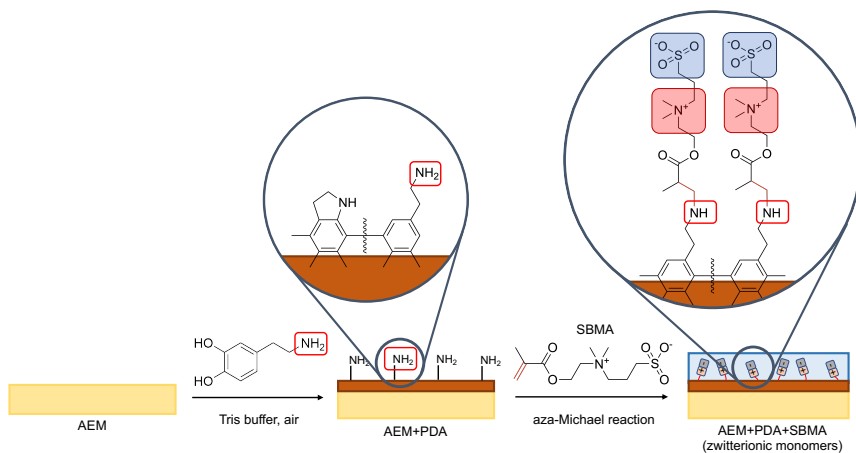
Figure S3.2 Schematic representation of the AEM surface modification by deposition of polydopamine and aza-Michael reaction to introduce zwitterionic monomers as presented in [39].
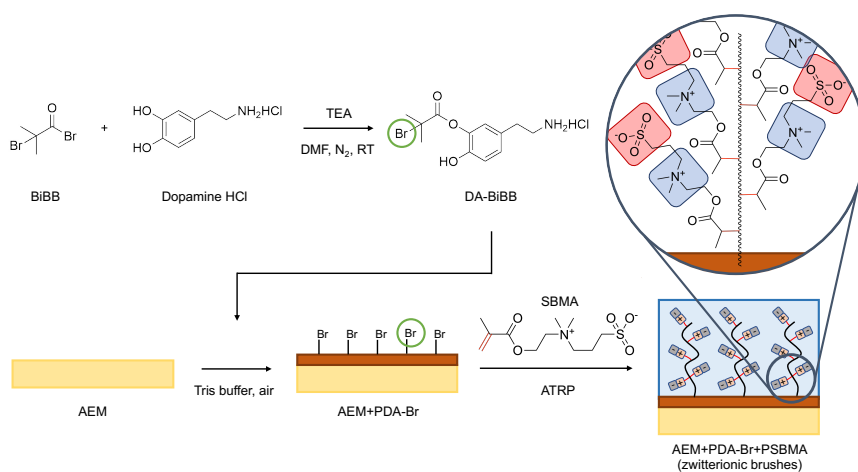
Figure S3.3 Schematic representation of the AEM surface modification process with ATRP, similar to the process in [40]. First, synthesis of the dopamine-BiBB. Second, deposition of the modified polydopamine-BiBB on the pristine AEM surface. Third, ATRP process to grow polysulfobetaine brushes on the modified AEM surface.
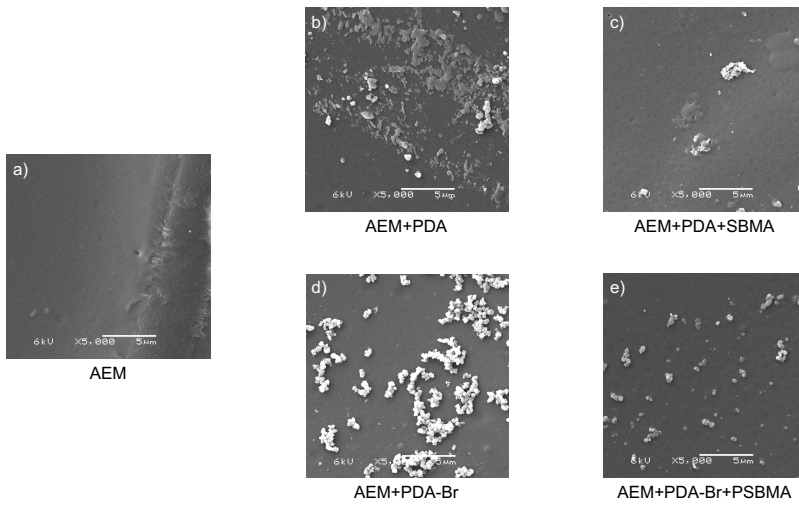
Figure S3.4 SEM imaging of the membranes at various stages of the surface modification process.
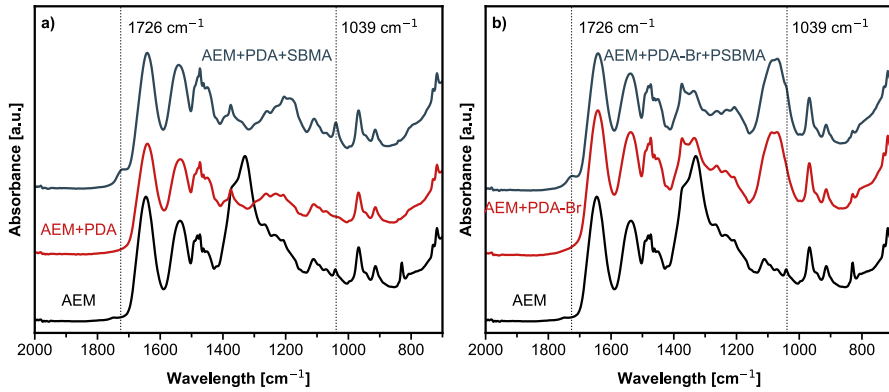
Figure S3.5 ATR-FTIR spectra of the membranes at various stages of the surface modification. a) surface modification with zwitterionic monomers (aza-Michael reaction). b) surface modification with zwitterionic brushes (ATRP).

Figure S3.5a presents the ATR-FTIR spectra for the membranes at various stages of the surface modification process with zwitterionic monomers via aza-Michael reaction. Figure S3.5b shows the ATR-FTIR spectra for the membranes during the different stages of the surface modification with zwitterionic brushes via atom transfer radical polymerization (ATRP). In all spectra, absorption bands at 1657 cm^{-1} and 1536 cm^{-1} can be observed, which derive from C=O (amide I) and N-H (amide II) vibrations, due to the amide groups in the Fujifilm membrane [40]. The extra band observed in Figure S3.5b in the 1150 – 1000 cm^{-1} region is likely derived from solvent (DMF) residues in the samples. For both modifications, the emergence of new peaks at 1726 cm^{-1} and 1039 cm^{-1} indicates the successful grafting of (poly)sulfobetaine to the membrane surface [40]. The peak at 1726 cm^{-1} derives from the carbonyl group of sulfobetaine, while the peak at 1039 cm^{-1} is attributed to vibrations of the sulfonate group in the zwitterionic monomer [39, 40].
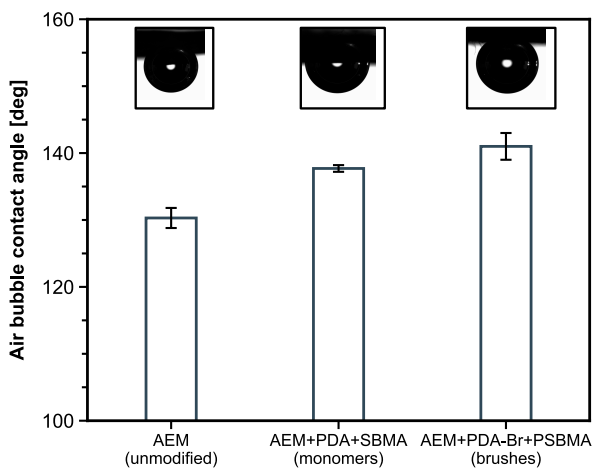
Figure S3.6 Air contact angle values measured during the captive bubble measurements for the unmodified AEM, AEM+PDA+SBMA (modified with zwitterionic monomers via aza-Michael reaction), and AEM+PDA-Br-PSBMA (modified with zwitterionic brushes via atom transfer radical polymerization, ATRP) immersed in water.

3

References

[1]   J.W. Post, J. Veerman, H.V.M. Hamelers, G.J.W. Euverink, S.J. Metz, K. Nymeijer, C.J.N. Buisman, Salinity-gradient power: Evaluation of pressure-retarded osmosis and reverse electrodialysis, Journal of Membrane Science. 288 (2007) 218–230. https://doi.org/10.1016/j.memsci.2006.11.018.

[2]   F. Giacalone, F. Vassallo, L. Griffin, M.C. Ferrari, G. Micale, F. Scargiali, A. Tamburini, A. Cipollina, Thermolytic reverse electrodialysis heat engine: model development, integration and performance analysis, Energy Conversion and Management. 189 (2019) 1–13. https://doi.org/10.1016/j.enconman.2019.03.045.

[3]   F. Giacalone, F. Vassallo, F. Scargiali, A. Tamburini, A. Cipollina, G. Micale, The first operating thermolytic reverse electrodialysis heat engine, Journal of Membrane Science. 595 (2020). https://doi.org/10.1016/j.memsci.2019.117522.

[4]   M. Tedesco, E. Brauns, A. Cipollina, G. Micale, P. Modica, G. Russo, J. Helsen, Reverse electrodialysis with saline waters and concentrated brines: A laboratory investigation towards technology scale-up, Journal of Membrane Science. 492 (2015) 9–20. https://doi.org/10.1016/j.memsci.2015.05.020.

[5]   M. Tedesco, A. Cipollina, A. Tamburini, G. Micale, Towards 1 kW power production in a reverse electrodialysis pilot plant with saline waters and concentrated brines, Journal of Membrane Science. 522 (2017) 226–236. https://doi.org/10.1016/j.memsci.2016.09.015.

[6]   J.W. Post, H.V.M. Hamelers, C.J.N. Buisman, Energy recovery from controlled mixing salt and fresh water with a reverse electrodialysis system, Environmental Science and Technology. 42 (2008) 5785–5790. https://doi.org/10.1021/es8004317.

[7]   J. Kuleszo, C. Kroeze, J. Post, B.M. Fekete, The potential of blue energy for reducing emissions of CO_2 and non-CO_2 greenhouse gases, Journal of Integrative Environmental Sciences. 7 (2010) 89–96. https://doi.org/10.1080/19438151003680850.

[8]   R.E. Lacey, Energy by reverse electrodialysis, Ocean Engineering. 7 (1980) 1–47. https://doi.org/10.1016/0029-8018(80)90030-X.

[9]   B.E. Logan, M. Elimelech, Membrane-based processes for sustainable power generation using water, Nature. 488 (2012) 313–319. https://doi.org/10.1038/nature11477.

[10]   A.H. Galama, J.W. Post, H.V.M. Hamelers, V.V. Nikonenko, P.M. Biesheuvel, On the origin of the membrane potential arising across densely charged ion exchange membranes: How well does the teorell-meyer-sievers theory work?, Journal of Membrane Science and Research. 2 (2016) 128–140.

[11]   J. Veerman, M. Saakes, S.J. Metz, G.J. Harmsen, Reverse electrodialysis: Evaluation of suitable electrode systems, Journal of Applied Electrochemistry. 40 (2010) 1461–1474. https://doi.org/10.1007/s10800-010-0124-8.

[12]   J. Moreno, S. Grasman, R. van Engelen, K. Nijmeijer, Upscaling Reverse Electrodialysis, Environmental Science and Technology. 52 (2018) 10856–10863. https://doi.org/10.1021/acs.est.8b01886.

3

[13]   J.W. Post, C.H. Goeting, J. Valk, S. Goinga, J. Veerman, H.V.M. Hamelers, P.J.F.M. Hack, Towards implementation of reverse electrodialysis for power generation from salinity gradients, Desalination and Water Treatment. 16 (2010) 182–193. https://doi.org/10.5004/dwt.2010.1093.

[14]   D.A. Vermaas, D. Kunteng, M. Saakes, K. Nijmeijer, Fouling in reverse electrodialysis under natural conditions, Water Research. 47 (2013) 1289–1298. https://doi.org/10.1016/j.watres.2012.11.053.

[15]   A. Daniilidis, R. Herber, D.A. Vermaas, Upscale potential and financial feasibility of a reverse electrodialysis power plant, Applied Energy. 119 (2014) 257–265. https://doi.org/10.1016/j.apenergy.2013.12.066.

[16]   E. Güler, K. Nijmeijer, Reverse electrodialysis for salinity gradient power generation: Challenges and future perspectives, Journal of Membrane Science and Research. 4 (2018) 108–110. https://doi.org/10.22079/JMSR.2018.86747.1193.

[17]   D.A. Vermaas, M. Saakes, K. Nijmeijer, Early detection of preferential channeling in reverse electrodialysis, Electrochimica Acta. 117 (2014) 9–17. https://doi.org/10.1016/j.electacta.2013.11.094.

[18]   R.S. Kingsbury, F. Liu, S. Zhu, C. Boggs, M.D. Armstrong, D.F. Call, O. Coronell, Impact of natural organic matter and inorganic solutes on energy recovery from five real salinity gradients using reverse electrodialysis, Journal of Membrane Science. 541 (2017) 621–632. https://doi.org/10.1016/j.memsci.2017.07.038.

[19]   H. Guo, L. Xiao, S. Yu, H. Yang, J. Hu, G. Liu, Y. Tang, Analysis of anion exchange membrane fouling mechanism caused by anion polyacrylamide in electrodialysis, Desalination. 346 (2014) 46–53. https://doi.org/10.1016/j.desal.2014.05.010.

[20]   H.-J. Lee, D.H. Kim, J. Cho, S.-H. Moon, Characterization of anion exchange membranes with natural organic matter (NOM) during electrodialysis, Desalination. 151 (2003) 43–52. https://doi.org/10.1016/S0011-9164(02)00971-2.

[21]   H.-J. Lee, M.-K. Hong, S.-D. Han, J. Shim, S.-H. Moon, Analysis of fouling potential in the electrodialysis process in the presence of an anionic surfactant foulant, Journal of Membrane Science. 325 (2008) 719–726. https://doi.org/10.1016/j.memsci.2008.08.045.

[22]   H.-J. Lee, M.-K. Hong, S.-D. Han, S.-H. Cho, S.-H. Moon, Fouling of an anion exchange membrane in the electrodialysis desalination process in the presence of organic foulants, Desalination. 238 (2009) 60–69. https://doi.org/10.1016/j.desal.2008.01.036.

[23]   V. Lindstrand, G. Sundström, A.-S. Jönsson, Fouling of electrodialysis membranes by organic substances, Desalination. 128 (2000) 91–102. https://doi.org/10.1016/S0011-9164(00)00026-6.

[24]   V. Lindstrand, A.-S. Jönsson, G. Sundström, Organic fouling of electrodialysis membranes with and without applied voltage, Desalination. 130 (2000) 73–84. https://doi.org/10.1016/S0011-9164(00)00075-8.

[25]   T. Rijnaarts, J. Moreno, M. Saakes, W.M. de Vos, K. Nijmeijer, Role of anion exchange membrane fouling in reverse electrodialysis using natural feed waters, Colloids and Surfaces A: Physicochemical and Engineering Aspects. 560 (2019) 198–204. https://doi.org/10.1016/j.colsurfa.2018.10.020.

[26]   N. Tanaka, M. Nagase, M. Higa, Organic fouling behavior of commercially available hydrocarbon-based anion-exchange membranes by various organic-fouling substances, Desalination. 296 (2012) 81–86. https://doi.org/10.1016/j.desal.2012.04.010.

[27]   J. Moreno, N. de Hart, M. Saakes, K. Nijmeijer, CO_2-saturated water as two-phase flow for fouling control in reverse electrodialysis, Water Research. 125 (2017) 23–31. https://doi.org/10.1016/j.watres.2017.08.015.

[28]   D.A. Vermaas, D. Kunteng, J. Veerman, M. Saakes, K. Nijmeijer, Periodic feedwater reversal and air sparging as antifouling strategies in reverse electrodialysis, Environmental Science and Technology. 48 (2014) 3065–3073. https://doi.org/10.1021/es4045456.

[29]   F. Kotoka, I. Merino-Garcia, S. Velizarov, Surface modifications of anion exchange membranes for an improved reverse electrodialysis process performance: A review, Membranes. 10 (2020) 1–22. https://doi.org/10.3390/membranes10080160.

[30]   E. Güler, W. van Baak, M. Saakes, K. Nijmeijer, Monovalent-ion-selective membranes for reverse electrodialysis, Journal of Membrane Science. 455 (2014) 254–270. https://doi.org/10.1016/j.memsci.2013.12.054.

[31]   I. Banerjee, R.C. Pangule, R.S. Kane, Antifouling coatings: Recent developments in the design of surfaces that prevent fouling by proteins, bacteria, and marine organisms, Advanced Materials. 23 (2011) 690–718. https://doi.org/10.1002/adma.201001215.

[32]   V. Kochkodan, N. Hilal, A comprehensive review on surface modified polymer membranes for biofouling mitigation, Desalination. 356 (2015) 187–207. https://doi.org/10.1016/j.desal.2014.09.015.

[33]   J.-S. Park, H.-J. Lee, S.-J. Choi, K.E. Geckeler, J. Cho, S.-H. Moon, Fouling mitigation of anion exchange membrane by zeta potential control, Journal of Colloid and Interface Science. 259 (2003) 293–300. https://doi.org/10.1016/S0021-9797(02)00095-4.

[34]   L. Hao, J. Liao, Y. Jiang, J. Zhu, J. Li, Y. Zhao, B. van der Bruggen, A. Sotto, J. Shen, "Sandwich"-like structure modified anion exchange membrane with enhanced monovalent selectivity and fouling resistant, Journal of Membrane Science. 556 (2018) 98–106. https://doi.org/10.1016/j.memsci.2018.03.082.

[35]   M. Vaselbehagh, H. Karkhanechi, S. Mulyati, R. Takagi, H. Matsuyama, Improved antifouling of anion-exchange membrane by polydopamine coating in electrodialysis process, Desalination. 332 (2014) 126–133. https://doi.org/10.1016/j.desal.2013.10.031.

[36]   M. Vaselbehagh, H. Karkhanechi, R. Takagi, H. Matsuyama, Effect of polydopamine coating and direct electric current application on anti-biofouling properties of anion exchange membranes in electrodialysis, Journal of Membrane Science. 515 (2016) 98–108. https://doi.org/10.1016/j.memsci.2016.05.049.

[37]   Y. Li, S. Shi, H. Cao, Z. Zhao, C. Su, H. Wen, Improvement of the antifouling performance and stability of an anion exchange membrane by surface modification with graphene oxide (GO) and polydopamine (PDA), Journal of Membrane Science. 566 (2018) 44–53. https://doi.org/10.1016/j.memsci.2018.08.054.

[38]   H. Ruan, Z. Zheng, J. Pan, C. Gao, B. van der Bruggen, J. Shen, Mussel-inspired sulfonated polydopamine coating on anion exchange membrane for improving permselectivity and anti-

fouling property, Journal of Membrane Science. 550 (2018) 427–435. https://doi.org/10.1016/j.memsci.2018.01.005.

[39] H. Ruan, J. Liao, R. Tan, J. Pan, A. Sotto, C. Gao, J. Shen, Dual Functional Layers Modified Anion Exchange Membranes with Improved Fouling Resistant for Electrodialysis, Advanced Materials Interfaces. 5 (2018). https://doi.org/10.1002/admi.201800909.

[40] C. Liu, J. Lee, J. Ma, M. Elimelech, Antifouling Thin-Film Composite Membranes by Controlled Architecture of Zwitterionic Polymer Brush Layer, Environmental Science and Technology. 51 (2017) 2161–2169. https://doi.org/10.1021/acs.est.6b05992.

[41] Q. Liu, W. Li, H. Wang, L. Liu, A facile method of using sulfobetaine-containing copolymers for biofouling resistance, Journal of Applied Polymer Science. 131 (2014) 9432–9440. https://doi.org/10.1002/app.40789.

[42] J. Wang, M. Qiu, C. He, A zwitterionic polymer/PES membrane for enhanced antifouling performance and promoting hemocompatibility, Journal of Membrane Science. 606 (2020). https://doi.org/10.1016/j.memsci.2020.118119.

[43] S. Jiang, Z. Cao, Ultralow-fouling, functionalizable, and hydrolyzable zwitterionic materials and their derivatives for biological applications, Advanced Materials. 22 (2010) 920–932. https://doi.org/10.1002/adma.200901407.

[44] Y.-C. Chiang, Y. Chang, C.-J. Chuang, R.-C. Ruaan, A facile zwitterionization in the interfacial modification of low bio-fouling nanofiltration membranes, Journal of Membrane Science. 389 (2012) 76–82. https://doi.org/10.1016/j.memsci.2011.10.017.

[45] Y.-L. Ji, Q.-F. An, Q. Zhao, W.-D. Sun, K.-R. Lee, H.-L. Chen, C.-J. Gao, Novel composite nanofiltration membranes containing zwitterions with high permeate flux and improved anti-fouling performance, Journal of Membrane Science. 390–391 (2012) 243–253. https://doi.org/10.1016/j.memsci.2011.11.047.

[46] D.M. Davenport, J. Lee, M. Elimelech, Efficacy of antifouling modification of ultrafiltration membranes by grafting zwitterionic polymer brushes, Separation and Purification Technology. 189 (2017) 389–398. https://doi.org/10.1016/j.seppur.2017.08.034.

[47] Q. Sun, Y. Su, X. Ma, Y. Wang, Z. Jiang, Improved antifouling property of zwitterionic ultrafiltration membrane composed of acrylonitrile and sulfobetaine copolymer, Journal of Membrane Science. 285 (2006) 299–305. https://doi.org/10.1016/j.memsci.2006.08.035.

[48] S.P. Nunes, Can fouling in membranes be ever defeated?, Current Opinion in Chemical Engineering. 28 (2020) 90–95. https://doi.org/10.1016/j.coche.2020.03.006.

[49] E. Virga, K. Žvab, W.M. de Vos, Fouling of nanofiltration membranes based on polyelectrolyte multilayers: The effect of a zwitterionic final layer, Journal of Membrane Science. (2020). https://doi.org/10.1016/j.memsci.2020.118793.

[50] M. He, K. Gao, L. Zhou, Z. Jiao, M. Wu, J. Cao, X. You, Z. Cai, Y. Su, Z. Jiang, Zwitterionic materials for antifouling membrane surface construction, Acta Biomaterialia. 40 (2016) 142–152. https://doi.org/10.1016/j.actbio.2016.03.038.

[51] C. Zhang, Y. Ou, W.-X. Lei, L.-S. Wan, J. Ji, Z.-K. Xu, $CuSO_4$/H_2O_2-Induced Rapid Deposition of Polydopamine Coatings with High Uniformity and Enhanced Stability, Angewandte Chemie - International Edition. 55 (2016) 3054–3057. https://doi.org/10.1002/anie.201510724.

[52]   B.D. Mather, K. Viswanathan, K.M. Miller, T.E. Long, Michael addition reactions in macromolecular design for emerging technologies, Progress in Polymer Science (Oxford). 31 (2006) 487–531. https://doi.org/10.1016/j.progpolymsci.2006.03.001.

[53]   E. Güler, R. Elizen, D.A. Vermaas, M. Saakes, K. Nijmeijer, Performance-determining membrane properties in reverse electrodialysis, Journal of Membrane Science. 446 (2013) 266–276. https://doi.org/10.1016/j.memsci.2013.06.045.

[54]   P. Długołecki, K. Nymeijer, S. Metz, M. Wessling, Current status of ion exchange membranes for power generation from salinity gradients, Journal of Membrane Science. 319 (2008) 214–222. https://doi.org/10.1016/j.memsci.2008.03.037.

[55]   J. Veerman, J.W. Post, M. Saakes, S.J. Metz, G.J. Harmsen, Reducing power losses caused by ionic shortcut currents in reverse electrodialysis stacks by a validated model, Journal of Membrane Science. 310 (2008) 418–430. https://doi.org/10.1016/j.memsci.2007.11.032.

[56]   J. van Engelen, Composite membranes, WO2013/014420 A1, 2013.

[57]   E. Mastan, L. Xi, S. Zhu, Factors Affecting Grafting Density in Surface-Initiated ATRP: A Simulation Study, Macromolecular Theory and Simulations. 25 (2016) 220–228. https://doi.org/10.1002/mats.201500081.

[58]   M. Vaselbehagh, H. Karkhanechi, R. Takagi, H. Matsuyama, Biofouling phenomena on anion exchange membranes under the reverse electrodialysis process, Journal of Membrane Science. 530 (2017) 232–239. https://doi.org/10.1016/j.memsci.2017.02.036.

[59]   P. Oymaci, K. Nijmeijer, Z. Borneman, Development of polydopamine forward osmosis membranes with low reverse salt flux, Membranes. 10 (2020). https://doi.org/10.3390/membranes10050094.

[60]   D. Pintossi, M. Saakes, Z. Borneman, K. Nijmeijer, Electrochemical impedance spectroscopy of a reverse electrodialysis stack: A new approach to monitoring fouling and cleaning, Journal of Power Sources. 444 (2019). https://doi.org/10.1016/j.jpowsour.2019.227302.

3

Chapter 4

Electrode segmentation in reverse electrodialysis:
Improved power and energy efficiency

Abstract

Reverse electrodialysis harvests energy from salinity gradients establishing a renewable energy source. High energy efficiencies are fundamental to up-scale the process and to minimize feedwater pre-treatment and pumping costs. The present work investigates electrode segmentation to strategically optimize the output power density and energy efficiency. Electrode segmentation allows the current density to be tuned per electrode segment. Segmentation experiments were performed with a dedicated electrode configuration in a cross-flow stack using a wide range of residence times. Moreover, an experimentally validated model was extended and used to further compare single and segmented electrode configurations. While operating the electrode segments, the highest efficiencies were obtained when considering the overall power, i.e., not maximized by segment. Results show that at a given net power density (0.92 $W \cdot m^{-2}$), electrode segmentation increases the net energy efficiency from 17% to 25%, which is a relative increase of 43%. Plus, at 40% net energy efficiency the net power output for a segmented electrode configuration (0.67 $W \cdot m^{-2}$) is 39% higher than in a single electrode configuration. Higher power density reduces capital investment and higher energy efficiency reduces operating costs. Electrode segmentation increases these parameters compared to a single electrode and can be potentially applied for up-scaling.

4.1 Introduction

Given the growing global energy demand, there is a great societal need for clean and renewable energy sources to replace the use of polluting fossil fuels and reduce CO_2 emissions [1]. One promising source of renewable energy is salinity gradient (also known as blue energy) where the energy results from the reversible mixing of two streams with different salinities. The salinity gradient is widely available anywhere a river runs into the sea, being a non-intermittent renewable energy source, opposite to solar and wind energy [2]. The theoretical energy that can be generated from mixing 1 m^3 of river water (1 g $NaCl·L^{-1}$) with 1 m^3 of seawater (30 g $NaCl·L^{-1}$) is 1.7 MJ [3]. Worldwide the technical potential for salinity gradient energy was estimated at 983 GW [4]. With its implementation, energy-related emissions could be reduced by 25 %, 27 %, and 8 % of CO_2, CH_4, and N_2O, respectively [4].

One main technology to harvest salinity gradient energy is reverse electrodialysis (RED) [5]. The RED process consists of a stack with an alternating series of cation (CEM) and anion (AEM) exchange membranes (Figure 4.1).
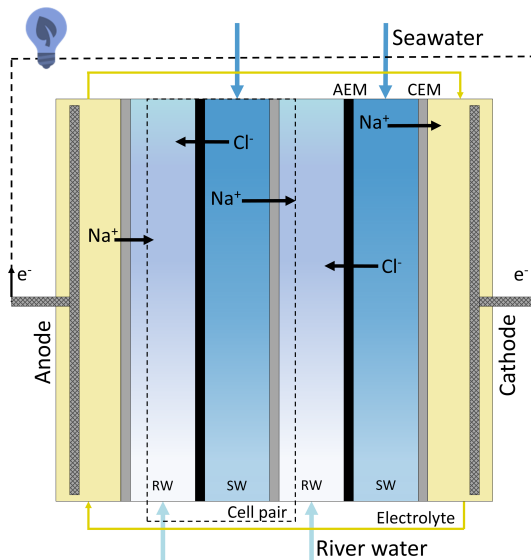
Figure 4.1 Working principle of RED. Two cell pairs are present in the scheme plus an extra CEM to shield the feedwater from the electrode rinse solution. One cell pair is composed of one AEM, one CEM, river compartment and seawater compartment. In a RED stack, multiple cell pairs are placed between the electrodes.

Compartments are established with spacers between the membranes, where seawater and river water flow alternately alongside the membrane. Since ion exchange membranes

(IEMs) have selectivity either toward cations (CEMs) or anions (AEMs), a Donnan potential is generated across the membranes. One cell pair comprises of one AEM, one CEM, one river compartment, and one seawater compartment. When multiple cell pairs are stacked, this potential is accumulated. The potential difference over the membranes drives the transport of ions through the membranes from the seawater towards the river water compartment. Finally, enclosing the membrane pile, an electrode is placed at each end of the stack. A redox solution is recirculated to convert the ionic current into an electrical current, which powers an external load [6]. In the past years, several studies were conducted to improve the process' power density as well as its efficiency. This includes membrane modification, such as monovalent-ion-selective membranes, surface modifications and profiled membranes [7–10], fouling prevention and monitoring [11–15], spacer thickness effect or no spacer present by using corrugated membranes [16,17], flow velocity of the feedwaters [18], scalability of the cross-flow stack [19], prevention of ionic shortcut currents [20], modelling of the RED process with different flow strategies (co-flow, counter-flow and cross-flow) and model optimization of the RED process [21–24]. Furthermore, the potential for large scale application has been proven with pilot plants [25,26].

To establish RED as a commercial technology, it is crucial to use large scale stacks with sufficient energy efficiency [27]. With more ion exchange, to allow sufficient energy efficiency, the salt concentration in the river water increases significantly along the length of the stack, resulting in a drastic decrease of the local ohmic electrical resistance and a drop of electromotive force inside the stack along the flow path length. This leads to a non-homogeneous current distribution over the length of the active membrane area [22]. When using a stack with a single pair of electrodes, i.e. one anode and one cathode, only one external load can be set to harvest the energy. While this single load can be tuned for maximum power production, this represents a compromise between the optimal loads of different sections of the active area [28].

For a given stack size, the required pumping energy is reduced at longer residence times due to a lower flow velocity [19]. Moreover, feedwaters need to be pre-treated to avoid fouling inside the RED stacks [29]. The extraction of more energy per m^3 of seawater and river water compensates the energy consumption associated with pumping and pre-treatment of the feedwaters. In brief, the operation of stacks to achieve sufficient energy efficiency introduces new challenges that limit the maximum RED power output [30].

A promising strategy to increase energy efficiency without incurring additional power output losses is electrode segmentation. Segmentation has been used before to map the

current density inside electrochemical cells, such as proton-exchange membrane fuel cell [31,32] or redox flow batteries [33,34], and for process optimization in electrodialysis [35,36]. In RED, segmentation allows the optimization of the performance by tuning the resistive load per segment. In this way, the external load can be adjusted to the local electrode segment electrical resistance. Such adjustment enables a higher power density output and energy efficiency. Veerman et al. [28] made the first experimental study of segmentation in RED with a scaled-up stack (active area of 25 cm x 75 cm). Segmentation was studied using three-electrode segments (25 cm x 25 cm, each). The stack was operated horizontally with a co-flow feed configuration. The optimal resistance was found for each electrode segment and the corresponding current was extracted. This resulted in a power density increase of 11 %, from 0.44 to 0.49 W·m^{-2}, when compared with the same stack with the three-electrode segments connected as one electrode. The same author published a model regarding electrode segmentation [21], which proved an increase of power by about 15 % when using an infinite number of segments. In this model, the non-ideal behaviour of membranes was accounted for and the stack (10 cm x 10 cm) was operated with a co-flow feed configuration. Besides infinite segmentation, the model also predicted the effect of 2 to 5 electrode segments, with a power increase between 13 and 17 %, respectively. While surprising, the higher increase for a limited number of segments rather than for an infinite number of electrode segments can be explained by the trade-off between high power in the first stages and the need to preserve gradient for the last segments. More recently, Vermaas et al. [22] modelled a RED stack to study the influence of the feed flow configuration, the seawater fraction and the electrode segmentation on the energy efficiency. The model of Vermaas et al. assumed ideal IEMs, no concentration polarization effects and considered a fixed residence time for river water. The results showed that for all configurations higher efficiencies were achieved when the electrode was segmented. The energy efficiency increases by approximately 15 % for the same ratio of seawater and river water when using two electrode segments compared to a single electrode.

The present research aims to investigate experimentally and by modelling the behaviour of electrode segmentation in a RED cross-flow stack. This includes the integration of previous modelling works [21,22] into a new dedicated model, able to characterize the cross-flow stack either with a single electrode or different electrode segments. Furthermore, besides studying the interaction between electrode segments, the overall maximum power density of the electrode segments was optimized.

4.2 Materials and methods

4.2.1 RED modelling

To model the RED stack with segmented electrodes in a cross-flow configuration, two models presented in the literature were combined: the model proposed by Veerman et al [21] and the model by Vermaas et al [22]. Veerman's model includes membrane properties, osmosis and salt transport, but it is limited to co-flow and counter-flow configurations, while Vermaas' model includes the cross-flow configuration, but it only considers ideal membranes (having zero electrical resistance and perfect permselectivity). The models were combined and used as reported with the addition of segmentation along the seawater direction to simulate a 2 by 2 segmented electrode configuration. Figure S4.1a describes the segmented cross-flow stack, while Figure 4.2 depicts the discretization scheme.
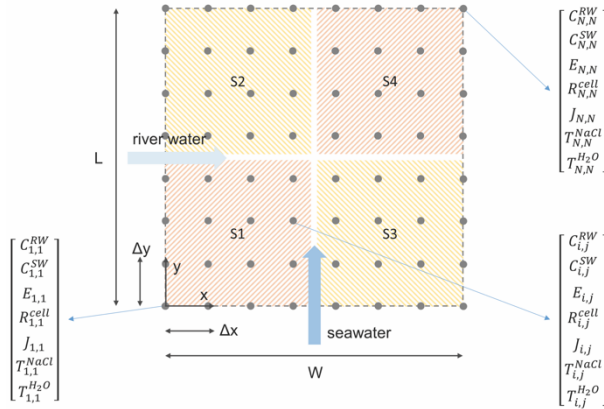
Figure 4.2 Scheme of the discretization strategy adopted in the RED model. The cell pair is reduced to a matrix where to each point a set of properties relative to the feedwaters and membranes is associated.

The modified Nernst equation expresses the electromotive force (V) available at each point in the grid:

$$E_{i,j} = (\alpha_{AEM} + \alpha_{CEM}) \frac{RT}{zF} ln \left(\frac{\gamma_{i,j}^{SW} C_{i,j}^{SW}}{\gamma_{i,j}^{RW} C_{i,j}^{RW}} \right) \qquad \text{(Eq. 4.1)}$$

Where α is the permselectivity of AEM and CEM (-), R is the universal gas constant (J·mol^{-1}·K^{-1}), T is the absolute temperature (K), z is the ion valence (-), F is the Faraday constant (C·mol^{-1}), γ is the molar activity coefficient (-) estimated with the TCPC model

of Ge et al. (a semi-empirical model combining Pitzer long-range interactions and short-range solvation effect) [37], and C is the salt concentration (mol·m^{-3}).

The area resistance ($\Omega \cdot m^2$) of the cell was given by:

$$R_{i,j}^{cell\ pair} = R_{AEM} + R_{CEM} + \frac{1}{f}\frac{d_{RW}}{\kappa_{i,j}^{RW}} + \frac{1}{f}\frac{d_{SW}}{\kappa_{i,j}^{SW}} + \frac{R_{blank}}{N_{CP}} \qquad \text{(Eq. 4.2)}$$

$$\kappa = \Lambda \cdot C \qquad \text{(Eq. 4.3)}$$

Where R_{AEM} and R_{CEM} are the area electrical resistance of the AEM and CEM ($\Omega \cdot m^2$), respectively, f is the spacer shadow factor (-), a fitting parameter accounting for the presence of non-conductive spacers in the water compartments, d is the water compartment thickness (m), κ is the conductivity of feedwaters (S·m^{-1}), R_{blank} is the area electrical resistance of the shielding CEMs and electrodes ($\Omega \cdot m^2$), N_{CP} is the number of cell pairs (-), and Λ is the molar conductivity of NaCl (S·m^{-1}·mol^{-1}).

To implement electrode segmentation in the model, the four load voltages (U_{S1}, U_{S2}, U_{S3}, and U_{S4}) were used for the four segments (S1, S2, S3, and S4 in Figure 4.2). The load voltages (V) applied to the segments were:

$$U_{i,j}^{load} = U_{S1} \quad for\ 0 \leq i < \frac{N}{2}, \qquad 0 \leq j < \frac{N}{2}$$

$$U_{i,j}^{load} = U_{S2} \quad for\ 0 \leq i < \frac{N}{2}, \qquad \frac{N}{2} \leq j \leq N$$

$$U_{i,j}^{load} = U_{S3} \quad for\ \frac{N}{2} \leq i \leq N, \qquad 0 \leq j < \frac{N}{2}$$

$$U_{i,j}^{load} = U_{S4} \quad for\ \frac{N}{2} \leq i \leq N, \qquad \frac{N}{2} \leq j \leq N$$

When the loads were applied to the segments, the current density (A·m^2) at all points was:

$$J_{i,j} = \frac{E_{i,j} - U_{i,j}^{load}}{R_{i,j}^{cell}} \qquad \text{(Eq. 4.4)}$$

The salt flux (mol·m^{-2}·s^{-1}) at each point of the discretization grid was expressed as the sum of current transport and co-ion transport through the AEM and CEM:

$$T_{i,j}^{NaCl} = \frac{J_{i,j}}{F} + 2\left(C_{i,j}^{SW} - C_{i,j}^{RW}\right)\frac{D_{NaCl}}{l_m} \qquad \text{(Eq. 4.5)}$$

Where D_{NaCl} is the average diffusion coefficient of NaCl through the AEM and CEM (m^2·s^{-1}), l_m is the membrane thickness (m), and factor 2 is introduced to account for the diffusion through both membrane types.

The volumetric flux of water through the membranes (m·s^{-1}) was given by [21]:

$$T_{i,j}^{H_2O} = -2\left(C_{i,j}^{SW} - C_{i,j}^{RW}\right)\frac{D_{H_2O}}{l_m}\frac{MW_{H_2O}}{\rho_{H_2O}} \qquad \text{(Eq. 4.6)}$$

Where D_{H_2O} is the average diffusion coefficient of water through the AEM and CEM $(m^2 \cdot s^{-1})$, the factor 2 was introduced to account for the diffusion through both membrane types, MW_{H_2O} is the molecular weight of water $(kg \cdot mol^{-1})$, and ρ_{H_2O} is the density of water $(kg \cdot m^{-3})$.

The change in concentration in the active area can be described by the sum of the salt transport due to migration and diffusion (co-ions), plus water transport, as in the following partial differential equations (PDEs):

$$\frac{\partial C_{i,j}^{SW}}{\partial y} = -\frac{\Delta x}{\Delta \phi_{SW}} T_{i,j}^{NaCl} + C_{i,j}^{SW} \frac{\Delta x}{\Delta \phi_{SW}} T_{i,j}^{H_2O}$$
$$= -\frac{W}{\phi_{SW}} T_{i,j}^{NaCl} + C_{i,j}^{SW} \frac{W}{\phi_{SW}} T_{i,j}^{H_2O} \qquad \text{(Eq. 4.7)}$$

$$\frac{\partial C_{i,j}^{RW}}{\partial x} = +\frac{\Delta y}{\Delta \phi_{RW}} T_{i,j}^{NaCl} - C_{i,j}^{RW} \frac{\Delta y}{\Delta \phi_{RW}} T_{i,j}^{H_2O}$$
$$= +\frac{L}{\phi_{RW}} T_{i,j}^{NaCl} - C_{i,j}^{RW} \frac{L}{\phi_{RW}} T_{i,j}^{H_2O} \qquad \text{(Eq. 4.8)}$$

Where Δx and Δy are the discretization intervals (m), ϕ is the feed flow rate $(m^3 \cdot s^{-1})$, $\Delta \phi$ is the feed flow rate in Δx or Δy $(m^3 \cdot s^{-1})$, L is the length of the active area (m), and W is its width (m). The two governing PDEs are solved numerically using the Forward Euler method (Eq. 4.9 and 4.10), thus obtaining the matrix of the concentrations at steady state.

$$C_{i+1,j}^{SW} = C_{i,j}^{SW} + dy \left(-\frac{W}{\phi_{SW}} T_{i,j}^{NaCl} + C_{i,j}^{SW} \frac{W}{\phi_{SW}} T_{i,j}^{H_2O} \right) \qquad \text{(Eq. 4.9)}$$

$$C_{i,j+1}^{RW} = C_{i,j}^{RW} + dx \left(+\frac{L}{\phi_{RW}} T_{i,j}^{NaCl} - C_{i,j}^{RW} \frac{L}{\phi_{RW}} T_{i,j}^{H_2O} \right) \qquad \text{(Eq. 4.10)}$$

From the solution concentrations, the electromotive force, cell resistance, current density, power (and power density), and efficiencies were calculated. Custom Python 3.6 scripts and functions were developed for this purpose. The grid size was 500 x 500 points. Further grid refinement did not significantly affect the model results, while it increased the computation time.

The total power output was maximized by varying the ohmic loads applied to the four segments using a SLSQP (sequential least squares programming) algorithm. The scypy.optimize.minimize function was used for this purpose (- P_{gross} was the minimized function).

Table S4.1 summarizes all the model input parameters used in the present work and how they were evaluated.

For both model and experimental data, the gross power produced by the stack was given by:

$$P_{gross} = U_{load} \, I \qquad \text{(Eq. 4.11)}$$

Where U_{load} is the voltage drop measured if a load is applied to the stack (V) and I is the current extracted from the stack (A).

To calculate the efficiency of the stack operation, the total Gibbs energy available in the salinity gradient (J), was considered:

$$\Delta G = T \cdot \Delta S = T \cdot (S_{mix} - S_{SW} - S_{RW}) \qquad \text{(Eq. 4.12)}$$

$$S = -Rn_{TOT} \sum_i x_i ln(\gamma_i x_i) \; with \; i = Na^+, Cl^-, H_2O \qquad \text{(Eq. 4.13)}$$

Where S is the entropy (J·K^{-1}), n_{TOT} is the total number of moles (mol), x_i is the fraction of element i (-).

Considering in Eq. 4.13 the flow rates of the feedwaters (m^3·s^{-1}) rather than the compartment volumes (m^3), n_{TOT} becomes the number of moles per second (mol·s^{-1}). The entropy was calculated per unit of time (W·K^{-1}), and Eq. 4.12 expressed the available power (W), which can be directly compared to the stack power output to calculate the energy efficiency.

The (gross) energy efficiency (%) considered the gross power produced compared to the total available Gibbs energy at the inlet (complete mixing was assumed):

$$\eta_{energy} = 100 \frac{P_{gross}}{\Delta G_{in}} \qquad \text{(Eq. 4.14)}$$

The pumping losses (W) were calculated as the energy consumed to pump the seawater and the river water respectively [21]:

$$P_{pump} = \phi_{SW} dP_{SW} + \phi_{RW} dP_{RW} \qquad \text{(Eq. 4.15)}$$

$$dP_{RW} = K \frac{W \phi_{RW}}{L d_{RW}{}^3} \qquad \text{(Eq. 4.16)}$$

$$dP_{SW} = K \frac{L \phi_{SW}}{W d_{SW}{}^3} \qquad \text{(Eq. 4.17)}$$

Where dP is the pressure drop between feedwater inlet and outlet (Pa), K is the fitting coefficient (Pa·s) used to describe the pumping energy, and ϕ is the flow rate of the feedwater (m^3·s^{-1}).

By subtracting the pumping losses from the gross power, the net power (W) was obtained:

$$P_{net} = P_{gross} - P_{pump} \qquad \text{(Eq. 4.18)}$$

From the net power, the net energy efficiency (%) was determined:

$$\eta_{net} = 100 \frac{P_{net}}{\Delta G_{in}} \qquad \text{(Eq. 4.19)}$$

All power figures were converted to power densities by dividing the power values by the total membrane area ($A_{total} = 2W \cdot L \cdot N_{CP}$, accounting for the area of CEMs and AEMs in all cell pairs).

$$P_d = \frac{P}{2W \cdot L \cdot N_{CP}}$$
(Eq. 4.20)

4.2.2 Stack configuration & electrodes

A cross-flow reverse electrodialysis stack (REDstack BV, the Netherlands) was used to investigate the effect of electrode segmentation on performance. The stack design details can be found in previous research [16,29,38]. The stack, with 22 cm x 22 cm active membrane area, contained 10 cell pairs (0.968 m² of total active membrane area). The number of cell pairs was chosen according to the desired experiment duration and volume of the feedwater reservoirs (at the highest flow rate, water consumption is approximately 2.5 L·h⁻¹ per cell pair). Each cell pair consisted of one Fujifilm type 10 CEM and one Fujifilm type 10 AEM (FUJIFILM Manufacturing Europe BV, the Netherlands). The properties of these membranes are reported by Moreno et al. [19]. To close the electrode compartments, two CEMs are placed at each end, for double-shielding purpose, adding a total of three extra Fujifilm type 10 CEMs, instead of one extra CEM. The membranes were separated by 155 µm thick woven net-spacers (Deukum GmbH, Germany), with netting Saatifil PES 153/55 (Saati SpA, Italy). For the model validation, standard 22 cm x 22 cm (Figure 4.3b) Ti-mesh 1.0 electrodes with 2.5 µm Pt galvanic coating were used as anode and cathode (MAGNETO Special Anodes BV, the Netherlands).

For segmentation, a dedicated electrode configuration was manufactured (REDstack BV, the Netherlands) with four 10 cm x 10 cm electrodes placed at the endplates with 1.5 cm distance between each other (Figure 4.3d, Figure S4.1b), while the total active membrane area was kept at 0.968 m². The electrodes were made of Ti-mesh with a Ru/Ir mixed metal oxide coating for anode and cathode (MAGNETO Special Anodes BV, the Netherlands). As electrode rinse solution a mixture of 0.2 M K₄Fe(CN)₆, 0.2 M K₃Fe(CN)₆ and 0.15 M NaCl was used (96 %, 96 % and 100 % purity, respectively, VWR Chemicals, Belgium). Due to the special electrode configuration, the electrode rinse solution was pumped independently into each electrode compartment (Figure S4.1b) at a flow rate of 150 mL·min⁻¹ using a peristaltic pump (Cole-Palmer, Masterflex L/S Digital drive, USA) with two double pump heads to avoid pulsations (Cole-Palmer, Masterflex L/S Two-Channel Easy-Load II, USA). Figure 4.3a provides a schematic illustration of the feed water

directions, electrical connections and sensors during the segmented electrode stack operation.
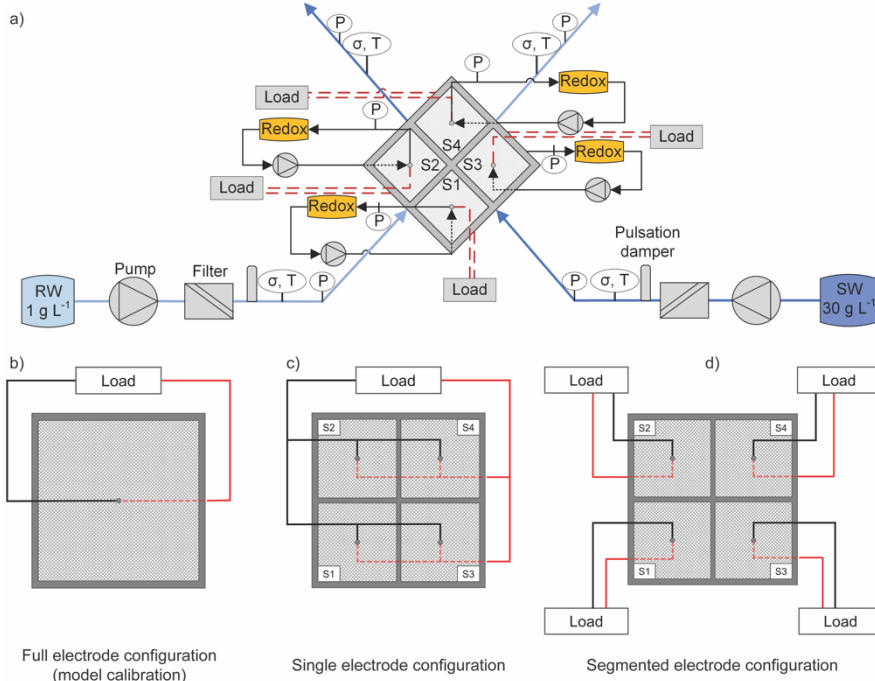
Figure 4.3 a) Flow diagram for the operation of the segmented electrode stack configuration. b) Electrode and external load representation of the stack with a 22 cm x 22 cm electrode (full electrode configuration). c) Electrode and external load representation of the stack with four 10 cm x 10 cm electrode segments connected to a single external load (single electrode configuration). d) Electrode and external load representation of the stack with four 10 cm x 10 cm electrode segments connected to four separate external ohmic loads (segmented electrode configuration).

4.2.3 Feedwaters and sensors

Artificial feedwaters were made of 30 g NaCl·L⁻¹ and 1 g NaCl·L⁻¹ (99.9 % purity, Regenit, Esco, the Netherlands), for seawater and river water, respectively. The two solutions were pumped at the same flow velocity using diaphragm pumps (Grundfos DDA220, Denmark). Pulsation dampers (PDS250 PVC/FKM, Prominent GmbH, Germany) were placed between the pumps and the stack to mitigate the pump pulsation. Also, cartridge filters with 1 µm pore size (Filter Technics, Belgium) were placed before the stack (Figure 4.3a). Outlet flow velocities were measured gravimetrically. Conductivity and temperature were measured in-line (VStar22, Thermo Fisher Scientific, USA) at the inflow and outflow of each stream. The inlet temperatures were set to 25 °C.

The absolute pressure was measured with calibrated sensors (MIDAS SW, JUMO GmbH, Germany) in the same points as the conductivity and at the electrode rinse solutions. The data were collected with a data logger (Memograph M, Endress + Hauser, Germany). Salt concentrations were calculated from conductivity values based on an experimental calibration curve (Figure S4.2). The hydrodynamic losses were determined as the product of the differential pressure across the stack and the flow rate (Eq. 4.15) [28].

4.2.4 Experimental procedure
4.2.4.1 Experiments for model validation with standard stack

To identify the spacer shadow factor and the average salt diffusion coefficient values through the membranes, a separate experiment with full electrode configuration (Figure 3b) was performed and data were fitted with the model. The 22 cm x 22 cm electrode stack (Figure 4.3b) was used to determine the power density and energy efficiency at different current densities fixing the residence time at 22 s (flow velocity of 1.0 cm·s^{-1}). This was done by increasing the current density in 6.2 A·m^{-2} steps (0.3 A in current over 22 cm x 22 cm area) for 10 minutes each, taking the average of the last 2 minutes of the current and voltage values as measured with the potentiostat (IVIUM.XRi, IVIUM Technologies BV, the Netherlands) to obtain the power (Eq. 4.11). The blank resistance was measured to be 0.071 Ω, given by REDstack [39], which comprised the resistance of the electrodes, the rinse solution and the three extra CEMs. This was used to discard the contribution of the electrodes to the stack resistance, which would be negligible when using hundreds of cell pairs. To validate the model, experimental power data were corrected for the blank resistance [39], to avoid the presence of the blank resistance (Eq. 4.2) as an additional fitting parameter. Pumping losses across the stack were determined experimentally, and the model parameter K (Eq. 4.16 and 4.17) was adjusted to fit the experimental data. The shadow factor f was adjusted to fit the experimental data, starting with 0.55, corresponding to the open area of the spacer netting.

4.2.4.2 The relation between electrode segments

To understand the mutual response of the electrode segments, the relation between electrode segments (Figure 4.3d) was established by measuring the potential of each segment with a multi-channel potentiostat (IVIUM n-stat, IVIUM Technologies BV, the Netherlands) at a fixed residence time of 22 s (flow velocity of 1.0 cm·s^{-1}). This consisted in operating one electrode segment, first at open-circuit voltage (OCV) conditions for 60 s followed by a stepwise increase in the extracted current with 16.5 A·m^{-2} current density

steps (0.2 A in current over 11 cm x 11 cm area), for 120 s each, until the stack voltage crossed 0 V. Simultaneously, the OCV of the other three electrode segments was measured continuously. Segment current densities were calculated by dividing the applied current (in A) by one-fourth of the active membrane area.

4.2.4.3 Comparison between single and segmented electrode configurations

The performance of four-electrode segments electrically connected to a single load (referred to as single electrode configuration, Figure 4.3c) was compared to the independent performance of the four electrode segments (referred to as segmented electrode configuration, Figure 4.3d) and characterized at five different residence times: 88, 44, 22, 15, and 11 s (corresponding to flow velocities of 0.25, 0.50, 1.00, 1.50 and 2.00 cm·s^{-1}, respectively). This approach was chosen since connecting the four electrode segments as a single electrode does not change the total electrode area nor the electrode rinse solution distribution, thus providing a fair comparison. In this third experiment, electrochemical measurements were done using sliding rheostats (4.5 Ω 9 A, Eisco, USA) as a variable external load. Each rheostat was connected to a multimeter (Digital Multimeter VC165, Voltcraft, Germany) monitoring the external load voltage. The segment voltage was measured at the electrodes (Figure S4.3), while the current was measured using a calibrated shunt of 0.1 Ω. The power per segment was calculated from the measured shunt voltage for each segment and the measured segment voltage (Eq. 4.11). The overall power was calculated by summing all segments powers (P1+P2+P3+P4). The experimental power of each electrode segment was monitored automatically inside the data logger as well as the total power. For the single electrode, the maximum power was determined by sliding the rheostat until the peak in the power curve was reached. For the segmented electrode, the individual rheostats were adjusted manually until the overall power value reached its maximum.

The stack power density was obtained by dividing the power by the total active membrane area. The power density per segment was obtained by dividing the segment power by a quarter of the total active membrane area.

4.3 Results and discussion

4.3.1 Model calibration

Figure 4.4 shows that the calibrated model correctly predicts the power density and energy efficiency for different external loads. The determined model values of the spacer shadow

factor (0.61) and salt diffusion coefficient (6.5×10^{-12} $m^2 \cdot s^{-1}$) are in line with the values reported by Veerman et al. [21] and in the normal range for ion exchange membranes [40].
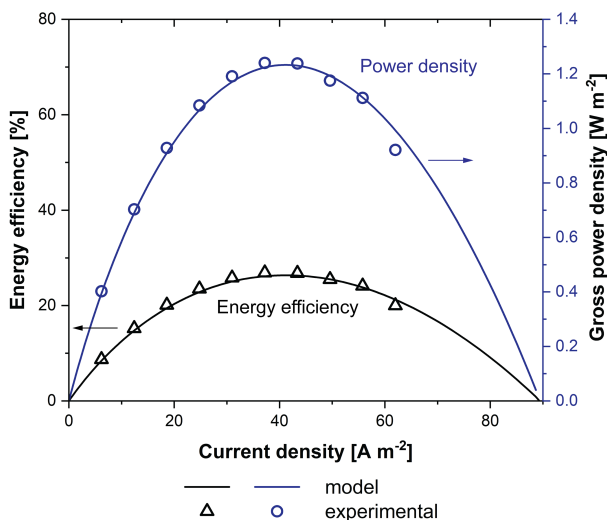
Figure 4.4 Experimental and modelled gross power density and energy efficiency values for a 22 cm x 22 cm cross-flow stack with 155 μm thick spacers at a residence time of 22 s (flow velocity of 1.0 cm·s⁻¹).

4.3.2 The relation between electrode segments

Experimentally obtained I-V curves for each case of one active electrode segment are shown in Figure 4.5 for a residence time of 22 s. The first 60 s period, at OCV conditions, shows a different OCV value for each electrode segment depending on their position. Segment 1 (S1) has the highest potential (1.548 V) because the gradient is the largest in this area. This segment receives fresh seawater and river water, i.e. it is the first contact between both solutions and the first opportunity for ion exchange. And it is then followed by S2 (1.543 V), S3 (1.522 V) and S4 (1.514 V). At this stage, the stack is in stationary condition and no current is extracted, thus, the decrease in potential across the stack indicates undesired water and salt diffusion through the membranes, which is expected when using ion-exchange membranes [19]. This is confirmed by the change in concentration between the inlet and outlet of the river and seawater measured at OCV (Figure S4.4a). The same behaviour was detected in further experiments at different residence times (Table S4.2). The decrease in potential across the electrode segments is more evident at longer residence times since the feedwaters have extended contact periods with the membranes. For a single electrode, these phenomena would only be detected through a change in concentration at the final outlets and a difference between the

theoretically calculated and the experimentally measured membrane potential. The segmented electrode configuration allows visualization of the effect of undesired salt and water transport. Moreover, it is visible that the potential of each electrode segment is dependent on its position in the stack.
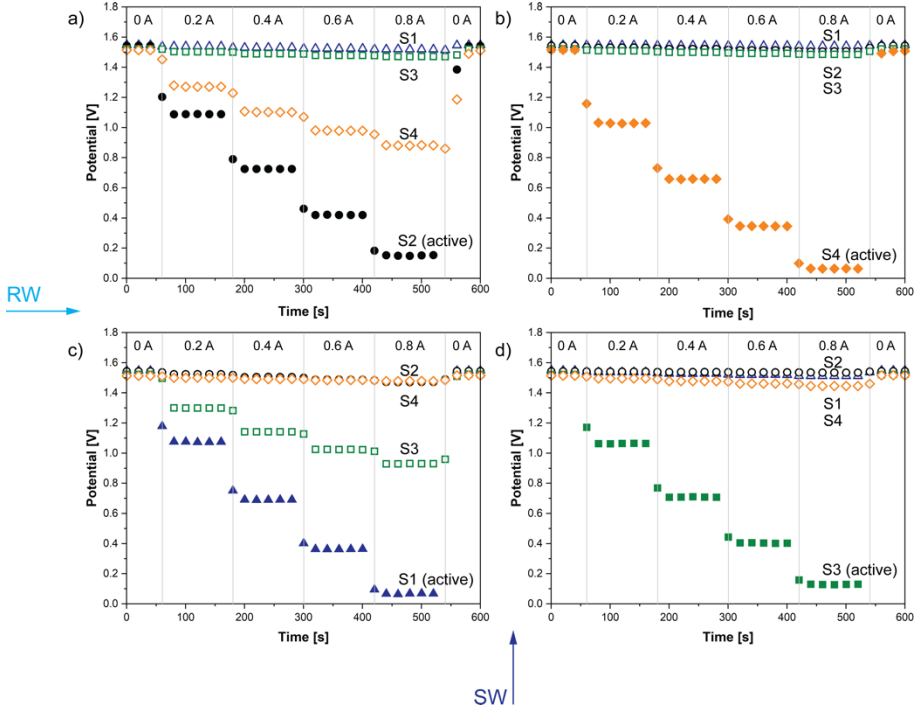
Figure 4.5 Relation between electrode segments at a residence time of 22 s (1.0 cm·s^{-1} flow velocity). Current density steps of 16.5 A·m^{-2} (0.2 A current divided by 11 cm x 11 cm area) were extracted from one segment (solid marker, also indicated in the plot) and the segment voltage response was measured. In the same time frame, remaining segments (open markers) were measured at OCV conditions. Each plot corresponds to one active electrode segment a) S2 b) S4 c) S1 d) S3, the order was chosen to mimic the position of the segments concerning the RW and SW flow path inside the stack (indicated in the bottom and left by arrows).

Figure 4.5 shows how the electrode segments influence each other when active. When current is extracted from S1 (Figure 4.5c), the OCV of S3 drops. This is caused by the increase in salinity of the river water, which flows from S1 to S3. The potential of S2 exhibits a small decrease compared to the drop in OCV of S3, showing that the salinity drop of the seawater has a smaller influence on the OCV of the adjacent segment rather than the increase in salinity of the river water, following the Nernst equation. Additionally,

it is worth noting that the potential of S4 is minimally affected. This shows that the feedwaters and the ions follow a straight flow path inside the stack (Figure 4.3a). Similarly, when S2 generates current (Figure 4.5a), the potential of S4 drops due to the increased salinity of the river water. OCV values of S1 and S3 are not affected, providing a further indication that a straight flow path is present inside the stack. When S3 is active (Figure 4.5d), only S4 has a shallow drop in potential, supporting the conclusion that the salinity drop in the seawater is not crucial for the driving force. Finally, when S4 is generating current (Figure 4.5b), as expected, the OCV values of the other segments are not influenced, indicating that the segments do not communicate with each other, i.e. the electrical field is only working in the electrode segment area. These results indicate that the increase in salinity of the river water mainly determines changes in the electromotive force over the active area [28] and that the electric fields introduced by the electrode segments stay separate through the stack when using a limited number of only 10 cell pairs.

4.3.3 Power density distribution model in a single electrode and segmented electrode

The current density inside the RED stack has a non-homogeneous distribution, as the local currents are a function of 3 parameters: 1) the electromotive force, 2) the internal resistance and 3) the external load. The first two parameters are determined by the local salinity gradient and local concentrations, respectively. This directly affects the local power density output [22,41]. Experimentally this phenomenon can be measured but it is limited to the number of electrode segments available. With a modelling approach, it can be simulated and mapped. For co-flow and counter-flow configurations, the decrease of electromotive force along the flow direction has been shown in several studies [21,24,26,41]. For cross-flow configuration, Vermaas et al. displayed the current density distribution in the active area, albeit for a RED system with ideal membranes [22].

Figure 4.6 compares the gross power density distribution on the active membrane area inside the stack for single electrode configuration (Figure 4.6a), segmented electrode configuration at maximized power per segment (Figure 4.6b), i.e. when the load is sequentially optimized to maximize the power produced by the individual segments (in the order S1, S2, S3, and S4 due to the flow of the feedwaters from one segment to the next), and segmented electrode configuration at maximized overall power (Figure 4.6c), i.e. when the sum of the electrode segments power is maximum. Furthermore, it compares the gross power density contribution (Figure 4.6d) per equivalent segment in the single

electrode configuration or per independent segment (segmented electrode configuration). The residence time of 44 s was chosen since the electrode segmentation effect is pronounced at longer residence times. In addition to Figure 4.6, Figure S4.5 illustrates the distribution of the sodium chloride concentration in the river and seawater, the electromotive force, the cell pair resistance, and the current density.
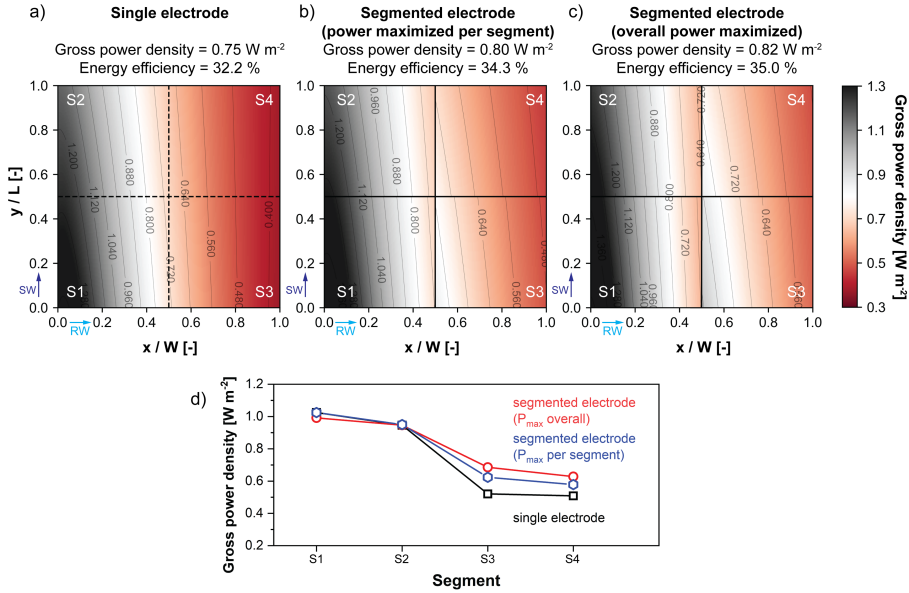
Figure 4.6 Model results for gross power density distribution inside a 22 cm x 22 cm RED stack in a) the single electrode configuration, b) the segmented electrode configuration at maximized power per segment, and c) the segmented electrode configuration at overall maximum power at a residence time of 44 s (flow velocity of 0.5 cm·s^{-1}). The x-axis is the river water path and the y-axis the seawater path. Note, the grid division in a) is only used to allow an easier comparison with b) and c), as in the single electrode configuration the electrode segments electrically work as one. d) Gross power density contribution per equivalent electrode segment (single electrode) and per electrode segment (segmented electrode at maximized power per individual segment and overall maximum power).

For the single electrode configuration (Figure 4.6a), the electrode segments are electrically connected, and the current is controlled by a single external load (Figure 4.2c). The gross power density value decreases alongside the river water direction (x-axis) since the electromotive force decreases the most with the increase in salinity of the river water (Figure S4.5g), which also results in lower electrical resistance (Figure S4.5j). The outcome is different local current densities while the same external load is applied to the stack (Figure S4.5m). The highest gross power density is obtained close to the point where the feedwaters first meet, where the electromotive force is still high, but the electrical

resistance of the river water is decreasing due to the rising salt concentration. It can be noted that the current distribution (Figure S4.5m) and the one Vermaas et al. [22] reported are different. This is due to the membrane electrical resistances, they were assumed zero by Vermaas et al., but are considered in the present work. Figure 4.6b and Fig 4.6c show the power distribution using a segmented electrode configuration, with four independent external loads (Figure 4.2d). Again, the gross power density value decreases along the river water due to mixing. However, by adjusting each external load to the internal segment resistance (Figure S4.6), the harvested gross power density is higher compared to the single electrode configuration. Figure S4.5g-i shows the difference between the electromotive force and the external loads (*E-U* in Eq. 4.4), which together with the local stack resistance contributes to determining the local current density. In Figure 4.6d segments S3 and S4 produce a higher gross power density for both segmented electrode configurations. When adjusting the different loads to reach the overall maximum power density, S1 is underperforming the equivalent segment in the single electrode configuration. This is because to reach the overall maximum power density, it is beneficial that S1 does not work at its maximum power density, as in Figure 4.6b, but preserve part of the salinity gradient for the following electrode segments, thus allowing higher electromotive force in S3 and S4. It may seem counter-intuitive that segments S3 and S4 produce more power when the overall power is maximized rather than when the power per segment is maximized. When the power per segment is maximized the high performance of S1 and S2 comes at the expense of S3 and S4, which experience a lower salinity gradient. At 44 s residence time, the model predicts a 9 % increase in gross power density from a single electrode configuration to the segmented electrode configuration at overall maximum power density. This increase is mainly gained in S3 and S4 (these segments increase power by 24 % and 19 %, respectively). Furthermore, for optimization, it is important to note that the electrode segments work towards the overall maximum power instead of being maximized segment individually.

4.3.4 *The behavior of a single electrode and a segmented electrode with residence time*

In addition to the model results, Figure 4.7 presents a comparison of the experimental and model overall stack gross power densities (Figure 4.7a) and energy efficiencies (Figure 4.7b) for the single electrode and segmented electrode configurations at different residence times when the overall stack power is maximized. In all cases, the model predictions closely resemble the experimental results.
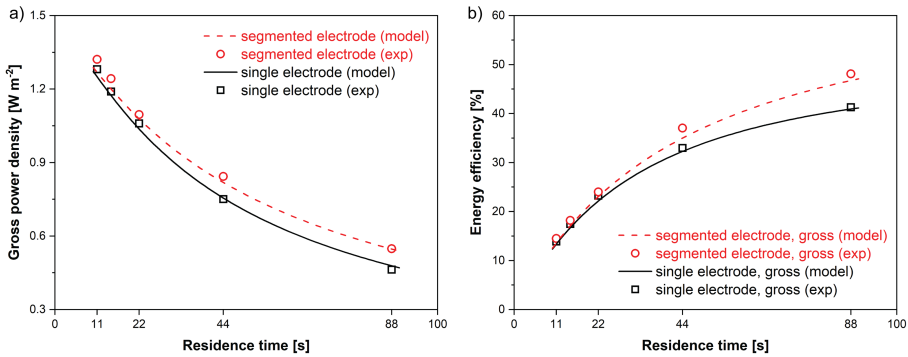
Figure 4.7 – a) Gross power density and b) energy efficiency, for single electrode and segmented electrode configurations, as a function of residence time; symbols represent the experimental data (residence time of 11, 15, 22, 44 and 88 s) and the lines represent the model results. Model parameters can be found in Table S4.1.

Figure 4.7a shows that the gross power density decreases for increasing residence time. This is consistent with the results from the literature [16,19,28]. The opposite trend is observed in Figure 4.7b, where energy efficiency increases for longer residence times. These trends have been explained by Moreno et al. as the consequence of lower Gibbs free energy per unit time available at longer residence times, in addition to the non-homogenous distribution of electromotive force, cell resistance, and current density in the active membrane area [19]. Additionally, at longer residence times more ion exchange occurs, which results in a lower electromotive force and stack resistance for the segments further away from the water inlets. At longer residence times, for the single electrode configuration, in the region close to the outlets, the locally available electromotive force becomes close to the external voltage load ($E \sim U$), which leads to small current production (Eq. 4.4), hence only a small power output comes from this region. When the single electrode and the segmented electrode configuration are compared, the adaptation of the external loads to the local electromotive force and local stack resistance (i.e. a lower external load on segments S3 and S4), allows to produce a higher current and therefore a higher power output close to the outlets of the stack. If this is combined with the strategy of saving gradient in the first segments (S1 and S2) to reach the overall maximum power, it explains the higher power production for the segmented electrode configuration compared to the single electrode configuration at all residence times, with a pronounced gain at 44 and 88s.

4.3.5 Electrode segments contribution at different residence times

Data in Figure 4.7 provide the overall stack output, based on the contribution of each electrode segment. The contribution of each electrode is shown in Figure 4.8, providing the voltage load and gross power density for each electrode segment in the segmented electrode configuration at different residence times, when the maximum overall power is achieved.
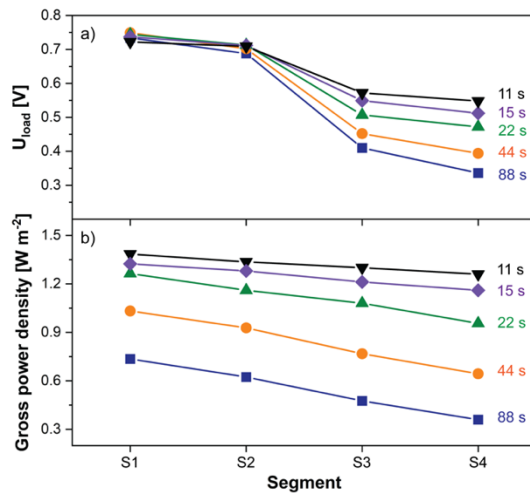
Figure 4.8 Individual segment contribution (experimental) at different residence times (11, 15, 22, 44, and 88 s) when the overall stack power is maximized. a) The voltage drops over the external load voltage per segment. b) Gross power density per electrode segment.

In Figure 4.8a, for all residence times, the external load voltages on S1 and S2 are similar despite the different extent of ion exchange occurring at different residence times. This indicates that to maximize the overall power segments S1 and S2 work at a sub-optimal point to save gradient for segments S3 and S4. When the feedwaters reach segments S3 and S4, major ion exchange has occurred and the salinity gradient has significantly decreased, with the highest decrease in S4. Since the salinity gradient is considerably lowered in S3 and S4, the external loads need to be adjusted accordingly. Figure 4.8a shows that for increasing residence times, the external load voltages for S3 and S4 are decreasing. To achieve maximum power output on these electrode segments, the required external load voltage is lower than for S1 and S2. It can be noted in Figure S4.7 that the predicted load voltages, with the model, at maximum power density in the segmented electrode configuration closely resembles the experimentally identified set of values. This

agreement between model and experiment highlights the value of the model in guiding the optimization of the external loads. In Figure 4.8b, the gross power density per electrode segment is presented. At short residence times, the power output of the four segments is very similar, but with increasing residence times and consequently increased ion exchange, the power density produced by the electrode segments located further away from the river water inlet (S3 and S4) decreases. Interestingly, at short residence times, the load voltages required to produce similar power densities are lower for S3 and S4 than for S1 and S2. This is the case because S1 and S2 operate with a higher electromotive force, but also higher stack resistance. S3 and S4 have a lower electromotive force available but benefit from the increased conductivity of the river water, leading to lower stack electrical resistance and comparable gross power density for all segments.

Figure 4.8a shows that the optimal load voltages for S1 and S2 are similar, and the same applies to S3 and S4. The large difference in an optimal external load along the river water and small difference along the seawater flow direction indicates that segmentation along the river water is more beneficial than along the seawater. This is the case because the electromotive force is most sensitive to the salinity of the river water (Figure S4.5g and Figure S4.5i).

To investigate this hypothesis in further detail, Figure 4.9 presents the model results of a 2 x 2 electrode segmentation (Figure 4.3d) and a 2 x 1 configuration (along the river flow direction only).
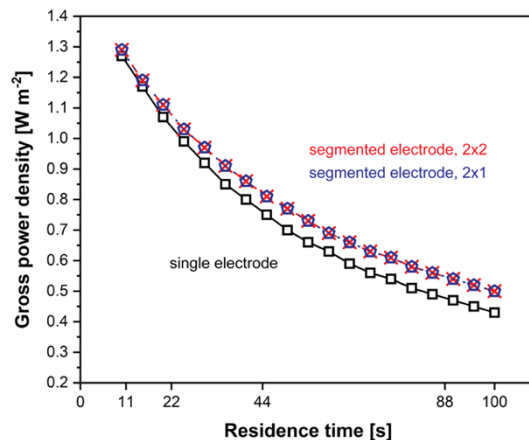
Figure 4.9 Modelled gross power density as a function of the residence time for a single electrode, two electrode segments (2 x 1, in the river water flow direction), and four-electrode segments (2 x 2) in a 22 cm x 22 cm stack.

The results are nearly identical, with only very small differences at high residence times, between the segmented electrode configurations. This confirms that a simpler configuration with electrode segmentation only along the river water direction, as proposed by Vermaas et al [22], would yield the same power increase as segmentation along both river and sea directions. Nevertheless, the additional complexity of a 2 x 2 configuration allows for the operational flexibility required by feedwater switch strategies, i.e. changing seawater for river water and vice versa, which have been proved to be beneficial for fouling management [42].

4.3.6 Net power density and net energy efficiency

Figure 4.10a shows the pumping power density, which significantly decreases with increasing residence time as longer residence times imply lower feed flow velocities. At short residence times, the pumping power densities are increasing rapidly due to the increase in pressure drop inside the stack [16]. Meanwhile, at long residence times, a flat region is reached where the pumping losses become negligible, being the ideal working region to avoid pumping losses.
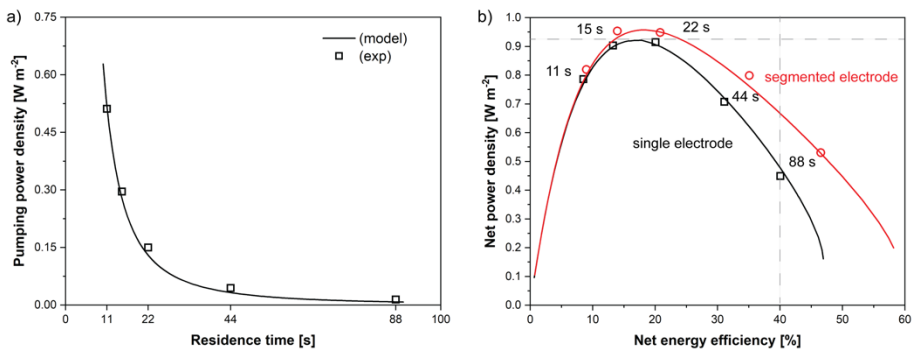
Figure 4.10 a) Pumping power density as a function of residence time. b) Net power density as a function of net energy efficiency for the single electrode and segmented electrode configurations at different residence times. Symbols represent experimental data (residence time of 11, 15, 22, 44 and 88 s) and lines show the model results.

Figure 4.10b shows the net power density, i.e. the gross power density minus the pumping power density, plotted against the net energy efficiency. Electrode segmentation leads to higher net power density and efficiency at residence times longer than 11s. This is the case due to the maximized overall power production. The increased ion exchange for the segmented electrode is evident in the decreased gradient at the stack outlet in Figure S4.4b.

The greatest benefit of applying electrode segmentation is reported in Figure 4.10b. Both configurations achieve maximum net power density at approximately 17 % net energy efficiency and short residence times. This relatively low net energy efficiency is not beneficial for up-scaling RED when the cost of water pre-treatment to decrease fouling is a relevant fraction of the operating costs. To minimize this cost, the energy efficiency should be as high as possible without sacrificing power density. Figure 4.10b shows that electrode segmentation accomplishes this requirement. Comparing both electrode configurations at the net power density at the peak performance for a single electrode (0.92 W·m^{-2}), segmentation increases the net energy efficiency from 17 % for the single electrode to 25 % for the segmented electrode (horizontal line in Figure 4.10b), which is a remarkable 43 % relative efficiency increase. This increase in efficiency allows the extraction of the same power from less water, which is likely to reduce the operating costs of a full-scale RED power plant by reducing the need for water pre-treatment. At 40 % net energy efficiency (vertical line in Figure 4.10b) the net power output for the segmented electrode configuration is enhanced by 39 % relative to a single electrode, which is likely to translate in a lower capital cost for a full-scale plant, as a smaller membrane area is required to achieve a given power production target. Although promising, testing in a larger scale RED system, i.e., more cell pairs, fed with natural feedwaters is necessary to confirm the benefits of electrode segmentation on capital and operating costs. For a segmented electrode, the same net energy efficiency can be reached at a shorter residence time. As the process is more efficient, higher net power densities can be achieved. Therefore, the increase in net power density for a segmented electrode results from combining the increase in power due to shorter residence time (more Gibbs free energy available per unit time) and the increased energy extraction enabled by electrode segmentation. This is especially true in the long residence time region (20-90 s), due to the tuning of the external loads allowing additional power production in S3 and S4. Electrode segmentation thus reduces the trade-off between energy efficiency and power density generation, which is a critical element of the RED process to be considered for large scale RED plants.

4.4 Conclusions

The present work shows with a validated RED model and experimental investigation that electrode segmentation potentially reduces operating cost or capital expenditure. Operating cost likely decreases by increasing net energy efficiency at a given net power density (43 % relative increase in efficiency), which is beneficial in case of high water

pre-treatment costs to control fouling. Capital expenditure likely lowers at high net energy efficiencies by increasing the net power density with electrode segmentation decreasing the membrane area needed. The highest gain is attained when optimizing the external loads for overall maximum power, rather than sequentially maximizing the power output of individual segments. At 40 % net energy efficiency, the net power output for a segmented electrode is 39 % higher (0.67 W·m^{-2}) than a single electrode (0.47 W·m^{-2}). This increase in net power density at equal net energy efficiency results from combining the increase in power due to shorter residence time and the increased ion exchange enabled by electrode segmentation. This is especially true in the long residence time region (20-90 s), due to the tuning of the external ohmic loads allowing additional power production in the segments adjacent to the river water outlet. These experiments were conducted at a laboratory scale with 10 cell pairs. The effect of electrode segmentation in a larger membrane pile needs therefore further study. Experiments and the model confirm that segmenting along the river water direction in a cross-flow stack gives the most benefit, indicating that segmentation can be simplified to two rectangular electrode segments when switching the feedwaters is not required.

4

Supporting information

RED stack

a)

b)
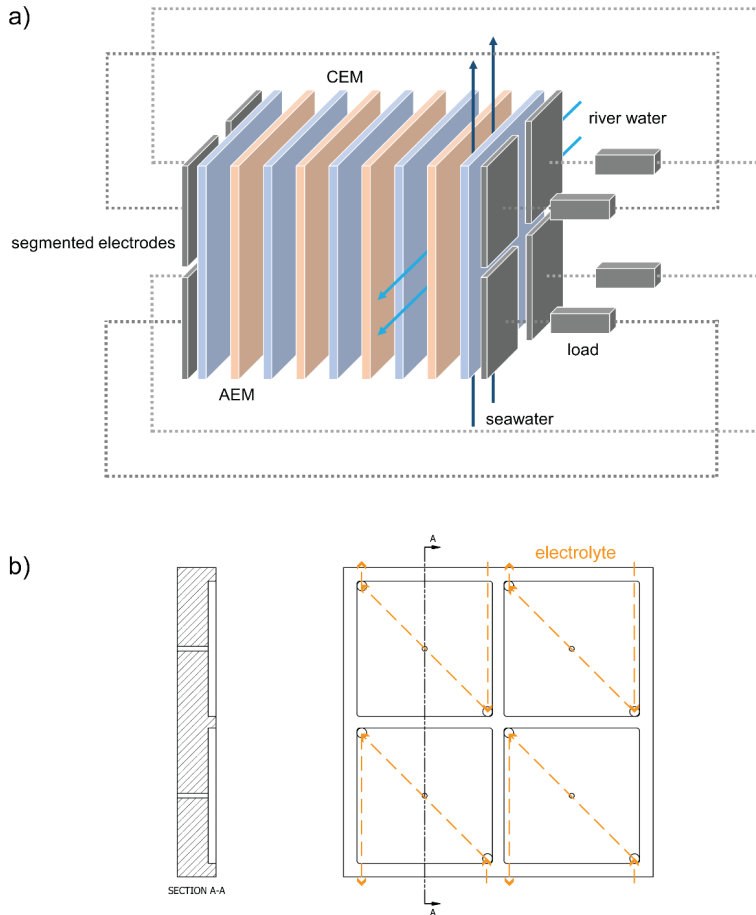
Figure S4.1 a) Schematic representation of the cross-flow stack with segmented electrodes. b) Schematic drawing of the end-plate housing with four electrode segments (not intended as a technical drawing, design and dimension do not reflect the real end-plate). The electrodes are separated by a ridge of 1.5 cm width and the electrolyte solutions are recirculated in four independent circuits. The end-plate housing was designed and made by REDstack BV (the Netherlands).

Table S4.1 Parameters used in the model calculations and procedures to evaluate them.

Parameter	Symbol	Value	Unit	Evaluation procedure
Width of the active area	W	0.22	m	Known stack parameter.
Length of the active area	L	0.22	m	Known stack parameter.
Compartment thickness	d	155×10^{-6}	m	Known stack parameter.
AEM permselectivity	α_{aem}	94.5	%	Literature data [19].
CEM permselectivity	α_{cem}	94.7	%	Literature data [19].
AEM electrical resistance	R_{aem}	1.77×10^{-4}	$\Omega \cdot m^2$	Measurement in a six-compartment cell at 0.5 M NaCl, according to a literature procedure [43].
CEM electrical resistance	R_{cem}	2.69×10^{-4}	$\Omega \cdot m^2$	Measurement in a six-compartment cell at 0.5 M NaCl, according to a literature procedure [43].
Spacer shadow factor	f	0.61	-	The initial value is 0.55, corresponding to the open area of the spacer netting. The value is then adjusted based on I-V data from 22 cm x 22 cm stack with a single electrode.
Average water diffusion coefficient (through the membranes)	D_{H2O}	1.5×10^{-10}	$m^2 \cdot s^{-1}$	Literature data [19]. Permeability converted into a diffusion coefficient based on the measurement procedure presented in [44].
Average salt diffusion coefficient (through the membranes)	D_{NaCl}	6.5×10^{-12}	$m^2 \cdot s^{-1}$	Calibration with I-V data from 22 cm x 22 cm stack with single electrode.
Membrane thickness	l_m	125×10^{-6}	m	Literature data [19].
Blank resistance	R_{blank}	37.5×10^{-4}	$\Omega \cdot m^2$	Calibration with data from 22 cm x 22 cm stack with single electrode.
Pressure drop coefficient	K_{dP}	0.1945	$Pa \cdot s$	Calibration with experimental pressure drop data from 22 cm x 22 cm stack with single electrode.

4

Calibration curve: salt concentration and electrical conductivity
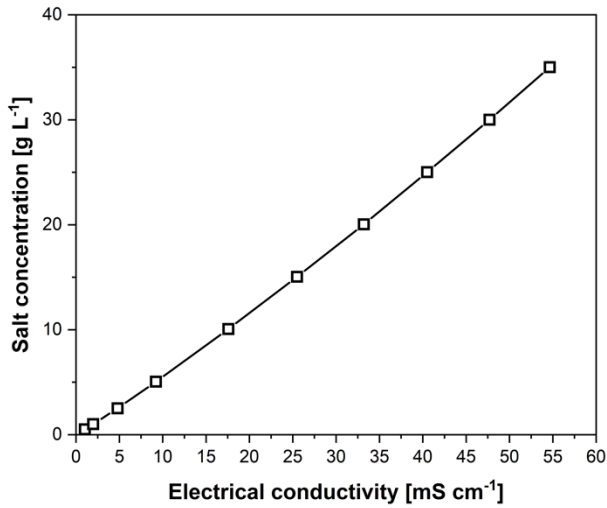
Figure S4.2 Relationship between NaCl concentration and electrical (ionic) conductivity of the solution at 25°C.

4

Electrical circuit for segmented electrode configuration
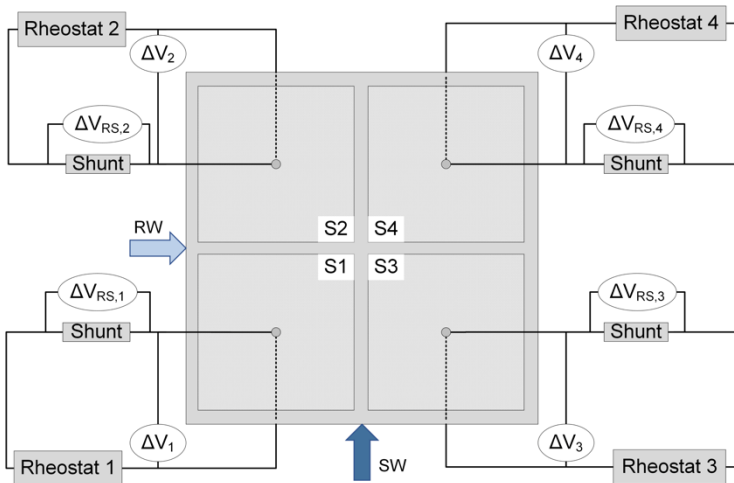
Figure S4.3 – Electrical circuit for the segmented electrode stack configuration with separate external loads.

Change in NaCl concentration at the outlet
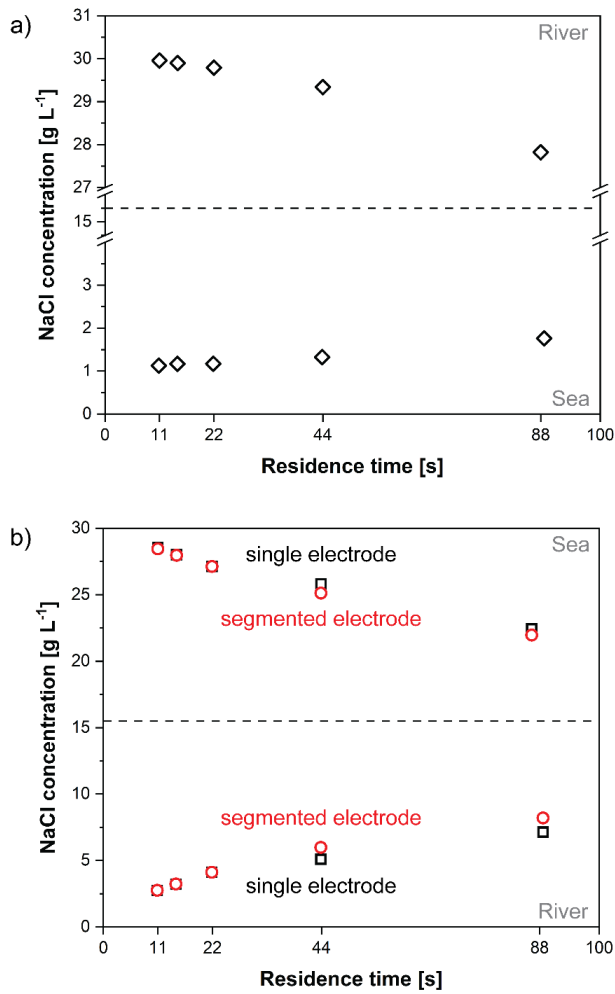
Figure S4.4 - Sodium chloride concentration at the river and seawater outlets as a function of the residence time inside the stack. a) stack under OCV conditions (the electrode configuration does not influence this experiment). b) stack working at maximum power density, single and segmented electrode configurations.

Experimental open circuit voltage for a segmented electrode (per segment) and a single electrode at different residence times

Table S4.2 - OCV values, in Volts, for each electrode segment of a segmented electrode and for a single electrode configuration, at different residence times. The OCV values for each electrode segment/ single electrode were found to be reproducibly different.

	S1	S2	S3	S4	Single Electrode
88 s	1.478	1.458	1.387	1.362	1.400
44 s	1.524	1.513	1.469	1.455	1.473
22 s *	1.542	1.533	1.512	1.499	1.521
15 s	1.552	1.549	1.531	1.526	1.534
11 s	1.552	1.550	1.534	1.532	1.543

* These values differ slightly from the ones in section 4.3.2 since they belong to a different set of experiments.

4

NaCl concentration, potential, cell pair resistance, and current density plots for 44 s residence time
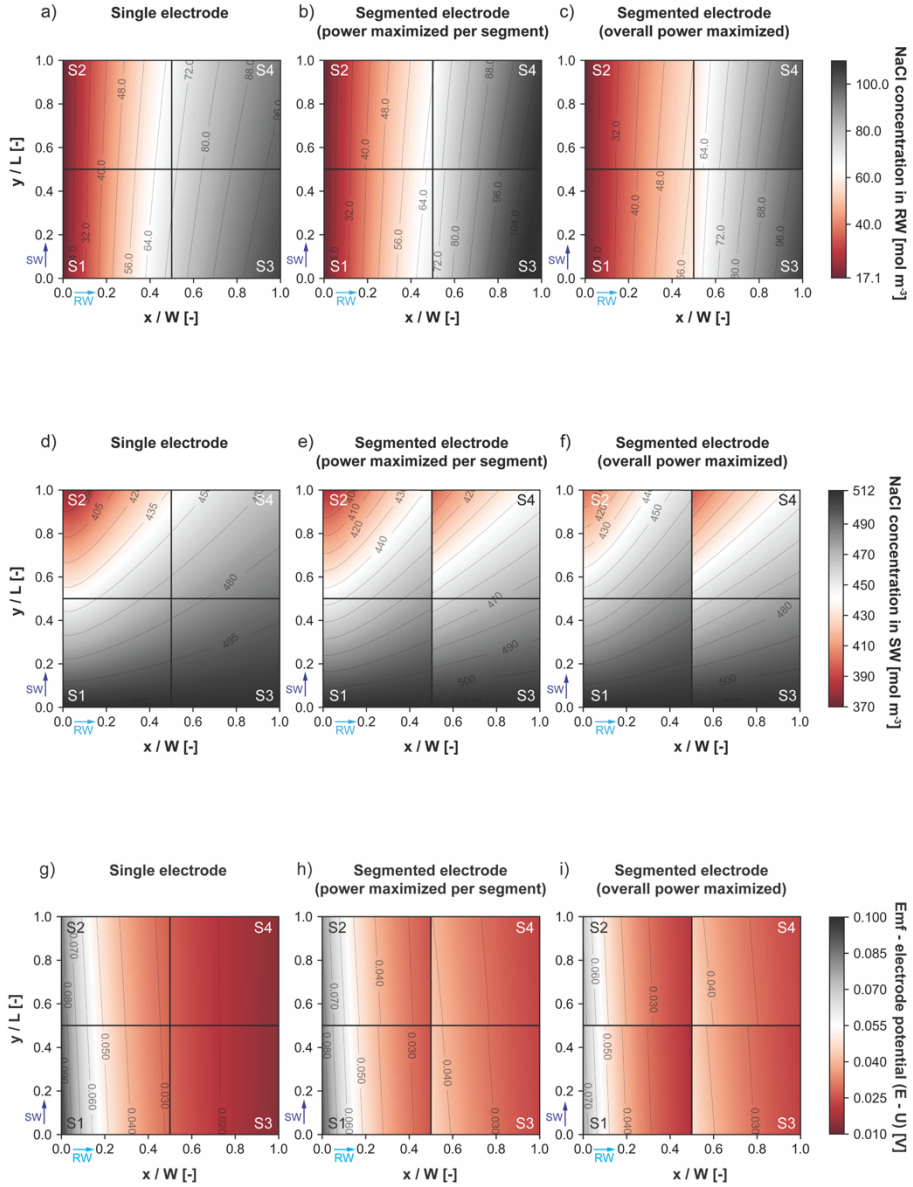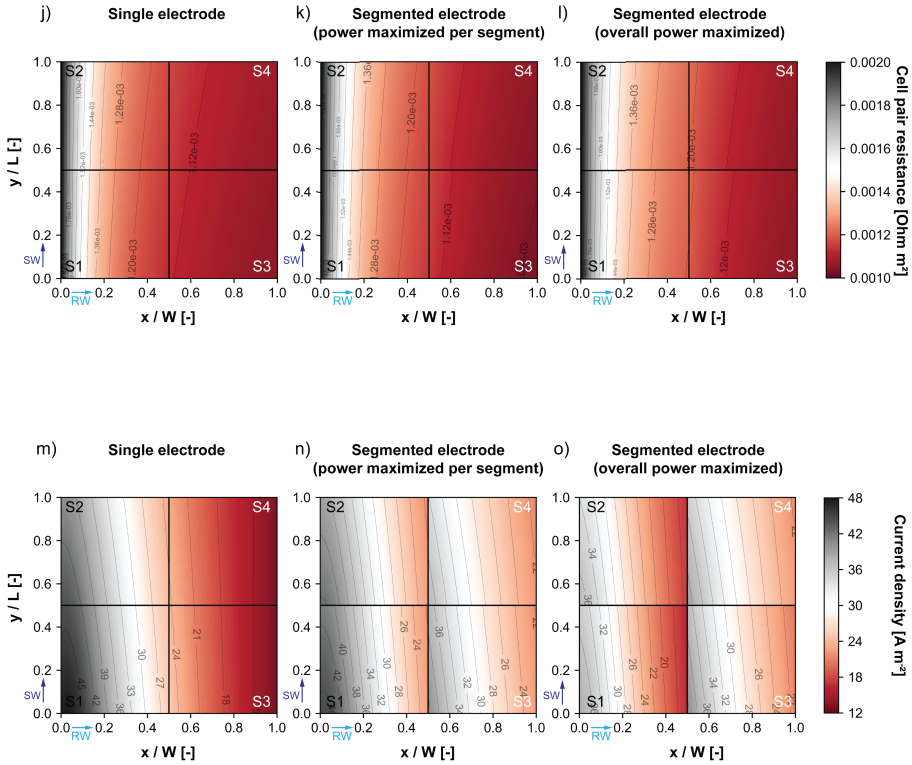
Figure S4.5 - Model results for a 22 cm x 22 cm RED stack at a residence time of 44 s (flow velocity of 0.5 cm·s⁻¹). NaCl concentration in river water for a) the single electrode configuration, b) the segmented electrode configuration at maximized power per segment, and c) the segmented electrode configuration at overall maximum power. NaCl concentration in seawater for d) the single electrode configuration, e) the segmented electrode configuration at maximized power per segment, and f) the segmented electrode configuration at overall maximum power. Difference between the electromotive force (emf) and the electrode potential (E-U in Eq. 4.4) for g) the single electrode configuration, h) the segmented electrode configuration at maximized power per segment, and i) the segmented electrode configuration at overall maximum power. Cell pair resistance for j) the single electrode configuration, k) the segmented electrode configuration at maximized power per segment, and l) the segmented electrode configuration at overall maximum power. Current density distribution for m) the single electrode configuration, n) the segmented electrode configuration at maximized power per segment, and o) the segmented electrode configuration at overall maximum power. The x-axis is the river water path and the y-axis is the seawater path. Note, the grid division in a single electrode configuration is only used to allow an easier comparison with a segmented electrode configuration.

123

Model of the individual segment contribution for different configurations at 44 s residence time
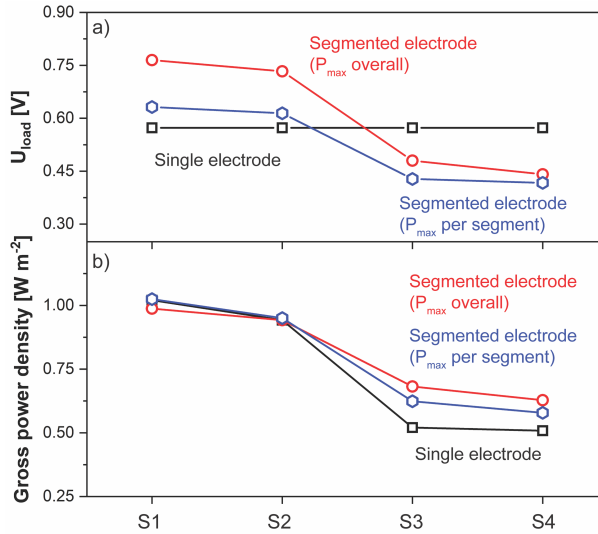
Figure S4.6 - Individual segment contribution (model) for a single electrode configuration, a segmented electrode configuration with maximized power per segment, and a segmented electrode configuration with overall maximum power, at 44 s residence time.

External load voltages
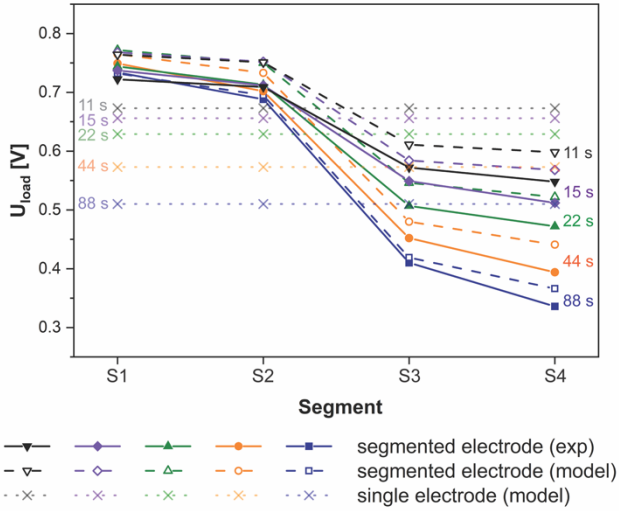
Figure S4.7 - External load voltage of the four electrode segments at maximum power density for the five investigated residence times. Full symbols and solid lines for experimental values are shown for a segmented electrode configuration. Empty symbols and dashed lines are given for the model values in a segmented electrode configuration. Crosses and dotted lines for the model values are displayed in a single electrode configuration.

References

[1]   U.N.F. Convention on Climate Change, Paris Agreement, (2015). https://unfccc.int/files/essential_background/convention/application/pdf/english_paris_agreem ent.pdf (accessed January 21, 2020).

[2]   W.J. Van Egmond, M. Saakes, S. Porada, T. Meuwissen, C.J.N. Buisman, H.V.M. Hamelers, The concentration gradient flow battery as electricity storage system: Technology potential and energy dissipation, J. Power Sources. (2016). doi:10.1016/j.jpowsour.2016.05.130.

[3]   J. Veerman, M. Saakes, S.J. Metz, G.J. Harmsen, Reverse electrodialysis: Performance of a stack with 50 cells on the mixing of sea and river water, J. Memb. Sci. (2009). doi:10.1016/j.memsci.2008.11.015.

[4]   J. Kuleszo, C. Kroeze, J. Post, B.M. Fekete, The potential of blue energy for reducing emissions of CO2 and non-CO2 greenhouse gases, J. Integr. Environ. Sci. (2010). doi:10.1080/19438151003680850.

[5]   R.E. Pattle, Production of electric power by mixing fresh and salt water in the hydroelectric pile, Nature. (1954). doi:10.1038/174660a0.

[6]   R.E. Lacey, Energy by reverse electrodialysis, Ocean Eng. 7 (2005) 1–47. doi:10.1016/0029-8018(80)90030-x.

[7]   E. Güler, W. van Baak, M. Saakes, K. Nijmeijer, Monovalent-ion-selective membranes for reverse electrodialysis, J. Memb. Sci. (2014). doi:10.1016/j.memsci.2013.12.054.

[8]   H. Gao, B. Zhang, X. Tong, Y. Chen, Monovalent-anion selective and antifouling polyelectrolytes multilayer anion exchange membrane for reverse electrodialysis, J. Memb. Sci. (2018). doi:10.1016/j.memsci.2018.09.035.

[9]   X.L. Wang, M. Wang, Y.X. Jia, B.B. Wang, Surface Modification of Anion Exchange Membrane by Covalent Grafting for Imparting Permselectivity between Specific Anions, Electrochim. Acta. (2015). doi:10.1016/j.electacta.2015.06.115.

[10]   D.A. Vermaas, M. Saakes, K. Nijmeijer, Power generation using profiled membranes in reverse electrodialysis, J. Memb. Sci. (2011). doi:10.1016/j.memsci.2011.09.043.

[11]   D.A. Vermaas, M. Saakes, K. Nijmeijer, Early detection of preferential channeling in reverse electrodialysis, Electrochim. Acta. (2014). doi:10.1016/j.electacta.2013.11.094.

[12]   Z. He, X. Gao, Y. Zhang, Y. Wang, J. Wang, Revised spacer design to improve hydrodynamics and anti-fouling behavior in reverse electrodialysis processes, Desalin. Water Treat. (2016). doi:10.1080/19443994.2016.1186569.

[13]   J. Moreno, N. de Hart, M. Saakes, K. Nijmeijer, CO 2 saturated water as two-phase flow for fouling control in reverse electrodialysis, Water Res. (2017). doi:10.1016/j.watres.2017.08.015.

[14]   E.J. Bodner, M. Saakes, T. Sleutels, C.J.N. Buisman, H.V.M. Hamelers, The RED Fouling Monitor: A novel tool for fouling analysis, J. Memb. Sci. (2019). doi:10.1016/j.memsci.2018.10.059.

[15]   D. Pintossi, M. Saakes, Z. Borneman, K. Nijmeijer, Electrochemical impedance spectroscopy of a reverse electrodialysis stack: A new approach to monitoring fouling and cleaning, J. Power Sources. 444 (2019) 227302. doi:10.1016/j.jpowsour.2019.227302.

4

[16]   D.A. Vermaas, M. Saakes, K. Nijmeijer, Doubled power density from salinity gradients at reduced intermembrane distance, Environ. Sci. Technol. (2011). doi:10.1021/es2012758.

[17]   S. Pawlowski, T. Rijnaarts, M. Saakes, K. Nijmeijer, J.G. Crespo, S. Velizarov, Improved fluid mixing and power density in reverse electrodialysis stacks with chevron-profiled membranes, J. Memb. Sci. (2017). doi:10.1016/j.memsci.2017.03.003.

[18]   I. Choi, J.Y. Han, S.J. Yoo, D. Henkensmeier, J.Y. Kim, S.Y. Lee, J. Han, S.W. Nam, H.J. Kim, J.H. Jang, Experimental investigation of operating parameters in power generation by lab-scale reverse electro-dialysis (RED), Bull. Korean Chem. Soc. (2016). doi:10.1002/bkcs.10810.

[19]   J. Moreno, S. Grasman, R. van Engelen, K. Nijmeijer, Up-scaling reverse electrodialysis, Environ. Sci. Technol. (2018). doi:10.1021/acs.est.8b01886.

[20]   J. Veerman, J.W. Post, M. Saakes, S.J. Metz, G.J. Harmsen, Reducing power losses caused by ionic shortcut currents in reverse electrodialysis stacks by a validated model, J. Memb. Sci. (2008). doi:10.1016/j.memsci.2007.11.032.

[21]   J. Veerman, M. Saakes, S.J. Metz, G.J. Harmsen, Reverse electrodialysis: A validated process model for design and optimization, Chem. Eng. J. 166 (2011) 256–268. doi:10.1016/j.cej.2010.10.071.

[22]   D.A. Vermaas, J. Veerman, N.Y. Yip, M. Elimelech, M. Saakes, K. Nijmeijer, High efficiency in energy generation from salinity gradients with reverse electrodialysis, ACS Sustain. Chem. Eng. (2013). doi:10.1021/sc400150w.

[23]   M. Ciofalo, M. La Cerva, M. Di Liberto, L. Gurreri, A. Cipollina, G. Micale, Optimization of net power density in Reverse Electrodialysis, Energy. 181 (2019) 576–588. doi:10.1016/j.energy.2019.05.183.

[24]   M. Tedesco, A. Cipollina, A. Tamburini, W. van Baak, G. Micale, Modelling the Reverse ElectroDialysis process with seawater and concentrated brines, Desalin. Water Treat. 49 (2012) 404–424. doi:10.1080/19443994.2012.699355.

[25]   J.W. Post, C.H. Goeting, J. Valk, S. Goinga, J. Veerman, H.V.M. Hamelers, P.J.F.M. Hack, Towards implementation of reverse electrodialysis for power generation from salinity gradients, Desalin. Water Treat. 16 (2010) 182–193. doi:10.5004/dwt.2010.1093.

[26]   M. Tedesco, A. Cipollina, A. Tamburini, G. Micale, Towards 1 kW power production in a reverse electrodialysis pilot plant with saline waters and concentrated brines, J. Memb. Sci. 522 (2017) 226–236. doi:10.1016/j.memsci.2016.09.015.

[27]   A. Daniilidis, R. Herber, D.A. Vermaas, Upscale potential and financial feasibility of a reverse electrodialysis power plant, Appl. Energy. (2014). doi:10.1016/j.apenergy.2013.12.066.

[28]   J. Veerman, M. Saakes, S.J. Metz, G.J. Harmsen, Electrical power from sea and river water by reverse electrodialysis: A first step from the laboratory to a real power plant, Environ. Sci. Technol. (2010). doi:10.1021/es1009345.

[29]   D.A. Vermaas, D. Kunteng, M. Saakes, K. Nijmeijer, Fouling in reverse electrodialysis under natural conditions, Water Res. (2013). doi:10.1016/j.watres.2012.11.053.

[30]   A.M. Weiner, R.K. McGovern, J.H. Lienhard V., A new reverse electrodialysis design strategy which significantly reduces the levelized cost of electricity, J. Memb. Sci. 493 (2015) 605–614. doi:10.1016/j.memsci.2015.05.058.

4

[31]   M. Geske, M. Heuer, G. Heideck, Z.A. Styczynski, Current density distribution mapping in PEM fuel cells as an instrument for operational measurements, Energies. (2010). doi:10.3390/en3040770.

[32]   M. Noponen, T. Mennola, M. Mikkola, T. Hottinen, P. Lund, Measurement of current distribution in a free-breathing PEMFC, in: J. Power Sources, 2002. doi:10.1016/S0378-7753(01)01063-1.

[33]   J.T. Clement, D.S. Aaron, M.M. Mench, In situ localized current distribution measurements in all-vanadium redox flow batteries, J. Electrochem. Soc. (2016). doi:10.1149/2.0241601jes.

[34]   A. Bhattarai, N. Wai, R. Schweiss, A. Whitehead, G.G. Scherer, P.C. Ghimire, T.D. Nguyen, H.H. Hng, Study of flow behavior in all-vanadium redox flow battery using spatially resolved voltage distribution, J. Power Sources. (2017). doi:10.1016/j.jpowsour.2017.06.039.

[35]   D. Tvrzník, Effect of electrode area on demineralization performance and the distribution of current density in an industrial-scale electrodialysis stack, Desalination. (2017). doi:10.1016/j.desal.2017.03.002.

[36]   G. Doornbusch, H. Swart, M. Tedesco, J. Post, Z. Borneman, K. Nijmeijer, Current utilization in electrodialysis: Electrode segmentation as alternative for multistaging, Desalination. 480 (2020) 114243. doi:10.1016/j.desal.2019.114243.

[37]   X. Ge, X. Wang, M. Zhang, S. Seetharaman, Correlation and prediction of activity and osmotic coefficients of aqueous electrolytes at 298.15 K by the modified TCPC model, J. Chem. Eng. Data. (2007). doi:10.1021/je060451k.

[38]   J. Moreno, E. Slouwerhof, D.A. Vermaas, M. Saakes, K. Nijmeijer, The Breathing Cell: Cyclic Intermembrane Distance Variation in Reverse Electrodialysis, Environ. Sci. Technol. (2016). doi:10.1021/acs.est.6b02668.

[39]   J. Moreno, Private communication, 2019.

[40]   J. Veerman, R.M. de Jong, M. Saakes, S.J. Metz, G.J. Harmsen, Reverse electrodialysis: Comparison of six commercial membrane pairs on the thermodynamic efficiency and power density, J. Memb. Sci. (2009). doi:10.1016/j.memsci.2009.05.047.

[41]   M.L. La Cerva, M. Di Liberto, L. Gurreri, A. Tamburini, A. Cipollina, G. Micale, M. Ciofalo, Coupling CFD with a one-dimensional model to predict the performance of reverse electrodialysis stacks, J. Memb. Sci. 541 (2017) 595–610. doi:10.1016/j.memsci.2017.07.030.

[42]   D.A. Vermaas, D. Kunteng, J. Veerman, M. Saakes, K. Nijmeijer, Periodic feedwater reversal and air sparging as antifouling strategies in reverse electrodialysis, Environ. Sci. Technol. (2014). doi:10.1021/es4045456.

[43]   P. Długołecki, K. Nymeijer, S. Metz, M. Wessling, Current status of ion exchange membranes for power generation from salinity gradients, J. Memb. Sci. (2008). doi:10.1016/j.memsci.2008.03.037.

[44]   J.A.W. Van Engelen, Composite membranes, U.S. 9,713,792, 2017.

4

4

Chapter 5

Influence of sulfate on anion exchange membranes in reverse electrodialysis

Abstract

Reverse electrodialysis (RED) is a technology producing renewable energy from the mixing of river and seawater. In natural salinity gradients, multivalent ions are present, which lead to a reduced RED power output. Transport of multivalent ions against the concentration gradient and their trapping inside the membranes leads to a lower driving force and increased membrane resistance. The present work focuses on the effect of sulfate ions on anion exchange membranes in RED. A monovalent ion selective membrane ability to retain a higher open circuit voltage is offset by the higher resistance in the presence of sulfate, leading to losses in normalized power outputs (- 25 %) comparable to a standard grade membrane. Longer term experiments revealed that membrane resistance increases over time. This study highlights the need to address uphill transport, resistance increase, and decreased permselectivity of anion exchange membranes in presence of multivalent ions.

5

5.1 Introduction

To reduce the impact of global warming and climate change, reducing greenhouse gas emission is a key target. To achieve this, clean energy sources are essential. One emerging renewable energy source is salinity gradient energy, which is the generation of electricity from the controlled mixing of solutions with different salt contents [1]. To harvest salinity gradient energy, reverse electrodialysis (RED) is a promising technology [2]. Salinity gradients naturally occur where rivers meet the sea, but artificial sources such as desalination brines were also investigated [3–5]. Alternative applications of RED include energy storage systems and waste heat engines based on thermolytic salt gradients [6–11]. In RED, anion exchange membranes (AEMs) and cation exchange membranes (CEMs) are stacked alternately to create feedwater channels where the high and low concentration solutions flow [12]. The concentration gradient across each membrane generates a voltage, which is the electromotive force to drive a current through the stack [13]. To power an external load, redox reactions at the two ends of the stack convert the ionic current flowing through the membranes into an electrical current (Figure 5.1) [14].
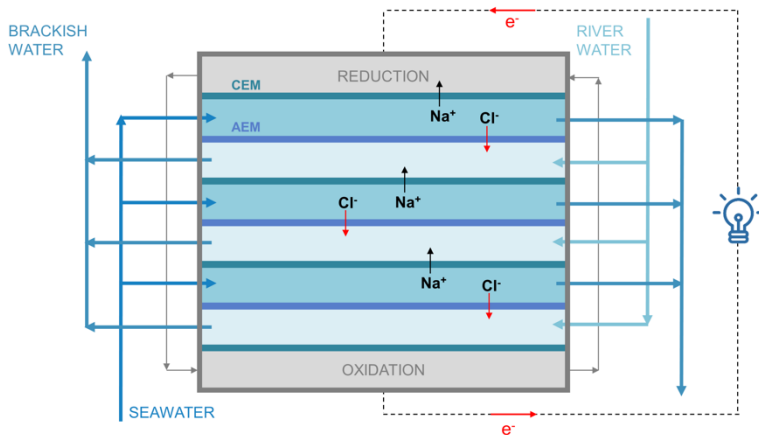
Figure 5.1 Schematic representation of a reverse electrodialysis stack. The repeating unit consists of a CEM, seawater compartment (with spacer), an AEM, and a river water compartment (with spacer).

When harvesting energy from natural salinity gradients, the power output of RED depends on the extent of the salinity gradient and the composition of the feedwaters. Clay particles, multivalent ions, natural organic matter, and micro-organisms in the feedwaters induce negative interactions with the membranes and clogging of the channels [15]. These interactions are referred to as fouling and cause the power generated by the RED stack to decrease over time. In particular, multivalent ions present a significant challenge because

they affect power generation by simultaneously decreasing the available electromotive force and increasing the membrane resistance. The first effect results from uphill transport of multivalent ions from the river to the seawater side, while the second results from trapping of multivalent ions inside the membranes (Figure S5.1).

Uphill transport results from the different electromotive force for monovalent and multivalent ions [16,17]. These two gradients act like DC generators connected in parallel [18]. The generator with the highest voltage spends energy to charge the one with the lowest voltage until they reach an equilibrium. Inside the RED stack, this means that the monovalent ion potential is decreased to increase the extent of the multivalent ion electromotive force. This transport is electroneutral, with two monovalent ions exchanged for each divalent ion. Therefore, no net current is produced and no energy is harvested in the uphill transport process [18]. The net result is a lower available electromotive force.

In addition to the lower voltage, multivalent ions also negatively affect the membrane properties. A multivalent ion entering an ion exchange membrane (IEM) may (1) be transported through the membrane, (2) bind to a single fixed charge group, or (3) bind to multiple fixed charge groups in the membrane (Figure S5.1b). If (1) occurs, the electrical resistance for multivalent ions transport is higher than for monovalent ions, therefore a higher ohmic drop is measured. If (2) happens, the multivalent ion reverses the charge of the fixed group and decreases the ion exchange capacity of the membrane, which in turn decreases its permselectivity and increases its resistance [19]. If (3) takes place, the multivalent ion neutralizes two fixed charged groups in the membrane and is trapped, causing a higher membrane resistance over time due to the lower ion exchange capacity of the membrane and the decreased free volume available for transport of other ions [20]. Studies on the effects of multivalent ions on RED performance and strategies to mitigate them focused mainly on cations, i.e. mixtures of multivalent cations and anions [16,18] or on multivalent cations [21,22]. The lack of focus on multivalent anions was justified by the assumption that the negative effect of multivalent anions is limited due to the smaller hydrated radii of multivalent anions and the hypothesized presence of sulfate as a monovalent species ($NaSO_4^-$) [18,22]. However, Rijnaarts et al. recently reported a study on AEM fouling in natural conditions [23]. Their results prove that organic fouling alone cannot justify the measured loss in power density, thus highlighting the need to investigate the negative impact of other forms of fouling on AEMs, including multivalent anions.

This work thus investigates and elucidates the effect of sulfate on AEMs in RED. Testing of standard grade and monovalent ion selective membranes was carried out with different sulfate fractions in the feedwaters. Stack and membrane characterizations were used to

quantify the impact of sulfate on the open circuit voltage, electrical resistance, and power output. The results of this systematic study of the effect of multivalent anions on AEMs in RED contribute to (1) quantifying the differences between fouling due to multivalent anions and cations, (2) understanding fouling in natural conditions, and (3) guiding future AEM development.

5.2 Materials and methods

5.2.1 Theory

5.2.1.1 Open circuit voltage and uphill transport theory

The open circuit voltage (OCV) is the voltage measured at the electrodes of a RED stack when no current is flowing through it. In the case of a NaCl gradient, it can be evaluated with the modified Nernst equation [24]:

$$E = \alpha_{CEM} \frac{RT}{zF} ln \left(\frac{\gamma_{SW,Na^+} c_{SW,Na^+}}{\gamma_{RW,Na^+} c_{RW,Na^+}} \right) + \alpha_{AEM} \frac{RT}{zF} ln \left(\frac{\gamma_{SW,Cl^-} c_{SW,Cl^-}}{\gamma_{RW,Cl^-} c_{RW,Cl^-}} \right)$$
$$= 2\alpha_{avg} \frac{RT}{zF} ln \left(\frac{\gamma_{SW,NaCl} c_{SW,NaCl}}{\gamma_{RW,NaCl} c_{RW,NaCl}} \right)$$

(Eq. 5.1)

Where E is the electromotive force [V], α_{CEM} is the permselectivity of the cation exchange membrane (CEM) [-], α_{AEM} is the permselectivity of the anion exchange membrane (AEM) [-], R is the universal gas constant [J mol^{-1} K^{-1}], T is the absolute temperature [K], z is the valence of the ions [-], F is the Faraday constant [C mol^{-1}], γ is the molar activity coefficient, c is the molar concentration [mol L^{-1}], and α_{avg} is the average membrane permselectivity [-].

When considering mixtures of monovalent and multivalent ions, like chloride and sulfate, the electromotive force for chloride is higher than that of sulfate, because of the higher valence and lower activity coefficients of sulfate than of chloride. The difference between the two potentials acts as a driving force to move sulfate from river to sea (against the concentration gradient, hence uphill), while moving chloride from sea to river (downhill). In this process, the gradient of sulfate increases and so does its potential, while the opposite happens for chloride. Such a process, known as uphill transport, goes on until the two potentials are equilibrated and there is no driving force available for the exchange. The result is a lower OCV than the one predicted for the chloride gradient alone. Vermaas et al. presented a model to evaluate the open circuit voltage after uphill transport for perfectly permselective membranes in batch conditions [18]. The model developed by Vermaas et al. was used in this work as reported, only applied to multivalent anions.

It consists of two water compartments separated by an anion exchange membrane (Vermaas presented the case with a cation exchange membrane). On one side, a high concentration salt mixture is present. On the other side, there is a low concentration salt mixture. The considered salts for uphill transport across an AEM are sodium chloride and sodium sulfate.

The potential of the monovalent (e.g. chloride) and multivalent (e.g. sulfate) salts can be described by the modified Nernst equation (membrane permselectivity is assumed to be 100 %):

$$E_{Cl^-} = \frac{RT}{F} ln \left(\frac{\gamma_{SW,Cl^-} \, c_{SW,Cl^-}}{\gamma_{RW,Cl^-} \, c_{RW,Cl^-}} \right) \qquad \text{(Eq. 5.2)}$$

$$E_{SO_4^{2-}} = \frac{RT}{2F} ln \left(\frac{\gamma_{SW,SO_4^{2-}} \, c_{SW,SO_4^{2-}}}{\gamma_{RW,SO_4^{2-}} \, c_{RW,SO_4^{2-}}} \right) \qquad \text{(Eq. 5.3)}$$

Uphill transport terminates when the two potentials are equilibrated, which yields the following condition for the concentration of the ions on both sides:

$$\left(\frac{\gamma_{SW,Cl^-} \, c_{SW,Cl^-}}{\gamma_{RW,Cl^-} \, c_{RW,Cl^-}} \right) = \left(\frac{\gamma_{SW,SO_4^{2-}} \, c_{SW,SO_4^{2-}}}{\gamma_{RW,SO_4^{2-}} \, c_{RW,SO_4^{2-}}} \right)^{\frac{1}{2}} \qquad \text{(Eq. 5.4)}$$

The molar amount of sulfate travelling uphill, $J_{up,eq}$ [mol L^{-1}] can be found by solving the following equation, derived from S3:

$$\left(\frac{\gamma_{SW,Cl^-} \, (c^0_{SW,Cl^-} - 2J_{up})}{\gamma_{RW,Cl^-} \, (c^0_{RW,Cl^-} + 2J_{up})} \right) = \left(\frac{\gamma_{SW,SO_4^{2-}} \, (c^0_{SW,SO_4^{2-}} + J_{up})}{\gamma_{RW,SO_4^{2-}} \, (c^0_{RW,SO_4^{2-}} - J_{up})} \right)^{\frac{1}{2}} \qquad \text{(Eq. 5.5)}$$

The activity coefficients are assumed to be constant (for small changes in concentration). Figure S5.2 shows the graphical solution of equation S4. At equilibrium, the open circuit voltage for monovalent and multivalent ions is equal to:

$$\begin{aligned} OCV = E_{Cl^-} = E_{SO_4^{2-}} &= \frac{RT}{F} ln \left(\frac{\gamma_{SW,Cl^-} \, (c^0_{SW,Cl^-} - 2J_{up,eq})}{\gamma_{RW,Cl^-} \, (c^0_{RW,Cl^-} + 2J_{up,eq})} \right) \\ &= \frac{RT}{2F} ln \left(\frac{\gamma_{SW,SO_4^{2-}} \, (c^0_{SW,SO_4^{2-}} + J_{up,eq})}{\gamma_{RW,SO_4^{2-}} \, (c^0_{RW,SO_4^{2-}} - J_{up,eq})} \right) \end{aligned} \qquad \text{(Eq. 5.6)}$$

5.2.1.2 Stack electrical resistance theory

The ohmic component of the stack electrical resistance can be described by the following equation [25]:

$$R_{stack} = R_{el} + \frac{N}{A}\left(R_{CEM} + R_{AEM} + \frac{1}{f}\frac{d_{RW}}{\kappa_{RW}} + \frac{1}{f}\frac{d_{SW}}{\kappa_{SW}}\right) \qquad \text{(Eq. 5.7)}$$

Where R_{stack} is the stack electrical resistance [Ω], R_{el} is the electrode resistance [Ω] (less relevant for increasing number of cell pairs), N is the number of cell pairs [-], A is the active membrane area [cm^2], R_{CEM} and R_{AEM} are the areal resistance of CEM and AEM [Ω cm^2], f is the obstruction factor [-] accounting for the presence of non-conductive spacers in the feedwater channels, d is the compartment thickness [cm], and κ is the conductivity of the feedwaters [S cm^{-1}]. It is worth noting that substituting equimolar amounts of monovalent salt in the feedwater with multivalent salt will have a detrimental effect on the membrane resistance, but at the same time it will result in increased water conductivity, which is beneficial for the overall stack resistance.

5.2.1.3 Gross power density
The gross power density of a RED stack is calculated as the ratio between the maximum power point and the total membrane area of the stack. The maximum power point is achieved when the stack is working at half of the OCV, powering a load which is equal to the stack electrical resistance [26]. Therefore, the gross power density is given by:

$$P_{dens,gross} = \frac{1}{2NA}\frac{OCV^2}{4R_{stack}} \qquad \text{(Eq. 5.8)}$$

Where P_{dens} is the gross power density [W m^{-2}] and $2NA$ is the total membrane area [m^2].

5.2.2 Experimental procedures
5.2.2.1 RED stack
Cross-flow RED stacks (REDstack BV, the Netherlands) with an active area of 10 x 10 cm^2 were used in the experiments. The stack end-plates embedded mesh electrodes (9.8 x 9.8 cm^2) made of platinized titanium (MAGNETO Special Anodes BV, the Netherlands). Spacers with a woven netting (Saati PES 740/53, Saati S.p.A. Italy) and integrated silicone rubber gaskets (DEUKUM GmbH, Germany) were used to accommodate the feedwaters and seal the compartments. All stacks examined in the present study consisted of five cell pairs (five AEM and CEM pairs) plus an extra CEM to seal the electrolyte compartment. For the stack assembly, the chosen AEMs were: Fujifilm AEM type I and type 10 (FUJIFILM Manufacturing Europe BV, the Netherlands), Neosepta AMX-fg and the monovalent ion selective Neosepta ACS (ASTOM Corp. Ltd., Japan). Neosepta CMX-fg (ASTOM Corp. Ltd., Japan) was used as CEM to seal the electrolyte compartment of all stacks. The main properties of the membranes are compared in Table 5.1.

Table 5.1 Measured membrane properties of the AEM used in the study.

Membrane	Grade	Electrical resistance (0.5 M NaCl)	Permselectivity (0.1 / 0.5 M NaCl)	Water content
Fujifilm AEM type I	Standard	Low (1.46 ± 0.11 Ω cm^2)	Low (88.7 %)	High (50 %)
Fujifilm AEM type 10	Standard	Medium (1.89 ± 0.05 Ω cm^2)	Medium (93.2 %)	High (41 %)
Neosepta ACS	Monovalent ion selective	High (4.49 ± 0.12 Ω cm^2)	Medium (94.3 %)	Low (26 %)
Neosepta AMX-fg	Standard	High (3.82 ± 0.15 Ω cm^2)	High (95.5 %)	Low (21 %)
Neosepta CMX-fg	Standard	High (3.14 ± 0.11 Ω cm^2)	High (99.0 %)	Low (32 %)

5.2.2.2 Feedwaters

Sodium chloride (NaCl, 99.5 % purity, ESCO, the Netherlands) solutions with 17 mM and 508 mM concentrations were used as artificial river water and seawater, respectively. To evaluate the effect of multivalent anions on AEMs in RED, sodium sulfate ($\geq$ 99 % purity, VWR Chemicals, Belgium) was added to the feedwaters in different configurations. The scenarios differed based on to which feedwater the sulfate was added (river, sea, or both) and to the fraction of sulfate (10, 25, and 50 mol %). Table 5.2 illustrates the sequence of feedwaters used in each stack experiment. The sulfate fractions were chosen to resemble the amounts found in natural salinity gradients. Rijnaarts et al. reported 11 mol. % sulfate in seawater (Wadden Sea, the Netherlands) and 30 mol. % sulfate in river water (IJsselmeer, the Netherlands) [23]. The choice of substituting equimolar amounts of NaCl with Na_2SO_4 is to maintain the extent of the chloride gradient constant when adding multivalent ions on both sides. Table 5.3 shows the ionic radii, hydration free energy, and pK_a for selected monovalent and multivalent ions.

Table 5.2 Sequence of the feedwaters compositions for RED stack experiments. The sulfate fraction x was equal to 10, 25, and 50 mol. % in three sets of experiments.

Time [h]		0 – 1	1 – 2.5	2.5 – 3.5	3.5 – 5	5 – 6	6 – 7.5	7.5 – 8.5
Sea	NaCl [mol. %]	100	100 - x	100	100	100	100 – x	100
	Na₂SO₄ [mol. %]	0	x	0	0	0	x	0
River	NaCl [mol. %]	100	100 – x	100	100 – x	100	100	100
	Na₂SO₄ [mol. %]	0	x	0	x	0	0	0

Table 5.3 Hydrated radii, hydration free energy and pK_a of selected monovalent and multivalent ions.

Ion	Ionic radius [nm][27]	Hydrated radius [nm][27]	Hydration free energy [kJ mol^{-1}][27]	pK_a [-][28]
Cl^-	0.181	0.332	-363	
SO_4^{2-}	0.258	0.379	-1145	1.99 (2nd)
PO_3^{2+}	0.238	0.339	(-)	2.16 (1st), 7.21 (2nd), 12.32 (3rd)
CO_3^{2-}	0.156	(-)	(-)	6.4 (1st), 10.3 (2nd)
Na^+	0.117	0.358	-365	14.8
Ca^{2+}	0.100	0.412	-1504	12.6
Mg^{2+}	0.072	0.428	-1828	11.4

The electrode rinse solution was a mixture of 0.05 M potassium hexacyanoferrate(II) / 0.05 M potassium hexacyanoferrate(III) (both ≥ 96 % purity, VWR Chemicals, Belgium). Sodium chloride (0.25 M) was added as a supporting electrolyte. Experiments were performed in the laboratory at 23.0 ± 0.5 °C. Temperature and conductivity of the artificial feedwaters were measuredbefore each experiment. The flow velocity was chosen to be 1 cm s^{-1}. Fresh feedwaters were continuously supplied to the RED stacks, in a single-pass configuration, while the electrolyte was recirculated though the electrode compartments in a closed loop. For the long term ED experiment, the feedwaters (initially 0.1 M 100

mol. % NaCl, then 50 mol. % Na_2SO_4) were also recirculated. Peristaltic pumps (Masterflex L/S Digital drive, Cole-Palmer, USA) were used to pump the liquids through the hydraulic circuits. A diaphragm pressure control valve (KNF FDV 30, KNF-Verder BV, the Netherlands) was used to keep the electrolyte at 0.3 bar overpressure to avoid bulging of the water compartments.

5.2.2.3 Stack measurements

All electrochemical measurements at the stack level were performed with an Iviumstat (IVIUM Technologies BV, the Netherlands). The IviumSoft Electrochemistry Software was used to control the potentiostat. For RED experiments, electrochemical measurements were continuously repeated in a loop for 8.5 h. A loop cycle consisted of one constant current step (10 A m^{-2}, in galvanostatic mode) and a chronopotentiometric series consisting of four current steps separated by open circuit steps (7.5, 10, 12.5 and 15 A m^{-2}), in galvanostatic mode. The duration of one loop cycle was 15 min (7.5 min constant current). The effluents from the sea and river water compartment were sampled during every other constant current step. The concentration of anions was measured with ion chromatography (IC) (Metrohm Compact IC Flex 930, Metrohm Nederland, the Netherlands). The open circuit steps at the beginning of each chronopotentiometric series was used to evaluate the open circuit voltage (OCV). Stack electrical resistance was evaluated from the slope of the I-V curve obtained from the chronopotentiometric series, no blank correction was performed. Figure S5.3 illustrates how the results from the time series of chronopotentiometry and different feedwaters were used to obtain the normalized parameters vs. sulfate fraction plots. For the ED experiment, a loop cycle consisted of one constant current step (10 A m^{-2}, in galvanostatic mode) and two chronopotentiometric series consisting of four current steps separated by open circuit steps (7.5, 10, 12.5 and 15 A m^{-2}), in galvanostatic mode. The duration of one loop cycle was 45 min (30 min constant current). Matlab software (The MathWorks Inc., USA) was used for data analysis. Matlab scripts were developed for the specific purpose of processing the data from the chronopotentiometric series. For ease of comparison, the results have been normalized to the values measured with clean waters (before introducing multivalent anions in the feedwaters). Stack experiments were performed at least in duplicate (except ED experiments).

5.2.2.4 Membrane characterizations

The membrane characterizations (water uptake, permselectivity, and membrane resistance) were performed based on procedures available in the literature [26]. For permselectivity measurement in the presence of multivalent ions, the solution concentrations and voltages used in the experiment and calculations were the ones after uphill transport (as predicted by the model; further details of the compositions in Table S5.3). Equilibration of the membranes prior to permselectivity measurements was carried out in the 0.1 M solution containing amounts of sodium chloride and sulfate corresponding to the equilibrium after uphill transport (further details of the compositions in Table S5.3). The composition of the solutions for the permselectivity measurement was chosen to avoid uphill transport as that would introduce an undesired potential loss, which would lead to a wrong measurement. Electrical resistance and permselectivity measurements were performed with an Autolab PGSTAT30 (Metrohm Nederland, the Netherlands). The NOVA 2.1.3 software was used to control the potentiostat. Membrane characterizations were performed at least in triplicate.

5.3 Results and discussion

To evaluate the impact of sulfate on RED performance, the following stack properties for four different membrane types in the presence or absence of sulfate were monitored: open circuit voltage (OCV), stack electrical resistance and gross power density. Additionally, the effect of sulfate ions on the membrane properties (electrical resistance and permselectivity) were investigated.

The four different AEM membranes used are Fujifilm type I (low electrical resistance, low permselectivity, high water content), Fujifilm type 10 (medium electrical resistance, medium permselectivity, high water content), Neosepta ACS (a monovalent ion selective membrane with a high electrical resistance, medium permselectivity, low water content), Neosepta AMX-fg (high electrical resistance, high permselectivity, low water content). These membranes are selected because they cover a broad range of the most essential properties relevant for power generation in RED. Details of the membranes are given in the experimental section (Table 5.1).

The experimental results are compared to a model calculating the OCV in the presence of multivalent ions in one or in both of the feedwaters (developed by Vermaas et al. and used as reported, further information in the materials and methods section) [18]. This model is based on the equilibration between the electromotive force of monovalent and multivalent

ions when increasing amounts of multivalent ions in the river water are exchanged for monovalent ions in the seawater.

5.3.1 Open circuit voltage and uphill transport

Figure 5.2 shows the normalized OCV as a function of the sulfate fraction (10, 25, and 50 mol. %) present in the feedwaters (both sides, river water only and seawater only), measured in a stack experiment. Table S5.1 in the supporting information reports the OCV values prior to normalization.
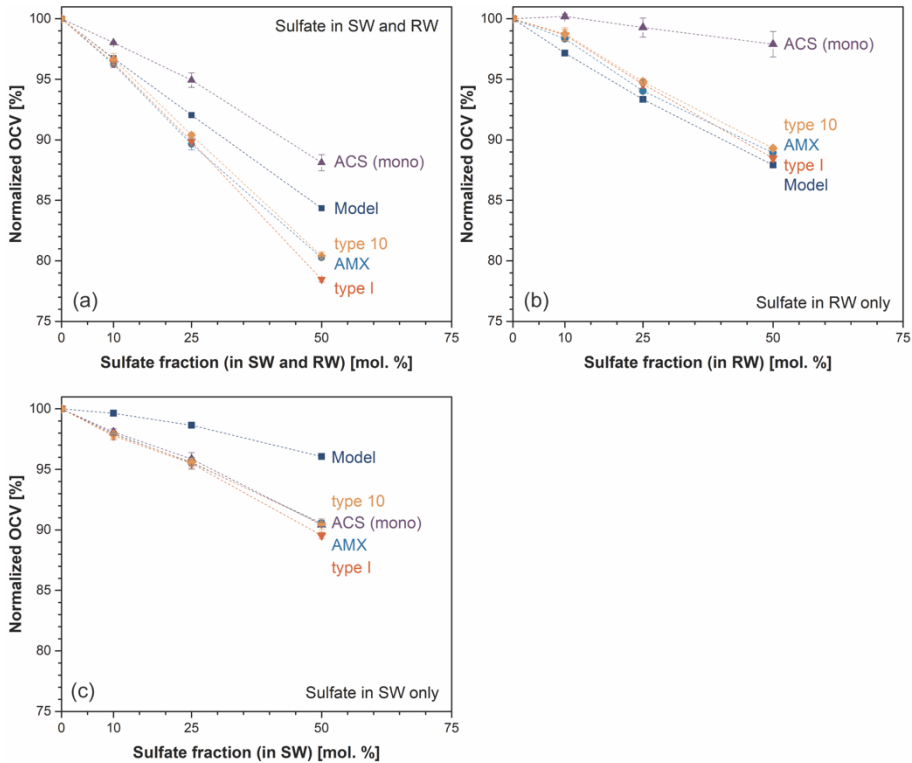
Figure 5.2 Normalized OCV versus sulfate fraction for the scenarios with (a) equal amounts of sulfate in both feedwaters, (b) sulfate present in the river water only, and (c) sulfate present in the seawater only. SW = seawater; RW = river water. Results have been normalized to the values measured with clean waters (before introducing multivalent anions in the feedwaters). All experiments were performed in duplicate with error bars illustrating the minimum and maximum points.

Figure 5.2a illustrates the results of the stack experiments with equivalent fractions of sulfate on both sides, river and seawater. The normalized OCV decreases for all

membranes in accordance with the model. The monovalent ion selective ACS membrane (high electrical resistance, medium permselectivity, and low water content) outperforms the model, while the standard grade membranes all exhibit similar losses of OCV and perform worse than the model, independent of their properties. The monovalent ion selective membrane ACS limits sulfate transport; therefore, uphill transport is hindered and the stack is able to operate at higher OCV than predicted by the model. Nevertheless, at increasing fractions of sulfate in the feedwaters, also ACS increasingly allows sulfate transport, leading to a decrease in normalized OCV, albeit over the full range less than for the other membranes. The deviation from the model of the standard grade membranes is attributed to a loss in permselectivity induced by the presence of sulfate ions. This explanation is supported by the membrane permselectivity measurements using mixtures of NaCl and Na_2SO_4 (Figure 5.3a, Table S5.2). The loss in permselectivity is larger for the type I (low electrical resistance, low permselectivity, and high water content), which is the membrane with the lowest starting permselectivity and the highest swelling degree. Similar results were reported for CEMs and multivalent cations by Rijnaarts et al. and Moreno et al. [21],[22]. Permselectivity and its decrease due to sulfate presence are not accounted for in the model, explaining the discrepancy between the model and the experimental results.

Figure 5.2b illustrates the scenario with sulfate ions only present in the river water. In this case uphill transport plays a role. The loss in normalized OCV is not as severe as for the scenario with sulfate ions on both sides, but quite significant though. The amount of sulfate ions that the membranes experience is lower due to the low absolute amount of sulfate ions in the river water. Therefore, the monovalent ion selective membrane is able to retain its full OCV, and the loss in permselectivity for the standard grade membranes is limited as well. It can be noted that the standard grade membrane data lie slightly above the model. This is the case because the predicted batch model OCV is attained at a very low sulfate ion fraction (Figure S5.2b in Supporting Information), which cannot be reached in the stack experiments since fresh solutions are continuously supplied. Despite this limitation, the model still provides a close estimation of the OCV with sulfate present in river water only.

The last scenario, with sulfate ions only present in the seawater, is visualized in Figure 5.2c. Unlike the other two scenarios, uphill transport of sulfate ions is not possible and the only species that are transported against their gradient are chloride ions. Nevertheless, the increase in OCV due to chloride uphill transport is balanced by the decreased chloride gradient. Thus, the overall effect is a reduced OCV at increasing fractions of sulfate for

5

all membranes. Membrane permselectivity decreases due to the large amount of sulfate ions present in the seawater, leading to deviations from the behavior predicted by the model. The loss of permselectivity observed at the stack level for Neosepta ACS seems to contradict the permselectivity values obtained at the membrane level (Figure 5.3a). This is explained by taking into account the slow access (diffusion limitation) of sulfate ions to the membrane, which are equilibrated at a low sulfate fraction (Table S5.3).

To further verify the occurrence of uphill transport, the outlet feedwater composition was analyzed. Figure 5.3b illustrates the results of the ion chromatography (IC) analyses.
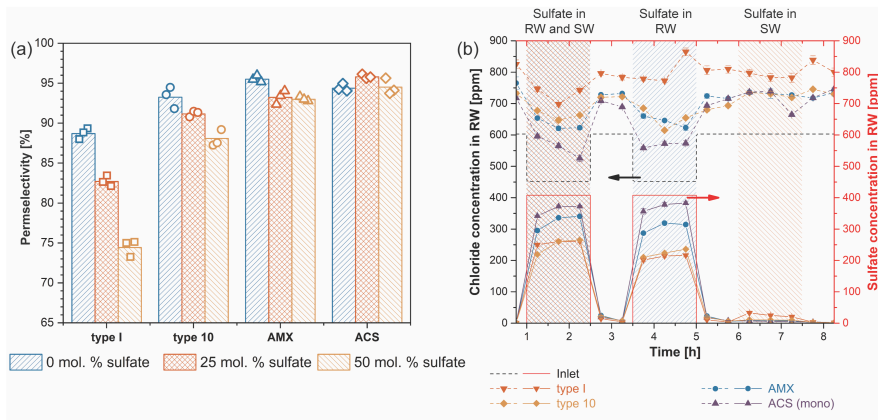
Figure 5.3 (a) apparent permselectivity of the four AEMs at a fraction of 0, 25, and 50 mol. % sulfate and the remaining part chloride ions, measured for a single membrane. Measurements were performed in triplicate, with error bars illustrating the minimum and maximum value. (b) In- and outlet chloride and sulfate concentrations in the river water during the constant current step for the stack experiments with 25 mol. % sulfate. The solid lines represent the sulfate concentrations while the dotted lines represent the chloride concentrations. The black and red line are the concentration of chloride and sulfate respectively supplied at the stack inlet (feed). The symbols represent the corresponding concentrations measured at the stack outlet for the different membranes. The low sulfate concentrations measured in the third scenario (sulfate in seawater) for the four membranes are significant compared to control samples. Experiments were performed in duplicate and each water samples was analyzed in duplicate, with error bars illustrating the minimum and maximum value.

The lower concentration of sulfate in the river water at the outlet than at the inlet during the constant current step confirms the movement of multivalent anions from river to sea. This is especially visible for the two membranes with lower permselectivity and higher water content (type I and type 10), as these are much more permeable for the bivalent sulfate ions than especially the monovalent ion selective ACS membrane, which keeps the highest river water sulfate concentration over the full duration of the process. Additionally,

144

in the third scenario (sulfate in seawater only), sulfate is found in the river water outlet, showing its transport downhill as a consequence of the applied current, which is carried by both chloride and sulfate, and the uphill transport of chloride.

5.3.2 Electrical resistance

Figure 5.4 and Figure 5.5 illustrate the membrane electrical resistance and the stack electrical resistance respectively measured in the presence of increasing fractions of sulfate in the feedwaters.
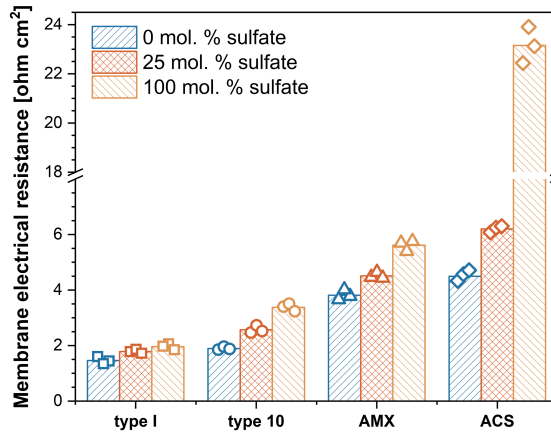
Figure 5.4 Membrane electrical resistance of the investigated AEMs in 100 mol. % sodium chloride (0.5 M), a mixture of 75 mol. % sodium chloride (0.375 M) and 25 mol. % sodium sulfate (0.125 M), and 100 mol. % sodium sulfate (0.5 M), measured in a six-compartment cell. Measurements were performed in triplicate, with error bars illustrating the minimum and maximum value

The transport selectivity for chloride over sulfate of an AEM is expressed as the ratio between its resistance measured in NaCl only and its resistance measured in Na_2SO_4 only.[22] The membrane electrical resistance increases for all AEMs in the presence of sulfate. The monovalent ion selective ACS exhibits a Cl^-/SO_4^{2-} selectivity equal to 5.15, thus confirming its preferential transport of monovalent ions, which is granted by its high crosslinking degree, allowing for size exclusion of multivalent ions. The standard grade membranes are more permeable to sulfate and their Cl^-/SO_4^{2-} selectivities range between 1.34 and 1.78, with type 10 (medium electrical resistance, medium permselectivity, and high water content) and type I (low electrical resistance, low permselectivity, and high water content) having a low selectivity due to their high water content (Table 5.1), while AMX (high electrical resistance, high permselectivity, and low water content) compensates its low water content with a high charge density [23].
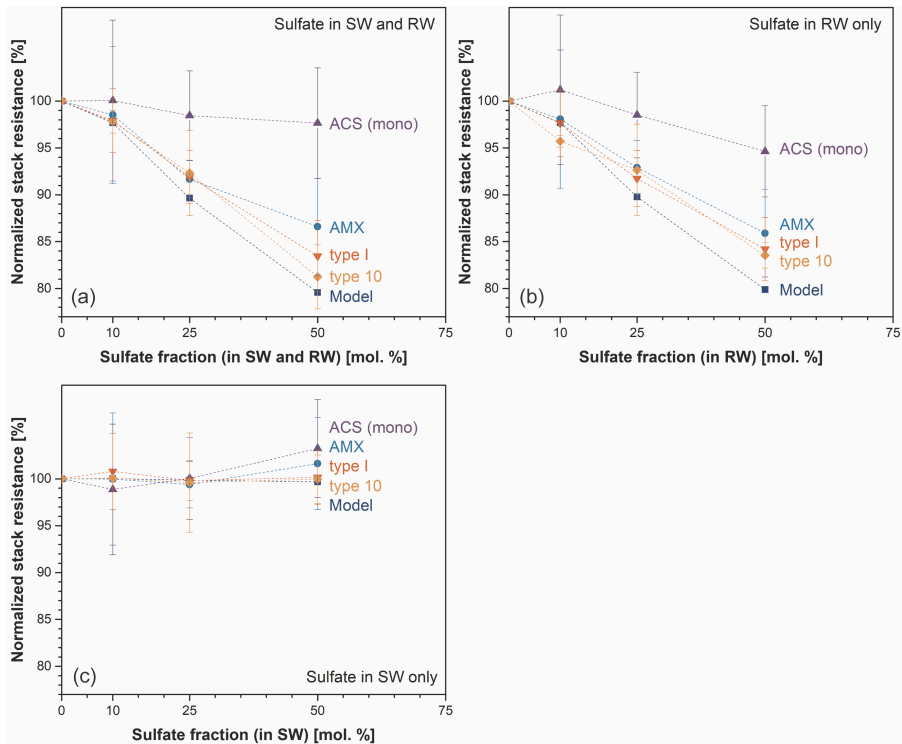
Figure 5.5 Normalized stack electrical resistance versus sulfate fraction (a) with sulfate in both feedwaters, (b) with sulfate present on the river side only, and (c) with sulfate present on the sea side only. SW = seawater; RW = river water. Results have been normalized to the values measured with clean waters (before introducing multivalent anions in the feedwaters). All experiments were performed in duplicate with error bars illustrating the minimum and maximum points.

The evolution of the stack electrical resistance (Figure 5.5, measured as the slope of the current-voltage plot, without blank correction) is consistent with the measurements at the membrane level. Figure 5.5a shows the scenario with sulfate present in both sea and river water. Although the overall stack resistance is decreasing due to the increased water conductivity and this is included in the model calculations, the experimental data in Figure 5.5 are positioned still well above the model values, showing an increased AEM resistance. The stack with the monovalent ion selective ACS has almost constant electrical resistance as it is designed to reduce sulfate transport. Hence, the increase in AEM resistance (Figure 5.3) balances the increased water conductivity. On the contrary, the standard grade membranes are more permeable to sulfate and are positioned slightly above

146

the model, with a small AEM electrical resistance increase, as measured at the membrane level (Figure 5.4).

Similar behavior is observed for Figure 5.5b, with sulfate in the river water only. In Figure 5.5c, with sulfate in the seawater only, there is no increase in the conductivity of the river water, which is the main component of the stack electrical resistance. Therefore, the effect of sulfate on the stack electrical resistance is less evident. Nevertheless, at high sulfate fractions, ACS (monovalent ion selective) still shows the highest resistance increase as it is designed to limit sulfate transport.

The negative effect of sulfate on the AEM resistance is limited compared to the effect of multivalent cations on CEMs [21,22] due to the smaller hydrated radius and hydration free energy of sulfate compared to magnesium and calcium (Table 5.3 in materials and methods). Comparing the results presented here with those of Moreno et al. for standard grade membranes, at the same molar fractions of multivalent ions (10 and 25 mol. %), the increase in electrical resistance for the CEMs compensates the increased electrical conductivity of the feedwaters, leading to an increased stack resistance. For the AEMs that is not the case, with an overall decrease in stack resistance despite the increased membrane resistance (Figure 5.4 and 5.5).

Figure 5.6 shows the evolution over time of the stack electrical resistance when exposing ACS or type 10 first to NaCl only, followed by 25 mol. % of sulfate on both sides and subsequently NaCl only again. When switching from NaCl to a mixture containing sulfate (at 1h in the plot), the stack electrical resistance drops initially due to the increased water conductivity, then it increases slowly due to the trapping of sulfate in the AEM. The opposite happens when switching back to waters with only NaCl (at 2h in the plot). This shows that the change in membrane resistance is not instantaneous due to limitations in ion transport rate, while the effect of water conductivity has an immediate effect on stack resistance. Interestingly, the evolution of stack resistance over time for the type 10 membrane (standard grade membrane) is different as the resistance initially drops due to the increased water conductivity and then plateaus (Figure 5.6), which is due to the faster transport of sulfate through the standard grade membrane. These results differ from the finding of Moreno et al. for CEMs exposed to magnesium, as the electrical resistance of the standard grade CEMs used in their study increases over time when exposed to magnesium [21]. The standard grade AEMs used in our study behave similarly to the multivalent ion permeable Fujifilm CEM T1 reported in the study of Moreno et al. due to the smaller hydrated radius and lower hydration energy of sulfate than magnesium (Table

5

5.3 in materials and methods) combined with the high water content (type I and 10) or charge density (AMX) of the standard grade AEMs used in our study.
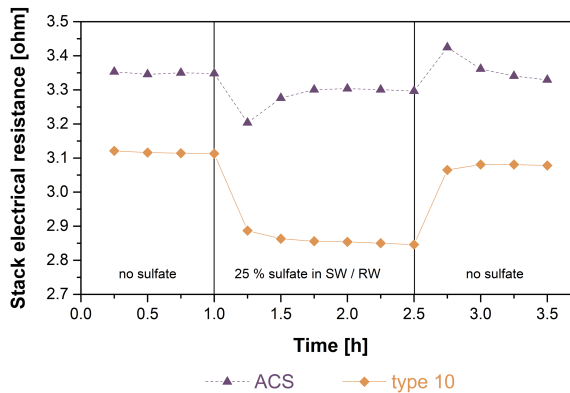
Figure 5.6 Electrical resistance of the stack with ACS (monovalent ion selective membrane) and type 10 (standard grade) in the transients from 100 mol. % NaCl to the mixture with 25 mol. % Na_2SO_4 and back to the 100 mol. % NaCl feedwaters. Data are reported for one experiment per membrane type.

This conclusion is also supported by the chloride over sulfate selectivity of the three standard grade AEMs investigated in our study, which is lower than 2 (which is comparable to the selectivity of sodium over magnesium of the multivalent ion permeable Fujifilm CEM T1 [22]). Such a low Cl^-/SO_4^{2-} selectivity implies that the standard grade membranes transport multivalent ions almost in equal amounts as the monovalent ions. Therefore, sulfate trapping is less likely, which leads to the stable electrical resistance for type 10 in Figure 5.6.

These different electrical resistance evolutions over time in the presence of multivalent anions or cations for AEMs and CEMs stem from the smaller hydrated radii and lower hydration energies of multivalent anions than cations [29], which make the multivalent anions easier to transport than multivalent cations. Nevertheless, multivalent anions are still larger than monovalent ones [30] and can be trapped inside the AEMs, covering the fixed membrane charges and causing an increase in electrical resistance. At the same time, multivalent anions are more difficult to selectively reject than their cationic counter parts since they span a smaller range of ionic radii and hydration energies (Table 5.3 in materials and methods) [31]. Epsztein et al. recently showed the role played by the ion hydration free energy in transport selectivity for ion exchange membranes [32]. The Cl^-/SO_4^{2-} selectivity of the monovalent ion selective Neosepta ACS is around 5, while the Neosepta CMS (monovalent ion selective CEM) exhibits a Na^+/Mg^{2+} selectivity of 34 [22,33].

While this benefits the standard grade AEMs in terms of limited electrical resistance increase in presence of multivalent ions, it is detrimental in terms of OCV loss.

Although the stack electrical resistance results reported above suggest that for standard grade membranes sulfate has a limited impact on stack resistance, these experiments were only conducted during one day. A longer experiment (11 days) was carried out to investigate the effect on the AEMs of longer exposure to sulfate. The results of this long-term experiment (Figure S5.4, Supporting Information) show that on the longer term, multivalent anions do have a negative impact on the resistance of both membranes, independent of the type and that monovalent ion selective membranes are even more severely affected than standard grade membranes. Considering the mechanisms presented in Figure S5.1b, the results from Figure S5.4 and Figure 5.6 show that sulfate trapping is relevant on longer term experiments, while on the short term only the monovalent-ion selective ACS experiences a reversible increase in electrical resistance and all membranes experience permselectivity loss.

5.3.3 Gross power density

Figure 5.7 shows the evolution of gross power density in RED with increasing sulfate fractions for all membranes and the three exposure scenarios. The normalized gross power density is based on the open circuit voltage and stack electrical resistance (Eq. 5.3).

Figure 5.7a shows the results for the scenario with sulfate in both sea and river water. For all membrane types and the model, the normalized power density decreases with increasing sulfate fraction because the OCV decreases in presence of sulfate, while the stack electrical resistance increases and both are detrimental for gross power density. The model predicts a smaller loss in power density than measured experimentally, as the experimental loss in membrane permselectivity in the presence of sulfate is not accounted for in the model. Remarkably, the monovalent ion selective ACS membrane does not outperform the standard grade membranes. Despite retaining a higher OCV in presence of sulfate, its large increase in electrical resistance due to sulfate trapping and limited sulfate transport lowers its performance to a level comparable to that of the standard grade membranes. Among the standard grade membranes, the type 10 membrane outperforms type I and AMX, especially at high sulfate fractions, thanks to its combination of intermediate resistance and permselectivity. The other standard grade membranes analyzed, type I and AMX, perform slightly worse than the type 10. Type I has the benefit of a low resistance thanks to its high water content, but its low permselectivity is reflected in a larger OCV loss in the presence of sulfate. AMX has a high permselectivity but also

a high electrical resistance. Since transport of sulfate through the AMX is possible, the OCV loss and high electrical resistance limit its gross power density in the presence of sulfate.
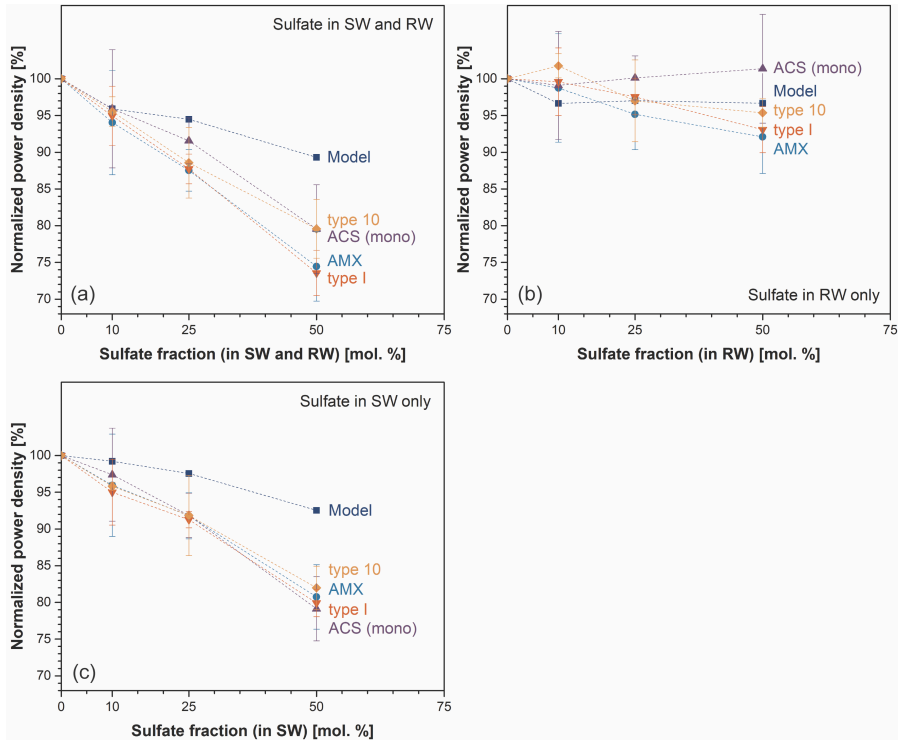
Figure 5.7 Normalized gross power density versus sulfate fraction for the scenario with (a) sulfate in both feedwaters, (b) sulfate present in the river water only, and (c) sulfate present in the seawater only. SW = seawater; RW = river water. Results have been normalized to the values measured with clean waters (before introducing multivalent anions in the feedwaters). All experiments were performed in duplicate with error bars illustrating the minimum and maximum points.

Figure 5.7b shows the results for the scenario with sulfate only in the river water. In this case, the decrease in normalized power density is far less pronounced because the OCV decreases in presence of sulfate in river water, but the stack electrical resistance also decreases, due to its increased conductivity, and that is beneficial for the gross power density. The monovalent ion selective ACS membrane performs better than the model and the standard grade membranes thanks to its fully retained OCV, especially at high sulfate fractions. Type 10 performs better than the type I and AMX membrane as it combines a smaller OCV loss (type I loses more than type 10) with a smaller increase in electrical

resistance (AMX increases more than type 10). Figure 5.7c illustrates the results of the scenario with sulfate only in the seawater. Here, again a steep decrease in normalized power density is observed for all membranes and the model because the partial substitution of sodium chloride with sodium sulfate in the seawater decreases the extent of the gradient and thus the OCV, which is detrimental for gross power density. Moreover, the decrease is equal for all membranes as the OCV loss is mainly due to the reduced extent of the sodium chloride gradient. Additionally, the conductivity of river water is not increased as sulfate is not present, therefore the changes in stack electrical resistance are comparable for the different membranes, which leads to similar losses in normalized gross power density for all membranes.

5.4 Conclusions

Our experiments on the effect of multivalent anions on AEMs in RED with standard grade and monovalent ion selective membranes show that sulfate deteriorates RED performance due to the decreased open circuit voltage resulting from uphill transport and loss in membrane permselectivity, and increased membrane resistance, which increases during long term exposure to the multivalent anions. While these effects of multivalent anions are similar to those of multivalent cations, the narrower range of hydrated radii and hydration energies for anions results in a smaller electrical resistance increase over time, but also in lower monovalent-ion selectivities, which are detrimental for the open circuit voltage. When sulfate is present on both sides of the membranes, for the standard grade membranes gross power density losses up to 25 % are measured. Similar losses can be expected also for other multivalent anions based on their hydrated radii and hydration energies. As an example, phosphate has been found to severely increase the electrical resistance of anion exchange membranes, while decreasing membrane permselectivity in ED processes [34]. Monovalent ion selective membranes can reduce the uphill transport of multivalent ions, but they do so at the expense of high electrical resistance, which increases even further in the presence of sulfate. Therefore, the normalized power density of the monovalent ion selective ACS is not higher than that obtained with standard grade membranes. Although they are subject to the negative effect of uphill transport and loss in permselectivity in the presence of sulfate, standard grade membranes have a limited increase in resistance only, in presence of multivalent anions. Thanks to its intermediate resistance and permselectivity, the standard grade type 10 membrane can match the performance of the monovalent ion selective ACS membrane. Nevertheless, when exposed to high sulfate fractions for a long time, both monovalent ion selective and

standard grade membranes suffer from an increased electrical resistance. The results of the present study highlight the need to consider the negative effect of multivalent anions when developing new membranes that find a balance between RED performance and fouling. For sulfate, the main mechanisms to be addressed are: (1) uphill transport, (2) decreased permselectivity and (3) long term increase in membrane resistance in the presence of multivalent anions.

5

Supporting information

Multivalent ions: uphill transport and electrical resistance increase
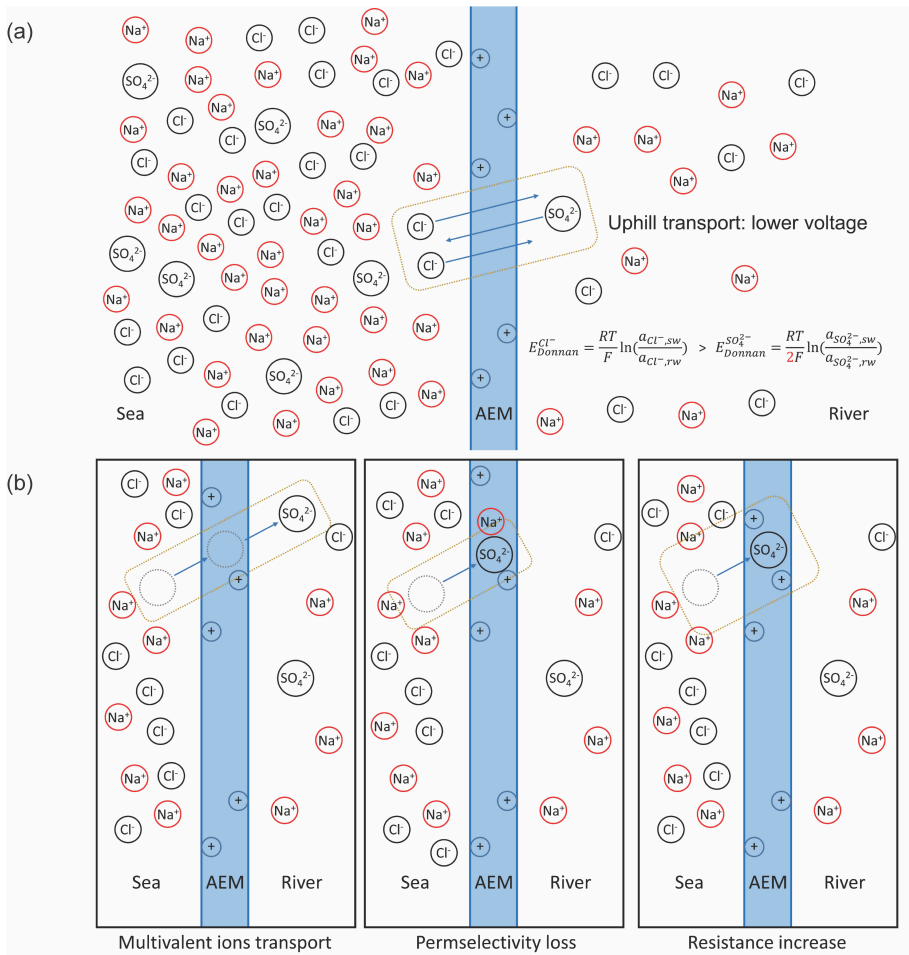
Figure S5.1 a) Schematic illustration of the mechanisms of uphill transport for an anion exchange membrane in presence of chloride and sulfate gradients. b) Schematic illustration of transport through the membrane, permselectivity loss, and sulfate trapping inside the AEM.
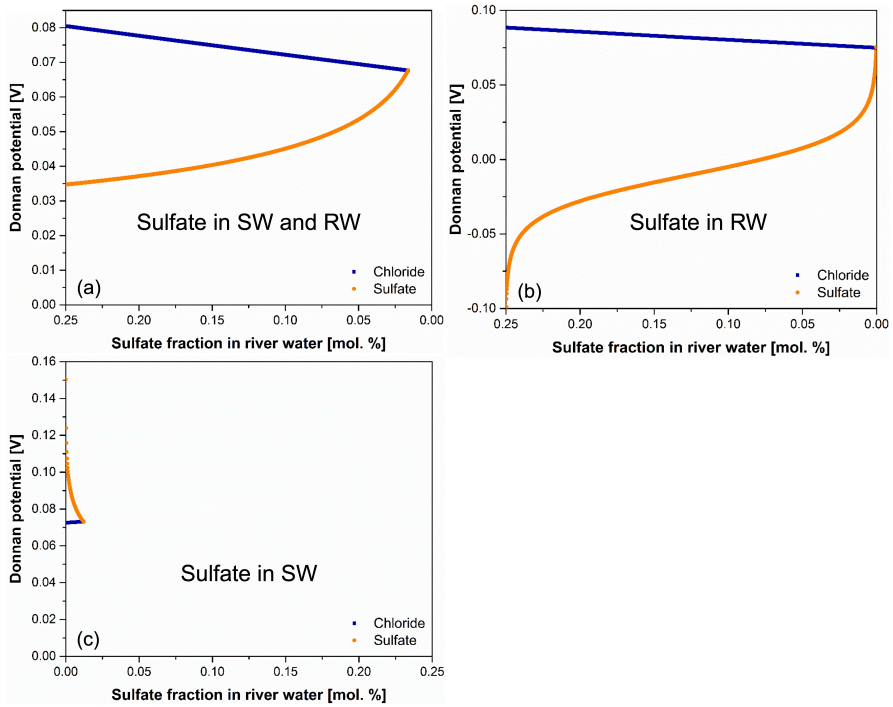
Figure S5.2 Evolution of the potential for chloride and sulfate with uphill transport according to the model of Vermaas et al. [18]. (a) sulfate initially added on both sides. (b) sulfate initially added only on the river side. (c) sulfate initially added only on the sea side. It should be noted that in the scenarios (a) and (b), sulfate is transported uphill, while in scenario (c), chloride is the species moving against its gradient.

Data analysis method
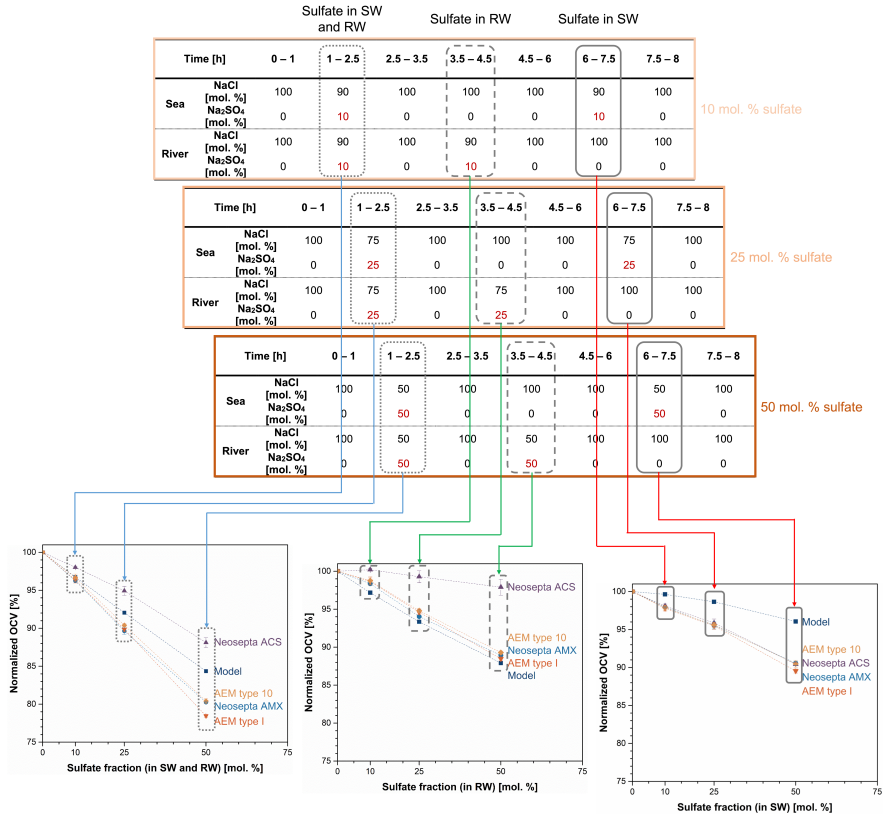
Figure S5.3 Flow chart illustrating how data from single experiments are used to construct the plots with normalized OCV, stack electrical resistance and gross power density data.

Open circuit voltage measurement in clean water

Table S5.1 Open circuit voltage (OCV) values measured in clean water. Values reported in the main text are normalized by these values and expressed in percentage. The values reported are the average of 24 measurements (three experiments per sulfate concentration, repeated in duplicate, with four clean water steps per experiment).

Membrane	OCV [V]
AMX	0.762 ± 0.005
Type 10	0.757 ± 0.004
Type I	0.743 ± 0.003
ACS	0.761 ± 0.004

5

Permselectivity loss with increasing sulfate fractions (in both sea and river)

Table S5.2 Comparison of the permselectivity loss measured at the stack and membrane levels for the three standard grade membranes (Figure 5.2, main text). At the stack level the AEM permselectivity loss corresponds to twice the difference between the model value and the membrane value (assuming no loss in CEM permselectivity). Stack level data are for the scenario with sulfate in both sea and river water.

	Stack level permselectivity loss [%]	Membrane level permselectivity loss [%]
type I (low ER, low α), 25 mol. % sulfate	- 4.6	- 6.7
type I (low ER, low α), 50 mol. % sulfate	- 13.8	- 16.1
type 10 (mid ER, mid α), 25 mol. % sulfate	- 3.4	- 2.1
type 10 (mid ER, mid α), 50 mol. % sulfate	- 7.8	- 7.0
AMX (high ER, high α), 25 mol. % sulfate	- 5.2	- 2.4
AMX (high ER, high α), 50 mol. % sulfate	- 8.2	- 11.9

Table S5.3 Composition of the solutions used to equilibrate the membranes (24+ h) and to test electrical resistance and permselectivity in the presence of sulfate. The compositions used for permselectivity measurements correspond to the concentrations of NaCl and Na_2SO_4 after uphill transport. This composition was chosen to avoid uphill transport as that would introduce an undesired potential loss, which would lead to a wrong measurement. (Permselectivity = 100 * $E_{measured}$ / E_{theory}, if uphill transport occurs, the theoretical potential changes by an amount that cannot be exactly predicted).

	Sulfate	Equilibration solutions	Testing solutions (low conc.) / (high conc.)
Electrical resistance	0 mol. %	0.5 M NaCl	0.5 M NaCl / 0.5 M NaCl
	25 mol. %	0.125 M Na_2SO_4, 0.375 M NaCl	(0.125 M Na_2SO_4, 0.375 M NaCl) / (0.125 M Na_2SO_4, 0.375 M NaCl)
	100 mol. %	0.5 M Na_2SO_4	0.5 M Na_2SO_4 / 0.5 M Na_2SO_4
Permselectivity	0 mol. %	0.1 M NaCl	0.1 M NaCl / 0.5 M NaCl
	25 mol. %	0.011 M Na_2SO_4, 0.103 M NaCl	(0.011 M Na_2SO_4, 0.103 M NaCl) / (0.139 M Na_2SO_4, 0.347 M NaCl)
	50 mol. %	0.033 M Na_2SO_4, 0.084 M NaCl	(0.033 M Na_2SO_4, 0.084 M NaCl) / (0.267 M Na_2SO_4, 0.216 M NaCl)

5

Electrical resistance vs time (11 days)

To ensure that the ED results are representative for RED operation, the same intermembrane distance, flow rate and current levels were applied. The inlet concentration of the feedwaters was chosen to be intermediate between that of that of the river and seawater. Figure 5.5 shows the stack electrical resistance evolution over 11 days in the presence of 50 mol. % sulfate for the monovalent ion selective ACS (medium resistance and permselectivity, high water content) and the standard grade (high resistance, medium permselectivity, low water content) Fujifilm AEM type 10 membranes.
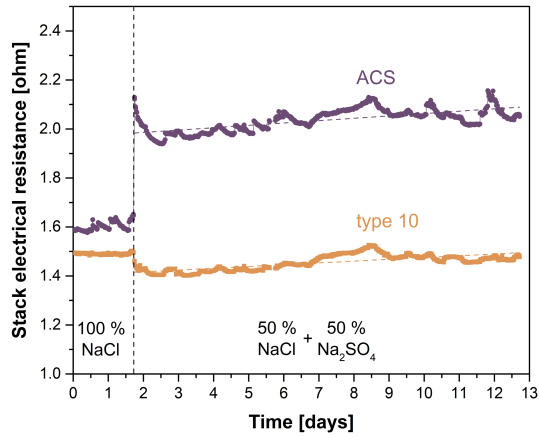

Figure S5.4 Evolution of the stack electrical resistance during the ED experiment with 0.1 M NaCl in the first 1.7 days and then a mixture of 0.05 M NaCl and 0.05 M Na_2SO_4 during the next 11 days.

References

[1]   B.E. Logan, M. Elimelech, Membrane-based processes for sustainable power generation using water, Nature. 488 (2012) 313–319. https://doi.org/10.1038/nature11477.

[2]   J.W. Post, J. Veerman, H.V.M. Hamelers, G.J.W. Euverink, S.J. Metz, K. Nymeijer, C.J.N. Buisman, Salinity-gradient power: Evaluation of pressure-retarded osmosis and reverse electrodialysis, Journal of Membrane Science. 288 (2007) 218–230. https://doi.org/10.1016/j.memsci.2006.11.018.

[3]   W. Li, W.B. Krantz, E.R. Cornelissen, J.W. Post, A.R.D. Verliefde, C.Y. Tang, A novel hybrid process of reverse electrodialysis and reverse osmosis for low energy seawater desalination and brine management, Applied Energy. 104 (2013) 592–602. https://doi.org/10.1016/j.apenergy.2012.11.064.

[4]   M. Tedesco, E. Brauns, A. Cipollina, G. Micale, P. Modica, G. Russo, J. Helsen, Reverse electrodialysis with saline waters and concentrated brines: A laboratory investigation towards technology scale-up, Journal of Membrane Science. 492 (2015) 9–20. https://doi.org/10.1016/j.memsci.2015.05.020.

[5]   M. Tedesco, A. Cipollina, A. Tamburini, G. Micale, Towards 1 kW power production in a reverse electrodialysis pilot plant with saline waters and concentrated brines, Journal of Membrane Science. 522 (2017) 226–236. https://doi.org/10.1016/j.memsci.2016.09.015.

[6]   A. Tamburini, M. Tedesco, A. Cipollina, G. Micale, M. Ciofalo, M. Papapetrou, W. Van Baak, A. Piacentino, Reverse electrodialysis heat engine for sustainable power production, Applied Energy. 206 (2017) 1334–1353. https://doi.org/10.1016/j.apenergy.2017.10.008.

[7]   B. Ortega-Delgado, F. Giacalone, P. Catrini, A. Cipollina, A. Piacentino, A. Tamburini, G. Micale, Reverse electrodialysis heat engine with multi-effect distillation: Exergy analysis and perspectives, Energy Conversion and Management. 194 (2019) 140–159. https://doi.org/10.1016/j.enconman.2019.04.056.

[8]   F. Giacalone, F. Vassallo, L. Griffin, M.C. Ferrari, G. Micale, F. Scargiali, A. Tamburini, A. Cipollina, Thermolytic reverse electrodialysis heat engine: model development, integration and performance analysis, Energy Conversion and Management. 189 (2019) 1–13. https://doi.org/10.1016/j.enconman.2019.03.045.

[9]   F. Giacalone, F. Vassallo, F. Scargiali, A. Tamburini, A. Cipollina, G. Micale, The first operating thermolytic reverse electrodialysis heat engine, Journal of Membrane Science. 595 (2020). https://doi.org/10.1016/j.memsci.2019.117522.

[10]   R.S. Kingsbury, K. Chu, O. Coronell, Energy storage by reversible electrodialysis: The concentration battery, Journal of Membrane Science. 495 (2015) 502–516. https://doi.org/10.1016/j.memsci.2015.06.050.

[11]   W.J. van Egmond, M. Saakes, I. Noor, S. Porada, C.J.N. Buisman, H.V.M. Hamelers, Performance of an environmentally benign acid base flow battery at high energy density, International Journal of Energy Research. 42 (2018) 1524–1535. https://doi.org/10.1002/er.3941.

5

[12]   J.W. Post, H.V.M. Hamelers, C.J.N. Buisman, Energy recovery from controlled mixing salt and fresh water with a reverse electrodialysis system, Environmental Science and Technology. 42 (2008) 5785–5790. https://doi.org/10.1021/es8004317.

[13]   A.H. Galama, J.W. Post, H.V.M. Hamelers, V.V. Nikonenko, P.M. Biesheuvel, On the origin of the membrane potential arising across densely charged ion exchange membranes: How well does the teorell-meyer-sievers theory work?, Journal of Membrane Science and Research. 2 (2016) 128–140.

[14]   J. Veerman, M. Saakes, S.J. Metz, G.J. Harmsen, Reverse electrodialysis: Evaluation of suitable electrode systems, Journal of Applied Electrochemistry. 40 (2010) 1461–1474. https://doi.org/10.1007/s10800-010-0124-8.

[15]   D.A. Vermaas, D. Kunteng, M. Saakes, K. Nijmeijer, Fouling in reverse electrodialysis under natural conditions, Water Research. 47 (2013) 1289–1298. https://doi.org/10.1016/j.watres.2012.11.053.

[16]   J.W.J.W. Post, H.V.M.H.V.M. Hamelers, C.J.N.C.J.N. Buisman, Influence of multivalent ions on power production from mixing salt and fresh water with a reverse electrodialysis system, Journal of Membrane Science. 330 (2009) 65–72. https://doi.org/10.1016/j.memsci.2008.12.042.

[17]   M. Higa, A. Tanioka, K. Miyasaka, Simulation of the transport of ions against their concentration gradient across charged membranes, Journal of Membrane Science. 37 (1988) 251–266. https://doi.org/10.1016/S0376-7388(00)82432-1.

[18]   D.A.D.A. Vermaas, J. Veerman, M. Saakes, K. Nijmeijer, Influence of multivalent ions on renewable energy generation in reverse electrodialysis, Energy Environ. Sci. 7 (2014) 1434–1445. https://doi.org/10.1039/C3EE43501F.

[19]   R.E. Lacey, Energy by reverse electrodialysis, Ocean Engineering. 7 (1980) 1–47. https://doi.org/10.1016/0029-8018(80)90030-X.

[20]   T. Badessa, V. Shaposhnik, The electrodialysis of electrolyte solutions of multi-charged cations, Journal of Membrane Science. 498 (2016) 86–93. https://doi.org/10.1016/j.memsci.2015.09.017.

[21]   J. Moreno, V. Díez, M. Saakes, K. Nijmeijer, Mitigation of the effects of multivalent ion transport in reverse electrodialysis, Journal of Membrane Science. 550 (2018) 155–162. https://doi.org/10.1016/j.memsci.2017.12.069.

[22]   T. Rijnaarts, E. Huerta, W. Van Baak, K. Nijmeijer, Effect of Divalent Cations on RED Performance and Cation Exchange Membrane Selection to Enhance Power Densities, Environmental Science and Technology. 51 (2017) 13028–13035. https://doi.org/10.1021/acs.est.7b03858.

[23]   T. Rijnaarts, J. Moreno, M. Saakes, W.M. de Vos, K. Nijmeijer, Role of anion exchange membrane fouling in reverse electrodialysis using natural feed waters, Colloids and Surfaces A: Physicochemical and Engineering Aspects. 560 (2019) 198–204. https://doi.org/10.1016/j.colsurfa.2018.10.020.

[24]   J.N. Weinstein, F.B. Leitz, Electric power from differences in salinity: The dialytic battery, Science. 191 (1976) 557–559. https://doi.org/10.1126/science.191.4227.557.

5

[25]   J. Veerman, M. Saakes, S.J. Metz, G.J. Harmsen, Reverse electrodialysis: A validated process model for design and optimization, Chemical Engineering Journal. 166 (2011) 256–268. https://doi.org/10.1016/j.cej.2010.10.071.

[26]   P. Długołecki, K. Nymeijer, S. Metz, M. Wessling, Current status of ion exchange membranes for power generation from salinity gradients, Journal of Membrane Science. 319 (2008) 214–222. https://doi.org/10.1016/j.memsci.2008.03.037.

[27]   B. Tansel, Significance of thermodynamic and physical characteristics on permeation of ions during membrane separation: Hydrated radius, hydration free energy and viscous effects, Separation and Purification Technology. 86 (2012) 119–126. https://doi.org/10.1016/j.seppur.2011.10.033.

[28]   W.M.Haynes, CRC Handbook of Chemistry and Physics 97th ed, 97th editi, CRC Press, 2016.

[29]   E.R. Nightingale Jr., Phenomenological theory of ion solvation. Effective radii of hydrated ions, Journal of Physical Chemistry. 63 (1959) 1381–1387. https://doi.org/10.1021/j150579a011.

[30]   E.R. Nightingale Jr., Phenomenological theory of ion solvation. Effective radii of hydrated ions, Journal of Physical Chemistry. 63 (1959) 1381–1387. https://doi.org/10.1021/j150579a011.

[31]   T. Luo, S. Abdu, M. Wessling, Selectivity of ion exchange membranes: A review, Journal of Membrane Science. 555 (2018) 429–454. https://doi.org/10.1016/j.memsci.2018.03.051.

[32]   R. Epsztein, E. Shaulsky, M. Qin, M. Elimelech, Activation behavior for ion permeation in ion-exchange membranes: Role of ion dehydration in selective transport, Journal of Membrane Science. 580 (2019) 316–326. https://doi.org/10.1016/j.memsci.2019.02.009.

[33]   J. Liao, X. Yu, N. Pan, J. Li, J. Shen, C. Gao, Amphoteric ion-exchange membranes with superior mono-/bi-valent anion separation performance for electrodialysis applications, Journal of Membrane Science. 577 (2019) 153–164. https://doi.org/10.1016/j.memsci.2019.01.052.

[34]   L. Paltrinieri, L. Poltorak, L. Chu, T. Puts, W. van Baak, E.J.R. Sudhölter, L.C.P.M. de Smet, Hybrid polyelectrolyte-anion exchange membrane and its interaction with phosphate, Reactive and Functional Polymers. 133 (2018) 126–135. https://doi.org/10.1016/j.reactfunctpolym.2018.10.005.

5

5

Chapter 6

Predicting reverse electrodialysis performance in the presence of divalent ions for renewable energy generation

Abstract

Reverse electrodialysis (RED) is an electro-membrane process to harvest renewable energy from salinity gradients. RED process models have been developed in the past, but they mostly assume that only NaCl is present in the feedwaters, which results in unrealistically high predictions. In the present work, an existing simple model is extended to accommodate the presence of magnesium ions and sulfate in the feedwaters, and potentially even more complex mixtures. All power loss mechanisms deriving from the presence of multivalent ions are included in the new model: increased membrane electrical resistance, uphill transport of multivalent ions from the river to the seawater compartment, and membrane permselectivity loss. This new model is validated with experimental and literature data of membrane electrical resistance, RED stack performance, and ion transport showing very good agreement between model predictions and experimental data. Finally we showed that the developed model not only describes experimental data but can also predict RED performances under a variety of conditions and configurations (single-stage with and without electrode segmentation, multi-stage in co-current and counter-current mode) and feedwater compositions (only NaCl, with Na_2SO_4, with $MgCl_2$, and with $MgSO_4$). It thus provides a very valuable tool to design and evaluate RED process systems.

6

6.1 Introduction

In the effort to limit global warming and reduce climate change, renewable energy plays a key role [1–3]. Among renewable energy sources, a promising candidate is salinity gradient energy (SGE), also known as blue energy, which is the energy derived from the controlled mixing of solutions with different salinities, e.g., river and seawater [4–6]. To harvest SGE, reverse electrodialysis (RED) gained prominence in recent years, with pilot installations and plans for demonstrations at a larger scale [7,8]. As described in Figure 6.1, the basic principle of RED consists of a stack of cation exchange membranes (CEMs, selective for cations) and anion exchange membranes (AEMs, selective for anions), piled alternately and separated by feedwater compartments. In the feedwater compartments, kept open by non-conductive spacers or by patterns on the surface of profiled membranes [9,10], river and seawater flow alternately, and the salt gradient across each membrane generates a voltage difference [11]. An electrode pair placed at both ends of the stack and a redox couple recirculating in the electrode compartments allow the conversion of the ionic current flowing through the membranes into an electronic current when an external load is connected to the electrode and the circuit is closed [12].
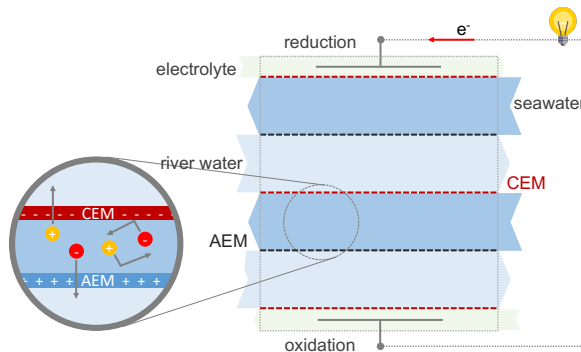
Figure 6.1 Working principle of RED.

A major challenge to the adoption of RED as a renewable energy source is fouling [13–15]. When harvesting SGE from natural salinity gradients, many undesired elements are present in the feedwaters, e.g., silica particles, natural organic matter, multivalent ions, and microorganisms that cause fouling on the membranes and spacers [14,16–18], leading to reduced RED power output [13,14]. Next to organic fouling, especially multivalent ions play an important role in RED as their presence results in a reduction of the electromotive force available and an increase in the electrical resistance of the membranes [19–23]. The reduced electromotive force is the consequence of reduced membrane permselectivity and

uphill transport. Uphill transport is the spontaneous transport of multivalent ions against their concentration gradient (from the river to the seawater), while monovalent ions are transported from the sea to the river water to balance the charge, maintaining electroneutrality. It derives from the disparity in electromotive forces produced by monovalent ions (higher) and multivalent ions (lower), due to their different valences, which have to be equilibrated [23]. Thus, with uphill transport, the concentration gradient for monovalent ions is reduced, without any energy production, leading to a reduced electromotive force [23]. Additionally, multivalent ions have larger radii, charge, and dehydration energies [24]. This slows down their transport through the membranes and can lead to the trapping of multivalent ions in the membrane due to electrostatic bridging of the ionic charges with the fixed membrane charges [21]. As a consequence, the membrane electrical resistance increases.

To estimate RED performance in a wide range of process conditions, modeling is a useful tool complementing experimental work. In recent years, different approaches were followed to model RED. In the frequently developed semi-empirical models the RED stack is represented as an electrical system and only macroscopic parameters (e.g., membrane electrical resistance and permselectivity) are taken into account [25–27]. Veerman et al. validated this kind of modeling approach for RED in co-flow and counter-flow configurations, showing the benefits of electrode segmentation [26]. Simões et al. also investigated the effect of electrode segmentation and multi-staging, albeit in the cross-flow configuration, showing that higher power densities and energy efficiencies are enabled [27,28]. Vermaas et al. used the same approach to prove that very high efficiencies (> 90%) are possible with RED when electrode segmentation and asymmetric flow rates are employed [29]. Tedesco et al. extended this modeling approach to RED with brine and seawater, including the effect of salt concentration on the membrane electrical resistance [25].

An alternate approach consists of the use of the Nernst-Planck equation coupled with electroneutrality conditions. This allows the description of the RED process based on microscopic quantities (e.g., ion diffusion coefficients in the solution and in the membrane phase). The advantage of this approach is that properties such as membrane resistance and permselectivity are predicted by the model, although this may require the use of fitting parameters to correctly describe experimental data [30]. Moreover, the approach based on the Nernst-Planck equation can take the effect of diffusion boundary layers into account as well [31]. Tedesco et al. provided an example of this approach applied to RED and

6

electrodialysis quantifying the impact of co-ion transport, water transport, and membrane thickness [31–33].

Although they provide valuable indications, the downside of these models is the assumption that the feeds only contain sodium chloride. This results in potentially large overestimation of the power densities that can be generated. As such, the development of RED models that take into account the presence of multivalent ions in the feedwaters is a major step toward more realistic power density predictions.

Moya used a Nernst-Planck based approach to show that it is possible to describe uphill transport within that theoretical framework [36], while Honarparvar et al. used the same approach to model electrodialysis in the presence of multivalent ions [37]. Culcasi et al. also used a Nernst-Planck based approach to model an acid-base flow battery [38]. The approaches based on the Nernst-Planck equation are able to accommodate the effect of multivalent ions without changes to the underlying theory, but correctly describing experimental trends may require even more adjustments and fitting than in the case with monovalent ions only, e.g., for the value of diffusion coefficients inside the membrane phase [30]. Additionally, another downside of a Nernst-Planck based approach is that for a cross-flow RED configuration a full 3D model is required, as discretization is needed not only in the flow directions, but also along the membrane and compartment thicknesses, making it more computationally demanding than a semi-empirical model, where discretization is performed only along the flow directions.

Semi-empirical RED models seem promising thanks to the lower number of parameters, which can be easily measured or found in literature, and their light computational nature. However, existing RED models describing performance with NaCl only need adaptation to include the effect of multivalent ions. Ortiz-Martinez et al. presented an approach based on the use of the same semi-empirical model developed by Veerman et al., but including the membrane electrical resistances measured in mixtures of mono- and multivalent ions to include the effect of multivalent ions on RED [26,34]. While valid, its limitation lies in the absence of permselectivity loss and uphill transport, which both have a major impact on power density. Hong et al. also used a semi-empirical model and focused on the effect of multivalent ions on the open circuit voltage (OCV) and feedwater conductivity, but uphill transport, permselectivity loss, and increase in membrane resistance were not taken into account [35]. Therefore, the existing semi-empirical models for RED in the presence of multivalent ions are not accounting for all power loss mechanisms, but focus on a single one.

6

In the present work, a semi-empirical model is derived for RED in a cross-flow configuration with mixtures of sodium, magnesium, chloride, and sulfate in the feedwaters. This model extends the semi-empirical model approach proposed by Veerman et al. [26] and our previous work [27] to account for all power loss mechanisms due to the presence of multivalent ions: uphill transport, membrane permselectivity loss, and increased membrane resistance. The model is validated with RED stack experiments with mixtures of sodium chloride and sodium sulfate and with mixtures of sodium chloride and magnesium chloride. A comparison with experimental literature data on power density loss is also presented and shows good agreement between the model predictions and the experimental data. The potential of the model is then showcased by comparing RED simulations with sodium chloride and with mixtures of mono- and multivalent ions, highlighting their difference and the importance that this tool provides for more realistic predictions of obtainable power densities when using real natural feedwaters.

6.2 Methods

6.2.1 RED model

The RED model including the effect of sulfate and magnesium was derived from the model presented by Simões et al. [27], which in turn extended the semi-empirical models of Veerman et al. [26] and Vermaas et al. [29]. Where the earlier models describe RED behavior for feedwaters containing only sodium chloride, the present models is extended such that it also takes into account the effects of the presence of multivalent ions. To correctly predict RED performance with mixtures of mono- and multivalent ions, the following aspects are taken into account in the model: 1) uphill transport of multivalent ions against their concentration gradient; 2) higher membrane electrical resistance due to the larger size of the multivalent ions and the partitioning of current between different ionic species (downhill transport); 3) membrane permselectivity loss; and 4) change of electrical conductivity of the water compartments when more charges are introduced with the salts containing multivalent ions.

6.2.1.1 Uphill transport

The voltage produced by the concentration gradient across an ion selective membrane can be calculated with the modified Nernst equation [26], which includes the effect of membrane permselectivity:

$$E = \alpha \frac{RT}{zF} \ln \left(\frac{\gamma_{sw} c_{sw}}{\gamma_{sw} c_{rw}} \right) \qquad \text{(Eq. 6.1)}$$

Where α is the membrane permselectivity [-], R is the universal gas constant [J·mol^{-1}·K^{-1}], T is the absolute temperature [K], z is the ion valence [-], F is the Faraday constant [C·mol^{-1}], γ_{sw} and γ_{rw} are the molar activity coefficients [-] of sea and river water, and c_{sw} and c_{rw} are the molar ion concentrations [mol·L^{-1}] in sea and river water, respectively. Due to higher valence and lower activity coefficients, a gradient of multivalent ions generates a voltage difference across an ion exchange membrane that is lower than for monovalent ions [23]. To balance these two voltages, the monovalent ion gradient is partially consumed to increase the multivalent ion gradient, until the two voltages are balanced [23]. This process, known as uphill transport, involves the electroneutral transport of monovalent ions from the high to the low concentration side of the membrane, while an equal amount of charge is moved from the low to the high concentration side by the movement of multivalent ions.

To include uphill transport in the RED model, the batch model developed by Vermaas et al. [23] was converted in the form of equivalent circuits. This approach considers the mono- and multivalent ion gradients across a membrane as two voltage sources connected in parallel, where the generator with the largest electromotive force (emf) drives a current through the other generator to balance the voltage drop in the parallel circuit (Figure 6.2).
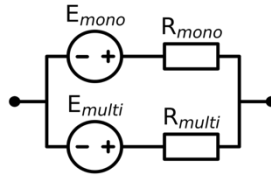
Figure 6.2 Equivalent circuit used to describe uphill transport of multivalent ions, as proposed in [23].

The uphill transport current is then calculated as:

$$J_{uphill} = \frac{E_{mono} - E_{multi}}{R_{mono} + R_{multi}}$$
(Eq. 6.2)

Where J_{uphill} is the uphill transport current density [A·m^{-2}], E_{mono} and E_{multi} are respectively the emf [V] for the monovalent and multivalent ions gradients, R_{mono} and R_{multi} are the cell resistances [Ohm·m^2] for the monovalent and multivalent ions, respectively. The sum of the resistances in the denominator in equation 2 physically represents monovalent and multivalent ions travelling through the same membrane in opposite directions.

6.2.1.2 Membrane resistance and current partitioning (downhill transport)

While the circuit in Figure 6.2 manages to predict the mono- and multivalent ion fluxes through the AEMs and CEMs due to uphill transport, it is not suitable to represent the downhill transport, i.e., the transport of ions according to their concentration gradient when an ionic current is flowing through the system. It is well known that the electrical resistance of membranes in a mixture of mono- and multivalent ions is higher than what is measured in a solution of monovalent ions only [19,21]. However, the parallel connection of two resistors results in an equivalent resistance that is smaller than each individual resistor. Therefore, if used to predict downhill transport (by closing the circuit with an external load), the circuit in Figure 6.2 would predict a reduction in electrical resistance when multivalent ions are introduced in the system, which is incorrect. For this reason, the circuit in Figure 6.2 is only used to calculate uphill transport, and its solution is superimposed to that of the circuit used to calculate downhill transport (Figure 6.3) to obtain the overall RED performance.
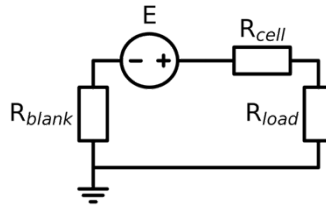
Figure 6.3 Electrical circuit used to model downhill transport in the RED system.

To predict downhill transport, the current partitioning between mono- and multivalent ions needs to be determined. To do so, it is necessary to know the membrane selectivity. In RED, membrane selectivity is calculated as [21]:

$$P_{multi}^{mono} = \frac{ER_{multi}}{ER_{mono}} \tag{Eq. 6.3}$$

Where P is the monovalent over multivalent ion selectivity of the membrane [-], and ER_{multi} and ER_{mono} are the membrane electrical resistances [Ohm·m²] measured in solutions of only multivalent and only monovalent ions, respectively. The selectivity of a membrane between two ions can also be calculated for any ion mixture based on the definition of Sata [39]:

$$P_B^A = \frac{\frac{z_A J_A}{z_B J_B}}{\frac{z_A c_A}{z_B c_B}} = \frac{J_A}{J_B} \frac{c_B}{c_A} = \frac{j_A}{j_B} \frac{z_B}{z_A} \frac{c_B}{c_A} \tag{Eq. 6.4}$$

Where P is the selectivity of the membrane for ion A (monovalent) over ion B (multivalent) [-], z is the ion valence [-], J is the ion flux [mol·m^{-2}·s^{-1}], $J_i = j_i/(z_i F)$, c is the ion concentration [mol·L^{-1}], and j is the current density [A·m^{-2}]. This definition of membrane selectivity expressed in terms of current densities allows the derivation of the current partitioning. Membrane selectivity can be calculated from equation 3 and its value can be used in equation 4 to relate the current densities of mono- (A) and multivalent (B) ions. The overall current density can then be expressed as:

$$j_{TOT} = j_A + j_B = j_A \left(1 + \frac{1}{P_B^A} \frac{z_B}{z_A} \frac{c_B}{c_A} \right)$$
(Eq. 6.5)

The fraction of current transported by ion A (sodium for a CEM, chloride for an AEM) is then:

$$f_A = \frac{j_A}{j_{TOT}} = \frac{1}{1 + \frac{1}{P_B^A} \frac{z_B}{z_A} \frac{c_B}{c_A}}$$
(Eq. 6.6)

In the case of a binary mixture with only two cations and two anions, the fraction of current transported by ion B (magnesium for a CEM, sulfate for an AEM) becomes:

$$f_B = \frac{j_B}{j_{TOT}} = 1 - f_A$$
(Eq. 6.7)

While for the case of more complex mixtures, the selectivity of the membrane for all counter-ions compared to a reference counter-ion needs to be known.

Through this approach, the current partitioning between ion A (monovalent) and B (multivalent) is directly related to the membrane selectivity. This approach relies on the definition of selectivity provided in equation 3, which considers the selectivity (P_B^A) as a constant. If this assumption is not true and the membrane selectivity is largely dependent on the composition of the feedwaters ($P_B^A = f(c_A, c_B)$), the current approach is valid, but more data on the dependence of the membrane selectivity on the feedwater composition are required.

The electrical resistance of a membrane in an ionic mixture of mono- and multivalent ions is then expressed as:

$$ER_{eq} = f_A \cdot ER_A + f_B \cdot ER_B$$
(Eq. 6.8)

Where ER_{eq} is the electrical resistance of a membrane in a mixture of ion A and B, f_A and f_B are the current partitioning coefficients for the given composition (equation 6 and 7), and ER_A and ER_B are the membrane electrical resistances measured in solutions containing only counter-ion A and B, respectively. Equation 8 assumes a transition between the electrical resistances measured with monovalent ions and the electrical resistance measured with multivalent ions only which is linearly dependent on the current

6

partitioning. For some membranes (e.g., monovalent-ion selective CEMs) this is not the case as small amounts of multivalent ions result already in a large increase of the effective membrane electrical resistance. This issue is further addressed in the model validation section of the results and discussion.

6.2.1.3 Membrane permselectivity loss

The apparent membrane permselectivity decreases when multivalent ions are present in the feedwaters [21,40]. The apparent membrane permselectivity is related to the transport of both counter-ions and of co-ions [39]. With larger counter-ions that are more difficult to transport through the membrane, the transport of co-ions becomes more significant, resulting in a reduced membrane permselectivity. Additionally, multivalent ions may bind to the fixed charges inside the membrane and decrease its effective charge density [21,41], thus decreasing the membrane permselectivity even further. To include these effects in the RED model, empirical fitting of experimental OCV and permselectivity data was used. For data on the permselectivity loss of CEMs with magnesium, the OCV data presented by Moreno et al. [20] were compared to the equilibrium values after uphill transport estimated with the batch model of Vermaas et al. [23]. The excess OCV loss was attributed to a loss in apparent membrane permselectivity following the procedure adopted in our previous study on the effect of sulfate on AEMs [19]. For the permselectivity loss of AEMs with sulfate, the experimental OCV and permselectivity data from our previous study were used [19]. The literature data and fitting equations are presented in the Supporting Information.

6.2.1.4 Conductivity of the feedwaters

Equation 8 (elaborated before) allows the prediction of membrane electrical resistance with a mixture of mono- and multivalent ions, but to predict stack resistances, the conductivity of the feedwaters needs to be estimated as well. To do so, a simple empirical relationship between the electrical conductivity of the feedwaters and the total dissolved solids exists (provided that all dissolved solids are ionic species) [42]:

$$TDS = K \cdot EC \qquad \text{(Eq. 6.9)}$$

Where TDS is the amount of total dissolved solids [g·L^{-1}], K is an empirical factor, and EC is the electrical conductivity of the solution [mS·cm^{-1}]. Due to the typical feedwater concentrations in RED, K is equal to 0.63 [42].

6.2.2 Model-based simulations

The approach elaborated in the previous sections leads to an extended version of the model of Simões et al. [27]. A detailed overview of all model equations used is reported in the Supporting Information.

The validation experiments were performed with a single stage unsegmented RED stack (Figure 6.4a). To explore the potential of the new RED model, three additional configurations were simulated and compared (Figure 6.4b-d).
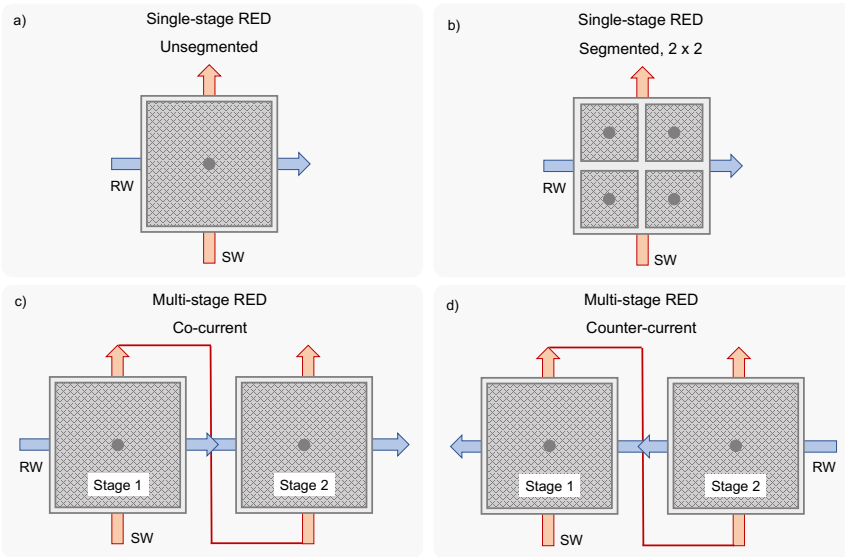
Figure 6.4 Simulated RED configurations: a) single stage RED with unsegmented electrodes; b) single-stage RED with four electrode segments in a 2 x 2 pattern; c) multi-stage RED in co-current mode between two cross-flow stages; and d) multi-stage RED in counter-current mode between two cross-flow stages.

The approach followed for each of these configurations is discussed below in detail. Membrane, stack, and process parameters were chosen to have representative values, similar to the parameters used in the previous studies on the effect of electrode segmentation and multi-staging in RED [27,28].

a) The single-stage RED stack with unsegmented electrode (Figure 6.4a) was realized by modeling a cross-flow stack (corresponding to those supplied by REDstack BV, The Netherlands) with 10 cell pairs and an active area of 22 cm × 22 cm. Fujifilm Type 10 AEM and CEM (Fujifilm Manufacturing Europe BV, The Netherlands) specifications and 155 µm spacers (corresponding to spacers from Deukum GmbH, Germany) were used for all simulations. Its external load was adjusted for maximum power density using an

optimization algorithm (Sequential Least Squares Programming, SLSQP) for different residence times (10 – 90 s). For the single-stage RED with unsegmented electrodes, the effect of the seawater ratio ($\phi_{sw}/(\phi_{sw} + \phi_{rw})$, where ϕ is the feedwater flow rate [$m^3 \cdot s^{-1}$]) was also investigated. A constant residence time (30 s, as in [29]) for river water was considered, while varying the seawater ratio between 0.05 and 0.95, similarly to the work of Vermaas et al. [29]. For simulations involving the seawater ratio, ideal membranes (negligible electrical resistance, 100 % permselectivity, and not allowing any undesired salt or water transport) were considered in addition to Fujifilm Type 10.

b) The single-stage RED with segmented (2×2) electrodes (Figure 6.4b) was obtained by modeling a cross-flow stack with 10 cell pairs and an active area of 22 cm $\times$ 22 cm, where the area is symmetrically divided into four adjacent square electrode segments. The four independent external loads were adjusted for overall maximum power density (considering the sum of the powers from each electrode segment) using SLSQP for residence times in the range 10 – 90 s. Two additional RED configurations were simulated considering multi-stage, where the feedwaters leaving a RED stack (first stage) are used to feed another RED stack (second stage).

c) Co-current and d) counter-current multistage RED configurations were considered. Each stage was modeled as a cross-flow RED stack equipped with 10 cell pairs, an active area of 22 cm $\times$ 22 cm, and unsegmented electrodes. For co-current (Figure 6.4c), river and seawater were fed to the first stage and then sequentially to the second stage. For the counter-current (Figure 6.4d), seawater was fed to the first stage and then to the second stage, while river water was fed into the second stage first and then to the first stage. For both co-current and counter-current multi-stage RED configurations, the independent external loads for the two stages were adjusted to maximize overall power density with SLSQP. The overall residence times under consideration for multi-stage RED simulations were in the range 20 – 88 s, which implies residence times in the 10 – 44 s range for each stage.

6.2.3 Model validation experiments

To validate the model results, experiments with a single-stage cross-flow RED stack (configuration *a* in Figure 6.4) were performed adding $MgCl_2$ and Na_2SO_4 in the feedwaters.

6.2.3.1 RED stack

A cross-flow stack with an active area of 10 cm x 10 cm (REDstack BV, The Netherlands) and titanium mesh electrodes coated with galvanized Pt (Ti mesh 1.0, coating thickness 2.5 µm, MAGNETO Special Anodes BV, the Netherlands) was assembled with ten cell pairs. Fujifilm Type 10 CEMs and AEMs (FUJIFILM Manufacturing Europe BV, The Netherlands) were separated by gasket-integrated spacers with 155 µm thickness (Deukum GmbH, Germany) with a polyester woven netting (Saatifil, Saati SpA, Italy). Double CEMs were used at both ends of the membrane stack to seal the electrode compartments and prevent electrolyte leakage into the feedwaters compartments.

6.2.3.2 Feedwaters and electrolyte

Artificial river water (17 mM) and artificial seawater (508 mM) were prepared adding sodium chloride (NaCl, 99.5 % purity, ESCO, The Netherlands) to demineralized water. To evaluate the effect of magnesium and sulfate, separate runs were performed substituting 10 mol. % NaCl both in river and seawater either with sodium sulfate or magnesium chloride hexahydrate (both > 99% purity, VWR Chemicals, Belgium). The electrode rinse solution was made of a mixture of 0.05 M potassium hexacyanoferrate(II) / 0.05 M potassium hexacyanoferrate(III) (both $\geq$ 96 % purity, VWR Chemicals, Belgium) as redox couple and 0.25 M sodium chloride as supporting electrolyte. River and seawater were fed to the stack with a flow velocity of 1 cm·s^{-1} in a single-pass configuration (150 mL min^{-1}) using peristaltic pumps (Cole-Palmer, Masterflex L/S Digital drive, USA). The electrolyte rinse solution was recirculated between the electrolyte compartments by a peristaltic pump. To prevent bulging of the membrane stack, the electrolyte was kept at a 0.3 bar overpressure by means of a diaphragm valve (KNF FDV 30, KNF-Verder BV, The Netherlands) placed at the outlet of the electrolyte circuit. The temperature and conductivity of the artificial feedwaters were measured before each experiment.

6.2.3.3 Electrochemical characterizations and water analyses

Two stack experiments were performed for model validation. First, the RED performance with 100 mol. % NaCl and with mixtures of 90 mol. % NaCl and 10 mol. % magnesium chloride was evaluated. Second, the same experiment was repeated with 100 mol. % NaCl and with mixtures of 90 mol. % NaCl and 10 mol. % sodium sulfate. RED performance was measured with constant current steps (0 – 5 – 10 – 12.5 – 15 – 17.5 – 20 – 22.5 – 25 – 30 A·m^{-2}), applied for 10 min each using a potentiostat (Iviumstat, Ivium Technologies BV, The Netherlands). Water samples were collected from the stack outlets after 2 min

from the beginning of each current step. The ion content of the water samples was analyzed with ion chromatography (Metrohm Compact IC Flex 930, Metrohm Nederland, the Netherlands) after appropriate dilution to be within the instrument detection limits (dilution factors: 70 for river water, 1400 for seawater).

6.3 Results and discussion

To assess the validity of the new RED model, its ability to predict membrane electrical resistance in multi-ionic mixtures, RED performance, and ion transport was evaluated by comparing the obtained model results with experimental literature data. Then, validation with stack experimental data was performed, including the current partitioning between mono- and multivalent ions. Finally, the validated model was used to investigate RED performance in a variety of stack and flow configurations.

To validate the model prediction of the membrane electrical resistance in mixtures of mono- and multivalent ions, literature data for a variety of CEMs (from Rijnaarts et al. [21]) and AEMs (from our previous work [19]) were considered. The electrical resistance data in 100 mol. % monovalent ions and in 100 mol. % multivalent ions were used to derive the membrane selectivity (according to equation 3), which was then used to predict the electrical resistance in the mixture of mono- and multivalent ions (following equation 4 – 8). Figure 6.5 compares the literature data with the model prediction for CEMs in a mixture containing 10 mol. % magnesium chloride and for AEMs in a mixture containing 25 mol. % sodium sulfate.
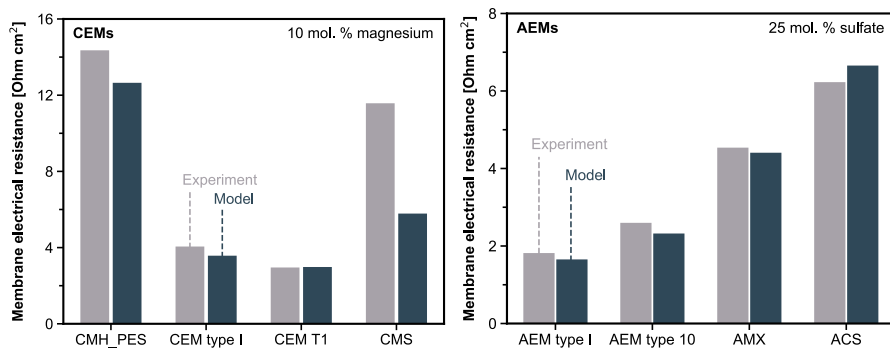
Figure 6.5 Comparison of experimental literature data [19,21] and model predictions for the membrane electrical resistance of CEMs and AEMs in mixtures of mono- and multivalent ions. For CEMs, measurements were performed in a mixture of 90 mol. % NaCl and 10 mol. % MgCl2 (0.5 M total salt) [21]. For AEMs, measurements were performed in a mixture of 75 mol. % NaCl and 25 mol. % Na2SO4 (0.5 M total salt) [19]. CEMs: 1) CMH_PES: heterogeneous, standard membrane (Ralex); 2) CEM type I:

homogeneous, standard (Fujifilm); 3) CEM T1: homogeneous, multivalent-ion permeable (Fujifilm); 4) CMS: homogeneous, monovalent-ion selective (Neosepta). AEMs: 1) AEM type I and 2) AEM type 10: homogeneous, standard membranes (Fujifilm); 3) AMX: homogeneous, standard membrane (Neosepta); 4) ACS: homogeneous, monovalent-ion selective membrane (Neosepta).

For both CEMs and AEMs, the model predictions are in good agreement with the literature data. Despite the more complex nature of ion transport in heterogeneous membranes (Ralex CMH_PES), the model prediction for the Ralex membrane is also good. The monovalent-ion selective CEM (Neosepta CMS) shows a large deviation from the model, which underestimates its electrical resistance. The Neosepta CMS membrane is designed to limit the transport of multivalent cations by size exclusion. The difference between of the model values and the experimental values indicates that even small fractions of magnesium result in a large increase in membrane resistance due to its difficulty in moving through the membrane and possibly due to trapping of the large ion in the membrane. This would suggest that for CEMs with a high monovalent over multivalent ion selectivity the approach described in equations 3 – 8 results in inaccurate predictions. However, the RED model can still be used for these membranes provided that more experimental data on the behavior of their electrical resistance in mixtures of mono- and multivalent ions are collected. To demonstrate this point, another example is described in the Supporting Information. This examples shows that, although the selectivity value calculated with equation 3 may not describe the reality, equations 4 – 8 are still valid, provided that a corrected value for the selectivity is considered (Figure S6.2 in the Supporting Information).

For AEMs, the model delivers a good prediction even for the monovalent-ion selective Neosepta ACS. This is explained by the smaller increase in membrane resistance that sulfate induces for AEMs compared to the increase induced by magnesium for CEMs [19]. The proposed approach clearly enables the accurate prediction of membrane electrical resistance in mixtures of mono- and multivalent ions for standard grade membranes and, with additional data, also for monovalent-ion selective CEMs.

Validation of the model predictions of membrane resistance with experimental data is the key to predict current partitioning and RED stack performance, where the effect of feedwater conductivity, uphill transport and decreased permselectivity also come into play. To validate the prediction of RED performance, two stack experiments were performed adding first 10 mol. % $MgCl_2$ and then 10 mol. % Na_2SO_4 to both feedwaters. Figure 6.6 shows the IV-curves and power density curves for the RED experiments with $MgCl_2$. To describe the RED behavior, the obstruction factor (accounting for the extra

6

resistance from the non-conductive spacers, equation S7 and S8 in the Supporting Information) was adjusted as fitting factor to the data measured for the run with 100 mol. % NaCl. With that value fixed, only the feedwater composition was then changed to describe the data for the run with 10 mol. % $MgCl_2$ in both feedwaters.
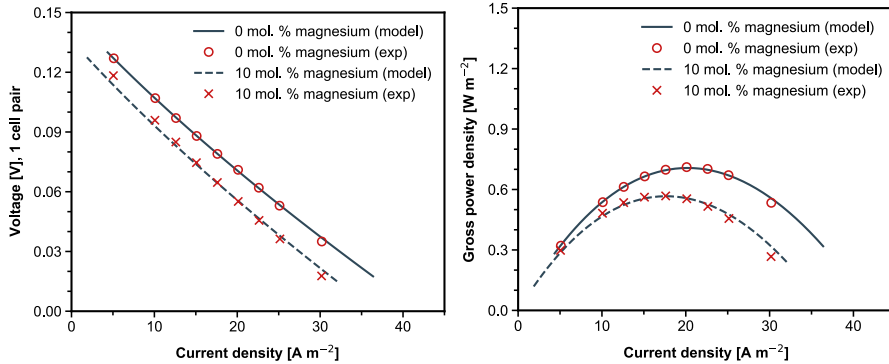

Figure 6.6 Model predictions and experimental data of the IV and power density curves for the experiments with 100 mol. % NaCl and with the 90 mol. % NaCl + 10 mol. % $MgCl_2$ mixture.

Both the IV-curve and the power density curve calculated according to the model show good agreement with the experimental data. This is a first indication that the stack electrical resistance, including the feedwater conductivities and membrane resistances, and emf, including uphill transport and permselectivity loss, are correctly predicted in the presence of magnesium chloride. The stack electrical resistance is dominated by the conductivity of the river water [43], which accounts for more than half of the overall resistance (slope of the IV-curve). Replacing an equal molar amount of NaCl with $MgCl_2$ increases the river water conductivity, while the presence of magnesium chloride in both feedwaters increases the resistance of the CEMs. These two opposite trends need to be correctly embedded in the model for an accurate RED performance prediction. Therefore, the agreement between model and experimental data indicates that not only the membrane resistances but also the feedwater conductivities are correctly predicted when multivalent ions are added to the feedwaters. For the power density, the OCV has a major role since the power density is proportional to the squared OCV (Equation S37 in the Supporting Information). Therefore, a good agreement between model predictions and experimental data indicates that the decrease in OCV when magnesium chloride is added to the feedwaters is correctly predicted by the model through uphill transport and permselectivity loss.

Figure 6.7 shows similar results obtained for the run with 10 mol. % Na₂SO₄ added to both feedwaters.
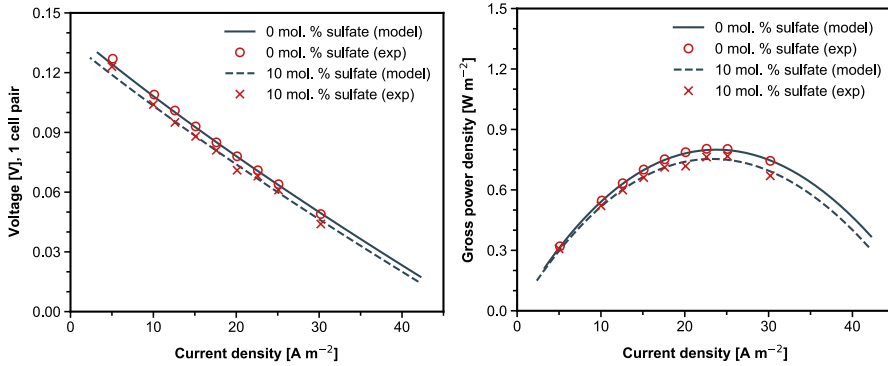

Figure 6.7 Model predictions and experimental data of the IV and power density curves for the experiments with 100 mol. % NaCl and with the 90 mol. % NaCl + 10 mol. % Na₂SO₄ mixture.

Also in this case, the agreement between experimental data and model predictions is good. It can be noted that the relative impact of sulfate on RED performance is lower than that of magnesium, due to the smaller permselectivity loss and electrical resistance increase [19]. The smaller electrical resistance and higher power density for the run without multivalent ions (100 mol. % NaCl, solid lines and circles) in Figure 6.7 compared to Figure 6.6 is likely due to air bubbles trapped in the spacer during the stack experiments illustrated in Figure 6.6. The results from the stack experiments with magnesium ions or sulfate added to the feedwaters prove the ability of the model to describe RED performance in the presence of multivalent ions.

The last step of the model validation is the comparison of feedwater compositions measured during the stack experiments, at OCV and at the maximum power point (m.p.p.) with the model predictions (Figure 6.8). This evaluates the ability of the model to predict uphill transport and current partitioning. Ion and water transport through the membranes determine the ion concentrations in the feedwaters. With multivalent ions present in the feedwaters, salt transport also happens under OCV conditions due to uphill transport, which redistributes mono- and multivalent ions across the membranes. Additionally, when current is applied, both mono- and multivalent ions can act as charge carriers, therefore it is important to correctly predict the current fraction transported by each ion, as this affects the composition of the feedwaters and in turn feedwater conductivity. Clearly, there is good agreement between the model predictions and the experimental data, both for OCV and the m.p.p.. The similarity in power density indicates the realistic inclusion of uphill

transport in the model, while the correct prediction of the feedwater compositions at m.p.p. validates the current partitioning described in equation 3 – 8.
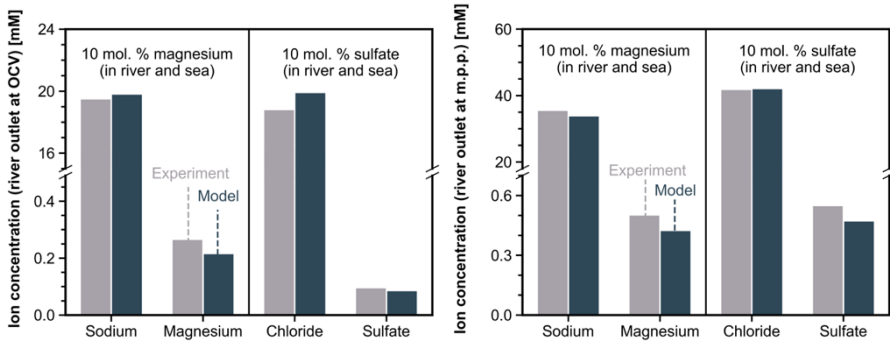
With the ability of the model to include all power loss mechanisms induced by multivalent ions verified, a comparison of predicted model power losses for increasing fractions (up to 50 mol. %) of magnesium and sulfate ions with literature data was performed (Figure 6.9). The experimental data from Moreno et al. [20] and our previous work [19] were used and compared to the model predictions obtained in the present work.
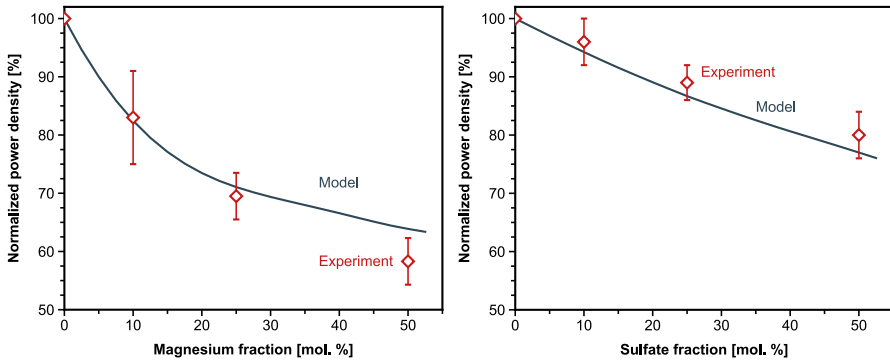
Figure 6.9 Comparison of literature data from Moreno et al. [20] (for magnesium ions) and our previous work [19] (for sulfate) with the model prediction for power density losses at increasing fraction of multivalent ions in the feedwaters.

It should be noted that OCV data from the same datasets were used to derive the empirical fit of permselectivity loss, therefore the comparison of predicted power density losses with the ones reported in these works only validates uphill transport, increased membrane electrical resistance and the increase in feedwater conductivity in the presence of

multivalent ions. Nevertheless, the agreement between model and literature data is good. Even at molar fractions of magnesium ions and sulfate significantly higher than those considered in the validation experiments, experimental data and model predictions almost coincide. The only exception is 50 mol. % of magnesium, where the experimental power density loss exceeds the model prediction. This is likely because at such high magnesium concentrations, the increase in membrane electrical resistance due to trapping of the magnesium ions inside the membrane starts to become more dominant, as shown by Moreno et al. [20].

The validated RED model including the effect of sulfate and magnesium ions has the potential to deliver more accurate predictions of obtainable power densities and to help in the design of up-scaled RED systems. It can now be used to predict the actual RED performance under realistic conditions. Figure 6.10 shows the behavior of net power density, net energy efficiency, and their product as a function of the seawater ratio.

Figure 6.10 a) net power density, b) net energy efficiency, and c) their product as a function of the seawater ratio for ideal membranes (with negligible resistance) and for real membranes with and without sulfate present in the feedwaters. For c), only values where both power density and energy efficiency are positive are displayed. Fujifilm type 10 membranes were chosen as representative RED membranes.

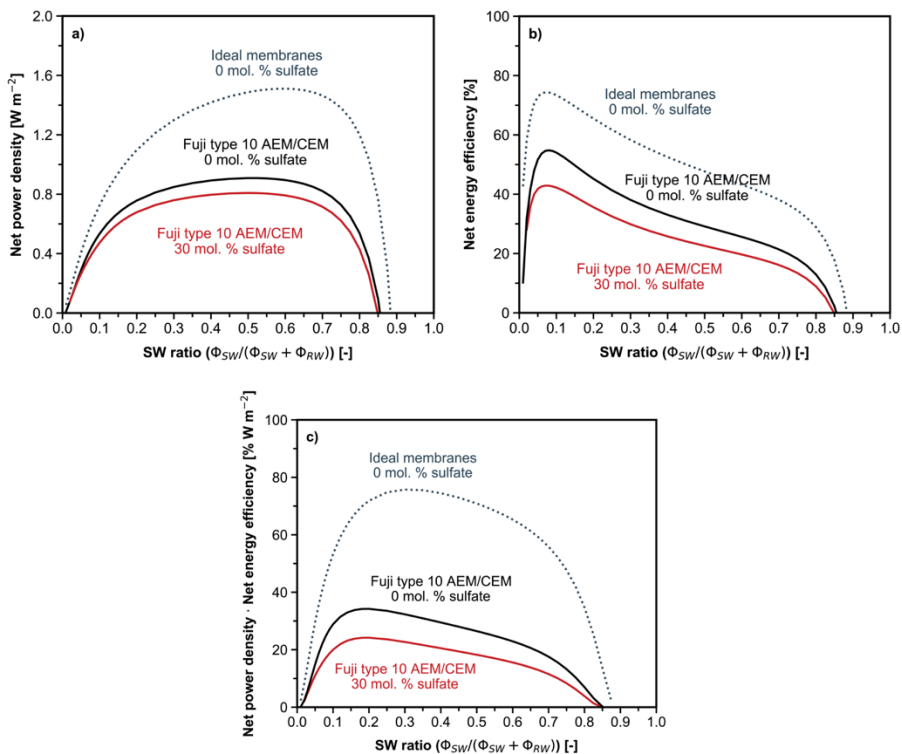Variations in the seawater ratio were used in the past to show that RED can achieve very high efficiencies, albeit considering only ideal membranes [29]. The product is chosen as a useful RED performance indicator as it accounts for both the power density and the energy efficiency granting them an equal weight. The opposite trends observed for net power density (Figure 6.10a) and net energy efficiency (Figure 6.10b) determine the shape of the curves in Figure 6.10c, with the power density peaking at intermediate seawater ratios (> 0.5), while the efficiency peaks at low seawater ratios (< 0.1). While ideal membranes provide a very high and optimistic prediction of the RED performance (peaking at a seawater ratio equal to 0.3 with a value of 75.8 %·W·m^{-2}), the inclusion of the behavior of real membranes shows already a more realistic prediction of the RED performance (peaking at a seawater ratio of 0.2 with a maximum value of 34.2 %·W·m^{-2}). The shift of the product peak to lower seawater ratios is due to the different evolution of the net power density, which is more sensitive to the seawater ratio in the range $0.3 - 0.8$ when ideal membranes are considered. In the same way, including the effect of multivalent ions (peaking at a seawater ratio of 0.18 with a value of 24.2 %·W·m^{-2}) gives an even more realistic estimation of the actual RED performance when using real feedwaters. As such, this model not only helps to predict realistic RED performance, but can also be used to choose optimum process conditions to achieve maximum performance.

The influence of the presence of multivalent ions on RED performance in a variety of different flow configurations, is presented in Figure 6.11. For all configurations, four feedwater compositions were considered: NaCl only, a mixture with NaCl and 30 mol. % Na$_2$SO$_4$, a mixture with NaCl and 30 mol. % MgCl$_2$, and a mixture with NaCl and 30 mol. % MgSO$_4$.

For all feedwaters compositions, a single stage with electrode segmentation (Figure 6.11b) yields the best performance, with increasing benefits at increasing residence times. Similarly, multi-stage configurations (Figure 6.11 c and d) outperform the single-stage unsegmented configuration at high residence times. Even though multi-staging yields the same (gross) energy efficiency of the segmented configurations, the higher pumping losses (two stacks against one) result in a lower value of the product between net power density and net energy efficiency (Figure 6.11, Figure S6.3 and S6.4 in the Supporting Information). The advantage of the segmented electrode and multi-stage configurations derives from the possibility to tune the external load to the locally available emf and stack electrical resistance, as discussed by Simões et al. [27,28]. However, when considering the presence of multivalent ions, particularly magnesium, the relative advantage of segmentation or multi-staging is reduced and this results in a larger relative loss of power

6

density and efficiency (Figure S6.5 in the Supporting Information). This is the case as uphill transport occurring near the river water inlet reduces the available emf. Additionally, the loss in membrane permselectivity in the presence of multivalent ions further reduces the available emf. These emf losses result in decreased inhomogeneity of the emf between inlet (high emf) and outlet (low emf), an aspect that segmentation and multi-staging address resulting in an increase in power density and efficiency.
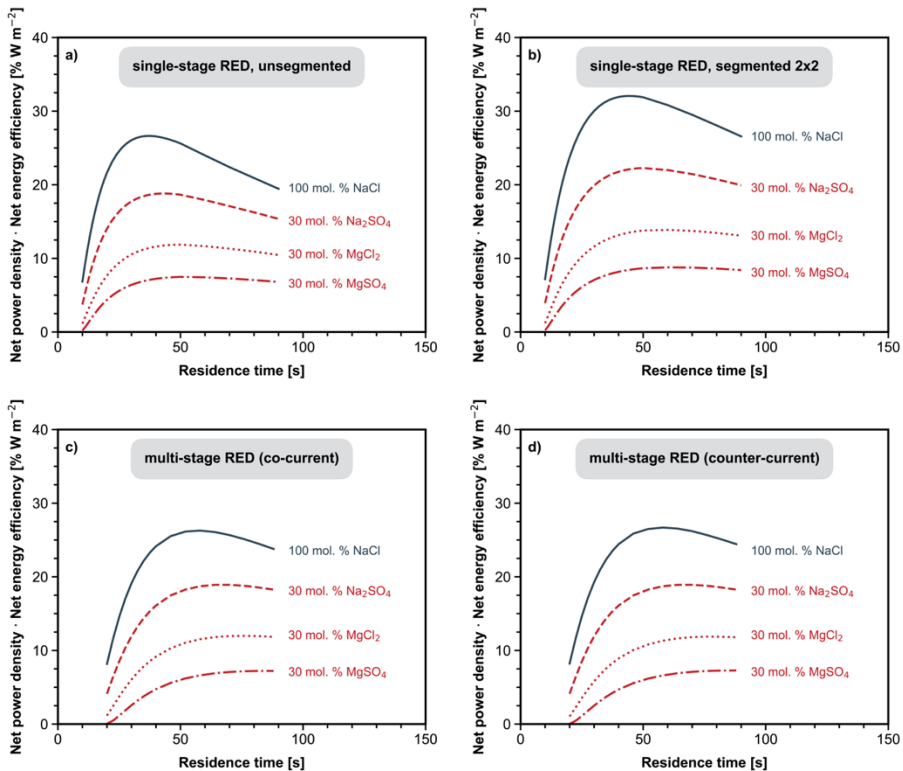
Figure 6.11 Simulation of RED performance for various flow configurations and feedwater compositions.

Clearly the presented model now allows predicting RED performances and evaluating operational conditions for realistic situations taking into account the complex effects of the presence of multivalent ions on RED performance when using natural feedwaters. With additional experimental selectivity and permselectivity data, the model can easily be extended to more complex, multicomponent ionic mixtures as well (as shown in the Supporting Information for a CEM exposed to a ternary mixture).

6.4 Conclusion

This work presents a model to predict RED performance taking into account the influence of the presence of magnesium and sulfate ions on power production with RED. The presence of multivalent ions results in loss in power due to several effects that are now included in the model. Uphill transport is accounted for in balancing two voltage sources, the increased membrane resistance is introduced based in experimental resistance and selectivity data, the membrane permselectivity loss is introduced by empirical fitting of experimental data, and the change in conductivity of the feedwaters is introduced based on the relationship between the total concentration of charged solids in the solutions and their electrical conductivity. Validation with experimental and literature data was performed and confirmed that the model effectively describes RED performance in the presence of sulfate or magnesium ions. Simulation of RED in various flow configurations and with a variety of feedwater compositions shows the importance of designing RED processes with the complexity of natural feedwaters in mind. Simulated RED behavior in the presence of 30 mol. % $MgSO_4$ drastically differs from the simulated behavior for feedwaters containing only NaCl. In particular, the advantages of electrode segmentation and multi-staging are mitigated by multivalent ions as the inhomogeneity of the electromotive force is reduced by uphill transport and permselectivity loss. The developed model is not only able to describe experimental data but can also predict RED performances at specific process conditions and as such provides a very valuable tool to design and evaluate RED process systems.

Supplementary information

Fitting of experimental data for the permselectivity loss factor

To include the permselectivity loss in the RED model, fitting of experimental data was performed. Data for RED experiments with magnesium ions were taken from Moreno et al. [20], while data for sulfate were taken from our previous study [19]. It should be noted that data with magnesium ions are not available for the same CEM (Fujifilm CEM Type 10), but only for the similar Fujifilm CEM Type I, which has a slightly lower starting permselectivity. The permselectivity loss is expected to be similar for the two membranes, as is the case for CEM type I and CEM T1 based on the data from Moreno et al. [19]. For the sulfate study, data are available for the same AEM used in the present study (Fujifilm AEM type 10).

The OCV data reported in the literature are compared with the expected equilibrium values after uphill transport, as estimated using the model developed by Vermaas et al. [23]. The difference is then entirely attributed to a loss in permselectivity (accounted for in the permselectivity loss factor K) for the membrane under investigation (Table S6.1).

Table S6.1 Permselectivity loss data calculated from the literature OCV data in [1, 2].

Multivalent ion	Multivalent ion fraction [-]	Permselectivity loss factor K [-]
	0	0
Mg^{2+}	0.1	0.15
	0.25	0.24
	0.5	0.26
	0	0
SO_4^{2-}	0.1	0.02
	0.25	0.06
	0.5	0.10

Fitting of the permselectivity loss factor as a function of the multivalent ion fraction is performed with linear interpolation for sulfate, while for magnesium ions a second-degree polynomial is used for fractions below 25 mol. % and linear interpolation is used for fractions higher than 25 mol. %. Figure S6.6.1 illustrates the experimental and fitting values for the permselectivity loss factors.
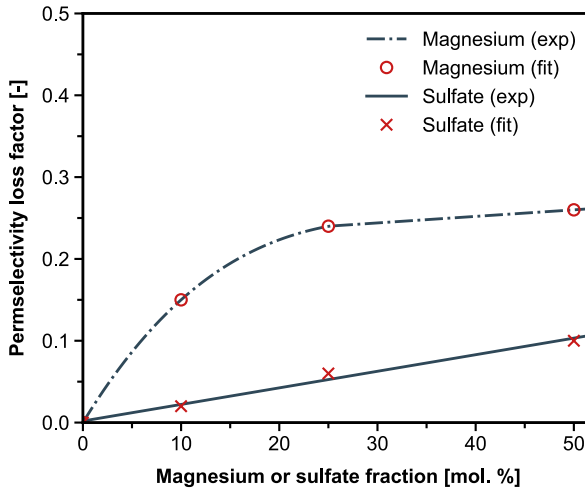
Figure S6.1 Literature values (dark red) and fitting values (dark blue) for the permselectivity loss factor.

RED model including magnesium and sulfate

The membrane monovalent over multivalent ion selectivities for the CEM and AEM (P [-]) are calculated based on the membrane electrical resistances measured with monovalent and multivalent ions only [21]:

$$P_{Mg}^{Na} = \frac{R_{CEM}^{Mg}}{R_{CEM}^{Na}} \qquad \text{(Eq. S6.1)}$$

$$P_{SO4}^{Cl} = \frac{R_{AEM}^{SO4}}{R_{AEM}^{Cl}} \qquad \text{(Eq. S6.2)}$$

Where R^x is the membrane electrical resistance [Ohm·m^2] measured in a solution containing x as counter-ion.

The current partitioning factor represents the fraction of the total current carried by the transport through the membrane of a certain ion. The current partitioning factors for magnesium, sodium, sulfate and chloride are calculated as follows.

$$f_{Mg} = \frac{1}{1 + 0.5 \cdot P_{Mg}^{Na} \cdot \frac{c_{Na}}{c_{Mg}}} \qquad \text{(Eq. S6.3)}$$

$$f_{Na} = 1 - f_{Mg} \qquad \text{(Eq. S6.4)}$$

$$f_{SO4} = \frac{1}{1 + 0.5 \cdot P_{SO4}^{Cl} \cdot \frac{c_{Cl}}{c_{SO4}}} \qquad \text{(Eq. S6.5)}$$

$$f_{Cl} = 1 - f_{SO4} \qquad \text{(Eq. S6.6)}$$

Where c are the molar concentrations of the ions in the seawater side [mol·L⁻¹], and the factor 0.5 derives from the ratio of the ion valences.

The river and seawater resistances are calculated as follows:

$$R_{rw} = \frac{1}{A_{open}} \cdot \frac{d_{rw}}{EC_{rw}} \qquad \text{(Eq. S6.7)}$$

$$R_{sw} = \frac{1}{A_{open}} \cdot \frac{d_{sw}}{EC_{sw}} \qquad \text{(Eq. S6.8)}$$

Where $1/A_{open}$ is the spacer shadow factor [-] accounting for the presence of the non-conductive spacers in the feedwater compartments (A_{open} is the fraction of the active area not occupied by the spacer) and for the non-ohmic component of the feedwaters resistance, d is the inter-membrane spacing [m], and EC is the solution conductivity [S·m⁻¹] calculated according to equation 8 of the main text.

With the membrane selectivities (eq. S6.1, S6.2), current partitioning factors (eq. S6.3-S6.6), and the resistances of the water compartments, the cell resistance [Ohm·m²] can be calculated:

$$R_{cell} = R_{blank} + N_{cp}\left(R_{rw} + R_{sw} + f_{Mg}R_{CEM}^{Mg} + f_{Na}R_{CEM}^{Na} + f_{SO4}R_{AEM}^{SO4} + f_{Cl}R_{AEM}^{Cl}\right) \qquad \text{(Eq. S6.9)}$$

Where R_{blank} is the blank resistance [Ohm·m²] accounting for the resistances of the electrodes and sealing CEM, and N_{cp} is the number of cell pairs [-].

The electromotive force (emf) for the different ions can be calculated using the modified Nernst equation and including the permselectivity loss factors (K [-]):

$$E_{Mg} = N_{cp}(1 - K_{CEM}^{loss})\alpha_{CEM}\frac{RT}{2F}\ln\left(\frac{\gamma_{sw}^{Mg} c_{sw}^{Mg}}{\gamma_{rw}^{Mg} c_{rw}^{Mg}}\right) \qquad \text{(Eq. S6.10)}$$

$$E_{Na} = N_{cp}(1 - K_{CEM}^{loss})\alpha_{CEM}\frac{RT}{F}\ln\left(\frac{\gamma_{sw}^{Na} c_{sw}^{Na}}{\gamma_{rw}^{Na} c_{rw}^{Na}}\right) \qquad \text{(Eq. S6.11)}$$

$$E_{SO4} = N_{cp}(1 - K_{AEM}^{loss})\alpha_{AEM}\frac{RT}{2F}\ln\left(\frac{\gamma_{sw}^{SO4} c_{sw}^{SO4}}{\gamma_{rw}^{SO4} c_{rw}^{SO4}}\right) \qquad \text{(Eq. S6.12)}$$

$$E_{Cl} = N_{cp}(1 - K_{AEM}^{loss})\alpha_{AEM}\frac{RT}{F}\ln\left(\frac{\gamma_{sw}^{Cl} c_{sw}^{Cl}}{\gamma_{rw}^{Cl} c_{rw}^{Cl}}\right) \qquad \text{(Eq. S6.13)}$$

$$E_{TOT} = E_{NaCl} = E_{Na} + E_{Cl} \qquad \text{(Eq. S6.14)}$$

Where α is the membrane permselectivity [-], R is the universal gas constant [J·mol⁻¹·K⁻¹], T is the absolute temperature [K], F is the Faraday constant [C·mol⁻¹], γ_{sw} and γ_{rw} are the activity coefficients [-] of sea and river water, and c_{sw} and c_{rw} are the ion concentrations [mol·L⁻¹] in sea and river water, respectively. The activity coefficients are estimated with

6

the three-characteristic-parameter correlation (TCPC) model of Ge et al. [44]. The overall emf is taken equal to that of sodium chloride (equation S14). When uphill transport balances the potentials of mono- and multivalent ions, this choice has no influence. However, for a small region of the active area close to the river water inlet, where the two potentials are not balanced, this choice for the total potential means considering the highest of the two electromotive forces, but this may result in only a small overestimation of the total current. Due to uphill transport, the emf of monovalent and multivalent ions is equal, with the exception of the region close to the river water inlet where uphill transport occurs and the two emfs are not balanced yet. In this region, the highest emf is considered to calculate downhill transport.

The overall current density for downhill transport is determined by the external load voltage (U_{load} [V]):

$$j_{TOT} = j_{Na} + j_{Mg} = j_{Cl} + j_{SO4} = \frac{E_{TOT} - U_{load}}{R_{cell}} \qquad \text{(Eq. S6.15)}$$

This formulation ensures continuity of the current across the CEMs and AEMs, while allowing for different partitioning of the current between monovalent and multivalent cations and anions. The downhill current densities (j [A·m^{-2}]) for each ion are calculated using the current partitioning factors:

$$j_{Mg} = f_{Mg} \cdot j_{TOT} = \frac{j_{TOT}}{1 + 0.5 \cdot P_{Mg}^{Na} \cdot \frac{c_{Na}}{c_{Mg}}} \qquad \text{(Eq. S6.16)}$$

$$j_{Na} = f_{Na} \cdot j_{TOT} = j_{TOT} - j_{Mg} \qquad \text{(Eq. S6.17)}$$

$$j_{SO4} = f_{SO4} \cdot j_{TOT} = \frac{j_{TOT}}{1 + 0.5 \cdot P_{SO4}^{Cl} \cdot \frac{c_{Cl}}{c_{SO4}}} \qquad \text{(Eq. S6.18)}$$

$$j_{Cl} = f_{Cl} \cdot j_{TOT} = j_{TOT} - j_{SO4} \qquad \text{(Eq. S6.19)}$$

To obtain the overall salt transport, the uphill transport current densities (equation 2 from the main text) need to be considered as well:

$$j_{uphill}^{Mg} = \frac{E_{Mg} - E_{Na}}{R_{CEM}^{Na} + R_{CEM}^{Mg}} \qquad \text{(Eq. S6.20)}$$

$$j_{uphill}^{Na} = -j_{uphill}^{Mg} \qquad \text{(Eq. S6.21)}$$

$$j_{uphill}^{SO4} = \frac{E_{SO4} - E_{Cl}}{R_{AEM}^{Cl} + R_{AEM}^{SO4}} \qquad \text{(Eq. S6.22)}$$

$$j_{uphill}^{Cl} = -j_{uphill}^{SO4} \qquad \text{(Eq. S6.23)}$$

The ion fluxes (J [mol·m^{-2}·s^{-1}]) from the sea to the river water compartment are obtained from the downhill and uphill current densities, together with an osmotic transport term:

$$J_{Mg} = \frac{j_{Mg} + j_{uphill}^{Mg}}{2F} + 2 \cdot D_{Mg} \frac{\left(c_{sw}^{Mg} - c_{rw}^{Mg}\right)}{l_m} \qquad \text{(Eq. S6.24)}$$

$$J_{Na} = \frac{j_{Na} + j_{uphill}^{Na}}{F} + 2 \cdot D_{Na} \frac{\left(c_{sw}^{Na} - c_{rw}^{Na}\right)}{l_m} \qquad \text{(Eq. S6.25)}$$

$$J_{SO4} = \frac{j_{SO4} + j_{uphill}^{SO4}}{2F} + 2 \cdot D_{SO4} \frac{\left(c_{sw}^{SO4} - c_{rw}^{SO4}\right)}{l_m} \qquad \text{(Eq. S6.26)}$$

$$J_{Cl} = \frac{j_{Cl} + j_{uphill}^{Cl}}{F} + 2 \cdot D_{Cl} \frac{\left(c_{sw}^{Cl} - c_{rw}^{Cl}\right)}{l_m} \qquad \text{(Eq. S6.27)}$$

Where D are the diffusion coefficients through the membrane [m^2·s^{-1}], l_m is the membrane thickness [m], and the factor 2 in the osmotic transport term derives from diffusion taking place through both the AEM and CEM. D_{Na} is assumed to be equal to D_{Cl} and their value is taken from our previous work [2]. D_{Mg} and D_{SO4} are taken from literature [36].

The osmotic water transport term [m·s^{-1}] as formulated by Veerman et al. [26] is given by:

$$J_{H2O} = -2 \cdot D_{H2O} \frac{\left(\sum_{salts} c_{sw}^i - \sum_{salts} c_{rw}^i\right)}{l_m} \frac{MW_{H2O}}{\rho_{H2O}} \qquad \text{(Eq. S6.28)}$$

Where MW_{H2O} is the molecular weight of water [kg·mol^{-1}] and ρ_{H2O} is the density of water [kg·m^{-3}].

The change in ion concentrations within the stack active area can be related to the ion and water fluxes, yielding the following partial differential equations (assuming river water flowing along the x direction, while seawater flows along the y direction):

$$\frac{dc_{sw}^{Mg}}{dy} = -W \left(\frac{J_{Mg}}{\phi_{sw}} - c_{sw}^{Mg} \frac{J_{H2O}}{\phi_{sw}} \right) \qquad \text{(Eq. S6.29)}$$

$$\frac{dc_{sw}^{Na}}{dy} = -W \left(\frac{J_{Na}}{\phi_{sw}} - c_{sw}^{Na} \frac{J_{H2O}}{\phi_{sw}} \right) \qquad \text{(Eq. S6.30)}$$

$$\frac{dc_{sw}^{SO4}}{dy} = -W \left(\frac{J_{SO4}}{\phi_{sw}} - c_{sw}^{SO4} \frac{J_{H2O}}{\phi_{sw}} \right) \qquad \text{(Eq. S6.31)}$$

$$\frac{dc_{sw}^{Cl}}{dy} = -W \left(\frac{J_{Cl}}{\phi_{sw}} - c_{sw}^{Cl} \frac{J_{H2O}}{\phi_{sw}} \right) \qquad \text{(Eq. S6.32)}$$

$$\frac{dc_{rw}^{Mg}}{dx} = L \left(\frac{J_{Mg}}{\phi_{rw}} - c_{rw}^{Mg} \frac{J_{H2O}}{\phi_{rw}} \right) \qquad \text{(Eq. S6.33)}$$

$$\frac{dc_{rw}^{Na}}{dx} = L \left(\frac{J_{Na}}{\phi_{rw}} - c_{rw}^{Na} \frac{J_{H2O}}{\phi_{rw}} \right) \qquad \text{(Eq. S6.34)}$$

$$\frac{dc_{rw}^{SO4}}{dx} = L \left(\frac{J_{SO4}}{\phi_{rw}} - c_{rw}^{SO4} \frac{J_{H2O}}{\phi_{rw}} \right) \qquad \text{(Eq. S6.35)}$$

6

$$\frac{dc_{rw}^{Cl}}{dx} = L\left(\frac{J_{Cl}}{\phi_{rw}} - c_{rw}^{Cl}\frac{J_{H2O}}{\phi_{rw}}\right)$$

(Eq. S6.36)

Where W and L are the width and length of the stack active area [m], and ϕ is the flow rate of the feedwaters [m³·s⁻¹]. The active area is discretized into a 500×500 grid, and the PDEs (eq. S6.29 – S6.36) are solved with the Forward Euler method using the inlet concentrations as boundary conditions. The power, power density (net and gross), energy efficiency (net and gross), and thermodynamic efficiency are calculated from the obtained concentration matrices equal to our previous work [27].

Briefly, the power [W] is calculated as follows:

$$P = E \cdot I = \frac{E^2}{R_{stack}}$$

(Eq. S6.37)

Where E is the electromotive force [V], I is the current [A], and R_{stack} is the stack resistance [Ω]. The net power is obtained by subtracting the pumping losses, while the power density is obtained by dividing it by the total membrane area (CEMs area + AEMs area).

The energy efficiency is calculated as follows:

$$\eta_{energy} = 100 \cdot \frac{P}{\Delta G_{in}}$$

(Eq. S6.38)

Where ΔG_{in} is the Gibbs free energy of mixing [J] of the two feedwaters calculated based on the compositions at the inlet. The net energy efficiency is obtained by using the net power in the efficiency calculations.

Model extension to ternary mixtures

The developed model can be easily extended to more complex mixtures as well. To illustrate this, a similar approach is followed for a ternary mixture and the equations are derived below (only for a CEM exposed to three generic cations A, B, and C, the same equations would apply to an AEM). All symbols and units in this derivation are consistent with the derivation presented in the previous section.

The selectivities based on membrane electrical resistance are:

$$P_B^A = \frac{R_{CEM}^B}{R_{CEM}^A}$$

(Eq. S6.39)

$$P_C^A = \frac{R_{CEM}^C}{R_{CEM}^A}$$

(Eq. S6.40)

While the selectivities as defined in equation 4 of the main text are:

$$P_B^A = \frac{j_A}{j_B}\frac{z_B}{z_A}\frac{c_B}{c_A}$$

(Eq. S6.41)

$$P_C^A = \frac{j_A}{j_C}\frac{z_C}{z_A}\frac{c_C}{c_A}$$ (Eq. S6.42)

The total current can be expressed as:

$$j_{TOT} = j_A + j_B + j_C = j_A\left(1 + \frac{1}{P_B^A}\frac{z_B}{z_A}\frac{c_B}{c_A} + \frac{1}{P_C^A}\frac{z_C}{z_A}\frac{c_C}{c_A}\right)$$ (Eq. S6.43)

The fraction of current transported by ion A is then:

$$f_A = \frac{j_A}{j_{TOT}} = \frac{1}{1 + \frac{1}{P_B^A}\frac{z_B}{z_A}\frac{c_B}{c_A} + \frac{1}{P_C^A}\frac{z_C}{z_A}\frac{c_C}{c_A}}$$ (Eq. S6.44)

The fractions of current transported by ion B and C can be calculated from j_A and equations S41 and S42:

$$f_B = \frac{j_B}{j_{TOT}} = \frac{\frac{j_A}{P_B^A}\frac{z_B}{z_A}\frac{c_B}{c_A}}{j_{TOT}}$$ (Eq. S6.45)

$$f_C = \frac{j_C}{j_{TOT}} = \frac{\frac{j_A}{P_C^A}\frac{z_C}{z_A}\frac{c_C}{c_A}}{j_{TOT}}$$ (Eq. S6.46)

Membrane electrical resistance model predictions

The example of Neosepta CMS shown in the main text shows that for CEMs having a relatively high selectivity (sodium over magnesium), e.g. monovalent-ion selective membranes, the approach described in equations 3 – 8 of the main text does not deliver an accurate prediction of the membrane electrical resistance in mixtures of monovalent and multivalent ions. This derives from the major increase in electrical resistance that even small fractions of magnesium ions produce for these membranes.

Avci et al. provided electrical resistance data for a Fujifilm CEM-80050 (a highly cross-linked membrane developed for RED applications with brines and seawater) at increasing fractions of magnesium ions in the test solutions [45]. Based on their data, the membrane selectivity is calculated to be 7.9 (equation 3 in the main text). Figure S6.2 shows a comparison of the experimental data with the prediction made using equations 4 – 8 of the main text using a selectivity value equal to 7.9. The observed trends are very different, with magnesium ions producing a much higher electrical resistance increase at low fractions than predicted by the model.

6
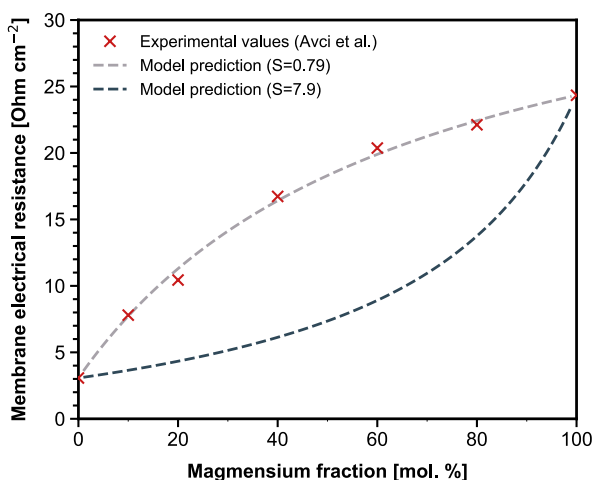
Figure S6.2 Experimental membrane electrical resistance for a Fujifilm CEM 80050 (from Avci et al. [9])(dark red markers) compared to the model predictions obtained for selectivity equal to 7.9 (dark blue dashed line) and 0.79 (grey dashed line).

To verify if the inconsistency between the results and the model derives from an invalid assumption in the model (e.g., non-constant selectivity), equations 4 – 8 from the main text were used to fit the experimental data. Interestingly, a constant selectivity value can fit the experimental data (Figure S6.2), but it is very different from what equation 3 (main text) would suggest. The fitted selectivity value of 0.79 (< 1) indicates that magnesium ions increase the resistance as if it was the preferential charge carrier. The data from Avci et al. [45] suggest that the proposed model would still be valid even for monovalent-ion selective membranes, provided that extra data are gathered to verify membrane electrical resistance and current partitioning predictions.

6

Unsegmented / Segmented 2x2 / multi-stage RED

Net power density
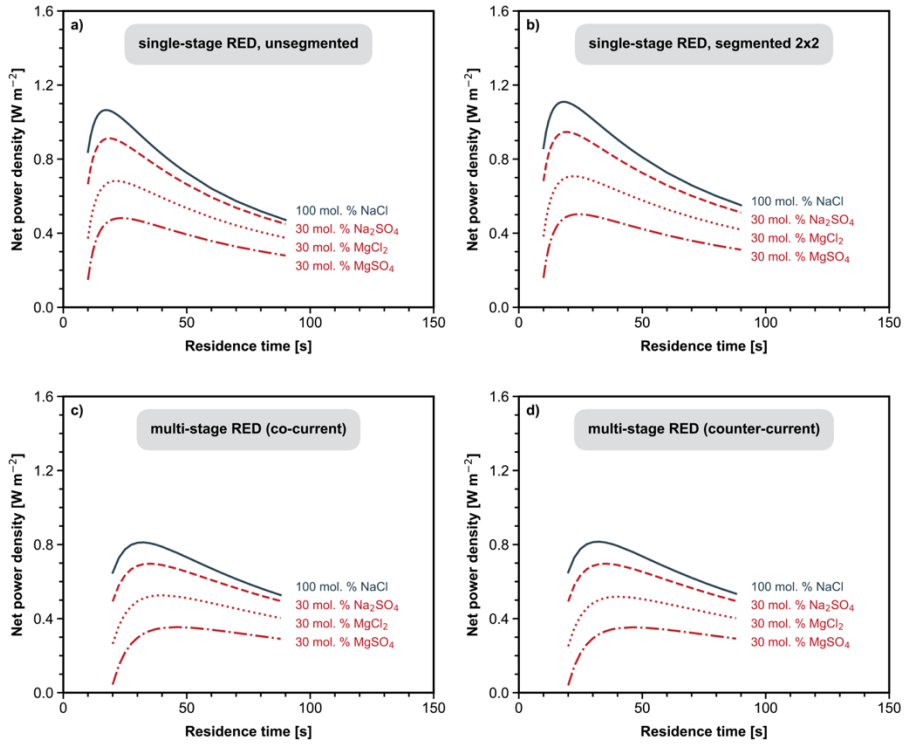
Figure S6.3 Net power density results from simulations of RED with various flow configurations and feedwater compositions

Net energy efficiency
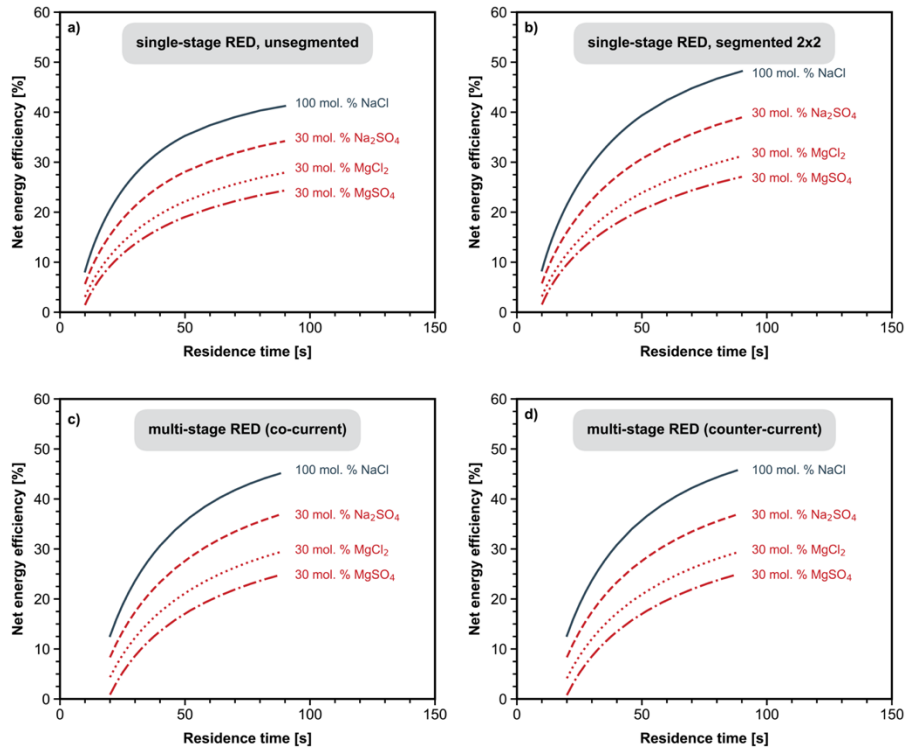
Figure S6.4 Net energy efficiency results from simulations of RED with various flow configurations and feedwater compositions.

Relative power density loss with 30 mol. % sulfate
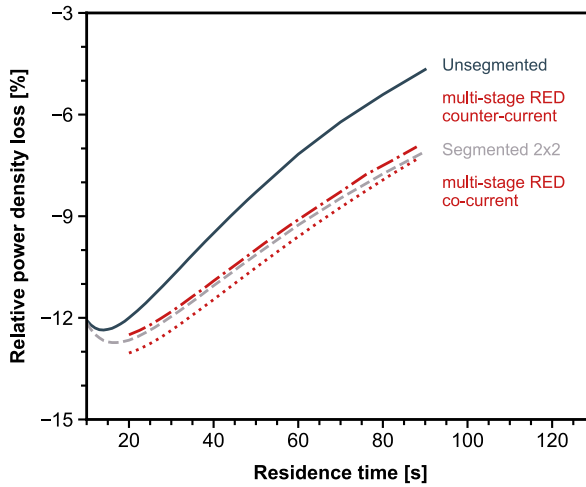
Figure S6.5 Relative power density loss as a function of residence time for the different flow configurations when comparing 100 mol. % NaCl in the feedwaters with a mixture containing 70 mol. % NaCl and 30 mol. % Na_2SO_4.

List of model parameters

| Parameter	Symbol	Value	Unit	Evaluation procedure
Width of the active area	W	0.22	m	Known stack parameter
Length of the active area	L	0.22	m	Known stack parameter
Compartment thickness	d	155×10^{-6}	m	Known stack parameter
AEM permselectivity	α_{aem}	94.5	%	Literature data [27]
CEM permselectivity	α_{cem}	94.7	%	Literature data [27]
AEM electrical resistance, 100 mol. % NaCl	R_{AEM}^{Cl}	1.8×10^{-4}	$\Omega \cdot m^2$	Measurement in a six-compartment cell at 0.5 M NaCl, according to literature procedure [46]
AEM electrical resistance, 100 mol. % Na_2SO_4	R_{AEM}^{SO4}	3.4×10^{-4}	$\Omega \cdot m^2$	Measurement in a six-compartment cell at 0.5 M NaCl, according to literature procedure [46]
CEM electrical resistance, 100 mol. % NaCl	R_{CEM}^{Na}	3.3×10^{-4}	$\Omega \cdot m^2$	Measurement in a six-compartment cell at 0.5 M NaCl, according to literature procedure [46]
CEM electrical resistance, 100 mol. % $MgCl_2$	R_{CEM}^{Mg}	11.0×10^{-4}	$\Omega \cdot m^2$	Measurement in a six-compartment cell at 0.5 M NaCl, according to literature procedure [46]
Open area (used to calculate the resistance of the feedwaters as in [8])	A_{open}	0.61 (Na_2SO_4 stack exp), 0.37 ($MgCl_2$ stack exp)	-	The initial value is 0.55, corresponding to the open area of the spacer netting (according to its specifications). The value is then adjusted based on I-V data measured for 100 mol. % NaCl.
Average water diffusion coefficient (through the membranes)	D_{H2O}	1.5×10^{-10}	$m^2 \cdot s^{-1}$	Literature data [27]

6

Parameter	Symbol	Value	Unit	Evaluation procedure
Monovalent ion diffusion coefficient (through the membranes)	D_{Na}, D_{Cl}	6.5×10^{-12}, 6.5×10^{-12}	$m^2 \cdot s^{-1}$	Literature data [27]
Multivalent ion diffusion coefficient (through the membranes)	D_{Mg}, D_{SO4}	3.3×10^{-12}	$m^2 \cdot s^{-1}$	The ratio between the diffusion coefficient of monovalent and divalent ions is taken from [36] and applied to the values from [27].
Membrane thickness	l_m	125×10^{-6}	m	Manufacturer specifications
Blank resistance	R_{blank}	$4 \times 37.5 \times 10^{-4}$	$\Omega \cdot m^2$	The extra CEM sealing the electrolyte compartment determines most of the blank resistance. Therefore, the value was take to be four times that reported in [27], since the active area is approximately ¼.
Pressure drop coefficient	$K_{\Delta P}$	0.1945	Pa·s	Literature data [27]

6

References

[1]   T.J. Crowley, Causes of climate change over the past 1000 years, Science. 289 (2000) 270–277. https://doi.org/10.1126/science.289.5477.270.

[2]   P.M. Cox, R.A. Betts, C.D. Jones, S.A. Spall, I.J. Totterdell, Acceleration of global warming due to carbon-cycle feedbacks in a coupled climate model, Nature. 408 (2000) 184–187. https://doi.org/10.1038/35041539.

[3]   M. Meinshausen, N. Meinshausen, W. Hare, S.C.B. Raper, K. Frieler, R. Knutti, D.J. Frame, M.R. Allen, Greenhouse-gas emission targets for limiting global warming to 2°C, Nature. 458 (2009) 1158–1162. https://doi.org/10.1038/nature08017.

[4]   J.W. Post, H.V.M. Hamelers, C.J.N. Buisman, Energy recovery from controlled mixing salt and fresh water with a reverse electrodialysis system, Environmental Science and Technology. 42 (2008) 5785–5790. https://doi.org/10.1021/es8004317.

[5]   J. Kuleszo, C. Kroeze, J. Post, B.M. Fekete, The potential of blue energy for reducing emissions of CO_2 and non- CO_2 greenhouse gases, Journal of Integrative Environmental Sciences. 7 (2010) 89–96. https://doi.org/10.1080/19438151003680850.

[6]   J.W. Post, J. Veerman, H.V.M. Hamelers, G.J.W. Euverink, S.J. Metz, K. Nymeijer, C.J.N. Buisman, Salinity-gradient power: Evaluation of pressure-retarded osmosis and reverse electrodialysis, Journal of Membrane Science. 288 (2007) 218–230. https://doi.org/10.1016/j.memsci.2006.11.018.

[7]   J.W. Post, C.H. Goeting, J. Valk, S. Goinga, J. Veerman, H.V.M. Hamelers, P.J.F.M. Hack, Towards implementation of reverse electrodialysis for power generation from salinity gradients, Desalination and Water Treatment. 16 (2010) 182–193. https://doi.org/10.5004/dwt.2010.1093.

[8]   M. Tedesco, A. Cipollina, A. Tamburini, G. Micale, Towards 1 kW power production in a reverse electrodialysis pilot plant with saline waters and concentrated brines, Journal of Membrane Science. 522 (2017) 226–236. https://doi.org/10.1016/j.memsci.2016.09.015.

[9]   D.A. Vermaas, M. Saakes, K. Nijmeijer, Power generation using profiled membranes in reverse electrodialysis, Journal of Membrane Science. 385–386 (2011) 234–242. https://doi.org/10.1016/j.memsci.2011.09.043.

[10]   E. Güler, R. Elizen, M. Saakes, K. Nijmeijer, Micro-structured membranes for electricity generation by reverse electrodialysis, Journal of Membrane Science. 458 (2014) 136–148. https://doi.org/10.1016/j.memsci.2014.01.060.

[11]   A.H. Galama, J.W. Post, H.V.M. Hamelers, V.V. Nikonenko, P.M. Biesheuvel, On the origin of the membrane potential arising across densely charged ion exchange membranes: How well does the teorell-meyer-sievers theory work?, Journal of Membrane Science and Research. 2 (2016) 128–140.

[12]   A. Daniilidis, D.A. Vermaas, R. Herber, K. Nijmeijer, Experimentally obtainable energy from mixing river water, seawater or brines with reverse electrodialysis, Renewable Energy. 64 (2014) 123–131. https://doi.org/10.1016/j.renene.2013.11.001.

[13]   D.A. Vermaas, M. Saakes, K. Nijmeijer, Early detection of preferential channeling in reverse electrodialysis, Electrochimica Acta. 117 (2014) 9–17. https://doi.org/10.1016/j.electacta.2013.11.094.

6

[14]   D.A. Vermaas, D. Kunteng, M. Saakes, K. Nijmeijer, Fouling in reverse electrodialysis under natural conditions, Water Research. 47 (2013) 1289–1298. https://doi.org/10.1016/j.watres.2012.11.053.

[15]   D.A. Vermaas, D. Kunteng, J. Veerman, M. Saakes, K. Nijmeijer, Periodic feedwater reversal and air sparging as antifouling strategies in reverse electrodialysis, Environmental Science and Technology. 48 (2014) 3065–3073. https://doi.org/10.1021/es4045456.

[16]   E.J. Bodner, M. Saakes, T. Sleutels, C.J.N. Buisman, H.V.M. Hamelers, The RED Fouling Monitor: A novel tool for fouling analysis, Journal of Membrane Science. 570–571 (2019) 294–302. https://doi.org/10.1016/j.memsci.2018.10.059.

[17]   S.P. Nunes, Can fouling in membranes be ever defeated?, Current Opinion in Chemical Engineering. 28 (2020) 90–95. https://doi.org/10.1016/j.coche.2020.03.006.

[18]   V. Lindstrand, G. Sundström, A.-S. Jönsson, Fouling of electrodialysis membranes by organic substances, Desalination. 128 (2000) 91–102. https://doi.org/10.1016/S0011-9164(00)00026-6.

[19]   D. Pintossi, C.-L. Chen, M. Saakes, K. Nijmeijer, Z. Borneman, Influence of sulfate on anion exchange membranes in reverse electrodialysis, Npj Clean Water. 3 (2020) 29. https://doi.org/10.1038/s41545-020-0073-7.

[20]   J. Moreno, V. Díez, M. Saakes, K. Nijmeijer, Mitigation of the effects of multivalent ion transport in reverse electrodialysis, Journal of Membrane Science. 550 (2018) 155–162. https://doi.org/10.1016/j.memsci.2017.12.069.

[21]   T. Rijnaarts, E. Huerta, W. van Baak, K. Nijmeijer, Effect of Divalent Cations on RED Performance and Cation Exchange Membrane Selection to Enhance Power Densities, Environmental Science and Technology. 51 (2017) 13028–13035. https://doi.org/10.1021/acs.est.7b03858.

[22]   J.W.J.W. Post, H.V.M.H.V.M. Hamelers, C.J.N.C.J.N. Buisman, Influence of multivalent ions on power production from mixing salt and fresh water with a reverse electrodialysis system, Journal of Membrane Science. 330 (2009) 65–72. https://doi.org/10.1016/j.memsci.2008.12.042.

[23]   D.A. Vermaas, J. Veerman, M. Saakes, K. Nijmeijer, Influence of multivalent ions on renewable energy generation in reverse electrodialysis, Energy Environ. Sci. 7 (2014) 1434–1445. https://doi.org/10.1039/C3EE43501F.

[24]   B. Tansel, Significance of thermodynamic and physical characteristics on permeation of ions during membrane separation: Hydrated radius, hydration free energy and viscous effects, Separation and Purification Technology. 86 (2012) 119–126. https://doi.org/10.1016/j.seppur.2011.10.033.

[25]   M. Tedesco, A. Cipollina, A. Tamburini, W. van Baak, G. Micale, Modelling the Reverse ElectroDialysis process with seawater and concentrated brines, Desalination and Water Treatment. 49 (2012) 404–424. https://doi.org/10.1080/19443994.2012.699355.

[26]   J. Veerman, M. Saakes, S.J. Metz, G.J. Harmsen, Reverse electrodialysis: A validated process model for design and optimization, Chemical Engineering Journal. 166 (2011) 256–268. https://doi.org/10.1016/j.cej.2010.10.071.

6

[27]   C. Simões, D. Pintossi, M. Saakes, Z. Borneman, W. Brilman, K. Nijmeijer, Electrode segmentation in reverse electrodialysis: Improved power and energy efficiency, Desalination. 492 (2020). https://doi.org/10.1016/j.desal.2020.114604.

[28]   C. Simões, D. Pintossi, M. Saakes, W. Brilman, Multistage Reverse Electrodialysis: An Experimental and Model Investigation with Artificial Sea and River Water, Manuscript Submitted for Publication. (2020).

[29]   D.A. Vermaas, J. Veerman, N.Y. Yip, M. Elimelech, M. Saakes, K. Nijmeijer, High efficiency in energy generation from salinity gradients with reverse electrodialysis, ACS Sustainable Chemistry and Engineering. 1 (2013) 1295–1302. https://doi.org/10.1021/sc400150w.

[30]   A.H. Galama, G. Daubaras, O.S. Burheim, H.H.M. Rijnaarts, J.W. Post, Seawater electrodialysis with preferential removal of divalent ions, Journal of Membrane Science. 452 (2014) 219–228. https://doi.org/10.1016/j.memsci.2013.10.050.

[31]   M. Tedesco, H.V.M. Hamelers, P.M. Biesheuvel, Nernst-Planck transport theory for (reverse) electrodialysis: I. Effect of co-ion transport through the membranes, Journal of Membrane Science. 510 (2016) 370–381. https://doi.org/10.1016/j.memsci.2016.03.012.

[32]   M. Tedesco, H.V.M. Hamelers, P.M. Biesheuvel, Nernst-Planck transport theory for (reverse) electrodialysis: II. Effect of water transport through ion-exchange membranes, Journal of Membrane Science. 531 (2017) 172–182. https://doi.org/10.1016/j.memsci.2017.02.031.

[33]   M. Tedesco, H.V.M. Hamelers, P.M. Biesheuvel, Nernst-Planck transport theory for (reverse) electrodialysis: III. Optimal membrane thickness for enhanced process performance, Journal of Membrane Science. 565 (2018) 480–487. https://doi.org/10.1016/j.memsci.2018.07.090.

[34]   L. Gómez-Coma, V.M. Ortiz-Martínez, J. Carmona, L. Palacio, P. Prádanos, M. Fallanza, A. Ortiz, R. Ibañez, I. Ortiz, Modeling the influence of divalent ions on membrane resistance and electric power in reverse electrodialysis, Journal of Membrane Science. 592 (2019) 117385. https://doi.org/https://doi.org/10.1016/j.memsci.2019.117385.

[35]   J.G. Hong, W. Zhang, J. Luo, Y. Chen, Modeling of power generation from the mixing of simulated saline and freshwater with a reverse electrodialysis system: The effect of monovalent and multivalent ions, Applied Energy. 110 (2013) 244–251. https://doi.org/10.1016/j.apenergy.2013.04.015.

[36]   A.A. Moya, Uphill transport in improved reverse electrodialysis by removal of divalent cations in the dilute solution: A Nernst-Planck based study, Journal of Membrane Science. 598 (2020). https://doi.org/10.1016/j.memsci.2019.117784.

[37]   S. Honarparvar, D. Reible, Modeling multicomponent ion transport to investigate selective ion removal in electrodialysis, Environmental Science and Ecotechnology. 1 (2020) 100007. https://doi.org/https://doi.org/10.1016/j.ese.2019.100007.

[38]   A. Culcasi, L. Gurreri, A. Zaffora, A. Cosenza, A. Tamburini, G. Micale, On the modelling of an Acid/Base Flow Battery: An innovative electrical energy storage device based on pH and salinity gradients, Applied Energy. 277 (2020) 115576. https://doi.org/https://doi.org/10.1016/j.apenergy.2020.115576.

[39]   T. Sata, Properties, Characterization and Microstructure of Ion Exchange Membranes, in: T. Sata (Ed.), Ion Exchange Membranes: Preparation, Characterization, Modification and

6

Application, The Royal Society of Chemistry, 2004: pp. 89–134. https://doi.org/10.1039/9781847551177-00089.

[40]   M. Higa, A. Tanioka, K. Miyasaka, Simulation of the transport of ions against their concentration gradient across charged membranes, Journal of Membrane Science. 37 (1988) 251–266. https://doi.org/10.1016/S0376-7388(00)82432-1.

[41]   T. Badessa, V. Shaposhnik, The electrodialysis of electrolyte solutions of multi-charged cations, Journal of Membrane Science. 498 (2016) 86–93. https://doi.org/10.1016/j.memsci.2015.09.017.

[42]   N.R.G. Walton, Electrical Conductivity and Total Dissolved Solids—What is Their Precise Relationship?, Desalination. 72 (1989) 275–292. https://doi.org/https://doi.org/10.1016/0011-9164(89)80012-8.

[43]   D.A. Vermaas, M. Saakes, K. Nijmeijer, Doubled power density from salinity gradients at reduced intermembrane distance, Environmental Science and Technology. 45 (2011) 7089–7095. https://doi.org/10.1021/es2012758.

[44]   X. Ge, M. Zhang, M. Guo, X. Wang, Correlation and Prediction of Thermodynamic Properties of Nonaqueous Electrolytes by the Modified TCPC Model, Journal of Chemical & Engineering Data. 53 (2008) 149–159. https://doi.org/10.1021/je700446q.

[45]   A.H. Avci, P. Sarkar, R.A. Tufa, D. Messana, P. Argurio, E. Fontananova, G. di Profio, E. Curcio, Effect of Mg^{2+}ions on energy generation by Reverse Electrodialysis, Journal of Membrane Science. 520 (2016) 499–506. https://doi.org/10.1016/j.memsci.2016.08.007.

[46]   P. Długołecki, K. Nymeijer, S. Metz, M. Wessling, Current status of ion exchange membranes for power generation from salinity gradients, J Journal of Membrane Science. 319 (2008) 214–222. doi:10.1016/j.memsci.2008.03.037.

6

Chapter 7

Conclusions and outlook

This chapter presents the conclusions of the thesis and outlook on future RED developments considering the scientific findings presented in the previous chapters on fouling monitoring, modeling, and control via membrane surface modification.

7.1 Conclusions

This thesis aimed to increase the understanding of fouling in reverse electrodialysis while providing tools for real-time fouling monitoring, validating promising surface modification strategies for fouling control, and developing a model that includes the effect of multivalent ions in the feedwaters.

In <u>Chapter 2</u>, electrochemical impedance spectroscopy (EIS) is presented as a tool for fouling monitoring at the RED stack level. The results of fouling and cleaning experiments with sodium dodecylbenzenesulfonate (SDBS) showed how fouling evolved differently for the AEM and CEM. Fouling was first observed with a rapid increase of the ohmic resistance of the AEM, followed by an increase of the non-ohmic component of the AEM resistance, when SDBS domains started to grow on the membrane. The non-ohmic resistance of the CEM started increasing after a longer time, as SDBS in the river water is driven to the CEM by the electric field. Upon cleaning, irreversible fouling of the AEM due to SDBS absorption in the membrane was observed, as the ohmic resistance recovered only partially. The non-ohmic components of the AEM and CEM resistances recovered completely. These results increased the understanding of how organic fouling negatively affects the different stack elements. Additionally, EIS was shown to be a valid tool for real-time fouling monitoring at the stack level.

In <u>Chapter 3</u>, a zwitterionic membrane surface chemistry is used to obtain anti-fouling AEMs. For this purpose, commercial AEMs were coated with either polydopamine followed by grafting of zwitterionic monomers on its surface or with a modified polydopamine coating followed by grafting of zwitterionic brushes on the membrane surface. The modification layers hardly affected the electrical resistance and the permselectivity of the membrane thanks to the net neutral charge of the coating and the thin grafting layers. The membrane hydrophilicity clearly increased, offering a method to mitigate fouling. The fouling resistance for both the membranes modified with zwitterionic monomers and those modified with zwitterionic brushes was improved. The zwitterionic monomers delayed the fouling onset, whereas the zwitterionic brushes delayed the fouling onset and also slowed down the fouling layer growth. Therefore, Chapter 3 validates the use of zwitterionic layers as an effective strategy to obtain anti-fouling AEMs.

7

In <u>Chapter 4</u>, a validated RED model and experimental investigation is presented that shows how electrode segmentation increases net power density and net energy efficiency. The gains were attained when optimizing the external loads simultaneously for overall maximum power, rather than sequentially maximizing the power output of individual segments. The net power density output for a segmented electrode was 39 % higher than for a single electrode when compared at the same net energy efficiency (40 %). This increase in net power density at equal net energy efficiency resulted from combining the increase in available power due to shorter residence time and the increased ion exchange enabled by electrode segmentation. Therefore, electrode segmentation is a promising strategy to increase the power density and energy efficiency of RED.

In <u>Chapter 5</u>, a study on the effect of multivalent anions on AEMs in RED with standard grade and monovalent-ion selective membranes concluded that sulfate and other multivalent anions can play an important role in reducing RED power density. Sulfate deteriorates RED performance due to the decreased electromotive force resulting from uphill transport and reduced membrane permselectivity, and increased membrane resistance in the course of long-term exposure to feedwaters containing multivalent anions. Despite the similarities between the effects of multivalent anions and those of multivalent cations, the narrower range of hydrated radii and hydration energies for anions compared to cations resulted not only in a smaller electrical resistance increase over time, but also in lower selectivity, which is detrimental for the open circuit voltage. With its focus on multivalent anions, Chapter 5 contributes to increasing the understanding of fouling in RED.

<u>Chapter 6</u> presents a RED model accounting for the presence of multivalent ions in the feedwaters and their negative influence on RED power production. Validation with experimental data was performed, showing that the model effectively described RED performance in the presence of sulfate or magnesium ions. Additionally, simulations of RED performed with various stack and flow configurations highlighted the need of designing RED processes with the complexity of natural feedwaters in mind. The results of the simulations showed that RED performance in the presence of $MgSO_4$ drastically differed from the simulated behavior for feedwaters containing only NaCl. In particular, the simulation results showed that the advantages of electrode segmentation and multi-staging were partially mitigated by multivalent ions, as uphill transport and permselectivity loss reduced the inhomogeneity of the electromotive force. The developed RED model provides a valuable tool to design RED process systems, considering not only NaCl in the feedwaters, but also multivalent ions.

7.2 Outlook

Fouling monitoring

In Chapter 2, real-time fouling monitoring at the RED stack level was presented, based on electrochemical impedance spectroscopy (EIS). The design presented in Chapter 2 can be further optimized by developing a dedicated fouling monitoring device based on a RED stack with small active area, without the need to use extensive gaskets to cover a large portion of the electrodes. Additionally, the number of monitored cell pairs can be increased, as their impedances would sum up in series, without affecting the characteristic frequencies of the system and without increasing the measurement time.

Another interesting development for fouling monitoring in RED would be the ability to measure local stack resistance or impedance. As most foulants are charged particles, the inhomogeneous current density distribution in the active area promotes different fouling rates (Figure 7.1a) [1]. The ability to measure local resistance would provide a deeper understanding of the relationship between local current densities and local fouling rates. Additionally, even without fouling, monitoring local resistances would be a useful tool to validate the results of RED models. For this purpose, in-situ measurements of impedance spectra can be performed with silver or platinum wires embedded in the non-conductive spacers (Figure 7.1b).

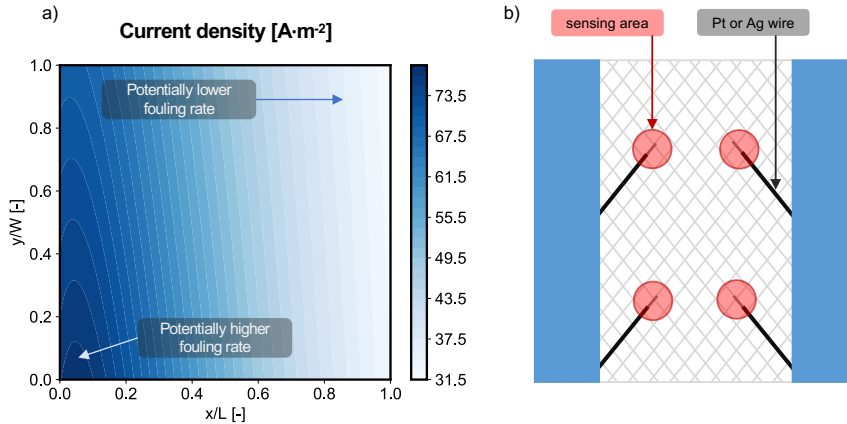**Figure 7.1** a) Distribution of the local current density in the active area of a RED stack at maximum power point. b) Gasket-integrated spacer embedding insulated metal wires in place of selected filaments of the polymeric netting to measure local resistances.

The modified spacers can be placed across a single membrane or across a cell pair, monitoring their local impedance. Segmented electrodes can be used to apply an AC input

over the selected areas, while the wires pick up the local AC output, measuring its amplitude and phase shift. Using a similar configuration, albeit without electrode segmentation, Pawlowski et al. reported the use of a single couple of silver wires clamped across a CEM inside the membrane stack to perform linear sweep voltammetry and chronopotentiometry measurements, yielding information on the thickness of the diffusion boundary layer [2].

Finally, fouling monitoring would benefit from the development of a unified RED fouling index, bundling the negative effects of colloidal particles, multivalent ions, natural organic matter, and biofouling into a single metric. This would have the advantage of quantifying the extent of fouling in a consistent manner across different experimental conditions. The idea of a fouling index is not new, as the membrane fouling index (MFI) is a standardized quantity in the field of membrane filtration, where models have been developed to predict the MFI based on the membrane properties and on the foulants present in the feed [3,4]. Similarly, the development of a RED fouling index and models to predict it would express a correlation between the properties of the feedwaters (e.g., ionic composition, turbidity, total organic carbon content, and temperature) and the expected negative impact of fouling on the membranes and RED stack properties. However, the development of a model including a quantitative description of all possible interactions between the stack elements and the foulants is a significant challenge. Evidence of this is found in the work of Park et al., who developed a model predicting MFI for microfiltration membranes [3]. The agreement between predicted MFI values and experimental data is very good for feeds containing only inorganic particles, but their predictions become consistently less accurate when organic matter is present in the feed [3]. For this reason, the development of a RED fouling index and models to predict it may be best suited for a data-driven approach, where advanced statistical tools (machine learning algorithms) are used to infer the relationship between inputs (feedwater characteristics and stack properties) and output (RED fouling index) from a sufficiently large dataset [5]. This topic is further discussed in section 7.3 on RED modeling.

Membrane development

The ion exchange membranes (IEMs) are the key element of the RED stack. For this reason, much of the developments in the RED field concerned the membranes. There are three key areas in membrane research: 1) membrane RED performance, typically benchmarked with measurements in a laboratory environment and NaCl solutions; 2) fouling resistance, evaluated both in laboratory environments (as presented in Chapter 3

and Chapter 5) and in RED pilots; and 3) membrane cost. While the first two areas of research have received much attention, membrane cost has been identified as a key factor determining the financial feasibility of RED [6], but little research has been reported in the literature on reducing membrane cost without sacrificing RED performance. Furthermore, research in these three areas is typically carried out separately with RED performance optimization rarely considering fouling, and surface modification studies that induce anti-fouling functionality having often detrimental effects on RED performance due to increased membrane resistance or decreased membrane permselectivity.

The future challenge for membrane development is to focus on the simultaneous optimization of membranes in all key areas: high RED performance, anti-fouling resistance, and low cost. Given the complexity of the issue, a promising strategy is the use of genetic algorithms (GAs) paired with a high-throughput (HT) platform for membrane fabrication and testing to explore the large number of possible combinations looking for the optimal result. GAs are stochastic search techniques inspired by the natural processes of selection and evolution, and they are part of the larger family of evolutionary algorithms [7]. Their principle is illustrated in Figure 7.2.

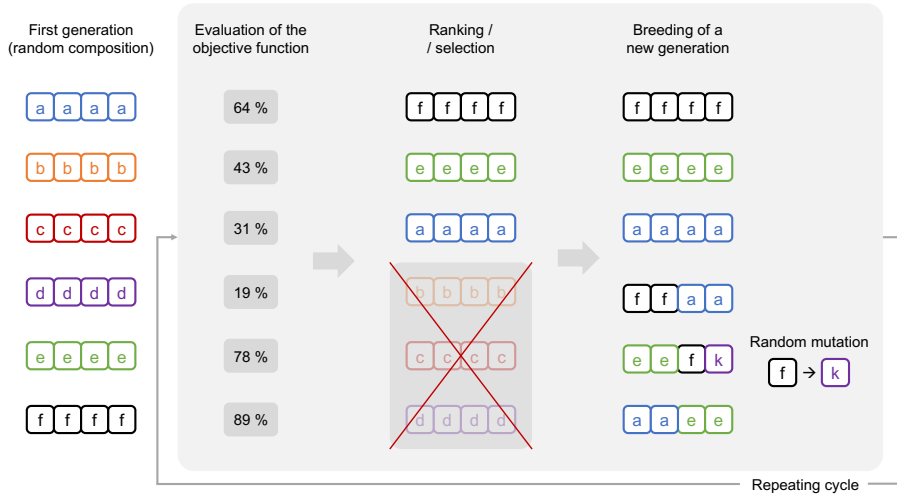**Figure 7.2** Working principle of genetic algorithms (GAs).

GAs explore a complex parameter space in an iterative manner, by generating successive sets of samples (generations) based on evolutionary operators (cross-over and mutation). Every sample is identified by a set of descriptors (e.g., for IEMs, the porous support characteristics, formulation of the ion conductive phase, characteristics of an eventual

surface modification layer, fabrication conditions). In the first generation, these descriptors are randomly initialized. Once the samples are fabricated, their fitness is evaluated to generate a sample ranking. This involves testing of the properties of the samples, which are then bundled in a single descriptor (objective function) expressing the desired parameter(s) that need to be optimized and, in evolutionary terms, representing the fitness (i.e., the probability of survival) of the sample. Once all samples are ranked based on their fitness, the worst ones are discarded, while the best ones make it to the next generation (selection process). Additionally, the size of population of the following generation is increased by breeding the best-performing samples to generate new combinations. The characteristics of the parent samples are combined and transmitted to their offspring (cross-over), with the possibility to have random variations (mutation). This breeding process is fitness-proportional, thus the probability of a sample to originate new combinations is proportional to its fitness value. A new cycle is then started by the evaluation of the fitness (objective function) for all samples in the new generation. This iterative process is terminated when the objective function is maximized or when a desired threshold value is reached. Thanks to this process, GAs have the ability to explore a large parameter space in a self-adaptive manner and they are not constrained by local optima [8]. For this reason, they have been used in a wide range of applications, starting with drug development and reaching also membrane science [9]. Among others, Vandezande et al. used GAs to optimize the performance of solvent-resistance nanofiltration membranes based on fabrication by phase inversion, exploring a nine-dimensional parameter space and reaching the desired objective function threshold in three generations (176 casting solution formulations, resulting in 125 membranes to test) [8].

Due to the large number of samples generated, GAs are frequently paired with HT platforms that facilitate the preparation and testing of large volume of samples. For membrane fabrication, this would involve automating the preparation of the solution used to impregnate the porous support, the membrane fabrication process, and possibly membrane testing.

A final aspect to be considered for the use of GAs paired with a HT platform for RED membranes development is the choice of the objective function to rank the samples based on fitness. RED performance can be evaluated starting with membrane characterizations. The measured membrane properties (e.g., electrical resistance, permselectivity, thickness, water and salt diffusion coefficients) are then used as an input in the model presented in Chapter 4 (NaCl only) or Chapter 6 (including multivalent ions), which produces data on net power density and net energy efficiency. Their product, also called response product,

is an effective descriptor of RED performance, bundling gross power density, pumping losses, and efficiency [10]. Anti-fouling performance is best evaluated with RED stack fouling experiments, but these would not be compatible with the large volume of samples produced by the HT platform due to the time needed for the assembly and testing of a RED stack. Therefore, a quicker fouling test, such as measurement of transition time in the presence of a model foulant, performed in a consistent manner for all samples and with an improved cell design, would be a more suitable choice as a descriptor of anti-fouling functionality. Finally, to evaluate cost, an estimate of the membrane fabrication cost, based on materials cost and processing cost, can be considered. The three descriptors can be assembled into an objective function (OF) as follows:

$$OF = \frac{R}{R^0} \cdot \frac{t}{t^0} \cdot \frac{C^0}{C} \qquad \text{(Eq. 7.1)}$$

Where R is the response product of the membrane (W·m^{-2}·%), R^0 is a target response product used to normalize the RED performance descriptor, t is the measured transition time (min), t^0 is the desired transition time used to normalize the anti-fouling functionality descriptor, C^0 is the target membrane cost (€·m^{-2}) to normalize the cost descriptor, and C is the membrane cost of the sample. With the objective function formulated in Equation 7.1, all parameters are given the same weight and the OF would exceed the unitary value when all threshold values are reached.

As an alternative objective function, the stochastic model reported by Daniilidis to predict the levelized cost of energy (LCOE, €·kWh^{-1}) for RED could be used to calculate the objective function [6]. In its present formulation, this model considers membrane cost, power density, and efficiency, which are used to evaluate the operation of a RED plant for a period of 30 years, divided in 5 years of pilot phase and 25 years of power production. If the model is adapted to accommodate anti-fouling functionality and its effect on RED operation over time (e.g., by adjusting the power density decline over time and by introducing stack cleaning costs), then the calculated LCOE would effectively act as an objective function considering all aspects: RED performance, anti-fouling resistance, and membrane cost. However, unlike the OF presented in Equation 7.1, when using the LCOE as OF, the weight attributed to the different aspects of RED is different, with membrane cost playing the biggest role in the determination of LCOE compared to RED performance and, possibly, fouling resistance.

7

Modeling

In Chapter 4, the benefit of electrode segmentation for power density and efficiency was highlighted, with a RED model improving the understanding and guiding the optimization of the external load voltages to achieve maximum power density. In recent years, RED models have assisted RED development as tools to explore the process parameters space rapidly. Veerman et al. used a model to optimize RED performance, identifying power density and response product as good parameters for optimization, and to improve RED stack design [11]. Vermaas et al. used modeling to prove that RED can achieve much higher efficiencies than it was thought [12]. Tedesco et al. studied the influence of co-ion transport, water transport, and membrane thickness to optimize RED performance [13–15]. While these models provide very valuable insight into RED process optimization, they are based on feedwaters containing only sodium chloride and on the description of RED based on a cell pair, or multiple cell pairs behaving in the same ideal way.

The future challenge for RED modeling is to move beyond the current paradigm by accounting for the non-ideal behavior of the RED stack, including ionic short-circuit currents (ISCCs) and the real complexity of the feedwaters. First steps in these directions were already made, as Veerman et al. reported a model approach including the effect of ISCCs [16]. Additionally, Culcasi et al. reproposed the approach of Veerman et al. without approximations in their solution strategy [16,17]. To account for more elements in the feedwaters than only NaCl, Chapter 6 presented a validated RED model predicting RED performance in the presence of multivalent ions in the feedwaters.

Further work can be done to model the RED stack including the effect of ISCCs. The approach of Veerman et al. is based on the interaction between two models: 1) a cell pair model, where ISCCs are neglected, which is solved to find the steady state salt concentration profiles in the sea and river water compartments, together with the electromotive force and cell resistance profiles; and 2) a stack model in the form of an electrical network including the ionic shortcut pathways, which uses the solution of the first model to determine the values of the voltage sources and resistors in the network, which is then solved based on Kirchhoff's circuit laws, yielding information on RED performance accounting for the presence of the ISCCs. The two models and their interaction are illustrated in Figure 7.3a. However, this approach suffers from some limitations, as information only flows from the cell pair model to the network model. The optimal external load predicted by the cell pair model and the optimal external load predicted by stack network model do not match. This results in the stack network model containing approximate values for the cell resistances, which are calculated at a different

7

external load value. For relatively low number of cell pairs, this approximation holds. However, at increasingly large numbers of cell pairs (100+), with increased magnitude of the ISCCs, this approach becomes increasingly less valid.
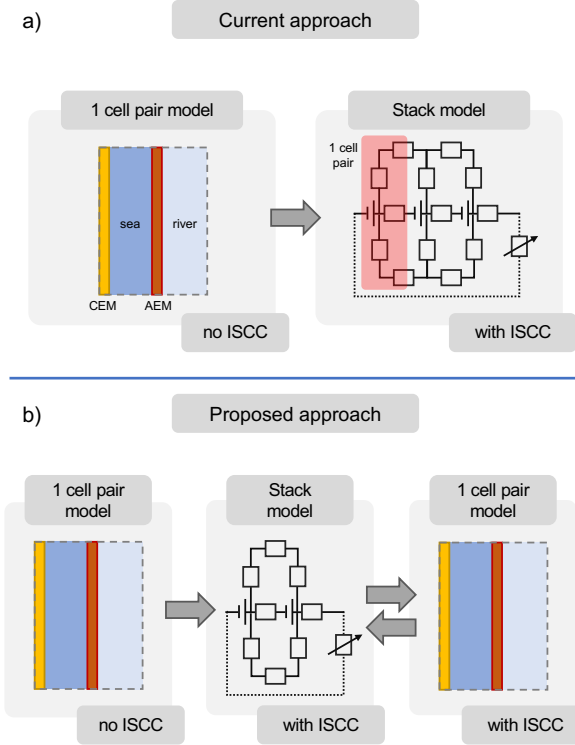

Figure 7.3 a) current RED modeling approach, where a single cell pair is modeled and its output is used for the inclusion of ionic short-circuit currents with a separate network model. b) proposed RED modeling approach, where an iterative process occurs between stack network model and an extended cell pair model, which includes the effect of ionic short-circuit currents.

To overcome this limitation, an iterative process can be introduced between the stack network model and the cell pair model (Figure 7.3b), with a corrected electromotive force accounting for the ohmic drop associated with the ISCCs

$$E_{w/ISCCs} = E_{Nernst} - \Delta E_{ISCCs}(U) \qquad \text{(Eq. 7.2)}$$

Where $E_{w/ISCCs}$ is the electromotive force in the presence of ISCCs, E_{Nernst} is the electromotive force calculated with the modified Nernst equation, not accounting for the ISCCs, and $\Delta E_{ISCCs}(U)$ is the electromotive force loss associated to the ISCCs, which is a function of the external load voltage (U).

With the cell pair model receiving information from the stack network model, the available electromotive force gets updated based on the effect of the ISCCs, and new concentration profiles can be calculated, together with updated cell resistance values. These values are then used to update the stack network model.

Finally, to take on the challenge of including real feedwaters and fouling into RED modeling, data-driven modeling approaches based on machine learning (ML) are a promising strategy. The underlying idea for this approach is that there is a relationship between membrane fouling and the characteristics of the membranes and feedwaters. Even though this relationship may be too complex to be framed by mechanistic models, if given a large amount of fouling data, machine learning or deep learning algorithms can infer the relationship and create a model that takes membrane and feed parameters as an input, yielding membrane fouling as an output, e.g., expressed as the MFI. These algorithms have been applied successfully to describe fouling in the field of porous membranes [5]. To predict fouling in a pilot-scale microfiltration system, Lee et al. used genetic programming, which uses an evolutionary process analogous to that of GAs to build a mathematical function describing the relationship between a given input and output [18]. Their results show good agreement between the predicted fouling degree and the measured value, with predictions based on the water temperature, turbidity, organic carbon content, and algae concentration [18]. Similarly, Park et al. used a convolutional neural network (CNN) to evaluate and predict fouling growth and flux decline in nanofiltration/reverse osmosis membranes. By using in-situ optical coherence tomography (OCT), they obtained images of the fouling layer, which were analyzed by the CNN to extract features, which were used to estimate fouling growth and flux decline. In another example, Jaegher et al. presented the development of a hybrid model (partly mechanistic and partly inferred from data), based on neural differential equations, to predict colloidal fouling in electrodialysis, reporting good agreement between the model prediction and the measured data [19,20]. Similarly, large amounts of data on RED fouling from the pilot installation at the Afsluitdijk can be used to build a ML model to relate RED stack and feedwater properties to the degree of RED stack fouling.

7

References

[1]   V. Lindstrand, A.-S. Jönsson, G. Sundström, Organic fouling of electrodialysis membranes with and without applied voltage, Desalination. 130 (2000) 73–84. https://doi.org/10.1016/S0011-9164(00)00075-8.

[2]   S. Pawlowski, P. Sistat, J.G. Crespo, S. Velizarov, Mass transfer in reverse electrodialysis: Flow entrance effects and diffusion boundary layer thickness, Journal of Membrane Science. 471 (2014) 72–83. https://doi.org/https://doi.org/10.1016/j.memsci.2014.07.075.

[3]   C. Park, H. Kim, S. Hong, S.-I. Choi, Variation and prediction of membrane fouling index under various feed water characteristics, Journal of Membrane Science. 284 (2006) 248–254. https://doi.org/https://doi.org/10.1016/j.memsci.2006.07.036.

[4]   H. Huang, T.A. Young, J.G. Jacangelo, Unified Membrane Fouling Index for Low Pressure Membrane Filtration of Natural Waters: Principles and Methodology, Environmental Science & Technology. 42 (2008) 714–720. https://doi.org/10.1021/es071043j.

[5]   M. Bagheri, A. Akbari, S.A. Mirbagheri, Advanced control of membrane fouling in filtration systems using artificial intelligence and machine learning techniques: A critical review, Process Safety and Environmental Protection. 123 (2019) 229–252. https://doi.org/https://doi.org/10.1016/j.psep.2019.01.013.

[6]   A. Daniilidis, R. Herber, D.A. Vermaas, Upscale potential and financial feasibility of a reverse electrodialysis power plant, Applied Energy. 119 (2014) 257–265. https://doi.org/10.1016/j.apenergy.2013.12.066.

[7]   A. Cano-Odena, M. Spilliers, T. Dedroog, K. de Grave, J. Ramon, I.F.J. Vankelecom, Optimization of cellulose acetate nanofiltration membranes for micropollutant removal via genetic algorithms and high throughput experimentation, Journal of Membrane Science. 366 (2011) 25–32. https://doi.org/https://doi.org/10.1016/j.memsci.2010.09.026.

[8]   P. Vandezande, L.E.M. Gevers, N. Weyens, I.F.J. Vankelecom, Compositional Optimization of Polyimide-Based SEPPI Membranes Using a Genetic Algorithm and High-Throughput Techniques, Journal of Combinatorial Chemistry. 11 (2009) 243–251. https://doi.org/10.1021/cc800135u.

[9]   C.W. Coley, N.S. Eyke, K.F. Jensen, Autonomous Discovery in the Chemical Sciences Part I: Progress, Angewandte Chemie International Edition. 59 (2020) 22858–22893. https://doi.org/https://doi.org/10.1002/anie.201909987.

[10]   J. Veerman, M. Saakes, S.J. Metz, G.J. Harmsen, Reverse electrodialysis: Performance of a stack with 50 cells on the mixing of sea and river water, Journal of Membrane Science. 327 (2009) 136–144. https://doi.org/10.1016/j.memsci.2008.11.015.

[11]   J. Veerman, M. Saakes, S.J. Metz, G.J. Harmsen, Reverse electrodialysis: A validated process model for design and optimization, Chemical Engineering Journal. 166 (2011) 256–268. https://doi.org/10.1016/j.cej.2010.10.071.

[12]   D.A. Vermaas, J. Veerman, N.Y. Yip, M. Elimelech, M. Saakes, K. Nijmeijer, High efficiency in energy generation from salinity gradients with reverse electrodialysis, ACS Sustainable Chemistry and Engineering. 1 (2013) 1295–1302. https://doi.org/10.1021/sc400150w.

7

[13]   M. Tedesco, H.V.M. Hamelers, P.M. Biesheuvel, Nernst-Planck transport theory for (reverse) electrodialysis: I. Effect of co-ion transport through the membranes, Journal of Membrane Science. 510 (2016) 370–381. https://doi.org/10.1016/j.memsci.2016.03.012.

[14]   M. Tedesco, H.V.M. Hamelers, P.M. Biesheuvel, Nernst-Planck transport theory for (reverse) electrodialysis: II. Effect of water transport through ion-exchange membranes, Journal of Membrane Science. 531 (2017) 172–182. https://doi.org/10.1016/j.memsci.2017.02.031.

[15]   M. Tedesco, H.V.M. Hamelers, P.M. Biesheuvel, Nernst-Planck transport theory for (reverse) electrodialysis: III. Optimal membrane thickness for enhanced process performance, Journal of Membrane Science. 565 (2018) 480–487. https://doi.org/10.1016/j.memsci.2018.07.090.

[16]   J. Veerman, J.W. Post, M. Saakes, S.J. Metz, G.J. Harmsen, Reducing power losses caused by ionic shortcut currents in reverse electrodialysis stacks by a validated model, Journal of Membrane Science. 310 (2008) 418–430. https://doi.org/10.1016/j.memsci.2007.11.032.

[17]   A. Culcasi, L. Gurreri, A. Zaffora, A. Cosenza, A. Tamburini, A. Cipollina, G. Micale, Ionic shortcut currents via manifolds in reverse electrodialysis stacks, Desalination. 485 (2020). https://doi.org/10.1016/j.desal.2020.114450.

[18]   T.-M. Lee, H. Oh, Y.-K. Choung, S. Oh, M. Jeon, J.H. Kim, S.H. Nam, S. Lee, Prediction of membrane fouling in the pilot-scale microfiltration system using genetic programming, Desalination. 247 (2009) 285–294. https://doi.org/https://doi.org/10.1016/j.desal.2008.12.031.

[19]   B. de Jaegher, W. de Schepper, A. Verliefde, I. Nopens, Enhancing mechanistic models with neural differential equations to predict electrodialysis fouling, Separation and Purification Technology. 259 (2021) 118028. https://doi.org/https://doi.org/10.1016/j.seppur.2020.118028.

[20]   B. de Jaegher, E. Larumbe, W. de Schepper, A. Verliefde, I. Nopens, Colloidal fouling in electrodialysis: A neural differential equations model, Separation and Purification Technology. 249 (2020) 116939. https://doi.org/https://doi.org/10.1016/j.seppur.2020.116939.

7

Acknowledgment

Thank you
Bedankt
Grazie
谢谢

Time flies. This short sentence is the one I most frequently repeated in the last four years. Incredibly, the end of my PhD is already here. It would have not been possible to reach this milestone without the many people who played an important role in my project.

The chair and members of the **Doctoral Committee**. The time and effort you put into reading this dissertation, critically evaluating it, and taking part to the defense is highly appreciated. Thank you.

Kitty Nijmeijer (1st promotor) and **Zandrie Borneman** (2nd promotor). Thank you for guiding me along the PhD path. None of this would have happened if you did not pick me, and I am grateful that you trusted me to deliver and granted me the freedom to take the research directions that I found most appealing. That freedom helped me grow as a researcher together with valuable lessons. The most precious ones being *Good enough is better than perfect* together with the value of a quick Friday afternoon experiment. I am not very fond of writing, but you convinced me that it is a necessary evil (*If it is not published, it did not happen*), and you helped me greatly to improve my scientific writing skills.

Michel Saakes (daily supervisor). Thank you for your guidance and the contagious enthusiasm. You lead by example. Seeing my daily supervisor tinkering in the lab was a great motivation to keep trying. I showed you a lot of results over the years, but for you no result is ever bad. When the results were good, you were the one who got most excited. I am amazed by how fast you can review a manuscript and reply instantaneously to my emails, despite being involved in so many different projects (and, as far as I know, not using a smartphone). You were always one step ahead, and trying to keep up made me a better researcher. Wetsus is lucky to have you on their roster, and so was I.

Blue energy (BE) theme. One of my predecessors prepared me for my first theme meeting by saying that the BE theme is *a train that moves fast, where you hop on in the back, and over time you move to the front*. True, there is a sense of purpose and a desire to deliver in the theme that keeps us running. Contributing to this theme was a great experience. I am grateful for the financial support, the exchanges during the meetings, and the feedback on reports, manuscripts, and presentations. In particular, many thanks to **Simon Grasman**, **Jordi Moreno**, **Kristan Goeting**, and **Joost Veerman** from REDstack for all the extra meetings and valuable discussions. Special thanks to Joost and his REDnews for making

it very easy to keep up with RED literature. Also, thanks to **Marcel Geers** from Qirion for the precious discussions on circuits and simulations, in addition to all other feedbacks and ideas. I am grateful to **Willem van Baak** (now at Water Future), **Ronny van Engelen**, and **Elisa Huerta-Martinez** for the discussions we had in the beginning of my PhD and for the endless supply of membranes to play with in the lab. Thanks to **AquaBattery** and their flexibility with the design of their AquaSeal spacers, which enabled my stack impedance studies.

Wetsus. The brainchild of **Cees Buisman**, **Bert Hamelers**, and **Johannes Boonstra**, Wetsus is an amazing place to do research. The concentration of expertise, resources, and support opens up possibilities that other researchers can only dream of. Thank you for making and keeping it possible.

Caroline (MM/P group secretary). You know all the details and helped me navigate forms, attachments, and deadlines. For that and all the work you do to keep MM/P running smoothly, thank you.

MM/P group. You are a diverse group of nice and talented people. I had a good time at our group lectures with lunch, and during our summer and winter activities. Thank you. In particular, **Cees** and **Sjoukje** deserve a special mention for all the help setting up the OGO courses and my experiments in the MM/P labs. Also, many thanks to **Anna** and **Niki**. Organizing the first OGO was a challenge, and having you to help on the second and third rounds made a huge difference. Thank you **Pelin** for the support in the OGO energy and for teaching me how to use some of the instruments. Many thanks to Cees and **Daniëlle** for analyzing membrane samples at TU/e. Thanks to Daniëlle also for our collaboration on layer-by-layer modification. I hope my follow-up will pick it up from where we left it. Special thanks to those of you who devoted time and energy to peer-review my work (**Anna, Niki,** Daniëlle**, Menno,** and Gijs). Also, many thanks to my (commuting) Wetsus-MM/P peers from the old days: **Andrew**, **Gijs**, and **Emad**. The trips to and from Eindhoven took much time, but you filled it with nice chats and jokes.

Blue energy PhDs. Many thanks to **Jordi** and **Timon** for all the discussions and precious advice in the early stages of my project. In particular, thanks to Jordi for all the RED tutorials in the experimental hall and at the Afsluitdijk. Thanks to **Jan Willem** for all the discussions on water transport and for giving me his equipment. Thanks to **Elias** for

sharing all the difficulties of the early stages of our projects. It's a pity not having you around now. Thanks to **Malgorzata** for all the membrane talks and for sharing your six-compartment cell wisdom. Thanks to **Bárbara** for the help in the lab and our fouling discussions. Special thanks to **Catarina** for our discussions and collaboration. Bárbara and Catarina, many thanks also for the extra support you provided as paranymphs in this last phase of my PhD journey.

My students. Doing research can be time consuming, so students can provide great help. I was lucky and had some of the best students. Thank you for all the help, **Twan, Jeffrey, Nynke, Pauline,** and **Yuris**. I learned a lot while working with you. I hope I was half as good a supervisor as you were good as students.

Analytical and technical support teams, HR, PR, secretaries, talent team, concierges, ICT, canteenees, cleaning staff, and gardeners. Thank you for all the hard work you do in the background of the scientific research. In particular, I am very grateful to **Harm** and **John** for all the help in building my experimental setup and keeping it running.

Wetsus people. Thank you all for living the Wetsus values (**innovation**, **partnership**, **cooperation**, **reliability**, and **joy**) and creating a very nice, fun, and supporting environment.

PV. Thank you to the PVs from 2017 to 2021 for all the activities they organized.

Chinese Wetsus crew. Special thanks to **Gaofeng** for being an amazing neighbor when we were living in Pieter de Swartstraat. Many thanks to uncle **Qingdian**, uncle **Ruizhe**, and auntie **Yujia** for all the love they bring to the little one when they visit. **Yin** and **Yang**, thank you for being such role models. Also, **Xiaoxia**, **Farid** and **Bingnan**, thank you for the nice meals together and the love you send to the little one.

Office 1.10C. I was lucky to have many amazing people as office mates: **Prashant, Hector, Sam, Mariana, Gosia, Emanuel, Rebeca, Kaustub, Rose, Emad, Bárbara & Marianne, Jolanda, Marco, João, Kestral** and (another) **Sam**. Thank you for the nice time together and good luck!

Family. Un grazie di cuore alla mia famiglia. Mamma, papà, Delia, Nadia (e Dario). Il vostro supporto e la vostra comprensione sono delle costanti su cui posso sempre contare. Devo ringraziare Nadia e Dario per avermi attirato nei Paesi Bassi ed essere sempre in prima linea a supportarci qui al Nord. Grazie di cuore a Delia, che si fa carico di tutto in nostra assenza.

Zexin. Thank you for all the love and the support. You are a loving wife and a wonderful mother.

Mia Qian. Ultima, ma non per importanza, la mia adorata patatina. Grazie di esistere. Hai dato un senso a tutto. Il tuo amore incondizionato mi sprona ad essere una persona migliore ogni giorno.

The people I forgot to mention. Sorry about that, and thank you.

Curriculum Vitae

Diego Pintossi was born in Bergamo (Italy) on June 17th, 1991. In 2010, he started his Bachelor of Science studies in Materials Engineering at Politecnico di Milano (Milan, Italy), which he completed with honors in 2013. He obtained his double Master of Science title with laude, also in Materials Engineering, from Politecnico di Milano and Politecnico di Torino. In parallel to the M.Sc, studies, Diego attended Alta Scuola Politecnica, an institution focusing on multidisciplinarity and innovation. After graduating in December 2015, he worked for one year as a research assistant in the laboratory of Chemistry and Characterization of Innovative Polymers at Politecnico di Milano. In 2017, Diego moved to the Netherlands and started his PhD in the Blue Energy research theme at Wetsus, in Leeuwarden, with affiliation to the Membrane Materials and Processes group at Eindhoven University of Technology. After completing his Ph.D. in 2021, Diego plans to join the research group of Timothy Noël at the University of Amsterdam as a post-doc, where he will merge his love for experimental work with his passion for code and automation.

List of publications

Journal articles:

Pintossi, D., Saakes, M., Borneman, Z., & Nijmeijer, K. (2019). Electrochemical impedance spectroscopy of a reverse electrodialysis stack: A new approach to monitoring fouling and cleaning. *Journal of Power Sources*, *444*, 227302.

Pintossi, D., Saakes, M., Borneman, Z., & Nijmeijer, K. Tailoring the surface chemistry of anion exchange membranes with zwitterions: towards anti-fouling RED membranes. [submitted to *ACS Applied Materials & Interfaces*]

Simões, C., Pintossi, D., Saakes, M., Borneman, Z., Brilman, W., & Nijmeijer, K. (2020). Electrode segmentation in reverse electrodialysis: Improved power and energy efficiency. *Desalination*, *492*, 114604. [shared first-authorship]

Pintossi, D., Chen, C. L., Saakes, M., Nijmeijer, K., & Borneman, Z. (2020). Influence of sulfate on anion exchange membranes in reverse electrodialysis. *NPJ Clean Water*, *3*(1), 1-10.

Pintossi, D., Saakes, M., Borneman, Z., & Nijmeijer, K. Predicting reverse electrodialysis performance in the presence of divalent ions for renewable energy generation [submitted to *Applied Energy*]

Simões, C., Pintossi, D., Saakes, M., & Brilman, W. (2020). Multistage reverse electrodialysis: an experimental and model investigation with artificial river and seawater. [second-author, submitted to *Applied Energy*]

Other contributions:

Poster presentation at NPS15 (2018) at University of Twente.

Lecture to the Japie-Octave Symposium (2018) – Sustainability in Chemical Industry: Challenges and Solutions at Eindhoven University of Technology.

Poster presentation at NPS16 (2019) at Eindhoven University of Technology.

Poster presentation at Chains 2020 (online conference).

Oral lecture at ICOM 2020 (online conference).